Coded Aperture Breast Tumour Imaging using a Full-size Clinical Gamma Camera

Mohammed Alnafea, MSc

Submitted for the Degree of
Doctor of Philosophy from the
University of Surrey

Department of Physics
School of Electronics & Physical Sciences
University of Surrey
Guildford, Surrey
GU2 7XH, U.K.

August 30, 2007

Abstract

Scintimammography is a promising functional radionuclide imaging technique that is generally undertaken using high resolution parallel-hole collimators with Anger cameras. This technique suffers from some clinical limitations as it is less reliable at detecting small (less than 1 cm in diameter) lesions. These limitations are due to resolution-efficiency trade-off that is inherent in the use of collimation.

As an alternative approach this study proposes using a simple Coded Aperture (CA) mask, instead of a collimator, coupled to a standard clinical gamma camera for breast tumour imaging. This is particularly attractive at General Hospital level, where the cost of running an additional dedicated imaging system may be prohibitive. In addition, CA imaging as originally developed for astronomical applications, is well suited to detecting faint pseudo-point like objects in a non-zero background; thus it appears to be well matched to the imaging objectives in SM.

The thesis introduces and investigates the applications of the CA imaging technique for breast tumour imaging using a combination of three methods. The first method is entitles binary mask shift which consists of superimposing a set of aperture pattern projections, the second method is based on pseudo-ray tracing and finally the third method is based on using Monte Carlo Simulation (MCS). All these methods successfully produce comparable results and predict the overall form of artefacts arising from the near-field imaging geometries. The predicted background can be used to correct the near-field effect of 3D sources, as might be found in SM using CA.

To emulate SM, 3D pseudo-anthropomorphic phantoms (including torso, heart, breast and tumors) have been developed and verified using MCS (using MCNPX) and used along with a realistic model of a clinical gamma camera. This study examines a moderately compressed breast phantom in a cranio-caudal-projection i.e. a similar view to that used in conventional X-ray mammography. The performance of such an imaging system is modelled by MCS method and images are reconstructed by correlation analysis. This imaging system was quantitaively evaluated using variable parameters: the detected photon from tumour, spatial resolution, photon statistics and lesion visibility of the system at several tumour-background activity ratios.

In addition, the effectiveness and the performance of the CA-SM system are also com-

pared with that of a low energy high resolution parallel-hole collimator and ultra-high resolution parallel-hole collimator image formation systems. The simulated planar images from these collimator-based image formation systems suggest tumors of 1 cm diameter may be observable with a tumour-background-ratio of 5:1. However, when tumour diameter is $\leq$ 0.8 cm these become less reliable detecting small (less than 1 cm in diameter) lesion unless a tumour-background-ratio of more than 10:1 is used. The results of the simulations demonstrate that with near-field artefacts corrections the CA-SM approach shows good performance in lesion detection for all lesions (located 3 cm deep in a 6 cm thick breast phantom) and for a tumour-background ratio as low as 3:1. This level of performance is highly competitive, in some cases, superior to conventional collimator-based image formation methods.

Acknowledgment

All praise is for Allah, the Exalted; may He send peace and blessings on Prophet Muhammad, on his family, and on his companions. I feel very fortunate to work with many knowledgeable and wonderful people in Surrey. I would like to express my gratitude to everyone of them who has a part in this thesis. First, I would like to express my deepest gratitude to my academic supervisor, Dr Kevin Wells for his experience and support throughout this project. He is a real scientist and his enthusiastic attitude has made this thesis possible. I thank him a lot for his excellent guidance, professional support, constant encouragement and contribution to this work. I am indebted to him for his willingness to write recommendation letters for me.

Special thanks go to my second supervisor Professor N.M. Spyrou for his careful review of my thesis and his excellent suggestions. It was because of his excellent teaching helped me get a unique perspective on radiation physics and broadened my horizon to nuclear medicine research. I am also grateful to Dr M.J. Guy and Dr P. Hinton for their help on the experimental work that has been carried out, at Royal Surrey County Hospital, to validate the Monte Carlo simulation.

I greatly appreciate the tremendous help and advice on research, life, and everything from, my close friend, Dr Djelloul Mahboub. He has always been able to answer my questions and he never refused giving his time and advice when needed.

My research would not be the same without the help from my colleagues at Surrey. Ali Alghamdi and Andy Ma for their assistance on Monte Carlo simulations. Another important person M.I. Saripan for sharing with him many useful information. I enjoy the wonderful time with my former and current office mates: in particular Najat Mohammed, Carol Butler, Mohammed Alkhorayef, Khalid Alzimami and Wejdan Kaabar. I would like also to thank all colleagues in the CVSSP. I wish to express my warmest thanks to all of them for sharing their talents, humour, and criticisms.

Most importantly, I thank my wife Nawal Albahlal and my children Ali, Zahra, Albara and Lyan for their unconditional love and warm support. They add a lot into my life in Surrey, and they were always there to share my joy and sadness. Without them, I would never have the chance to fulfil my dream. This dissertation is dedicated to to my parents, my father Ali who passed away half way through my PhD study and my mother Zahra.

Finally, my PhD study was fully funded by the Saudi Arabian Government through King Saud University and I would like to thank every one was contributed in the aspects releated to this scholarship.

Acronyms and Abbreviations

A list of acronyms and abbreviations used frequently in this thesis is given below.

SM	Scintimammography
DCIS	Ductal Carcinoma in situ
LEHR	Low Energy High Resolution
LCIS	Lobular Carcinoma In Situ
WHO	Worled Health Organisation
PPV	Positive Predictive Value
NPV	Negative Predictive Value
ROC	Receiver Operating Characteristic
DM	Digital Mammography
US	Ultrasonography
MRI	Magnetic Resonance Imaging
PET	Positron Emission Tomography
SPECT	Single Photon Emission Tomography
FDG	FluroDeoxyGlucose
PEM	Positron Emission Mammography
TBR	Tumour-to-Background-Ratio
2D	Two Dimensional
3D	Three Dimensional
PSPMT	Position Sensitive Photo-Mutiplier Tube
SNR	Signal-to-Noise-Ratio
CZT	Cadmium Zinc Telluride
CA	Coded Aperture
PMTs	Photo-Mutiplier Tubes
FoV	Field of View
PHA	Pulse Hight Analyzer
FWHM	Full Width at Half Maximum
NaI	Sodium iodide
FZP	Fresnel Zone Plate
NRA	Non-Redundant Arrays

PSF	Point Spread Function
S	cyclic difference set
URA	Uniformly Redundant Arrays
MURA	Modified Uniformly Redundant Arrays
NTHT	No-Two-Hole-Touching
FFT	Fast Fourier Transform
MCS	Monte Carlo Simulation
BMS	Binary Mask Shift
PRT	Pseudo-Ray Tracing
RoI	Region of Interest
MC	Monte Carlo
PTRAC	Particle Track Output Card
MTF	Mudulation Transfere Function
TEM	Tissue Equivalent Material

List of Symbols

The Mathematical operation indicates a discrete 2d function or matrix.

$\otimes$	correlation (periodic): $H(\vec{y}) = F(\vec{x}) \otimes G(\vec{x}) = \int\int F(\vec{x})G(\vec{y} \oplus \vec{x})d^2\vec{x}$
$\times$	correlation: $H(\vec{y}) = F(\vec{x}) \times G(\vec{x}) = \int\int F(\vec{x})G(\vec{y} + \vec{x})d^2\vec{x}$
$*$	convolution: $H(\vec{y}) = F(\vec{x}) * G(\vec{x}) = \int\int F(\vec{x})G(\vec{y} - \vec{x})d^2\vec{x}$
$\oplus$	sum modulo p

Capital bold indicates a discrete 2d function or matrix where as Capital and lowercase italic indicates a continuous 1d function or a scalar variable.

$\mathbf{A}$	aperture transmission function
$\mathbf{G}$	decoding array
$\mathbf{O}$	object intensity distribution
$\mathbf{I}$	the reconstructed image
N	total number of positions in a mask
M	side-lobe height
K	total number of open holes in a mask
c_r	quadratic residues modulo r
d_s	detector size
$\vec{r}$	position vector
FoV	field of view
m_s	the mask size
m_c	magnification coefficient
p_m	mask pixel size
d_s	the detector size
G_r	mask geometric resolution
a	object-to-mask distance
b	mask-to-detector distance
z	object-to-detector distance
δ	delta function
α	sampling parameter

Ω	solid angle
μ	attenuation coefficient

Contents

List of Figures

List of Tables

Chapter 1

Overview & Background

The goal of this chapter, is to introduce the problems caused by breast cancer. Starting with the structural anatomy of the normal breast, an overview of the pathology and the treatment options of breast cancer are then presented. The requirements for breast tumour imaging are briefly described and the diagnostic techniques used for breast cancer assessment are also discussed, highlighting the advantages and disadvantages of each technique. In addition, the problems associated with a relatively new functional breast imaging technique: Scintimammography (SM) is introduced and thus, the primary motivations for investigating the application of coded aperture approach for breast tumour imaging is highlighted. It is intended that this chapter provides the reader with sufficient background on the available diagnostic techniques of breast tumour imaging approach, as well as an overview of the literature.

1.1 Introduction

Cancer is a disease that starts in a localised organ or tissue and then grows out of control. Breast cancer is an important health problem as in the western world it is the second most frequent cause of cancer death in women (after lung cancer) [1, 2]. Statistics show that a large number of women in Europe, North America, Australia and many Latin-American Countries suffer from this life-threatening disease [3]. Worldwide, in the year of 2005, the number of new cases exceeded 1.2 million [2]. Breast cancer is rare in women below the age of twenty years and less common below the age of thirty years but it is more aggressive and thus has a lower survival rate. The incidence rate however, rises dramatically over the

age of 50 years. This is may be due to several risk factors such as family history, genetics, early menstruation, late menopause and other factors that have not yet been identified. Breast cancer can also occur in males and often fatal but it is extremely rare.

The above problems have prompted global governments to put constant efforts to increase patient's recovery level against this disease. Early and accurate detection with mass screening programs helps improves a woman's chances for successful treatment. It also minimises pain, suffering and anxiety that surrounds patient's and their families. The current and the most cost effective technique used for screening and diagnosis of breast cancer is X-ray mammography. It is the state-of-the-art for earlier detection to improve both prognosis and survival rate [4]. This is may be due to its good availability, high sensitivity and relatively low cost/patient.

Despite the above efforts the mortality rate of breast cancer still remains high and in the UK accounts for $\approx$ 17% of all female deaths [5]. This is due to some limitations of the current mammographic procedures. As a result, a large number of cases with positive mammography results undergo invasive surgical breast biopsies (see section 1.5.3). These techniques are often uncomfortable, stressful, and also increase patient's radiation exposure. In addition, such techniques are time consuming and causes large medical expenditure. However, breast biopsy still widely used and thus is the only failsafe method to determine whether a lesion is a malignant. Of all biopsy cases only about 25% prove to be malignant. Moreover, a majority of the diagnosed women below the age of 50 have a dense breast tissue. This is a problematic as it obscures lesions and results in false negative mammographies. For the aforementioned reasons, the use of complementary imaging techniques, to aid in the diagnosis, is necessary. A brief overview of these techniques and their strength and weakness is given in section 1.7.

Among these methods, non-invasive SM is becoming widely used for breast cancer diagnosis. This is a radionuclide imaging technique in which a radiopharmaceutical is injected into the patient and then gets trapped by the tumour tissue. This means that the tumour has a slightly higher uptake than the surrounding healthy (normal) breast tissue. A gamma camera, employing a Low Energy High Resolution (LEHR) parallel-hole collimator is used, to generate an image of the resulting radionuclide distribution. For details of the gamma camera assembly, how the camera works and a review of the literature of SM imaging see chapter two. The LEHR collimator geometrically selects

γ-photons from a predetermined direction and as a result a very small fraction of the total emitted photons reach the detector. This however, limits the statistics and thus, the quality of the observed image as the detection efficiency and spatial resolution of such a collimator are also trade-off. Factors like these, have generated massive research aimed to improve the accuracy and efficiency the current SM imaging systems and reduce the over all costs of breast surgical biopsies procedures but without the need for the new dedicated camera instrumentation development. This is one of the primary motivations to undertake this research project.

1.2 The Morphology of Normal Breast

The breast tissue extends from below the collarbone to the level of the sixth or seventh rib, and from the breast bone to the underarm (axilla). Each breast is made up of ducts and about 15-20 lobes [6] surrounded by fat cells and connective tissue as shown in Fig. 1.1. Each lobe contains hundreds of gland cells (lobules) that are responsible for producing milk in women following pregnancy. In the centre of the breast is the nipple and areola (circular area around the nipple).

Breast fluids are circulated by both blood stream and lymphatic vessels. Blood carries nutrients where as the lymphatic vessels carries the lymph. This is a clear fluid that contains waste product and immune system cells. Most lymphatic vessels, in the breast, drain into a network of lymph nodes. The location of these lymph nodes are around the breast edges, in the underarm, and near the collarbone. These lymph nodes are usually embedded within fat. Axillary lymph nodes are often the first site of breast cancer metastasis. At this stage, the cancer will continue to grow and will eventually spread out to other organs or parts of the body.

1.3 The Pathology of Breast

Breast cancer is a heterogeneous disease as it has different cell types, different behavioral characteristic and appearance. Understanding the types of breast cancer and their growth pattern is important for imaging purposes. Breast cancer is usually categorised into two main types; invasive (infiltrating) and noninvasive (in situ) cancer. In situ means that the cancer cells are at early stage i.e. remains localised to ducts (milk passages) or lobule

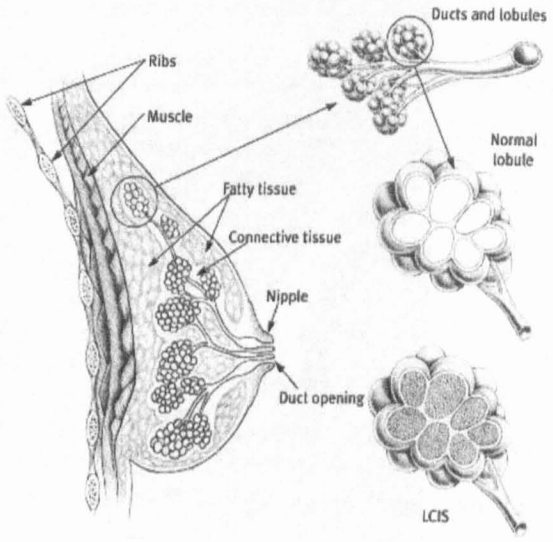

Figure 1.1: A schematic cross sectional diagram of the structural anatomy of the normal mammary gland. Figure taken from [7].

(milk producing glands) with no micro-invasion to the surrounding fatty tissue. Once the basement membrane is penetrated, the cancer cells break into the surrounding tissue and are refered to as invasive breast carcinoma.

1.3.1 Non-Invasive Carcinoma

In situ carcinoma is a non-invasive breast cancer that represents $\approx 90\%$ of all carcinoma [9]. It is often non-palpable and not life-threatening but it is regarded as a 'marker' (signal) that may develop invasive breast carcinoma. In situ carcinoma is subdivided into several groups depending on its location, appearance and microscopic characteristic.

Ductal Carcinoma In Situ

Ductal Carcinoma In Situ (DCIS) (see Fig. 1.2) is usually detected by the presence of microcalcification on mammography. Most detected DCIS cases present with no symptoms or signs of breast disease. DCIS is often subdivided into comedo and non-comedo types. The comedo type is characterised by a rapid growth of cancer cells but the centre of the involved ducts are necrotic (dead). This is because there is not enough blood supply and thus inadequate nutrition in the centre but the surrounding tissue are viable living cells.

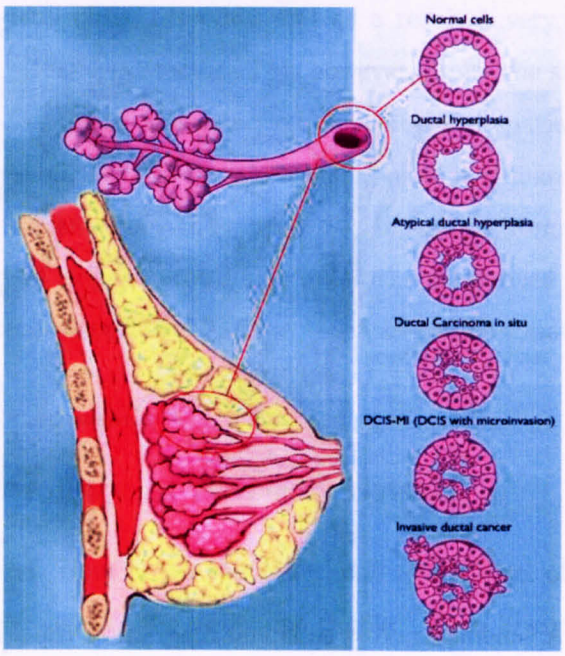

Figure 1.2: Types of of DCIS. Figure taken from [8]

The central area of necrosis (damaged tissue) often demonstrates soft tissue mineralization (calcification) [10].

Lobular Carcinoma In Situ

Lobular Carcinoma In Situ (LCIS) is also called lobular neoplasia. It is characterised by a sharp increase in the number, and appearance of lobular cells. This type of breast cancer is commonly occur in younger women and always non-palpable and thus, difficult to detect. However, it can be detected or diagnosed in two ways. First, if found close to clinically or mammographically detectable lesion. Second, through histopathological examination of tissue from breast biopsies. Involvement of one complete lobule in a biopsy is usually sufficient for the diagnosis. The histology shows that LCIS is often multi-centric (lesions found in more than one duct system). The LCIS frequently presents in both breasts (bilateral).

Papillary Carcinoma

Papillary carcinoma is a less common type of breast cancer with the papillary lesion presented within a distended duct. It is often attached to more than one site on the duct wall. It also occurs in the subareolar duct and thus, is often associated with a bloody nipple discharge.

1.3.2 Invasive Carcinoma

This is the most common and as the name suggests is the most aggressive type of breast cancer. This is because the cancer cells are capable of spreading to other part of the body via either bloodstream or lymphatic system. Thus, it is considered the main cause of cancer death. This type of breast cancer has also many forms and subtypes depending on its location.

Ductal Carcinoma

Ductal carcinoma originates in the duct and then invades the surrounding tissues as demonstrated in Fig. 1.2. The cancer cells also have the possibility to spread and metastasise other organs such as liver, lungs and bones. Ductal carcinoma comprises about 75-80% [2] of all invasive breast cancers. According to the World Health Organisation (WHO) classification, ductal carcinoma can be divided into two main subgroups [3]. The first group is characterised by reactive fibrosis (scar-like tissue). This type appears as a spiculated tumour on the mammogram. The second group, is less fibrotic and also more regular in outline with a predominant intraductal component.

Lobular Carcinoma

Lobular carcinoma grows through the wall of the lobules and is often difficult to detect either clinically or mammographically, because of the absence of associated microcalcifications. It is usually characterized by growth patterns of invasive carcinoma. This growth pattern may be intermixed with ductal forms of invasive carcinoma and sometimes associated with either LCIS or DCIS. Nearly 15-20% of invasive breast carcinoma originate in lobules [3].

Colloid Carcinoma

Colloid carcinoma is a slow growing cancer but characterised by large extracellular mucin (a family of large proteins scattered outside the cell) surrounding nests of carcinoma cells. Such carcinomas are typically circumscribed and may have adjacent foci of DCIS. However, this type of breast cancer is often associated with a relatively good prognosis [3].

Tubular Carcinoma

Tubular carcinoma is a well differentiated form of invasive breast carcinoma. It is usually seen to be associated with foci of DCIS, and is characterised microscopically by relatively uniform angulated small ducts which invade mammary stroma.

Medullary Carcinoma

Medullary carcinoma have similar presentation as other breast cancer but have a distinguished microscopical appearance marked by the presence of white blood cell in and around the lesion. This form of invasive breast carcinoma has aggressive histologic appearance but luckily it is often associated with a relatively good prognosis.

Adenoid Cystic

Adenoid cystic (fluid filled sacs) is a rare form of malignant breast cancers arises within secretory glands surrounding breast tissue. This form of invasive breast cancer has a distinctive microscopical appearance.

1.3.3 Other Benign Breast Diseases

Most breast problems are benign diseases [11] but need to be clearly distinguished from the malignant diseases. This is because the majority of benign disorders are harmless conditions and thus, the use of surgical breast procedures in these should be avoided. Benign breast disorders include some type of cysts, fibro-cystic nodular, fibrosis, adenosis (gland disorder), fibro-glandular and the most common tumour in young women fibro-adenomas (solid marble-like lumps). These conditions may begin to rise early in women life but with higher incidences occur after the age of forty. These abnormalities may be caused by tissue inflammations during tissue development (physiological changes) and

proliferations (cells growing and increasing in number) or due to hormone imbalances [11]. Careful assessment and follow up are needed as some of these disorders may develop breast cancer.

1.4 Requirements for Breast Imaging

The size, shape, and appearance of the female breast is not constant but undergoes a number of changes during the lifetime of women. For instance, changes occur with pregnancy, breast feeding, and during the menstrual cycle. In addition, the age of the subject not only influences the shape but also parenchymal density of the breast. That is why young women tend to have dense breasts (more fibro-glandular tissue), creating a rounded appearance. On the other hand, post-menopausal women have breasts containing a large amount of fat. This makes the X-ray mammogram far more effective in older women as the fat content is more radio-translucent (appears darker) compared to glandular tissue (appears under-exposed) in younger women [12].

The above discussion suggests that both the shape and parenchymal density of the breast imposes particular constraints on the choice of imaging modality. The imaging technique should be powerful for initial detection and subsequent follow-up of the diseases. At present, no single technique can be used for all cases of breast cancer detection without showing certain clinical or technical limitations. This implies necessity to address the specific needs that can help for breast tumour imaging to overcome these limitations. For instance, breast compression is often needed as it holds the breast still and enhances the spatial resolution. It also evens out the breast thickness and reduces scatter in X-ray or γ-ray imaging [13], thus increasing image sharpness. Moreover, it spreads out the tissue so that small abnormalities will not be obscured by the overlying breast tissue.

Since the breast is an external organ and extends to the chest wall it requires appropriate views to be taken. For instance, in X-ray mammography a lateral (from the side) view of the breast allows separation of the chest wall from lesions deep within the breast. On the other hand, in single photon γ-ray emission imaging, one needs to separate the breast from the heart by employing an appropriate prone (face down) position. However, it has been claimed that with prone imaging view there is a possibility of missing a small low-intensity medial lesion because of attenuation. This implies that another image is

needed but with the camera positioned in the lateral view. In addition, shielding the camera from the background cardiac flux is very useful in tumour detection in terms of contrast and resolution as will be demonstrated later in the thesis.

1.4.1 Interpreting Imaging Test

The idea in using any diagnostic test is to be able to correctly diagnose the disease and easily interpret the results. The latter is achieved by calculating the probability that a patient has a disease. The diagnostic test performance can be measured by calculating four important statistical parameters. These are the test's sensitivity, specificity, positive predictive value (PPV), and negative predictive value (NPV) [14, 15]. Table 1.1 illustrates these parameters and their relationship. In breast tumour γ-ray imaging these parameters are dependent on clinical history, biological factors such as size, site or location, the type of the lesion and patient's age. The test parameters may also depend on the physical and the practical aspects as well as the imaging technology parameters. Sensitivity and specificity are properties of a test that tell us how good the diagnostic test is at predicting the disease and whether it is to be used or not [14]. Sensitivity is the proportion of people with the disease who have a positive test for the disease [14]. Specificity is the proportion of people without the disease who test negative [14]. A high sensitivity test means that the test has a low rate of false-negatives and high specificity means that the test has a low rate of false-positives.

In clinical practice the decision to send patients for breast biopsies is arbitrary i.e. there is no fixed test threshold. Instead the decision is usually based on the needs of patients and clinicians for the different clinical situations. As a result, for any given image of a breast lesion, there is a kind of trade-off between the sensitivity and specificity i.e. sensitivity can only be increased by decreasing specificity of a test. For instance, if the decision is to only select patients with extremely abnormal images to have breast biopsy, then the test will become extremely specific but not very sensitive. In this case many patients are falsely diagnosed as not having breast cancer. On the other hand, if the decision is to send patients with borderline abnormal images to have biopsy, the test will then become more sensitive but less specific. As a result, many patients who do not have breast cancer may be sent for an unnecessary biopsy. This sensitivity specificity trade-off of the diagnostic test can be accurately illustrated by the analysis of the Receiver Operating Characteristic

(ROC) curve at each test threshold or cut-point. This curve is basically a plot of the true positive rate against the false positive rate for the different possible thresholds of the diagnostic test. The area under the ROC curve is a measure of test accuracy i.e. how well the test separates or classifies the patient population into those with the abnormality and those without. An area of 1 represents excellent performance test and an area of 0.5 represents a fail test.

Table 1.1: The main diagnostic test parameters [14, 15].

Test Outcome	Condition as determined by "gold" standard		
	True	False	
Positive	True positive	False positive	⇒ Positive predictive value
Negative	False negative	True negative	⇒ Negative predictive value
	⇓ Sensitivity	⇓ Specificity	

To know the probability that the imaging test is giving the correct diagnosis the positive and negative predictive values need to be calculated. The PPV of a test is the probability of a patient having the disease following a positive test result [15]. The NPV is the probability of a patient not having the disease following a negative test result [15]. These test performance measures are influenced by the prevalence (probability of disease in the entire population at any point in time) of the abnormality in the population tested [15]. The predictive values also vary as a function of disease prevalence depending on patient subpopulation. Thus, a combined measure of diagnostic performance, the likelihood ratio, is a clinically useful diagnostic test performance measure. Negative likelihood ratios measure the ability of the test to accurately "rule out" disease, and positive likelihood ratios measure the ability of the test to accurately detect disease.

1.5 Detection & Diagnosis of Breast Diseases

Breast lesion investigations may include self or clinical breast examination, X-ray mammography and biopsy. In addition, a variety of other efficient complementary imaging modalities (see section 1.7) that provide additional information to achieve a definite breast

diagnosis. The following subsections give an overview of the main diagnostic techniques used for breast tumour imaging.

1.5.1 Breast Physical Examinations

The initial steps in evaluating breast disease are with history and physical examination. Women are recommended to practice regular breast self-exams to gain familiarity of normal breast morphology so it becomes easier for a patient to find changes that may occur. Women are also recommended to have their breasts examined by physician at least every 2-3 years. The examination may include careful feeling the lesion and the tissue around it, its size, location and its texture. Nipple discharge examination is also included if needed. However, a high sensitive imaging method is still needed particularly for non-palpable or deep seated lesion smaller than 1 cm.

1.5.2 X-ray Mammography & Screening

Mammography is a low-energy (25-32 keV) X-ray examination of the soft tissues of the breast. It uses the variation in density between normal mammary features and abnormal tissue structures (lesion) to produce the image. The current widely used technique is based on screen-film technology. It is considered the gold standard in breast imaging as it is fast, available and has a lower cost than SM. It has two main applications: as a screening method in asymptomatic patients, and as a diagnostic method in symptomatic populations. The former application is extremely important and its introduction has significantly reduced the mortality rate of breast cancer in many countries [16, 17]. This is because the screening services accurately detect microcalcifications and non-palpable soft tissue masses which until now have been beyond other imaging methods thanks to the high spatial resolution ($\sim 50 - 100\ \mu m$). Normally, screening is achieved by exposing the breast to X-rays after being gently compressed between two plates, and then taking two views for each breast. A craniocudal (imaging from above to below) and lateral views are generally taken. A lead grid is used to reduce scattering photons that reach the film. Diagnostic mammography is used for assessing the size of the lesion, for pre-surgical localisation of suspicious areas of breast and in the guidance of needle biopsies.

The reported sensitivity (the fraction of patients actually having the disease and correctly diagnosed as positive) in lesion detection varied between 69% and 90% [18] depend-

ing on the breast density. The specificity (the fraction of patients without the disease, correctly diagnosed as negative) is the major drawbacks of conventional mammography. A variation in specificity between 87%-97% and a low positive predictive value as low as 15% has also been reported [19]. This 'less than perfect' performance may be due to several confounding factors e.g. poor mammographic technique, observer error, the lesions are non-palpable or at a cellular level, and/or the lesions are obscured by the normal breast tissues. In addition, the presence of scars or tissue distortion may hide true small tumours on the mammogram. Nevertheless, conventional mammography remains the most valuable and cost-effective technique for breast tumour diagnosis.

Over the last two decades, considerable efforts have been carried out to improve the current screen-film mammographic technique. These improvements include image quality, acquisition techniques, and interpretation protocol in order to reduce some of the mammographic limitations [20]. Furthermore, a new research effort started focusing on "Digital Mammography" (DM) as a possible future direction in breast imaging. This technique offers many advantages over the conventional screen film-based method [21, 22]. For instance, processing with digital systems increase dynamic range (two to four times the dynamic range of typical film-screen), improved quantum efficiency and storage and display mechanisms.

In addition, the use of computer-assisted image interpretation is claimed to be helpful for the physician. This may enhance different features such as computer-aided diagnosis which may further improve the visibility of lesions and improve mammographic sensitivity [23]. Therefore, repeated exposures (which are sometimes needed when using conventional mammography) are not required and this may reduce the radiation dose. Moreover, it does not need either cassettes or dark rooms or processors and thus allegedly saves space and time in archiving and retrieving DM images. However, DM requires large disk space for saving image data.

Despite several advantages, DM does not yet reach the level of detail to replace screen-film mammography. However, with continuous technical improvements of the digital system this may expected to change in the near future. Both conventional and DM systems suffer from substantial technical and clinical limitations. For instance, these system are unreliable in imaging patients with dense parenchyma tissue especially in the younger female population due to more glandular tissue. Mammographic findings are non-specific

(cannot always differentiate benign from malignant disease) and often underestimate the size of the detected lesion. X-ray based imaging is also not useful for breast diagnosis following surgery or radiotherapy as the patient's breasts in these cases have architectural distortion. Mammography is not recommended for women with breast implants and is also not useful following hormonal replacement therapy due to the increase of breast density. It is worth mentioning that X-ray mammography is not always useful for non-palpable tumours. Another group of women: close carrying a mutation in BRCA1 (human gene called breast cancer 1, early onset) or BRCA2 (breast cancer 2) genes are at high genetic risk of cancer, some even having opted for preventative bilateral mastectomy. It is preferred not to repeat scan this group due to X-ray dose and thus, a more sensitive diagnostic test would be advisable.

1.5.3 Diagnostic Biopsy

Once the diagnostic tests particularly mammography indicated or suspected breast cancer, breast biopsies are then performed. Breast biopsy is an invasive procedure used to remove tissue or cells from the breast for microscopic examination. This technique is generally performed under local anesthesia. Several types of biopsy are available depending on location, type and size of lesion. Fine needle aspiration biopsy performed by inserting a very thin needle to the lesion for taking a small sample of cells, fluid, or tissue. Core needle biopsy is used with a large needle to remove a small cylindrical shape of tissue. Surgical biopsy involves removing part (incisional biopsy) or entire (excisional biopsy) lesion tissue.

In addition, a special wire localisation technique my be used during surgery for deeply seated lesion. This technique is usually performed under X-ray or ultrasound guidance. There are special instruments and techniques that help to guide the needle biopsy. These include: stereotactic biopsy with a 3D mammographic technique, to find the exact location of breast lesion, and vacuum assisted biopsy using a tube to gently suctioned the breast lesion and a knife to remove tissue. This technique is much less traumatic than open biopsy. Moreover, a sentinel node (is the first lymph node to receive drainage from a breast cancer cells) biopsy may often be used to determine if cancer cells have spread to other tissue.

In summary, invasive breast biopsies play an important role for evaluating breast cancer particulary non-palpable lesions. These surgical procedures are important for staging

(see table 1.2) and are considered the "gold standard" [19] to determine the presence or absence of breast cancer. However, invasive breast biopsies procedures are expensive, time consuming, and are often associated with emotional stress. It also causes scar and tissue distortion that complicate the future mammography. As a result, additional imaging tests are being used to reduce the trauma, cost, avoid or minimises unnecessary invasive breast biopsies and more importantly to further improve breast cancer diagnosis.

1.6 Treatment of Breast Cancer

There are a range of treatment choices that have been used for breast cancer. Treatment options include Surgical, Radiation, Chemotherapy, Hormone (anti-estrogen) therapy or a combination of two or three treatment choices. The success of the treatment depends upon a range of factors that include the type of breast cancer, the breast compositions, the stage of the disease, the size of the lesion, involvement of lymph nodes and the patient history. A primary localised lesion is usually considered curable however, metastatic breast disease is generally fatal. The different form of treatment options are briefly outlined.

1.6.1 Surgery

Surgery or lumpectomy is used for small lesions to remove the area of the breast containing the lesion. However, if the lesion is large or appears in several places of the breast, then total removal of the breast (mastectomy) may be considered the appropriate treatment. Combining surgical lumpectomy plus irradiation of the remaining breast is sometimes used, and refered to as conservative treatment.

1.6.2 Radiation Therapy

Radiation therapy using external beam or radioactive seed implants may be used for treating the early-stage of breast cancer. Often after lumpectomy the whole breast is exposed to external beam radiation to kill the remaining cancer cells.

1.6.3 Chemotherapy

Chemotherapy is a systemic therapy as it affects the whole body. Chemical drugs are usually injected to the patients and pass through the bloodstream to the rapidly dividing cells

Table 1.2: The staging of breast cancer, adapted from [24]. Note: beyond stage IIIB the tumour is usually extended to either the skin or the chest wall and thus can be of any size. The N0= no regional lymph node, N1= metastasis in movable ipsilateral axillary lymph node(s), N2= metastasis in ipsilateral axillary lymph node(s) fixed or matted, N3= metastasis in ipsilateral infraclavicular lymph node(s) or clinically apparent.

Stage	**Tumour Size**	**Lymph Node Involvement**	**Metastasis**
0	Carcinoma in situ	N0	M0
I	$\leq$ 2 cm	N0	M0
IIA	No evidence of tumour	N1	M0
	$\leq$ 2 cm	N1	M0
	2-5 cm	N0	M0
IIB	2-5 cm	N1	M0
	$>$ 5 cm	N0	M0
IIIA	No evidence of tumour	N2	M0
	$\leq$ 2 cm	N2	M0
	2-5 cm	N2	M0
	$>$ 5 cm	N1	M0
	$>$ 5 cm	N2	M0
IIIB	Of any size	N0	M0
	Of any size	N1	M0
	Of any size	N2	M0
IIIC	Of any size	N3	M0
IV	Of any size	Any N	M1

to kill the cancer cells and prevent them from spreading to other part of the body. Unfortunately, most drugs have side effects as these tend to also kill rapidly dividing healthy cells such as blood, mouth, intestinal tract and hair cells. However, post-treatment, these normal cells can rapidly repair the damage that the drugs do.

1.6.4 Hormonal Therapy

Hormonal therapy is a very effective treatment especially if the cancer cells have hormone receptors (i.e. hormone-receptor-positive). It blocks the ability of the hormone estrogen to stimulate the growth of the cancer cells. Tamoxifen drug [25] is a breast common hormonal treatment and is recommended for early cancer cases. It basically lowers the risk of recurrence or getting a new cancer.

1.7 Complementary Diagnostic Techniques

From the previous discussion it is clear that there are some clinical situations where there are significant limitations to use mammography in isolation. In such cases, there is a great need to use sensitive tests to achieve a high confidence and accurate diagnostic decision. The use of breast biopsies is necessary if breast cancer is indicated or suspected in such cases. Of the performed breast biopsies $\approx$ 60-80% [19] are negative of breast cancer or have benign lesions. In these cases breast biopsies are considered unnecessary. This has lead many breast cancer experts to propose complementary imaging modalities to provide additional diagnostic information and reduce unnecessary breast biopsies.

1.7.1 Ultrasonography

Ultrasonography (US) uses high frequency acoustic waves that reflect at boundaries with different acoustic properties. It is a non-invasive technique, easily available, and relatively cheap. Breast US provides unique information in assessing both palpable, and non-palpable breast abnormalities. For instance, it clearly differentiates between solid masses and cystic lesions [26]. It is also considered to be useful in cancer staging, measuring tumour sizes, easy accessing lesions located in peripheries and reducing the number of unnecessary biopsies. It allows accurate needle placement during biopsy and is very useful for aspiration of cysts. The members of the European group for breast cancer screening

recommended using US as a complementary method to X-ray mammography. In addition, the use of high frequency transducers has improved spatial resolution and thus claimed to be useful in axillary node evaluation.

However, breast US technique is time consuming and operator/observer dependent. It has also a number of other limitations that may be due to overlapping in sonographic characteristics. For instance, it can not detect calcifications (microcalcifications or macrocalcifications) in DCIS. It could also miss solid lesions especially in a fatty breast and if detected can not determine whether a solid lump is benign or malignant. For these reasons, US is not used as a screening technique for asymptomatic breast cancer as it is difficult to ensure that the entire breast has been scanned.

1.7.2 Magnetic Resonance Imaging

Magnetic Resonance Imaging (MRI) images are created by the recording of signals generated after radio-frequency excitation of nuclear particles exposed to strong magnetic field. Breast MRI is a non-ionising tomographic functional technique that may be used when the diagnosis is uncertain with mammography [27]. The technique is valuable for specific clinical indications such as patients with (1) axillary adenopathy (enlargement or inflammation of lymph gland), (2) possible tumour recurrence after surgery or radiotherapy, (3) lesions overlying implants, or (4) those requiring staging of multi-focal carcinoma (two or more discrete lesions in one breast) [28].

Breast MRI with dedicated breast coil has excellent soft tissue resolution that enhances the ability to both identify the location and in some cases determines the full extent of the lesion. The use of intravenous contrast agent, gadolinium, which accumulates in tissues with a dense blood vessel network, has also increases the sensitivity of breast MRI [18]. However, the reported specificity (ability to determine if lesion is benign or malignant) is 56-72% [28]. This technique has a limited application in patients with implanted metal devices or other metallic materials inside the body. MRI cannot also differentiate between inflammatory breast cancer and abscesses. In addition, several clinical limitations have been reported in the literature suggested not use use MRI in pre-menopausal women. For example changes that do occur in the T1 value of the breast tissue during the menstrual cycle [28] mean that patients should be scanned between the 6th and 16th day of the cycle. In summary, researchers have concluded that breast MRI is limited by lack of availability

and inconsistent quality and the technique is too expensive for routine use in breast cancer screening.

1.7.3 Radionuclide Breast Imaging Techniques

The need to improve breast cancer detection and to reduce unnecessary invasive breast biopsies have stimulated researchers to investigate functional imaging modalities. These techniques produce a range of different imaging approaches such as Positron Emission Tomography (PET), Single Photon Emission Computed Tomography (SPECT), planar imaging and dedicated imaging instrumentation with and without breast compression. These imaging techniques of the breast potentially offer additional information in breast cancer diagnosis. This is because these imaging methods rely on the physiological and biochemical characteristics of a lesion. Thus, considered as the best hope to differentiate between benign/normal and malignant diseases. These functional techniques have also been used to assess and monitor the effect of cancer prevention drugs. The current radionuclide imaging techniques used for breast tumour imaging are briefly discussed.

(a) Positron Emission Mammography

In PET a small amount of positron emitter radio-tracer, ^{18}F fluorodeoxyglucose (FDG), is administered intravenously to the patient [29]. It then distributed in the body and as it decays, the radionuclide emits a positron in any random direction. If the positron while travelling interacts with an electron within the body the two particles then annihilate and produces two γ-rays of 511 keV each. Either a whole body scanner or a breast specific Positron Emission Mammography (PEM) camera [30] is used to detect the two γ-rays in coincidence (two events that are detected within $\approx$ 12 nanosecond). PEM is increasingly used in North America not only in cancer diagnosis but also in staging, planning and monitoring anticancer therapy. This information can be helpful not only in eliminating unnecessary axillary dissection [31] and biopsies but also in determining the appropriate treatment. The diagnosis of viable tumour tissue following chemotherapy is another application of PET [25, 32].

Imaging with ^{18}F-FDG has shown considerable promise in breast cancer imaging, but the exact role is still in evolution. Wahl [30] recommended that it is best applied to solve difficult clinical cases in specific patients rather than routinely. There are a number of

reasons that limit the wide use of PEM for routine cancer diagnosis: 1) the high cost (over £2 million) of PET coincidence imaging equipment, i.e. cyclotron, scanner and radiochemistry facility [29]; 2) the difficulty of producing and labeling the short half life PET radionuclides [23] and 3) the lack of centers with the required experience to develop more advanced methodology appropriate for breast oncology. In particular, more data are needed about the metabolism of different PET radiopharmaceuticals in breast tumours; 4) the lack of oncologists with a high knowledge of PET methodology [33].

(b) Scintimammography

Scintimammography (SM) is a promising non-invasive functional imaging technique. It has been proposed to complement X-ray mammography and to improve patient selection for biopsy. This single photon imaging of the breast involves injecting the patient in the arm vein with a small amount (555-740 MBq [34]) of radiopharmaceutical. The most commonly used radiopharmaceutical for SM is ^{99m}Tc labelled Sestamibi (see section 2.3.1 (a)). After a period of time, the tracer distributes in the breast tissue as well as in the body organs. It accumulates more in the target object (lesion) with uptake ratio nearly 9:1 Tumour-to-Background-Ratio (TBR) [35]. A standard full-size clinical gamma camera is then used to scan the patient and thus measure the 3D distribution of the radioactivity.

SM imaging using full size clinical γ-camera includes a range of different imaging approaches such as planar (2D) imaging or SPECT technique. The latter technique gives a 3D representation image but is not widely used because it is difficult with this technique to accurately localise the lesion [36]. In contrast, planar SM is the technique that is more widely used in clinical practice because it provides better lesion localisation particularly the prone images with lateral views [36]. In this case the gamma camera is usually equipped with a LEHR parallel-hole collimator and two views (prone and supine) are taken to the diagnosed breast. Since the energy imaged is 140 keV representing the photopeak, 20% energy window (symmetric $\pm$ 10%) is often used and thus centred over the photopeak. The main clinical applications of planar SM imaging is summarised here but detailed review of the literatures is given in chapter two.

In brief, SM with a general purpose γ-camera has been introduced to evaluate patients with dense breast prior and in a least cases after breast biopsy [37]. The technique may also be considered valuable for many clinical applications such as evaluating the axillary

lymph nodes, investigating patients with microcalcifications [38], assessing multifocal and multi-centric breast cancer diseases [39]. It is also useful for imaging patients following surgery, chemotherapy, hormonal replacement therapy and radiotherapy as well as for patients with breast implants [36]. The technique may also assist in the differentiation of benign and malignant breast abnormalities by measuring radiotracer uptake in the lesions as compared with surrounding breast tissues. Studies such as [40, 41] suggested that SM may be used as a second line diagnostic test in cases where the sensitivity of mammography is decreased or there is doubt about the presence of lesion.

In summary, SM using conventional γ-camera may be considered as a useful complementary imaging modality to aid the diagnosis and the detection of breast cancer [42]. It may also help to assess in patients selection for biopsies and this may reduced the number of unnecessary or negative breast biopsies. However, the major drawback of the current standard clinical gamma camera SM imaging systems is the use of mechanical collimator. This causes the camera imaging system to utilise a very small fraction, $\sim 0.01\%$, of the total number of the emitted photons. This limits the statistics and hence the quality and diagnostic value of the observed images. The collimator sensitivity and resolution are a trade-off and the camera is also limited by its intrinsic spatial resolution. As a result, these factors make it difficult to practically image cases of smaller, non-palpable, lesions (< 1 cm) that may be deep seated or those close to the chest wall. These have stimulated the development of new dedicated (breast specific) instrumentations that used for breast tumour imaging applications.

(c) Dedicated Breast Cameras

Recent years have seen considerable interest by scientists in developing new compact medical imaging detectors. These instruments were proposed for different clinical applications with the aim to improve image quality by building cameras of suitable size and shape for the part of the body under investigation. Among these designed detectors is the small dedicated gamma camera for functional breast tumour imaging. The justification for this development is that a standard full size clinical gamma camera is designed for whole-body imaging and thus, has not been optimised for breast tumour imaging. In other words, there are a number of shortcomings with such general purpose gamma camera such as the limiting sensitivity (on average 50% [43]) for lesions < 1 cm such as DCIS particularly the

medially located tumours. In addition, several studies have pointed out that due to the large FoV of the camera and the bulky collimators it is difficult to position the camera close to the breast and thus, imaging breast tissue adjacent to the chest wall may not be possible. This may, ultimately, decrease the spatial resolution of the camera imaging system and thus affect the diagnostic value of the test in detecting such a small lesion size.

To overcome some of the limitations offered by conventional gamma camera on breast imaging Gupta and colleagues [44] reported the first preliminary clinical data that performed with breast specific detectors and then compare it with the data obtained from standard full size camera. A limited number of patients were investigated in this study but interestingly reported a higher sensitivity for the dedicated camera. Following this and due to the large research activities new generation of detectors have been designed and developed for breast tumour imaging. For instance, the Position-Sensitive Photo-Multiplier Tubes (PSPMT), semiconductor arrays and scintillation crystals coupled to an array of solid-state photo-detectors. Table 1.3 summarises the features and the physical parameters of some of the currently under investigation and the commercially available dedicated breast camera. In general, these small FoV detectors have lead to the improvement of the overall spatial resolution of such imaging system.

The commercially available dedicated breast camera has two detectors and is designed and optimised to image only the breasts. It possesses a high intrinsic spatial resolution and the camera is also equipped with ultra-high resolution parallel-hole collimator and thus, optimised for high-resolution SM. The main advantage of such cameras is the ability to separate the breast from the chest wall by positioning the camera close to the breast. Thus, the camera can be used in areas with limited space (e.g. medial view can be possible), where the use of a full-sized camera is impractical or impossible. The use of moderate breast compression capabilities may improve both the Signal-to-Nose-Ratio (SNR) and the spatial resolution [45] and thus; increase the sensitivity for detecting smaller lesions.

The proposed clinical indications for such dedicated cameras are similar to the full size clinical gamma camera SM. There are some recent clinical studies associated with using these dedicated gamma cameras. For instance, a clinical preliminary study by Brem *et al.* [46, 47] using dedicated breast camera demonstrated a slight improvement in resolution and tumour sensitivity particularly for lesions $\leq$ 1 cm. Rhodes and colleagues reported [48] on SM performed on 40 women with small mammographic abnormalities ($<$ 2 cm)

scheduled to undergo biopsy. The SM examination identified (33/36) malignant lesions confirmed at biopsy. The authors concluded that this preliminary study suggested an important role for the dedicated SM camera in women with dense breasts. In another study Brem and colleagues [49] evaluated 94 women (median age 55 years) presented with normal mammographic and physical examination results but all considered at high risk of developing breast cancer. Of these women 35 had a history of previous breast carcinoma or atypical ductal hyperplasia. The authors concluded that with this camera they can depict small (8-9 mm) non-palpable lesions in women at high risk of breast cancer.

In summary, while these studies using breast-specific cameras are promising, all are considered preliminary in nature because they based on very few cases. Additional studies with a larger sample size are needed to accurately assess and reach scientific conclusions concerning these proposed cameras. They also need to be cost competitive with the general-purpose gamma cameras in order to be widely used in breast tumour imaging applications. In addition, the smallest lesion sizes that can be detected with these cameras claimed to be 3-3.3 mm [50] compared to 4-5 mm [51] with conventional camera. However, the evidence published to date did not demonstrate a statistically significant difference in lesion detection. The spatial resolution of these proposed cameras may further improve by increasing the pixel size but there are however, practical limitations in the development of cameras with small pixel sizes, including cost and detector design. More importantly due to the use of collimator these dedicated camera suffer from low detection efficiency.

1.7.4 Summary of the Role of Different Imaging Modalities

In many centres the current evaluation and primary diagnosis of breast is based on combination of physical examination, X-ray mammography and breast biopsy. Mammography represents a significant contribution and remains the gold standard for breast tumour imaging. This is because mammography is relatively simple, cost-effective and highly sensitive. However, in many clinical cases X-ray mammography may be non-specific and lesions cannot be detected. This is because a lesion is indistinguishable from normal breast tissue or covered by the dense parenchyma. Mammography is also not reliable following radiation therapy, surgery and hormonal replacement therapy. It is also not suitable for women with severe dysplastic (abnormal growth of breast tissue) disease or patients with breast implants. Consequently, breast biopsies are used for many cases as a

Table 1.3: Physical characteristic and specifications of dedicated gamma cameras proposed for scintimammography. All cameras are based on PSPMT(s) principle. The CZT detectors array absorb the γ-rays directly and converts their energy into electrical signal without the conversion to visible light as in the case with a scintillation detector. The spatial resolution is measured with general purpose collimator at 10 cm distance except the LumaGEM cameras that based on ultra-high resolution collimators. Note: n/a=not available

Cameras & Study (reference)	**Crystal sizes mm^3**	**FoV sizes cm^2**	**Intrinsic resolution (mm)**	**Spatial resolution (mm)**	**Energy resolution (%)**
CsI(Tl) [50]	2×2×3	10×10	2	9	n/a
CsI(Si) [52]	3×3×6	21×21	3	6.5	n/a
NaI(Tl) [53]	3×3×6	15×20	3	6.3	10%
LumaGEM NaI(Tl) [45, 53]	2×2×6	12.8×12.8	2.2	3.4	10%
LumaGEM 32000S/12K^2 (CZT) [54]	2.5×2.5×5	16×20	1.58	2.5	6%
LumaGEM (CsI) 5600 crystal [55]	3×3×6	10×10	1.7	n/a	n/a

second line diagnostic test to evaluate suspicious lesion. Unfortunately, many breast biopsies are performed on normal patients which results high cost and patients stress. Thus, other non-invasive imaging techniques are necessary and have been used as complementary method to minimises unnecessary breast biopsies.

US and MRI are adjunctive imaging techniques to X-ray mammography. Breast US is relatively inexpensive and is currently the commonest complementary method. This technique is also useful particularly when there is a cyst in the breast but have lower accuracy in solid lesions. Breast MRI is sensitive and relatively specific technique for some certain indications but are too expensive to be used routinely. Both US and MRI are useful tools in breast diagnosis, in particular for solving problems in selected applications. Thus, additional imaging methods are still needed.

Functional breast γ-ray imaging techniques have been proposed to aid the breast cancer diagnosis. Among the currently used techniques are planar SM with ^{99m}Tc labelled sestamibi and PET with ^{18}F-FDG. Both radionuclide techniques have been increasingly used particularly for imaging patients with fibrous or dense breasts.

Having obtained current imaging methodologies, various weaknesses in each approach lead to the need for new complimentary imaging methods. Of these approaches, SM is one of the most promising. The current research in this area is focused on dedicated collimator-based cameras. These dedicated camera suffer from low detection efficiency. In addition, this is an unattractive option for many health providers, due to limited clinical applications of such an imaging system. This provides the motivation for investigating the application of collimator-less imaging in breast tumour imaging.

1.8 Collimator-less Radionuclide Imaging

As previously mentioned SM (planar and SPECT) techniques are usually performed using standard clinical gamma cameras employing LEHR parallel-hole collimators.The use of a mechanical collimator limits the angular acceptance of the incident γ-rays, and thus degrades the efficiency (which is a measure of the proportion of γ-rays incident on the collimator that pass through to the detector).

The two most obvious means of increasing the number of detected events would be to increase the administered activity or to image the patient for a longer period of time

(or a combination of both). However, the radiation dose (activity) that can be safely administered to the patient is limited. In practice, the imaging time is also limited by the patient's ability to hold still during the scanning time. Thus, due to the collimator both the spatial resolution and the efficiency are a trade-off. This inverse relationship limits the statistics and hence, the quality and the diagnostic value of the observed image. Moreover, images are always photon limited and often need to be filtered to remove the effects of random noise. Several attempts have been made to overcome these limitations and one of the suggested alternative methods is the Compton camera principle.

1.8.1 Compton Camera Imaging

The Compton camera [56, 57, 58] is a method used for imaging the distributions of γ-ray without using conventional collimators. The collimator is replaced by a scattering detector and the Compton scattered photons are then detected in another absorption detector. Compton cameras can take different forms [58] but all are based on Compton scattering principle i.e the direction of the incoming photon is determined from the kinematics of Compton scattering.

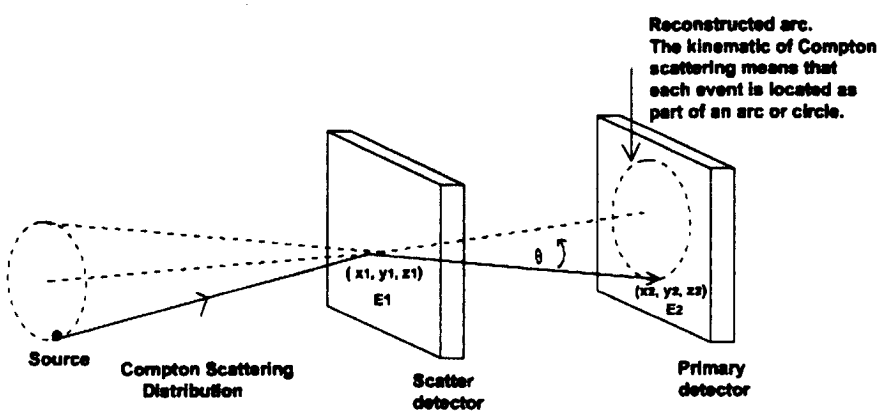

Figure 1.3: A schematic diagram of Compton camera demonstrating its principle on imaging a point-like object emitting γ-ray photons. This demonstrate that the image can be reconstructed from the knowledge of the first interaction coordinate (x_1, y_1, z_1) at the scatterer detector and the second interaction coordinate (x_2, y_2, z_2) of the absorber detector [58].

Figure 1.3 illustrates the principles of a Compton camera showing two position sensitive detectors. The gamma photon emitted from the source undergoes a Compton interaction in the scattering detector (scatterer) and is then scattered toward the primary detector (absorber) to be detected. To ensure that the two interactions in both detectors are from the same photon a time coincidence detection mode is employed. The energy loss associated with the first Compton interaction, E_1, can be used to determine the scattering angle θ from this relationship:

$$\cos\theta = 1 - m_0c^2\Big((\frac{1}{E_1}) - (\frac{1}{E})\Big) \tag{1.1}$$

where m_0c^2 is the electron, E is the incident photon energy, E_1 is the energy loss in the scatter process and θ is the scatter angle of the photon. Thus, the scatter process can be defined by the measurement of the first interaction coordinate (x_1, y_1, z_1), the second interaction coordinate (x_2, y_2, z_2) as well as the two energies E_1 and E_2 and from these knowledge θ can be easily determined. From the reconstruction method each emitted (incident) photon vector lies on the surface of a cone. The axis of that cone passes through both interaction points. A set of cones is usually generated as a results of many number of incident photons. These need to be reconstructed to obtain the distribution of photon source.

Due to the use of electronic collimation, Compton cameras can in principle provide good resolution and high sensitivity depending on the detector type but suffers from the following limitations:

- For low energy photons the Compton scattering distribution is broad and this affects the spatial resolution of the Compton camera.
- The uncertainties in both the energy and spatial measurements in the involved detectors (scatterer and absorber) affect the spatial accuracy in the image and thus, the resolution of the camera.
- At clinical photon energies (<< MeV) Compton cameras require a very high spatial and energy resolution for both detectors to accurately localise the source.

1.8.2 The use of Coded Apertures (CAs)

The last ten years have seen large efforts by scientists to develop advanced imaging instrumentation dedicated for SM imaging to aid the conventional method. As an alternative approach, this research hopes to add to this knowledge by investigating the application of CA for SM. This is certainly an attractive approach as it is simple, inexpensive and the CA has an open area significantly greater than the conventional collimator. Also the aperture itself is employed as a simple mask so that no collimation is used, thus providing, potentially, very high sensitivity compared with the parallel-hole collimator. The basic principle of CA imaging and how the image is formed by this approach is first introduced.

Introduction to Coded Aperture Imaging

The idea of replacing the conventional collimator by the use of CAs was first employed by Barrett [59]. It basically, involves the placement of CA (an open and close aperture pattern) between the source and the detecting device. Sources at different depths and positions cast a shadows (pattern) of the aperture onto the imaging detector (see Fig.1.4). Thus, the resultant (projected) image called a composite or multiplexed image represents the sum of all projections at different x,y positions and depths within the object. To locate the proper size and position of the desired objects, the projected image must be decoded by determining the correlation of the mask pattern in size and position. However, the advantage offered by the CA lies in its increased photon collection efficiency due to its large open area, which is several thousand times that of a single pinhole [60]. The technique has been successful at detecting small distance objects. The main current application is in astronomy for stellar γ-ray and X-ray imaging [61].

Choice of CA Design for Scintimammography

The early proposed CAs imaging techniques such as the Fresnel Zone Plate (FZP) [62] and the random array [63, 64] have been avoided in this study. This is because it has been shown by [65, 66] that these patterns fail to deliver superior results compared to collimators and pinhole camera systems, and suffer to some degree from distortion artefacts. However, the development of CA patterns based on "Cyclic Difference Sets" (see chapter 3) such as Uniformly Redundant Arrays (URAs) [67, 68], Modified Uniformly Redundant Arrays

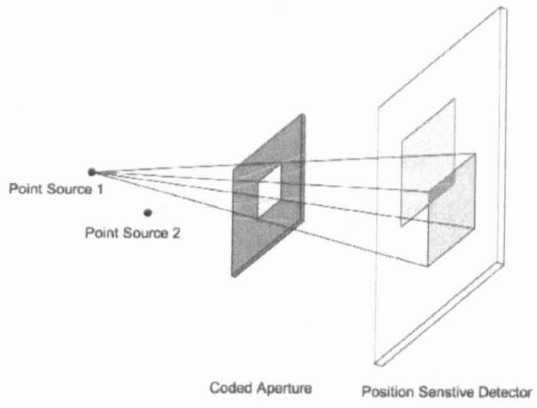

Figure 1.4: Schematic diagram of the CA, the production of a coded image and obtaining depth information. Increasing the source-aperture distance produces the smaller shadow of the CA on the detector. The lateral displacement of the shadow is proportional to that of the two sources (source plane). By correlating the recorded image with a postprocessing, G function, an image of the source distribution at different depths may be determined. Note that this simple CA pattern shown is only for illustration. Real CA designs are far more sophisticated (see section 3.2).

(MURAs) [69] and arrays based on MURAs such as No-Two-Hole-Touching (NTHT) [70] have been demonstrated to be the most promising of all the CA patterns. These optimum arrays, as originally developed and extended by Fenimore and Cannon [67, 68, 71, 60] have become widely used in the detection of X-ray and γ-ray sources in astronomy for imaging stars and more recently in nuclear medicine for small animal imaging [72].

These arrays combine the high transmission (have up to 50% open area for the MURA patterns) characteristic with flat (zero) side-lobes in their response function. The high transmission provides a potential capability to image low-contrast sources and may dramatically enhances the detection efficiency compared to collimators system. These patterns have an interesting property that one can generate the mask and its negative (anti-mask) along with the decoding patterns, G, for each one. Two separate images can be then taken one with the mask and the second with the anti-mask and then add these two images after decoding each projected image with its post-processing decoding array. This technique is of special interest in artefact reduction and has been used in the past for re-

ducing systemic non-uniform background [73]. Certainly, these advantages and properties have motivated the author to select this family of CA patterns as appropriate for use in SM.

In the last 10 years a number of attempts have been made to use URA-CAs for 3D (SPECT and PET) imaging e.g. [74, 75]. They have demonstrated that the use of URAs have improved sensitivity and resolution over single pinhole collimators. However, their resolution does not exceed that of planar parallel-hole collimators and this may be due to the complexity of the reconstruction or convolution algorithms for complex 3D imaging.

To the best of the author's knowledge, no research has systematically investigated the application of CA for planar SM. This thesis thus, aims to examine the state of CA imaging and develops some of the theory of its application to breast tumour imaging. The main advantages of this approach, is that a standard clinical gamma camera is utilised that combines image quality, affordability and ease of use and potentially reduces the need for dedicated breast camera instrumentations. This is an attractive option for health care providers with limited resources where investment in single-application dedicated instrumentation is unattractive.

Motivations

In this proposed approach a planar single photon imaging gamma camera is used after replacing the conventional collimator with a planar CA. The major anticipated advantages and motivations may be summarized as:

- First, CA imaging is well suited for detecting faint pseudo-point like objects in non-zero background. Imaging point-like small lesions (objects) in medicine is akin to imaging stellar points (objects) in astronomy. Thus, CA imaging appears well matched to the imaging objectives in SM.

- Theoretically, the selected CA patterns have wide open area and thus about half of the incident γ-rays will be transmitted. This may dramatically improve the photon collection efficiencies and thus may reduce the acquisition time of the imaging system compared to a collimator-based system.

- Combining CAs using geometric magnification with a full size standard γ-camera for imaging a relatively small organ such as breast has a potential ability to maintain the

resolution compared to using a conventional collimator. In addition, the hole size of the mask dominates the spatial resolution, making the CA-camera very attractive for early breast tumour imaging. Ultimately, high resolution could be achieved without the need for dedicated high resolution γ-camera instrumentations.

- In CA imaging photons impinging at a wide variety of angles are usually accepted, compared to the restricted angular acceptance when using collimator. This is because each hole of the CA provides a different view of the source object. Thus, inherent depth information contained in the data may be used to reconstruct a particular depth in the source object. This is achieved by re-scaling the magnification factor to the desired depth. This gives 3D information (limited angle tomography) from a single conventional 2D image.

- Displacing the gamma camera away from the breast may allow access to a larger FoV. Thus, one possible application of CA-SM may be determining lymph node involvement. In addition, this may help in monitoring the tumour response to chemotherapy and may used for post surgery and post chemotherapy applications.

- The use of CAs to replace the collimator minimises the effects of camera-associated scatter as the surface area presented to the scatter flux is dramatically reduced (although, the patient scatter flux may be enhanced without appropriate shielding).

Thus, CA imaging appears to be attractive for SM applications: it utilises a limited, well-defined FoV, and the targets are "high" intensity point-like objects (lesions) which CA imaging methods are well suited to image.

1.9 Thesis Overview

This thesis consists of Nine chapters. The foregoing chapter has aimed at providing an appreciation of the diagnostic techniques of breast tumour imaging, discussing the relative merits of each of the current techniques highlighting the role of NM techniques as a unique tool for the in vivo investigation. Moreover, the motivations associated with CA imaging is also introduced emphasizing its possible attractive application in SM.

The second chapter, provides an overview of the γ-camera, including the concept of image formation for single photon imaging. It also provides a review of the literature of

the state-of-the-art radionuclide breast imaging systems highlighting the role of SM. A general overview of the entire imaging problems associated with the collimator-based SM system closes the chapter.

The third chapter, describes the theory of CA imaging and provides an overview of the history of CA methods. The main focus is on the CA patterns used in this study which include their generation rules and the decoding properties. In addition, the possible mask camera configurations and designs in the case of near field CA imaging are also discussed. The chapter closes by describing the decoding correlation methods that have been used for CA imaging.

Chapter four, provides a description to the theoretical tools and the three methods used for investigating the application of CA for breast tumour imaging. The main method used in this study was based on the well known Monte-Carlo Simulation (MCS) approach. A realistic model for a single head clinical gamma camera, Toshiba (GCA 7100A), is developed. It explicitly models the transport and detailed physical interaction of photons from the object until these reach the detector. The effects of limiting energy and spatial resolution are also simulated. The presented results demonstrate a full camera simulation experimently validated against the aforementioned gamma camera. This is followed by a brief describtion of the Monte Carlo implementation of CA patterns and the basic mask design. This chapter is closed by describing the other two methods used specifically for CA imaging investigations. These are Pseudo-Ray Tracing (PRT) method and a new but simple Binary Mask Shift (BMS) method.

Having described the MCS framework used for this work, chapter five describes the various investigations undertaken using the proposed CA masks coupled to the aforementioned gamma camera, starting with an idealised point source in air and then in tissue equivalent material. The complexity of the source geometry is increased to finally explore different extended object sizes. This chapter also systematically investigates the imaging artefacts arising from different these different object geometries.

Chapter six investigates how the CA imaging approach might be applied to the particular case of SM. 3D pseudo-anthropomorphic phantom geometries have been modeled, verified for such investigations. The developed phantom contains torso, heart, breast and variable user defined tumour sizes. This chapter shows that introducing the torso and the heart is problematic due to the open field geometry. The chapter closes by developing

better shielding geometry for the CA and the camera from the non-specific background activities arising from torso/cardiac flux. The aim was to reduce the effect of volumetric background corruption from these non-target objects.

Chapter seven, describes the correction methods used to correct the near-field artefacts arising from the particular case of CA breast tumour imaging. These correction methods are used to solve the problems discussed in chapter six and optimize the CA for breast tumour imaging.

Chapter eight presents the results that investigate the effectiveness of CA for breast tumour imaging after the near field artefact corrections. These initial investigations include different lesion sizes and TBRs. The performance of the proposed CA-SM system was compared with that obtained from simulating two high resolution collimator-based camera systems. The effectiveness and the performance of these image formation methods were quantitatively evaluated. This is achieved by comparison of three fundamental parameters: lesion detection (contrast), the observed lesion resolution and tumour Contrast-Noise-Ratio under a variety of clinical imaging situations. The final part in this chapter demonstrates the various investigations using the PRT method of an isolated hot breast phantom with and without the lesion present.

Finally, chapter nine highlights and summaries the main achievements, findings and conclusions, and suggests the future work that can be done with the CA mask approach.

1.10 Achievements & Major Contributions

There are a number of achievements that have been obtained from this study:

1. This work represents the final systematic study into the application of CAs to breast tumour imaging. Whilst other prior work [74, 76] has suggested this approach, it has been characterised by gross simplifications. By contrast, in this thesis, the full implication of non-specific activity, confounding artefacts from cardiac and out-of-field activity, have been demonstrated, and novel solutions proposed to overcome these issues.

2. Chapter 5 demonstrates the effect of multiplexing on the performance of the decoded image by gradually increasing the complexity of the source using three different methods. These locally generated artefacts mainly arise from the near-field imaging

geometry of the hot uniform background and thus, tend to offset and degrade the decoded imaging. The presented results also suggest that the so-called near-field distortions can be easily predicted and corrected.

3. Two iterative methods, namely Pseudo-Ray Tracing (PRT) and Binary Mask Shift (BMS) were developed for performing the CA imaging investigations and used as the basis for artefact prediction and correction. One of the key results from developing these approaches is that the form of the background artefact arises mainly due to the 2D distributed source geometry. For slightly compressed breasts (6 cm compression), there are only minor contributions to the distributed activity artefact from depth-dependent activity.

4. Chapter six demonstrates how the selected CA camera, using a standard full size clinical gamma camera, can be applied for SM application. For these investigations pseudo-anthropomorphic phantom geometries were first developed and verified in order to emulate SM. This 3D phantom model contains torso, heart, breast and user defined tumour sizes. The influence and the contribution of out-of-field tracer uptake from the heart and other soft tissue are also presented. The results clearly demonstrate for the first time the effects of γ-ray emission from volumetrically distributed background from the torso and the heart in such an open geometry system. As a result, a shielding geometry is proposed to mitigate the effects of non-specific out-of-field background torso/cardiac flux.

5. Chapter 8 assesses the performance of the CA-SM data, after the near-field artefacts corrections, by comparing its results with corresponding results produced from two collimator-based image formation methods. Also the effectiveness of these image formation methods were evaluated by quantitative comparison of three fundamental parameters: the detected tumour events, lesion resolution (FWHM) and contrast under a variety of clinical imaging situations. The main simulation results demonstrate that all image formation methods have comparable result in term of the observed lesion resolution (a slightly lower values in the case of MURA-CA). Despite reducing the collimator-tumour distance to 3.1 cm in the case of Ultra-High Resolution (UHR) and LEHR parallel-hole collimators to enhance both the spatial resolution and the contrast the MURA-CA shows the highest performance in term of contrast.

These investigations demonstrated that with the use of near-field artefacts corrections it is possible to visualised small lesions (2 mm diameter) down to TBR of 3:1. The final part of this chapter demonstrates the intrinsic properties of the application of MURA-CA pattern in breast tumour imaging using Pseudo-Ray Tracing (PRT) method. The SM imaging characteristic of this imaging system was quantitatively assessed in term of Contrast-Noise-Ratio (CNR) and spatial resolution.

Chapter 2

Radionuclide Single Photon Imaging

This chapter is divided into two main parts. In the first part the concept and the basic principles of gamma camera operation is presented. The discussion include camera performance parameters i.e. collimator sensitivity, resolution and their relationship. In the second part a review of the state-of-the-art planar radionuclide breast tumour imaging systems using full size clinical γ-camera.

2.1 The Gamma Camera

The Anger camera [77, 78] also called gamma camera is the most commonly used device in radionuclide imaging to detect gamma photons. This is due to its image quality, low cost, and ease of use. The gamma camera imaging detector is usually composed of a collimator, scintillating crystal, several photomultiplier tubes (PMTs), an electronic chain and a digital computer for constructing the image. The gamma camera can have one, two, three or four heads mounted on a gantry where it can be moved easily in any direction. Current gamma camera imaging systems are capable of planar 2D image and 3D Single Photon Emission Computed Tomography (SPECT) and, are optimised for imaging 140 keV photons associated with the decay of ^{99m}Tc [29]. This radionuclide is widely available and can be produced locally using the generator system. This is achieved by eluting the ^{99m}Tc from ^{99}Mo that has a half-life of 66 hours. The cheap generation makes ^{99m}Tc the most widely used radioactive isotope. In addition, ^{99m}Tc offers a single detectable

γ-rays emission, has relatively short half life (6.02 hours) and thus, low radiation dose. The following subsections described the principle of the gamma camera operation but first the basic idea of how a camera works and the principle of single photon imaging is briefly summarised.

A small amount of radiopharmaceutical is first administered to the patient body through inhalation, orally or by injection. Then this radioactive substance physically decays via γ photon emission. This emission is isotropic and thus, exits the patient body in all directions. A γ-camera is then used to detect these γ-ray photons after passing through a collimator. The literatures show that gamma camera systems have undergone significant improvements over the last 50 years, but the imaging technology and the overall design of the γ-camera head has largely remained the same. The components and the main parts of the camera heads are illustrated in Fig.2.1 and are briefly described in the following subsections.

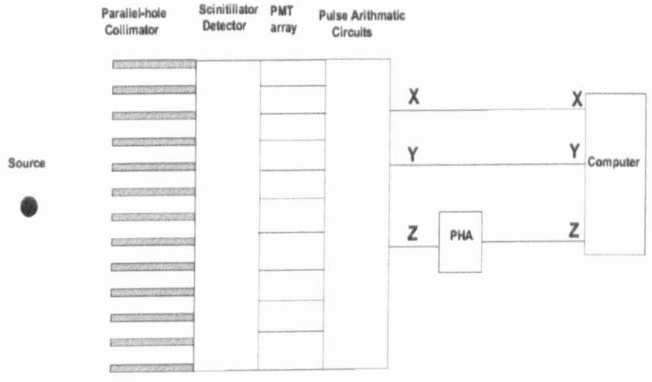

Figure 2.1: Schematic diagram showing various component of the camera. The γ-ray photon emitted from the source pass through the collimator to form an image in the scintillation crystal. The Anger logic (comprises pulse arithmetic and pulse hight analyzer (PHA)) is used to for position decoding. Figure adapted from [29].

2.1.1 The Collimator

The collimator is a device necessary for image formation. Based on its design it can magnify, minify and invert the resulting image. Parallel-hole collimators are the most commonly used collimator for single photon imaging. It provides large Field of View

(FoV), reasonable imaging capabilities but with no object magnification. It is usually formed from a lead structure containing precisely aligned holes. These holes are separated by septa with thickness ranges from 0.1-0.5 mm and can have circular, square or hexagonal shape. The main job of the parallel-hole collimator is to select photons according to their emission direction and thus, provide a directional information that form a projected image. In other words, it geometrically rejects photons with oblique incidence and allows only those γ-rays travelling near parallel directions to reach the detector crystal. This accurately provides the place of origin of the incident γ-ray photons flux. The camera is also shielded from the side and back with lead so that γ-rays from outside the FoV are prevented from reaching the detector.

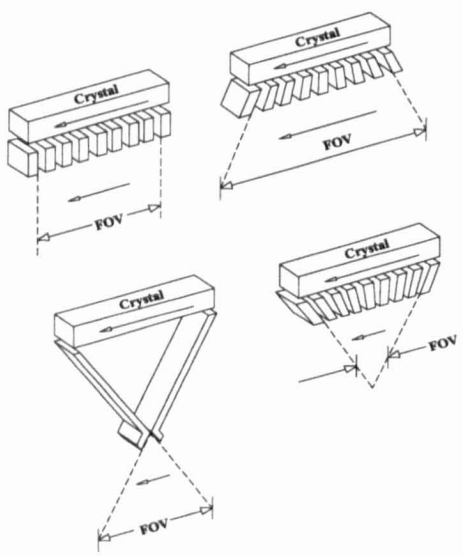

Figure 2.2: Schematic diagram showing the four types of the gamma camera collimators: parallel-hole (top left), diversion collimator (top right), pinhole (bottom left) and conversion collimator (bottom right). Figure adapted and redrawn from [80].

Apart from the parallel-hole collimators single photon devices can also use pinhole, converging (fan beam), and diverging collimators (see Fig. 2.2). The pinhole is the simplest collimator as it has a single hole (aperture) 3-6 mm in diameter at the top of a

hollow lead cone. The diameter of the cone base is similar to the camera dimension. As the aperture hole is located at a distance from the crystal this would produces a magnified image of a small object and thus, produces images of good resolution. However, the pinhole collimator is associated with small FoV and low detection sensitivity and thus, it is often used for thyroid scintigraphy, bone scintigraphy of small areas, and for pediatric nuclear medicine [79].

The collimator is the main limiting factor of the γ-camera as it affects both system spatial resolution and sensitivity. The former can be defined as the ability of the camera to discriminate between two point sources in the resulting image so that both can be seen as two separate sources [29], and the sensitivity is defined later. The resolution in this case is also expressed as the FWHM of the point spread function. Standard γ-camera has also an intrinsic resolution (due to statistical variation in the distribution of the PMTs) of ~ 3.7 mm FWHM that further worsen the resolution. In fact, the system spatial resolution R_s is the convolution of the collimator spatial resolution R_c and the intrinsic resolution, R_i and given as [29]:

$$R_s = \sqrt{R_i^2 + R_c^2} \tag{2.1}$$

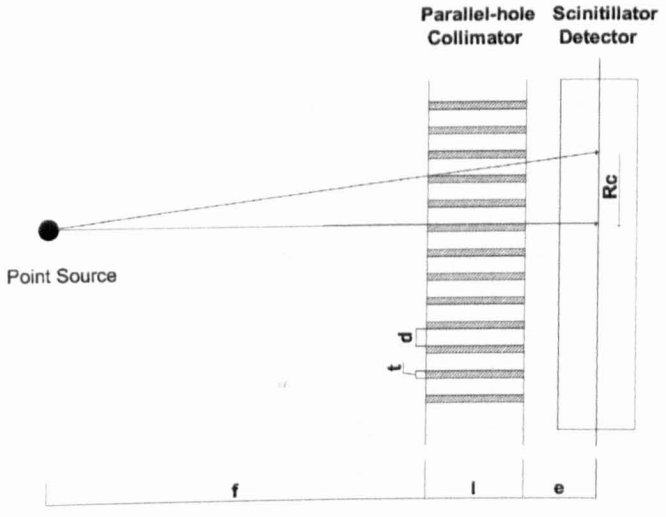

Figure 2.3: Schematic diagram of the parallel-hole determined.

This suggests that the collimator is the main factor that determine the system resolution particularly if it is slightly higher than the intrinsic resolution. With reference to Fig.

2.3 the collimator (of ideal absorber material) spatial resolution for the same parameters is given by [77]:

$$R_c = \frac{d(l+f+e)}{l} \tag{2.2}$$

where f is the distance between the collimator and the object being imaged, d is the hole diameter, l is the length of the septa and finally e is the distance from end of the collimator to the crystal. Equation 2.2 suggests that the collimator spatial resolution degrades linearly with imaging distance. Thus, for better resolution the camera should be positioned as close to the tissue of interest as possible.

On the other hand the sensitivity is defined as the proportion of γ-rays incident on the collimator and successfully pass through to the detector [29]. Thus, is also dominated by the collimator which rejects most of the incoming gamma rays only a small fraction of the incident photon flux, $\sim$ 0.1-0.01%, reach the detector. The resulting limited photon statistics image may also degrade the spatial resolution. The geometric efficiency (g) of a parallel-hole collimator is defined as the fraction of the γ-rays emitted by the source that successfully pass through the collimator. It is a function of the hole diameter d, shape k, length of the collimator hole l, and septal thickness t, and expressed as [78]:

$$g = k(\frac{d}{l})^2(\frac{d}{d+t})^2 \tag{2.3}$$

The k factor is a constant that depends on the hole shape ($\sim$ 0.24 for circular holes, $\sim$ 0.26 for hexagonal holes, and $\sim$ 0.28 for square holes). For non-ideal collimator absorbing material the effective length l_e of the collimator is shorter than the physical length, l, due to septal penetration and is given by [77]:

$$l_e \approx l - 2\mu^{-1} \tag{2.4}$$

where μ is the attenuation coefficient for gamma rays of the characteristic energy in the collimator material (e.g., lead). By combining Eq. 2.3 and 2.2 produces the following key relation:

$$g \propto (R_c)^2 \tag{2.5}$$

This mean R_c can only be improved by decreasing g, and vise versa. This trade-off limits the camera performance and unfortunately present in all collimator-based systems.

2.1.2 Scintillation Detector

Photons are not rejected by the collimator pass into the scintillating crystal. This is the main part of the γ-camera detector. It is made of a single block of thallium activated sodium iodide, NaI (Tl), scintillator. Pure NaI does not scintillate efficiently, and the use of Tl improves the scintillation process because it distributes itself uniformly throughout the crystal. The shape of the crystal (3D lattice) may be circular or more commonly rectangular with a dimension of $\sim$ 50 cm and a thickness between 9-12 mm [81, 82]. The high density (ρ=3.67 g/cm^3) combined with a high atomic number (Z=53), allows the crystal to absorb (by photoelectric effect) over 90% of the 140 keV γ-rays [29].

Once a gamma photon with sufficient energy (> 20 keV) hits the scintillation crystal it undergos an interaction that releases all or part of its energy to an electron in the crystal. The gamma radiation is completely absorbed by crystal atoms in the photoelectric absorption process (dominant in low energy γ-rays). In Compton scattering process, the incident γ-rays only transfer part of its energy and this often occurs in more than one position in the crystal for a single event. These are the main interactions process when imaging with the 140 keV photons.

As a result of these interactions, the crystal produces a flash of visible blue light. The amount of light produced is proportional to the energy deposited in each interaction. This light disperses throughout the crystal and thus, needs to be guided by the light guide. This is used to allow transmission of light from the crystal to the PMTs. The light guide is a few cm thick transparent material helps to minimises the light losses by guiding the light photons to the PMTs.

The PMTs are attached behind the crystal. Each tube consists of an evacuated glass envelop (5-7 cm in diameter) arranged in a hexagonal or circular shape. The hexagonal PMTs are better as with this close packed geometries the gaps between tubes can be eliminated. Thus a better detection efficiency can be achieved, albeit with increased cost per tube. Each camera has about 37-91 PMTs evenly distributed across the FoV. The higher the number of PMTs, the higher the intrinsic resolution of the camera [82]. Inside each tube one can find a photocathode, an anode and around 10 dynodes (electrodes). The main task of the photocathode is to detect (by the means of the photoelectric effect) the scintillation light emitted from the crystal and converts it into electrons. For every

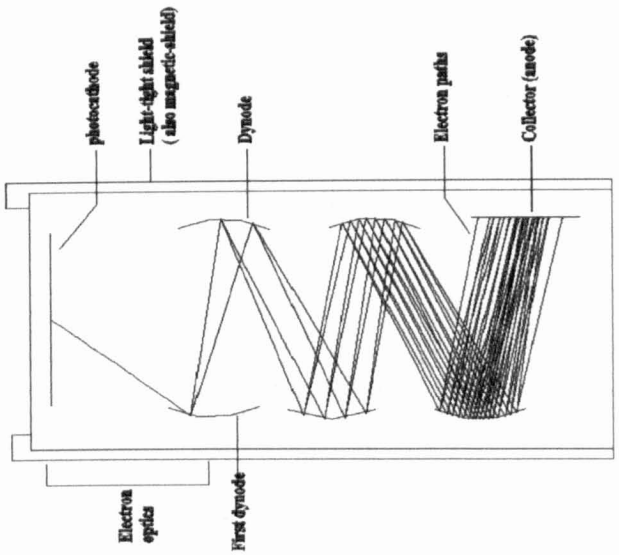

Figure 2.4: Schematic cross section through PMT, showing its basic components. Note that each PMT have 10-12 dynodes.

$\sim$10 photons incident on the photocathode, only around one electron is generated. The ejected electrons (photo-electrons) will then be accelerated toward the first dynode. The electrons are focused on a dynode which absorbs each electron and re-emits secondary electrons (normally 6 to 10). These will then be focused on the next dynode (have higher voltage than the first dynode). This process is repeated over and over until reachs the final dynode (see Fig. 2.4). Finally, the anode attracts the cascade of electrons producing an electrical pulse corresponding to each photon interaction in the scintillation crystal. Those pulses are then pass through a circuit containing preamplifier to amplify and shape the signal for further processing.

2.1.3 Signal Analysis & Processing

Now the spatial location and the energy of the γ-ray need to be accurately computed. The Anger logic or pulse arithmetic circuits (capacitor or resistance array) receives the electrical impulses from the PMT array. The main job of the position circuits is to determine where each scintillation event occurred in the detector crystal. The position coordinates depend on the X and Y locations at the point of scintillation. The final output signals gives the spatial information (X, Y) and the energy (Z) of the event.

Modern cameras digitize the X, Y and the energy signals after being computed by the analogue position encoding matrix and then store it. More recent digital system cameras completely replace the analogue circuits, and the thus, the signals from PMTs are first digitized, and then the position of the event is determined digitally [29].

The sum (size) of the Z signal (pulse) represents the energy of the detected gamma photon. This signal needs to be processed by the pulse height analyser which selects the photopeak for a particular radionuclide being imaged. Windowing is also done to bin energies of the γ-ray within a certain selected range into an energy channel. For simplicity consider imaging with ^{99m}Tc (of energy 140 keV) at certain depth in the body. Then some of the energy of the gamma photons get absorbed within the body, some gets Compton scattered (at energies < 140) and some gets transmitted at 140 keV. Ideally, it is desirable to measure the photopeak energy (a spike of 140 keV) but due to the energy resolution of the NaI (10% at 140 keV) the photopeak is rather a Gaussian shape. This is the energy response function of NaI at 140 keV. The width of this response can be measured by calculating the Full Width Half Maximum (FWHM) value of the full energy photopeak. Thus, the pulse height analyser is used to tests whether the observed pulse height is within the range of values expected. Typically, in this case, pulse heights corresponding to 126-154 keV i.e. 20% ($\pm$ 10%) of the photopeak [29] are used. This rejects a large portion of scattered photons. However, due to statistical uncertainty, there is an overlap between pulse heights corresponding to Compton events and those corresponding to photo-electric absorption. This produces unavoidable Compton scatter in the final image.

At this stage, the final image can be displayed in the camera associated workstation. In the workstation the user can select various image processing and reconstruction technique.

2.2 Single Photon Imaging

Single photon imaging categorised into two main techniques, planar and SPECT. A brief description of each technique is given hereunder.

2.2.1 Planar Imaging

Planar (2D) imaging is a fast, simple, less expensive and widely used investigation to assess the functional status or physiology of a patient. It basically involves taking a 2D

projection image from a single location. In this case, the data are acquired directly (no reconstruction is required) particularly when using parallel-hole collimator. However, this technique gives no depth information due to tissue superimposition. This may cause a slight loss in contrast, due to overlying and underlying activity, and thus for certain clinical applications the use of SPECT is preferred.

2.2.2 SPECT Imaging

SPECT is also widely used and requires scanning (at defined points) the patient or the organ of interest from different views. In this case the camera rotates about the patient collecting image information from different angles. Most clinical examinations requires a full 360 degree rotation of the camera head. In this case the camera rotating every 3-6 degrees and each rotation position being 15-20 sec, giving a total imaging time of 15-20 minutes. Thus, the multiple planar raw data images need to be reconstructed to produce a 3D image. These reconstructed images are typically of resolution 128×128 pixels and usually presented as cross-sectional slices.

The use of SPECT for breast tumour imaging when imaging with conventional γ-camera may be undesirable and challenging. This is because ^{99m}Tc-sestamibi is a heart agent and unevenly distributed and concentrate in the heart and thus potentially causes artefacts. The intense area of activity can also cause streaking of the images and this may obscure the surrounding area of activity. Thus, the reconstruction images from SPECT are of lower resolution and are more susceptible to noise than planar techniques. In addition, the position anatomy of the breast makes it perfect for planar imaging as SPECT application is usually performed for organ surrounded by tissue of overlying density such as the heart [51].

2.3 Radionuclide Breast Tumour Imaging

This section provides an overview of the state-of-the-art planar radionuclide breast imaging systems performed with conventional γ-camera. The aim is to highlight the main clinical application and provides a summary of the literature.

2.3.1 Scintimammography Imaging Using Standard γ-Camera

The use of radionuclide imaging for breast tumour imaging was discovered in the 1990s after using ^{99m}Tc-sestamibi for cardiac scanning [51]. An area of abnormal uptake was observed in the breast suggesting this agent as a suitable breast imaging agent. The imaging technique has been mainly proposed to aid in the diagnosis for particular clinical indications that can not be performed with X-ray mammography.

(a) Radiopharmaceuticals

Sestamibi has been used for breast tumour imaging since 1994. It was officially approved by the Food and Drug Administration in 1997 [51]. The ^{99m}Tc-sestamibi is a small lipophilic cationic molecule composed of six "2-methoxy-isobutyl-isonitrile" or MIBI moieties. This radiotracer is currently the most commonly used radiopharmaceutical may be due its large availability and cheap generation. The mechanism of uptake by cancer cells is not well understood but it has been suggested [86] that sestamibi may accumulate in the mitochondria and within the cytoplasm of tumour cells .

Various other radiopharmaceuticals have been used for breast tumour imaging including thallium (^{201}Tl), ^{99m}Tc-tetrofosmin, ^{99m}Tc-Methylene Diphosphonate (MDP), and ^{18}F-FDG [84]. The ^{201}Tl is limited by its long half life (73 hours) as well as by the poor physical characteristic of photons that limit the injected dose to about 110-185 MBq. However, ^{99m}Tc-labelled imaging agents are far more reliable for breast tumour imaging due to higher uptake level. In addition, the use ^{99m}Tc labelled tetrofosmin is promising and claimed [87] that it can cross the cell membrane and has faster clearance from lung and liver. This is advantageous in detecting tumours in the inferior quadrant of the breast [87]. However, the main limitation is the insufficient numbers of studies obtained with this agent and thus its performance need further evaluation [87, 88]. Furthermore, several groups are currently developing cancer specific pharmaceuticals and antibodies that may increase tumour uptake.

(b) Imaging Procedure

Breast tumour imaging requires injecting the patient with a small amount (555-740 MBq [83, 84]) of ^{99m}Tc-sestamibi. The site of injection is usually in the arm opposite to the

suspected breast lesion. After a period of time, the radiotracer distribute in the breast tissue with a slightly higher concentration (uptake) in cancer cells than normal cells. Sestamibi also distributes with higher concentration in other organs of the body such as liver and heart.

In planar imaging of the breast a combination of two views (prone and supine) are usually acquired 5-15 minutes after the injection. This is may be due to the tumour high metabolic activity compared to the surrounding normal tissue. If additional views are required a delayed image is performed 60-90 min after the injection. The left or right prone positions are best to provide a compression and to separate the breast tissue from the heart and the liver [85]. The prone position also allows imaging deep breast tissue that is close to the chest wall [84]. The supine position is more useful for visualizing the axillary region, upper and anterior part of the breast. This may also be useful and to evaluate any lymph node involvement. Additional views include lateral oblique with the patient in the prone position or a 90^o lateral view. The acquired image may be of size 128×128 pixels or larger matrix if needed and often displayed in grey scale.

(c) Clinical Applications

A large proportion of women screened by conventional X-ray mammography have dense breasts particularly in young women. This group of patients are advised to have a test that independent of breast density. SM imaging is the modality recommended for this group of patients as it is not affected by the density of the breast [51]. It has a higher sensitivity over mammography in such group of patients [51]. SM imaging play an important role, as a complementary imaging method to X-ray mammography, for many different clinical applications [51]. As discussed in section 1.7.3 (b), surgery, radiation therapy, hormonal replacement therapy, excisional biopsies and chemotherapy causes architectural distortion to the breast tissues. As a result, mammographic evaluation in these cases is very difficult. The best alternative is SM as its diagnostic accuracy is not affected by breast tissue distortions. It is also useful in determining the presence of recurrent disease in these circumstances. In North America SM may be regarded as a third line (in some clinical indications may considered as second line) diagnostic aid to assist in the evaluation of breast lesions [89].

SM may also considered to be useful for evaluating non-palpable breast lesions and thus

Table 2.1: A comprehensive review [51] from 20 studies and a total of 2009 patients to evaluate the accuracy of SM.

Test Parameters	**Summary of the results**
Total average sensitivity	85% (1,029/1,218 lesions)
Total average specificity	89% (963/1,086 lesions)
Total average accuracy	86% (1,992/2,304 lesions)
Total average PPV	89% (1,029/1,152 lesions)
Total average NPV	84% (963/1,147 lesions)

aid X-ray mammography. Using the two imaging modalities has been demonstrated [90] to improve the low positive predictive value (PPV) which may help in detecting non-palpable breast lesions. In addition, SM may also be valuable for the assessment of multifocal breast cancer [91]. This is clinically important since multifocal disease is very difficult to detect and the only treatment option is mastectomy. Moreover, two clinical reviews [51, 84] reported that SM may also be useful for monitoring and evaluating the tumour response to chemotherapy. Another clinical application of ^{99m}Tc-sestamibi reported in literature, is the investigation of patients with microcalcification [51]. Furthermore, SM may be clinically valuable for detecting axillary lymph nodes metastasis [83].

Taillefer [51] has reviewed the published papers between 1994 and 1998 to investigate the clinical capability and performance of SM using standard γ-camera. This review is based on 20 studies with a total of 2009 patients and show discrepancies in the reported data from these studies. These variations in the reported values was believed to be due to several factors such as different patient population and different type, size, location and tumour uptake. In addition, a variety of other factors related to the camera performance, resolution, settings, and acquisition, imaging time and the type and diameter of the collimator used. A summary of the results is given in table 2.1 [51]. This review confirms that SM may be used effectively as a complementary method to X-ray mammography. From this review Taillefer shows that no lesion less than 5 mm has been detected by the standard full-size clinical gamma camera detectors. He also demonstrated that the reported sensitivity varies between 80%-90% and it is higher in the group of patients with palpable lesions than those of non-palpable lesions. The reported average specificity of ^{99m}Tc-sestamibi SM for malignant breast lesions is 89% [51].

In another review evaluating the diagnostic accuracy of SM using standard γ-camera [92], it has been reported that the overall sensitivity and specificity average 83.3% and 81.3%, respectively. These results based on the detection of primary breast cancer taking histopathology as the gold standard. In a more recent comparative review published in early 2006, the Federal Agency for Healthcare Research and Quality (FAHRQ) [93] evaluated the performance of non-invasive diagnostic tests in women with breast abnormalities. These abnormalities were previously identified by either X-ray mammography or breast physical examination. This comparative report compares the effectiveness and the diagnostic accuracy of ultrasound, MRI, PET and SM and concluded that none of these non-invasive diagnostic met the suggested standard of having a less than 2% risk of having cancer particularly among women with negative diagnostic results. However, this is the only negative finding compared to all other studies, nevertheless, provides motivation for work in this thesis aimed at improving SM imaging performance using CA techniques.

(d) Limitations

The performance of the general purpose clinical γ-camera in lesion detection using ^{99m}Tc-sestamibi, is dependent on tumour size. Imaging patients with lesions of sizes > 1 cm in diameter are more likely to be detected. This mean that the sensitivity is higher for lesion > 1 cm in diameter than smaller lesion. Similarly, the sensitivity of lesion detection is higher for palpable lesion than non-palpable lesion. However, the technique becomes less reliable in lesions < 1 cm in diameter [89, 93] may be due to the small incident flux from such lesions. In this case photon noise may dominate the image and consequently reduce image resolution. The significant noise from the background activity further complicate the detection.

In order to improve the sensitivity of SM, many recent studies [50, 94, 45, 46, 47, 48, 49] have been performed using new dedicated detectors constructed for use in breast tumour imaging applications. The commercially available dedicated imaging systems (see table 1.3) are based on either modifications of the existing PMT-based scintillation camera technology or based on the new pixelated direct detection detector technology. Few studies have demonstrated slight improvements in sensitivity with respect to stage I cancers (of size ≤ 1 cm) when imaging with such high resolution cameras [47, 49]. Despite these slight advantages there is still difficulty imaging areas near the thoracic wall or axillary regions

because of the small FoV. These cameras are also not reliable to be used for screening purposes because of their limitations in visualizing small calcifications and soft tissue masses [89, 48]. In addition, a slight reduction in the specificity is shown as the sensitivity increases. The main important limitations in using such dedicated breast cameras are their high cost as well as their role in breast cancer diagnosis are not clearly established. Thus, further studies are necessary to evaluate their complementary role in the management of breast cancer as well as the indications in clinical practice.

In summary, most cited papers and review concluded that ^{99m}Tc-sestamibi SM imaging, using full-size clinical γ-camera, is valuable technique and can be effectively used to complement X-ray mammography. These studies suggest that SM is not indicated for breast cancer screening to confirm the presence or absence of malignancy. This technique is not sufficiently accurate to be used as an alternative method to breast biopsies. To be able to do so the diagnostic imaging test must possess a high accuracy so that it can clearly classify and assess the anatomical and physiological features of the imaged lesion. Thus, ideal imaging test must have both high spatial resolution and high contrast sensitivity with accuracy $>$ 98% [93]. However, many studies showed that SM might be useful as a complementary imaging technique to improve the sensitivity and specificity of conventional imaging modalities. The main technical problem of the current gamma-ray detection systems is believed to be due to the use of mechanical collimator. This is because the performance of the standard γ-camera is heavily dependent on the collimator and its geometry (see section 2.1.1). Since the LEHR collimator is always employed it tend to affect the spatial resolution and the sensitivity of the γ-camera and the resulting image will have low photon statistics. As a solution to these problems this study proposed using CA, alternative to LEHR collimator, coupled to standard γ-camera for breast tumour imaging application.

Chapter 3

Coded Aperture Imaging Theory

This chapter is divided into three main parts. The first part introduces the concept of Coded Aperture (CA) imaging as well as provides an historical background of the different types of apertures. The second part gives a brief description of the CA families having perfect mathematical imaging properties including their generation rules and correlation properties. The third part highlights the CA camera geometries describing the design methods of the proposed approach. This discusses the mask camera configuration and design with emphases on the size, the open fraction and the Field of View (FoV). The reconstruction methods used to decode and recover the encoded image close the chapter. The chapter begins with introduction to the principle of pinhole camera to give the reader the opportunity to appreciate the theory and the formation of coded image.

3.1 Introduction

Imaging γ-rays at $>$ few keV is not an easy task as it is difficult or often impossible to focus these photons with conventional mirrors or lenses. A form of geometrical collimator such as pinhole camera was introduced as a solution for this problem. As shown in Fig. 3.1(a), the gamma flux passes through a hole in an opaque plate and the image is formed in a position sensitive detector. The pinhole camera has ideal imaging properties as its response is $\approx \delta$ function. It is also associated with small Field of View (FoV) but produces images of good resolution. However, this direct-imaging system requires a long imaging time as it suffers from low efficiency due to its small hole size. As a result, a low signal poor quality image is obtained because the γ-ray photons detected are usually few in numbers.

(a) (b)

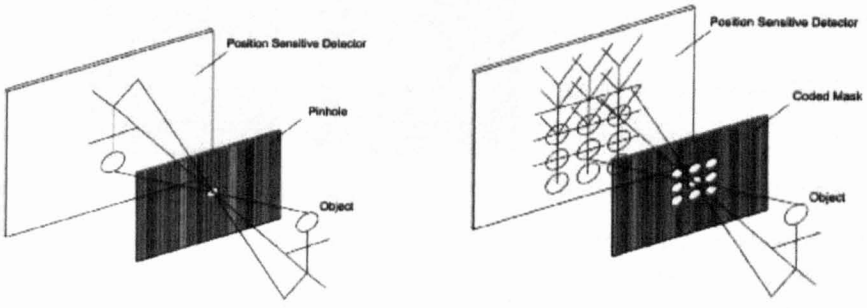

Figure 3.1: Schematic diagrams of two image formation principles: (a) a pinhole camera; the production of an image by a pinhole camera, (b) multiple pinholes camera (CA mask); the production of a coded image using signal multiplexing principle. Note: both techniques gives inverted image of the object.

The collimator imaging such as the parallel-hole is limited by the design and also provides a low detection efficiency (see chapter 2).

A camera with many pinholes (see Fig. 3.1(b)) was proposed as a solution to obtain a much larger fraction of the incident flux and permits high resolution imaging. The image produced from such camera is based on the principle of "Spatial Signal Multiplexing" [95]. It simply means that every incident point source, within the object FoV, is participating in encoding the flux into a predetermined pattern or code, thus called CA or mask, which casts a shadow of this pattern onto the detector surface. To obtain a useful image, the encoded pattern (projected image) is then decoded, most often by using the correlation analysis of the pattern produced by a point source, with that of the encoded image. Thus, this form of imaging is a two stage process. It begins with encoding (multiplexing) the source information and ends with decoding (de-multiplexing) to recover or reconstruct the image from that source. The main motivation to undertake this indirect image formation is the hope of combining the higher Signal-to-Noise-Ratio (SNR), due to the large open area of the CA, with the higher resolution, due to image magnification, compared to the collimator based imaging systems.

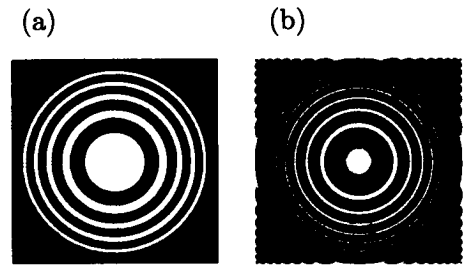

Figure 3.2: These show the FZP CAs [66]: (a) a binary FZP, (b) a sinusoidal zone plate that has infinite extent. The resulting image from such pattern is a hologram that can also be reconstructed with coherent optical system.

3.2 History of Coded Aperture Imaging

This section provides a brief descriptive overview of the various forms of CA imaging systems. A detailed review of CA imaging approaches can be found elsewhere [66, 96]. The first form of a viable CA pattern was proposed by Mertz and Young [62]. It was used for imaging faint stars in astronomy. In such imaging application, the problem is characterised by far field geometry i.e. the objects are located at infinity from the detector. In this case all the γ-rays travel in nearly straight line (parallel to each other) and fall perpendicular to the imaging detector. In the early days of this application, Fresnel Zone Plate (FZP) pattern [62] was the most widely used CA. As demonstrated in Fig. 3.2, the FZP consists of a series of circular patterns of equal area arranged in alternating design. One half of its area is open (transparent) and the other is closed (opaque) to γ-rays. This large open area means that photons at wide variety of angles may be accepted giving more depth information and thus, 3D information of the source position. It also mean that such patterns possess a higher sensitivity than collimator based-systems. Consequently, it was applied in medical gamma-ray imaging by Barrett [59] as an alternative to the pinhole collimator. A considerable amount of clinical work was followed by Rogers and colleague [97]. However, it has been reported [66, 98] that the FZP is not ideal in its imaging properties. This is because the auto-correlation function of such patterns have side lobes artefacts and its Fourier transform is not perfectly flat. It also possesses a poor resolution that limits its wide acceptance [66].

The random pattern [63, 64] (see Fig. 3.3(a)) is also one of the early CA that has been

proposed as an extension of the pinhole camera. The idea behind the random array is to increase the open area of the mask, while preserving its spatial resolution. The detection efficiency may further be increased by enlarging the mask hole size, but this will be at the cost of the resolution. The random character is necessary to get imaging properties that approximate a δ auto-correlation function. However, it has been reported [66, 99] that the random arrays suffer from inherent noise due to the presence of the side-lobes. As illustrated in Fig. 3.3(b) these side-lobes are the cause of non-perfect imaging properties.

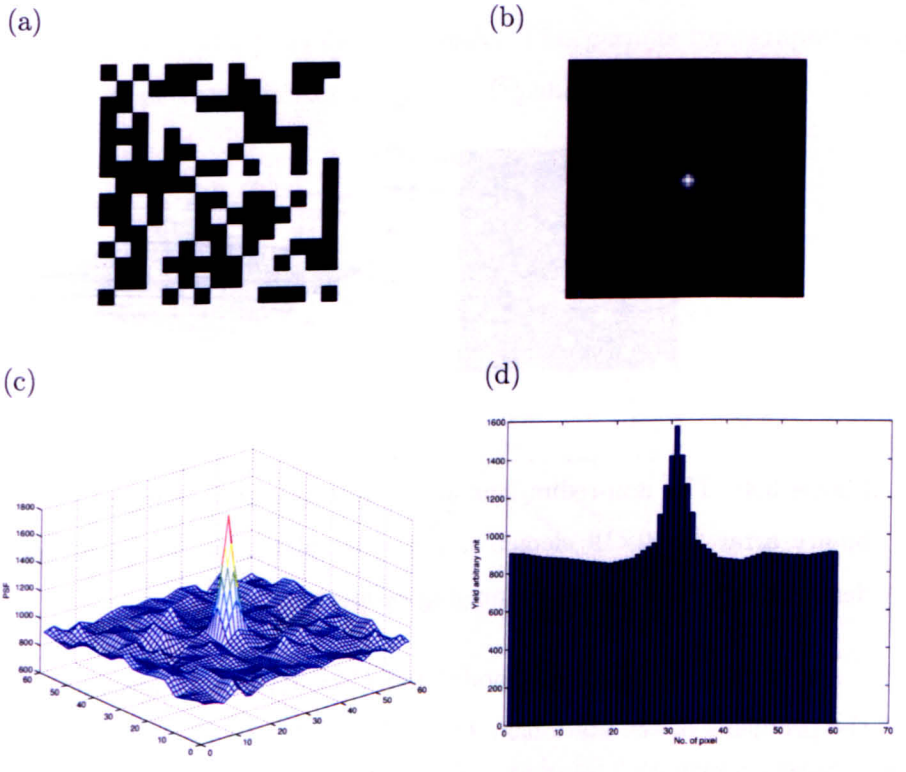

Figure 3.3: The random array and its auto-correlation response function: (a) a random binary mask of size 15×15, (b) the decoded image demonstrating the inherent noise of the random array, (c) 3D plot of the array auto-correlated image showing a peak on top of pyramid shapes with the ratio between the two equal to the open fraction, (d) vertical bar plot through the centre of the decoded image.

Soon after a considerable amount of work was undertaken to synthesis suitable patterns, demonstrating flat side-lobes, to be used for imaging. Various design patterns have been proposed with the hope to maximise the detection efficiency without degrading the

resolution. For instance, in 1971 Non Redundant Arrays (NRAs) [100] were introduced as an extension of the pinhole camera. As shown in Fig. 3.4(a) this type of CA is made up of small pinholes arranged in a non-redundant pattern i.e. with no repetition of hole pattern occurs [100]. In other words, the spacing between any two holes occur once over the whole plane. These arrays are compact and have nearly perfect imaging characteristics only on a very small FoV. However, its small number of holes prevent great improvements in the detection efficiency.

(a) (b)

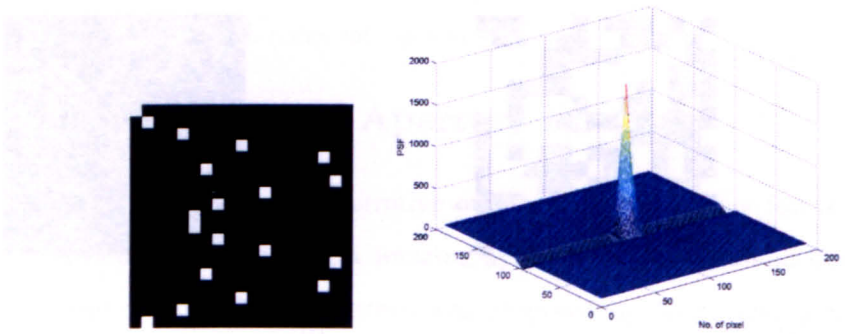

Figure 3.4: The non-redundant array and its response function: (a) a non-redundant binary array of 19×19 elements, (b) a 3D plot of its auto-correlation function clearly demonstrating the non-ideal imaging properties.

A few years later, time modulated CAs have been developed to eliminate some of the problems of the stationary CAs. The main principle is that the γ-ray transmission at different points in the aperture varied independently. Several other approaches have been proposed for instance the rotating slit suggested by Tanaka and Linuma [66] and the stochastic aperture proposed by May [66]. The former consists of a small transparent slit rotating about its centre but the latter is more sophisticated. This is because the aperture used for imaging is stepped through a sequence of positions so that all the elements are cyclic in the time domain. The most promising form of aperture is the planar pseudo-random binary sequence also called stochastic time modulated CA. This is because during scanning the CA is stationary but its elements CA are cyclically permuted for each sub-interval of the scan. This allow image decoding to be performed on a detector element by element basis.

Figure 3.5 illustrates a simple geometry of a stochastic time modulated CA, the imaging principle of such CA, using a single point source, is that as the aperture is moved in its plane the detector record the signal of the source. The aperture movement is through a sequence of positions encoded (in the time domain) the signal of the source as the phase or time is different. A simple correlation analysis with suitable decoding function is needed to recover the source information. The use of array of detectors as shown in Fig. 3.5 permits tomographic imaging for instance, the first detector recorded the same signal from sources number 1 and 3. In addition, point 1 and 3 have different positions and are projected to detector 4 and thus viewed from different angle. This permits tomographic imaging and the use of array of detectors makes this more simplified.

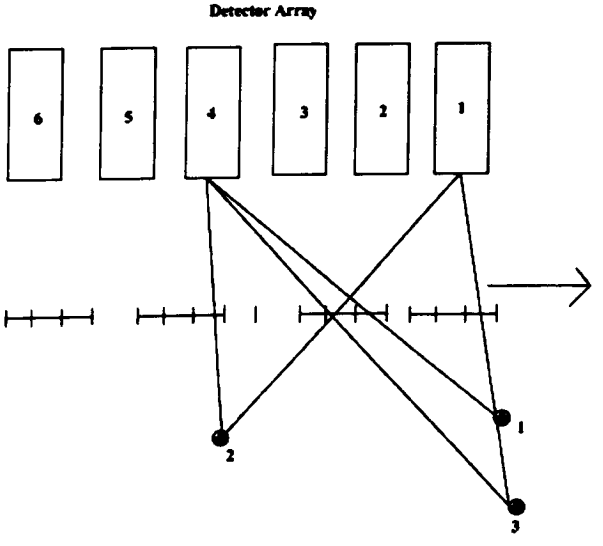

Figure 3.5: Simple geometry illustrating 1D pseudo-random sequence time-modulated coded aperture. Figure adapted and redrawn from [66].

In 1983 Gourlary [101, 102, 103] introduced several geometrical arrays. These arrays are flexible in their designs and having open fraction less than 50%. The main designs focus on L and X family arrays having a square shape. Two examples of these arrays are shown in Fig. 3.6 for the L family and Fig. 3.7 for the X family. Unfortunately, these arrays do not provide any advantages over the MURAs patterns. The imaging performance of these arrays depends on the location of the object within the FoV [101, 102, 103]. This may be because these geometric arrays are not cyclic in its nature.

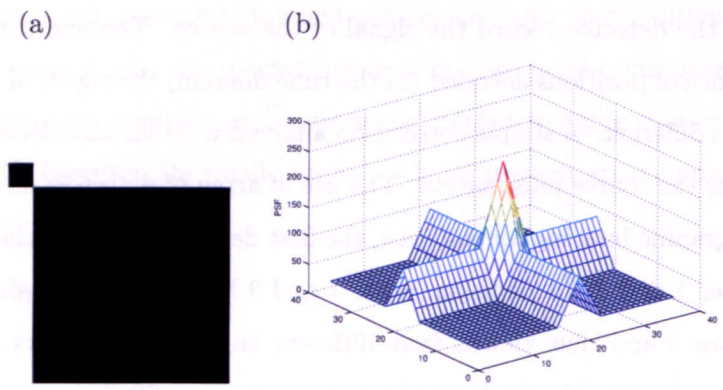

Figure 3.6: The L shape geometric array and its response function: (a) a geometric array of 9×9 elements, (b) a 3D plot of its auto-correlation function clearly demonstrating the non-ideal imaging properties.

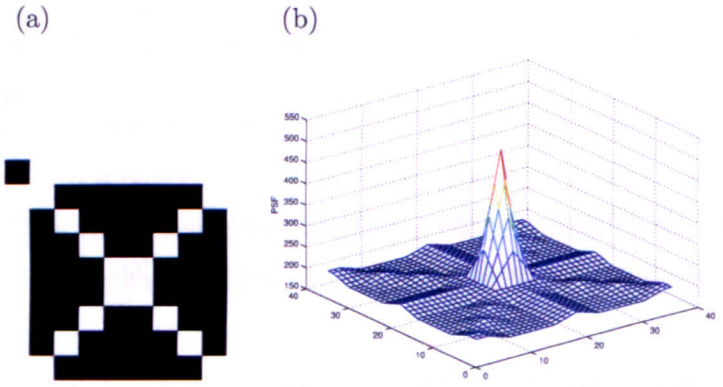

Figure 3.7: The X shape geometric array and its response function: (a) a geometric array of 9×9 elements, (b) a 3D plot of its auto-correlation function clearly demonstrating side-lobes in the image.

The majority of the above CA approaches are impractical and are rarely used in clinical practice. This is because the autocorrelation functions in these array are subject to coding noise or artefacts [99]. Some of these patterns had been mainly used in astrophysical field and did not achieve much success in medical imaging applications. However, CA imaging technique continued to be used by the astrophysics community.

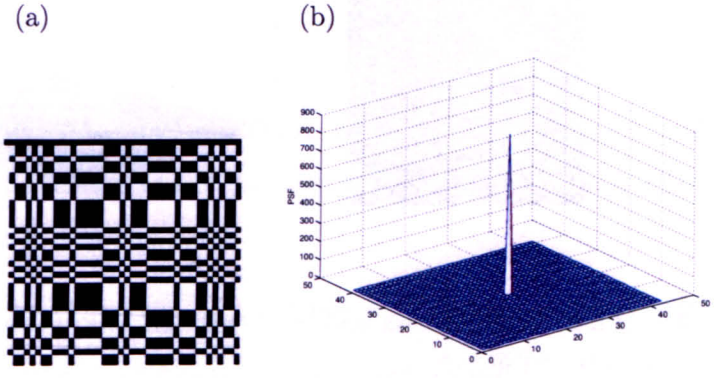

Figure 3.8: Binary URA mask and its correlation PSF: (a) 43×41 pattern where white corresponds to 1 and black corresponds to 0, (b) The correlation function of URA.

The drawbacks of the above patterns overcome in 1977, when Fenimore [67] introduced the rectangular Uniformly Redundant Arrays (URAs), which have attractive imaging properties (see Fig. 3.8) and are finite. These arrays have rapidly gained a widespread acceptance in the field of astronomy. A decade later, URAs were followed by the Modified URAs (MURAs) (see Fig. 3.9) [69], which have the additional convenience of being square. From the URAs and MURAs one can construct a self-supporting arrays called No-Two-Hole-Touching arrays (see 3.10). Such arrays also having perfect correlation property providing δ function of the imaging system.

All the aforementioned 2D arrays have many interesting properties given in more details in [67, 68, 99] and are summarised below:

- As their names suggest, the spacing between any two holes occurs a constant number of times.
- The construction methods generate these arrays and also generate the corresponding decoding arrays.

(a) (b)

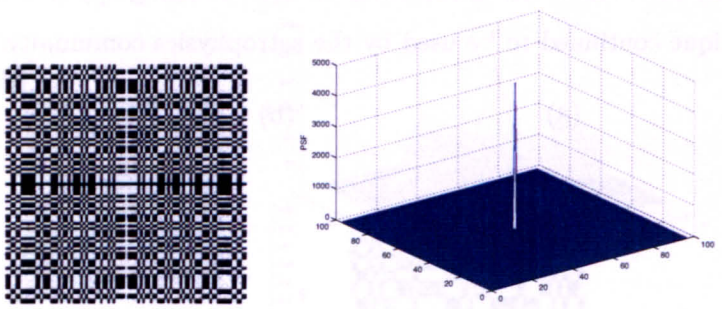

Figure 3.9: Binary MURA mask and its correlation PSF: (a) 97×97 pattern where white corresponds to 1 and black corresponds to 0, (b) The correlation function of the MURA.

(a) (b)

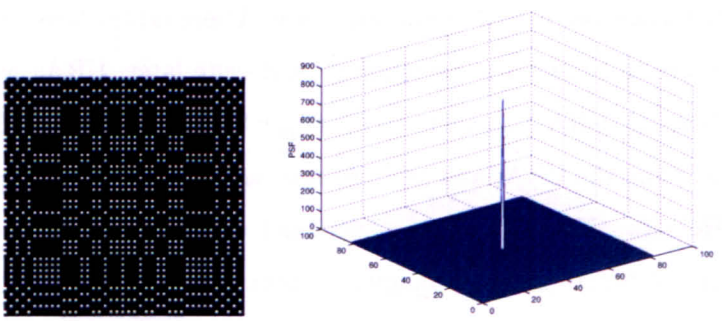

Figure 3.10: NTHT array of 82×82 elements and its response function: (a) NTHT array obtained from MURA pattern of size 41×41, (b) The correlation function of the NTHT-MURA.

- The main attraction of these arrays is the perfect correlation property providing a δ function of the imaging system.
- These arrays possess high transmission capability approximating 50% and can maintain resolution by image magnification.
- The design or the cyclic nature of such arrays and their decoding array provides another interesting advantage in which an arrangement involving a mosaic (2×2) of the basic pattern as demonstrated in Fig. 3.11. To reconstruct the image in this case one needs an area equal to the basic pattern [68]. This can be perfectly achieved by selecting the central area of the mosaic patten of size equal to the basic pattern (see section 8.2.3).
- The negative of a mask, i.e. a mask with open and opaque positions exchanged also has ideal imaging properties. Both masks can be used together to reduce the near-field artefacts.

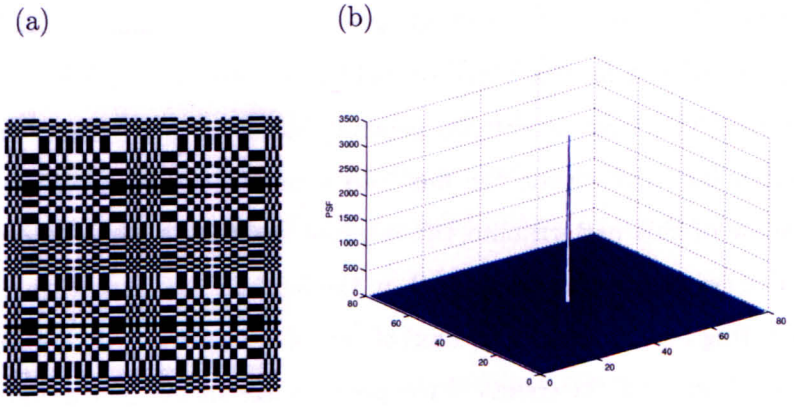

Figure 3.11: Mosaic MURA mask and its correlation PSF: (a) a 2×2 mosaic of the basic pattern 41×41 pattern, (b) The correlation function of the MURA.

In summary, the main advantages of CA imaging systems are the high photon transmission, the image magnification and to a lesser extent the (limited-angle) tomographic capability. The URAs and MURAs patterns developments have more attractive features providing a δ-like autocorrelation function of the imaging system. These properties have attracted the medical imaging community to renewed interest in the CA imaging technique. The increase in the resolution of imaging detectors as well as the increase in

computing power and speeds have made this possible. In fact, the current practical applications of such apertures include astronomy, physics and nuclear medicine applications. Multiple pinholes camera, MURAs and NTHT-MURAs are the most widely used devices in the current nuclear medicine research [72].

Based on the author's opinion the MURAs and NTHT-MURAs CA patterns are squares arrays and expected to produce good decoded images when used in breast tumour imaging applications. This is because the technique is ideal for imaging small isolated sources and thus provides a good match to the imaging objective of scintimammography. This thesis is therefore mainly concerned with the investigation and the understanding of the application of these CA patterns in breast tumour imaging. In particular, the evaluation of their potential and their performance under a variety of imaging conditions.

3.3 Coded Image Formation

Anger cameras use a collimator to form a projected image of the incident photon flux. This is achieved by geometrically rejecting photons with oblique incidence, and only permitting photons with a narrow range of incident directions to reach the detector surface. By contrast, CA imaging systems generally accept a much larger fraction of the incident photon flux and encode the flux into a predetermined pattern or code, which casts a shadow of this pattern onto the detector surface. For instance, when imaging a point source (with low statistical noise), in the far-field geometry, then each photon contributes to casting a shadow (encoded flux) of part of the aperture pattern onto the detector surface. This means that the counts of the point source spread over a non-point like surface area. The size or magnification of the aperture shadow depends on the distance of the point source from the CA. To obtain a useful image, the encoded pattern is then decoded, most often by using the correlation of the observed pattern with a suitable decoding function.

In the case of imaging an extended object the basic concept does not change. Each point in the object can be regarded as a point source casting an aperture shadow of a certain size and location on the detector. In other words, the number of photons passing through a single hole of the CA is independent of photons passing through all other aperture holes. The contributions from each aperture hole represent the total projections of the object being imaged. These projections, collected at the detector, are composed

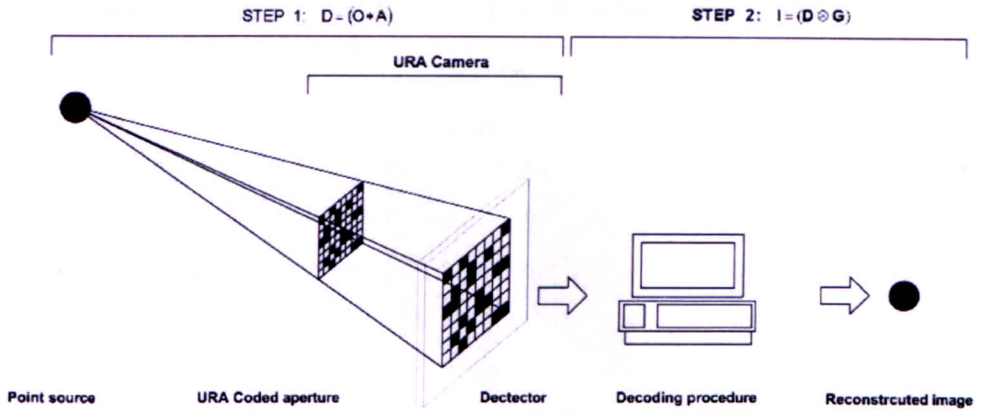

Figure 3.12: A schematic diagram of coded aperture principle imaging a point source.

of many shifted copies of the source object. The decoding process can be obtained in a similar way as in the case of point source.

As CAs have been historically developed for far field imaging applications, then the behavior of CAs in this geometry will be discussed initially. Near field application will then developed later in this chapter. For an object denoted by array O located at infinity from the aperture pattern that is given by the array A (a 2D function containing a 0 where the aperture is closed, and 1 where it contains a hole). The noise is denoted by array B (noise term). Following Fenimore [68] the recorded image, D, can be given as:

$$D = (O * A) + B \tag{3.1}$$

where: $*$, is the convolution operator and is used here because the process is physical.

As most aperture arrays have a large number of holes, D does not look like O at all. In other words, a point in the image is not represented on the detector by a point, but rather by the shadow of the mask pattern or part of it (see Fig. 3.12). This is what basically causes the signal or the information of the source to be encoded. In this sense the point source is not counted once, but once for every hole of the CA. This is expected to increase the counting statistics, and consequently, the quality of the image. On the other hand, on imaging an extended source object or many point sources, the source spatial information is then multiplexed (see Fig. 3.13). This is because each detector element receives as much information (signal) as the number of point sources incident on it. The recorded (projected) pattern, D, must be decoded to recover the source object information and

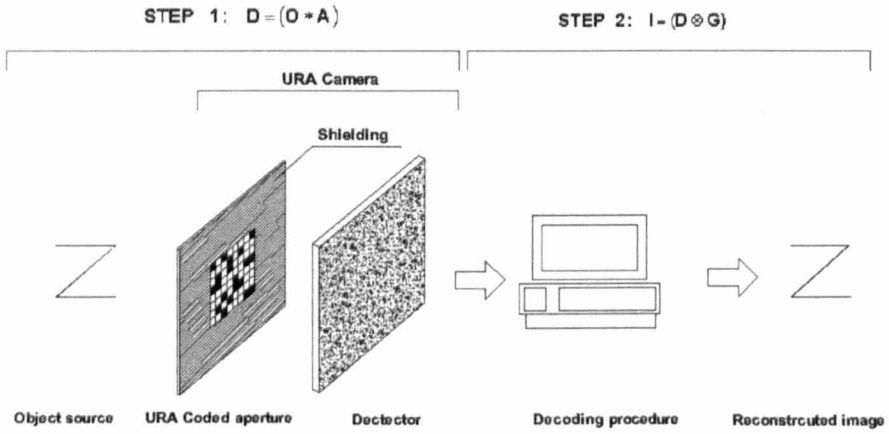

Figure 3.13: Coded aperture principle on imaging an extended object.

obtain a useful image. In other words, D must be scanned or correlated with the known pattern array to replace the shadowgram cast by a point source in order to separate the overlapped copies cast by an extended source object. The reconstructed image, (I), in the proposed patterns, is often obtained by correlating D with a post processing array, G (inverse filter of A), and is defined as:

$$I = D \otimes G \tag{3.2}$$

where: $\otimes$ indicates periodic correlation.

The particular imaging properties of the these patterns is that given arrays A and G then $(A \otimes G)$ approximates a δ function. The G function is obtained using the balanced correlation method [68] that contains 1 where there is a hole and -1 where it is closed. Using Eq. 3.1 but ignoring the noise term, I can be written as:

$$I = D \otimes G = O * (A \otimes G) \tag{3.3}$$

This suggests that the correlation of the projected image with the post-processing array is just the original image plus, of course, the ignored noise term. The quality of the object reconstruction therefore depends on the choice of the aperture A and the decoding function G [67, 68]. If G can be chosen so that:

$$A \otimes G = \delta \tag{3.4}$$

In this case Eq. 3.3 can be reduced to the convolution:

$$I = O * \delta = O \tag{3.5}$$

This indicates that the reconstructed image will perfectly represent the object (i.e. $I \approx O$). From the above equations one can infer that the final output of the CA imaging system is not directly the object but a convolution of the object with the system response or $(A \otimes G)$. This is refered as the system Point Spread Function (PSF) i.e. the image produced in response to a point source. From this definition, Eq. 3.5 becomes:

$$I = O * PSF \tag{3.6}$$

Thus, for a single point, then:

$$I = \delta * PSF = PSF \tag{3.7}$$

This suggests that a properly designed CA imaging system should spread (blur) the point over a very small area of the detector. Thus, the PSF clearly describes the behavior of the imaging system. This is because the output of the imaging system can be predicted by knowing both the input and the system PSF. Thus, in CA imaging the system PSF can be described by the convolution of the arrays A and G:

$$PSF = (A \otimes G) \tag{3.8}$$

From the above if the correlation of A and G i.e. the PSF gives a δ function then the construction is perfect. There are many types of arrays proposed in the literature that their generation of A and G satisfy the condition $A \otimes G \approx \delta$. The pattern families of these arrays and others are summarised in section 3.4.

Having demonstrated the CA image formation principle in simple terms more details of the fundamentals of CA imaging are given here. The basic mathematical formulation that describes the formation of the coded image when imaging a planar source is summarised below based on analysis in [104]. For simplicity, let us consider imaging a point source with a simple pinhole (one pixel) as illustrated in Fig. 3.14 (a). The recorded counts of photons from that point source in one detector pixel (assuming a=b and thus, the pixel size at the detector plane is twice the pixel size mask opening) is given by:

$$D(y_i = 0) = O(y_o = 0) \times \Omega \tag{3.9}$$

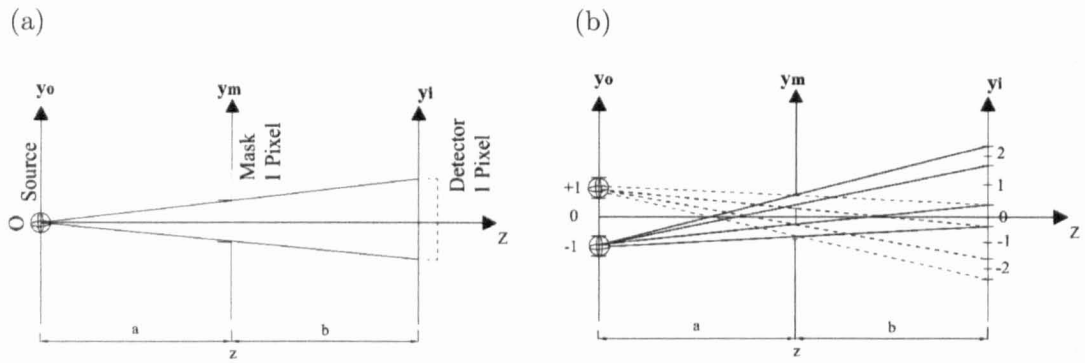

Figure 3.14: Schematic representation of projection geometry: (a) pinhole (one single hole of the mask) geometry demonstrating that $D(y_i = 0) = O(y_o = 0) \times \Omega$ and zero elsewhere, (b) consider two open hole geometry at y_i with the first hole at 0.5 and the second at -0.5, note that y_o is the coordinate of the source at the source axis and y_i is the coordinate of the detector pixel

Now consider the case of two pinholes (at **ym**) that illustrated in Fig. 3.14 (b) the recorded counts in each detector pixels at the centre of y_i are given by:

$$\begin{aligned} D(y_i = 0) &= O1 \times \Omega(pinhole1) + O2 \times \Omega(pinhole2) \\ D(y_i = 1) &= 0 \\ D(y_i = -1) &= 0 \\ D(y_i = 2) &= O2 \times \Omega(pinhole1) \\ D(y_i = -2) &= O1 \times \Omega(pinhole2) \end{aligned} \tag{3.10}$$

Equation 3.10 can be generalized as:

$$D(y_i) = \sum_{s=1}^{S1} O_s A(y_m) \Omega(y_o, y_m) \tag{3.11}$$

where $S1$ is the number sources, $A(y_m)$ is the mask opening when a ray is drawn from y_o to y_i and intercept the mask plane at y_m. Let us take this example with y_o=-1 and y_i=2 the ray pass through pinhole 1 at 0.5 with reference to Fig. 3.14 (b) $y_m = \frac{1}{2}(y_o + y_i) = 0.5$.

Now consider the case of a 2D source emitting at distance z from the detector, and encoded by a CA placed at distance b from the detector. The 2D planar source object, at

distance, $a = (z\text{-}b)$, from the CA, is denoted by O. The aperture pattern is given by the array A (a 2D function containing a 0 where the aperture is closed, and 1 where it contains a hole). Finally the noise is denoted by array B (noise term) but is initially ignored here to simplify the analysis. With reference to Fig. 3.15 the elemental distribution of the recorded counts in the detector at position $\vec{r}_i$, is represented by $dD(\vec{r}_i)$ such as:

$$dD(\vec{r}_i) = O(\vec{r}_o)\ A(\vec{r}_m)\Omega(\vec{r}_o, \vec{r}_m)d^2\vec{r}_o \tag{3.12}$$

where $O(\vec{r}_o)d^2\vec{r}_o$ is the intensity of the elemental 2D source @ $\vec{r}_o$.

The above equation suggest that the photon distribution from the object $\vec{r}_o$ recoded at the detector in position $\vec{r}_i$ is modulated by the mask. With $\vec{r}_m = \vec{r}_i + (\vec{r}_i - \vec{r}_o)a/z$ and it is the vector represent the intersection of the ray going from $\vec{r}_o$ to $\vec{r}_i$ with the mask plane. To understand the above a full description with some drawing through the positions is given in Appendix A.

To obtain the total photon distribution recorded at the detector one need to integrate over the object plane as:

$$D(\vec{r}_i) = \int\int_{\vec{r}_o} O(\vec{r}_o)\ A(\frac{a}{z}\vec{r}_i + \frac{b}{z}\vec{r}_o)\Omega(\vec{r}_o, \vec{r}_m)d^2\vec{r}_o \tag{3.13}$$

where:

$$\Omega(\vec{r}_o, \vec{r}_m) = \frac{p_m^2}{a^2}\cos^3(\theta) \tag{3.14}$$

where: $\theta = \arctan(|\vec{r}_i - \vec{r}_o|/z)$ and p_m is the mask pixel size (see appendix A).

The above geometric theory suggest that it is possible to calculate the projection from any aperture and object based on purely geometrical calculations. It also demonstrates that the photon distribution D recorded at the detector position $\vec{r}_i$ and due to the point source at $\vec{r}_o$ is equal to the source $O(\vec{r}_o)$, modulated by the mask transmission A. In far-field geometry $\cos^3(\theta) \cong 1$.

3.4 Coded Aperture Patterns

There are few CA pattern families proposed in the literature having the aforementioned ideal system PSF. These patterns have different methods of pattern generation and the majority are binary i.e. having two values, typically 0 and 1. This section provides a description of the classes of array patterns used in this work. The discussion includes the

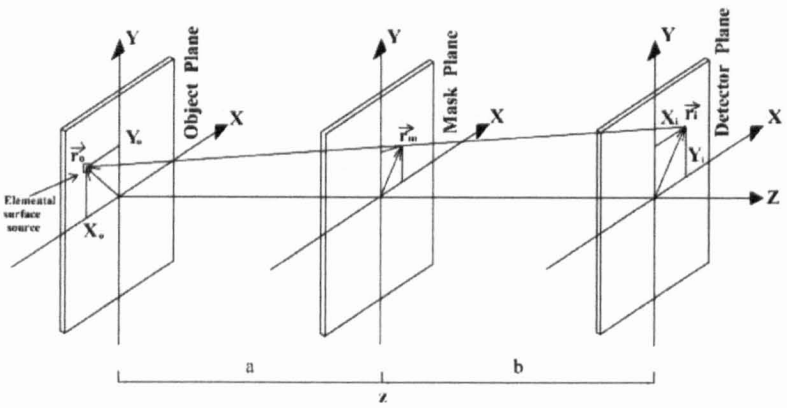

Figure 3.15: A schematic representation of the coded aperture geometry showing the point of intersection with the ray going from $\vec{r_o}$ to $\vec{r_i}$. Adapted from [104].

pattern generation rules and the correlation properties. Of note, the most practically used class of masks relies on the "cyclic difference sets" [105] and thus, is described first.

3.4.1 Cyclic Difference Sets Arrays

A cyclic difference set S modulo N, is a set of K ordered numbers which have values between 0 and N-1 that satisfy certain rules. Consider $S = \{d_0, d_1, d_2, ..., d_k - 1\}$, the first rule state that: all the values between 1 and N-1 should be represented (the same number of times M) by a difference modulo N between the numbers in the set S. In other words each element of $E = \{1, 2, 3, 4, ..., N-1\}$ must have a corresponding $(d_i - d_j)_{moduloN}$. Here the difference modulo N is defined as follow:

$$(d_i - d_j)_{moduloN} = \begin{cases} d_i - d_j & if\ d_i > d_j \\ d_i - d_j + N & if\ d_i < d_j \end{cases} \tag{3.15}$$

The second rule state that for each element in E there must be the same number M of representation $(d_i - d_j)$. The M is also called the redundancy of the set S. For simplicity, let us consider thes example of a 1D cyclic difference set S={0, 1, 2, 4} with N=7, here K=4 and M=2. The N is the total number of position and K is the size of the set and finally M is the redundancy. Now E would be equal to $\{1, 2, 3, 4, 5, 6\}$ and each element of it can be represented twice using the difference modulo 7 between the elements in set S i.e. 1 can be represented by $\{(1, 0); (2, 1)\}$, 2=$\{(2, 0); (4, 2)\}$, 3=$\{(4, 1); (0, 4)\}$,

4={(4,0);(1,4)} , 5={(0,2);(2,4)} and 6={(0,1);(1,2)} and NB: diff$(0,1)_{mod\,7}$=0-1+7.

The cyclic difference sets can also be represented by a binary array sequence a_i of size N such as:

$$a_i = \begin{cases} 1 & if\, i \in S \\ 0 & if\, i \notin S \end{cases} \tag{3.16}$$

with i having values between 0 and N-1. In the above example the sequence a_i is given by 1110100. The periodic auto-correlation,c_i, of these 1D sequences are a single peak on a flat background given by [105]:

$$c_i = \sum_{i=0}^{N-1} a_i a_{mod(i+l,N)} = \begin{cases} K & if\, mod(i+l,N) = 0 \\ M = \frac{K(K-1)}{N-1} & if\, mod(i+l,N) \neq 0 \end{cases} \tag{3.17}$$

The cyclic difference sets can be categorised into two subclasses, namely Singer sets and Hadamard sets [105]. These generate a 1D sequence pattern but can folded or wrapped to produce a 2-D pattern [107]. The parameter characterisation of Singer sets and Hadamard sets are listed in table 3.1 [96]. Singer sets are equivalent to sequences constructed from maximum length shift register sequence [106] where as Hadamard sets are related to the Hadamard matrices. These are type of square matrices whose elements have 1 or -1 with their rows are mutually orthogonal. As seen in table 3.2 Hadamard sets are also classified into three classes of binary sequence. A detailed discussion of the generation rule and correlation properties of these classes of arrays can be found elsewhere [105, 96]. However, the Pseudo-Noise (PN) sequence [106] is a special type of binary sequence having ideal correlation properties. Interestingly, in this class of array the spacing between a pair of holes occurs a constant number of time. This is of course regardless of which separation distance is under consideration. This sequence of arrays is indicated to generate the URAs.

Uniformly Redundant Arrays (URAs)

The URAs are the class of array constructed from PN sequences [107]. As demonstrated in Fig. 3.8 the auto-correlation properties of such array has a single peak and zero side-lobes. Their application to imaging was introduced and extended by Fenimore and Cannon [67, 68]. The uniform redundancy mean all separations between holes in the pattern occur a constant number of times (M).

Table 3.1: The two important subclasses of cyclic difference sets namely the Singer sets and Hadamard sets [96].

Cyclic difference sets subclasses	**Characterization**
Singer sets	Characterised by parameters for which: $N=(t^{m+1}-1)/(t-1)$ $K=(t^{m}-1)/(t-1)$ $M=(t^{m-1}-1)/(t-1)$ where t is a prime number.
Hadamard sets	Characterised by parameters for which: $N=4t-1$ $K=2t-1$ $M=t-1$ with t being an integer

Table 3.2: A characterization of the three important subclasses of the Hadamard Sets. These are quadratic residues, twin primes, and M-sequences arrays. According to Caroli and colleague [96] the M-sequences are also known as Pseudo-Noise (PN).

Hadamard sets subclasses	**Characterization**
Quadratic residues	A set given by the residual, mod(N), of the squares of the first $(N+1)/2$ integers with N being prime.
Twin primes	A set is twin prime if: $N=p\times q$ where p & q are primes and $\|q-p\|=2$
M-sequences	A set characterised by: $N=2^{m}-1$ with integer $m>1$.

There are many ways to construct URAs [96, 99] and the following only describes the Fenimore and Cannon [68] procedure to generate a 2D basic URA:

$$A_{i,j} = \begin{cases} 0 & if\, i = 0 \\ 1 & if\, j = 0, i \neq 0 \\ 1 & if\, C_r(i)C_s(j) = 1 \\ 0 & otherwise \end{cases} \tag{3.18}$$

Where:

$$C_r(i) = \begin{cases} 1 & if\, there\, exists\, an\, integer\, x,\ 1 \leq x < r \\ & such\, that\, i = mod_r x^2 \\ -1 & otherwise \end{cases} \tag{3.19}$$

The array is generated as an $r \times s$ (dimension of array) 2D array using two prime numbers with $|r - s| = 2$. This is the only case that provides a δ function auto-correlation. Thus, the URA referred to as twin-prime Hadamard array. The above equations suggest to evaluate $mod_r x^2$ for all x to r-1. Th resulting values gives the location (i) in C_r that contain +1 otherwise -1. The positive coefficients C_r are called quadratic residues modulo r and C_s is defined in a similar way. To simplified the discussion consider generating 2D URA array of dimension r=7 by s=5. For r=7 this mean that the value of x lies $1 \leq x < 7$ and similarly for s=5 the value of x lies $1 \leq x < 5$. Table 3.3 evaluates $mod_7 x^2$ for all x to 7-1. Similarly table 3.4 evaluate $mod_5 x^2$ for all x to 5-1. Th resulting values gives the location (i) in C_r that contain +1 otherwise -1 and similarly the the location (j) in C_s that also contain +1 otherwise -1.

Table 3.3: Evaluations of $mod_r x^2$ for all x to r-1 with r=7 and $1 \leq x < 7$.

x	1	2	3	4	5	6
x^2	1	4	9	16	25	36
$mod_7(x^2)$	1	4	2	2	4	1

$$C_7(i) = \begin{cases} 1 & for\, i = \{1, 2, 4\} \\ -1 & for\, i = \{3, 5, 6\} \end{cases}$$

$$C_5(j) = \begin{cases} 1 & for\, j = \{1, 4\} \\ -1 & for\, j = \{2, 3\} \end{cases}$$

Table 3.4: Evaluations of $mod_s x^2$ for all x to s-1 with s=5 and $1 \leq x < 5$.

x	1	2	3	4
x^2	1	4	9	16
$mod_5(x^2)$	1	4	4	1

Now from Eq. 3.18 it is clear that the first row is zeros and the first column is ones except the first element. Having obtained the $C_5(j)$ and $C_7(i)$ the resulting value gives the location of (i) and (j) in C_r and C_s respectively that contain +1 otherwise -1. Thus, the generated mask of of dimension (7×5) elements in this example is illustrated in Figure 3.16.

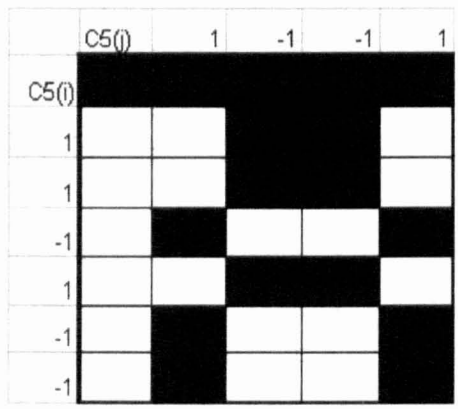

Figure 3.16: The generated URA mask of dimension (7×5) elements.

All 2D URAs are characterised by M=$K/2$, and K=N+1/2. The decoding (postprocessing array), G, is given as:

$$G_{i,j} = \begin{cases} 1 & if\, A_{i,j} = 1 \\ -1 & if\, A_{i,j} = 0 \end{cases} \tag{3.20}$$

3.4.2 Modified Uniformly Redundant Array (MURAs)

The MURAs (see Fig. 3.9) proposed by Gottesman and Fenimore [69] have imaging properties similar to URAs. However, class of arrays is based on quadratic residue arrays [107] and is not related to cyclic difference sets. Thus, these arrays do not belong to the family class of URAs. These can be generated or extended from the the 1D quadratic residue sequences [107], being the product of any two primes numbers p and q. This

means that many array sizes can be generated making them more attractive than URAs. MURAs can be produced in different sizes depending on whether $|q-p| = 0$, 2, 4, or 6. The pattern for which $|q-p| = 0$ are square arrays and are the only ones used in this thesis. The generation algorithm is similar to the URAs using:

$$A_{i,j} = \begin{cases} 0 & if\ i = 0 \\ 1 & if\ j = 0, i \neq 0 \\ 1 & if\ C_s(i)C_s(j) = 1 \\ 0 & otherwise \end{cases} \tag{3.21}$$

where:

$$C_s(i) = \begin{cases} 1 & if\, there\, exists\, an\, integer\, x, 1 \leq x < s \\ & such\, that\, i = mod_s x^2 \\ -1 & otherwise \end{cases} \tag{3.22}$$

It is worth noting that the $mod_s x^2$ is basically the remainder of x^2 after the division by s. In order to decode such array, a decoding array, G, is required, as described in section 3.3. However, the array G can not be equal to the array A because the auto-correlation will not be a δ function. Gottesman and Fenimore [69] pointed out that a slight modification in the definition of A gives the G resulting in ideal imaging properties so that $G \otimes A = \delta$. The decoding function is now:

$$G_{i,j} = \begin{cases} 1 & if\, i \oplus j = 0 \\ 1 & if\ A_{i,j} = 1, i \oplus j \neq 0 \\ 0 & if A_{i,j} = 0, i \oplus j \neq 0 \end{cases} \tag{3.23}$$

where $\oplus$ is sum modulo S.

From eq. 3.22 it can be seen that the only difference between URAs and MURAs is in one single element. It is basically in the element i⊕j=0 which is now 1 not 0. This means that square arrays of any prime numbers are now possible. The generated array need to be cyclically shifted to bring the upper left corner to the centre of the array i.e. the centre of symmetry is at the centre of rotation. This means that the totally closed and open line at the centre of the of the pattern resulting in the pattern shown in Fig. 3.17 (a). This is important as it brings the peak of the PSF into the centre.

The MURAs patterns are invariant for a 180° rotation about the centre. For a 90° rotation some arrays those called symmetric (have axial symmetry) arrays, are also invariant. However, other arrays exchange open and closed positions and are thus referred to

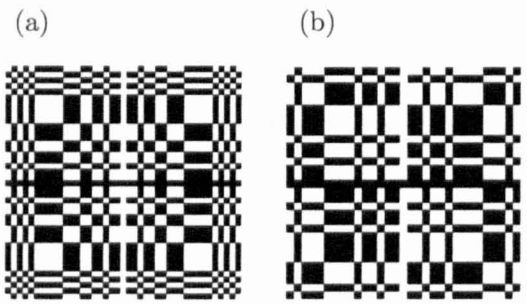

Figure 3.17: Two MURA patterns: (a) 41×41 symmetric mask, (b) 31×31 anti-symmetric

as anti-symmetric arrays (see Fig. 3.17 (b)). In other words, these arrays are rotationally anti-symmetric about the centre. This feature makes the mask/anti-mask camera design, that used in artefact reduction, more convenient [108]. This means that one design is needed for both masks because the anti-mask can simply obtained by rotating the mask by 90° about its centre. All these arrays are characterised by $M{=}K/2$, $K{=}(N\text{-}1)/2$ and the open fraction is $K/N \cong 50\%$. Thus, MURAs have also the same open fraction as URAs.

3.4.3 No-Two-Hole-Touching (NTHT) Arrays

The NTHT arrays are new families of arrays proposed by Fenimore [70] to produce arrays of the URAs having other than 50% open fraction. In fact any of the previously discussed patterns can be made as NTHT arrays by simply reducing their holes. This is achieved by adding a border around them so all holes become isolated. This is also a way of making these arrays self-supporting. If the mask is reduced by a factor $1/e$, it mean adding e-1 zeros with size $1/e$ between all array positions. The mask original open fraction is now reduced by a factor e^2. The following example illustrates the above discussion so if the original mask is $a_{i,j}$ then the NTHT array of that mask is given in $b_{i,j}$.

$$a_{i,j} = \begin{pmatrix} 1 & 0 & 1 & 0 & 1 \\ 0 & 1 & 1 & 1 & 0 \\ 0 & 0 & 0 & 0 & 0 \\ 0 & 1 & 1 & 1 & 0 \\ 1 & 0 & 1 & 0 & 1 \end{pmatrix}$$

$$b_{i,j} = \begin{pmatrix} 1 & 0 & 0 & 0 & 1 & 0 & 0 & 0 & 1 & 0 \\ 0 & 0 & 0 & 0 & 0 & 0 & 0 & 0 & 0 & 0 \\ 0 & 0 & 1 & 0 & 1 & 0 & 1 & 0 & 0 & 0 \\ 0 & 0 & 0 & 0 & 0 & 0 & 0 & 0 & 0 & 0 \\ 0 & 0 & 0 & 0 & 0 & 0 & 0 & 0 & 0 & 0 \\ 0 & 0 & 0 & 0 & 0 & 0 & 0 & 0 & 0 & 0 \\ 0 & 0 & 1 & 0 & 1 & 0 & 1 & 0 & 0 & 0 \\ 0 & 0 & 0 & 0 & 0 & 0 & 0 & 0 & 0 & 0 \\ 1 & 0 & 0 & 0 & 1 & 0 & 0 & 0 & 1 & 0 \\ 0 & 0 & 0 & 0 & 0 & 0 & 0 & 0 & 0 & 0 \end{pmatrix}$$

The postprocessing array, G, has to also be modified to match the new dimensions of the mask. This is done by adding lines of 0s corresponding to the new rows and columns in a similar way to the mask. The following example illustrate this discussion so if the original decoding function is $g_{i,j}$ then the NTHT decoding array is given in $gg_{i,j}$. The postprocessing array in this case is a three-leveled function. Both arrays are still valid arrays and thus, having ideal imaging properties or system PSF with zero side-lobes as demonstrated in Fig. 3.10. The NTHT patterns used in this work is based on MURAs.

$$g_{i,j} = \begin{pmatrix} 1 & -1 & 1 & -1 & 1 \\ -1 & 1 & 1 & 1 & -1 \\ -1 & -1 & -1 & -1 & -1 \\ -1 & 1 & 1 & 1 & -1 \\ 1 & -1 & 1 & -1 & 1 \end{pmatrix}$$

$$gg_{i,j} = \begin{pmatrix} 1 & 0 & -1 & 0 & 1 & 0 & -1 & 0 & 1 & 0 \\ 0 & 0 & 0 & 0 & 0 & 0 & 0 & 0 & 0 & 0 \\ -1 & 0 & 1 & 0 & 1 & 0 & 1 & 0 & -1 & 0 \\ 0 & 0 & 0 & 0 & 0 & 0 & 0 & 0 & 0 & 0 \\ -1 & 0 & -1 & 0 & -1 & 0 & -1 & 0 & -1 & 0 \\ 0 & 0 & 0 & 0 & 0 & 0 & 0 & 0 & 0 & 0 \\ -1 & 0 & 1 & 0 & 1 & 0 & 1 & 0 & -1 & 0 \\ 0 & 0 & 0 & 0 & 0 & 0 & 0 & 0 & 0 & 0 \\ 1 & 0 & -1 & 0 & 1 & 0 & -1 & 0 & 1 & 0 \\ 0 & 0 & 0 & 0 & 0 & 0 & 0 & 0 & 0 & 0 \end{pmatrix}$$

3.5 Near Field Coded Aperture Imaging

The above presented patterns have been demonstrated to theoretically possess perfect imaging properties. This is because such patterns are of finite size and can be successfully decoded with correlation analysis, and are thus, capable of achieving an approximately δ function-like system PSF. The interest is particularly on the square patterns composed of square aperture holes. This means the design is specifically limited to the MURAs and the NTHT-MURAs CA patterns. The following subsections provide an overview of the mask camera configurations, designs and consequences of theoretical and practical issues. The geometrical parameters such the imaging FoV and the geometrical spatial resolution are also discussed.

3.5.1 The Mask Camera Configurations

This section presents the possible geometrical arrangements of the mask and the detector. Figure 3.18 illustrates these mask camera configurations but in this particular example assumes a point source located at infinity. Thus, the projection of the mask on the detector has the same size as the mask itself as the projected lines of response through the mask are assumed to be parallel. The first arrangement is the one shown in Fig. 3.18 (a) where the mask and the detector are of the same size. This configuration is refered to as the box camera [109] and to be used, the source needs to be located on the instrument axis. This is necessary to ensure that the source casts a complete pattern on the detector. In the

second arrangement (see Fig. 3.18 (b)) a larger detector is used as a possible solution for the off central axis sources. If the available detector is small in size a third arrangement can also be made using a mosaic mask. This is a (2×2) replication of the basic mask pattern so that off-centre rays still project a full cyclic mask pattern onto the detector. These geometrical configurations of the mask and the camera are considered the initial step of determining the imaging FoV.

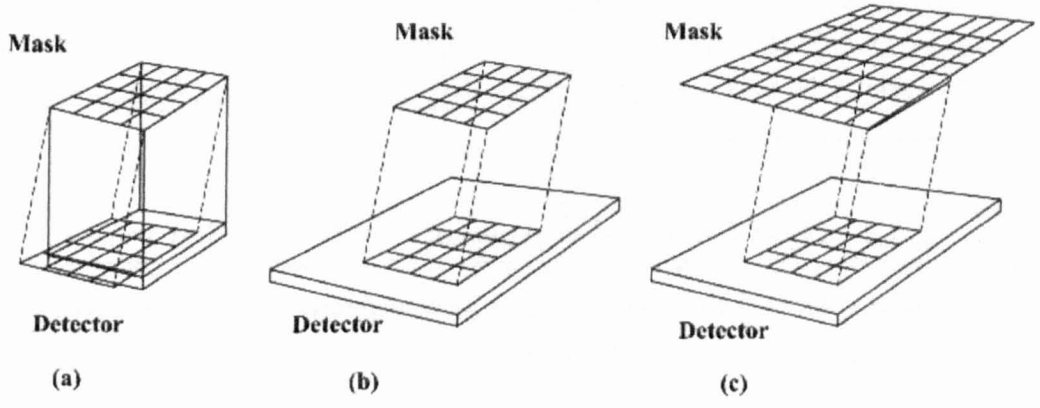

Figure 3.18: The three possible mask camera configurations: (a) both the mask and the camera have the same size, (b) the detector is larger than the mask, (c) The mask (2×2 mosaics of the basic pattern) is larger than the detector. These schematic diagrams are adapted from [96].

The above concepts and arrangements can also be used in the near-field geometries. However, in near field geometry (as found in nuclear medicine applications) the source object must placed as close as possible to the detector to have a magnified image. This basically eliminates the use of the box camera geometry due to enlarging of the projected image. The second and the third arrangements are the only options to ensure that the object within the FoV project the full mask pattern, i.e. a "fully coded FoV", or at least a large part of the mask pattern onto the detector. As will be seen later once the source projects only part of its pattern on the detector, then its image can not be reconstructed perfectly. This is due to the incomplete coded information of the projected image and often termed as "partially coded FoV". The simplest solution to solve this problem is to use a larger detector to cover oblique sources, but this depends on the object FoV and is not always possible. An alternative solution is to introduce a adequate shielding to reduce

the FoV that is with less interest. This is an attractive option but in practice it is difficult to exclude all the effect of partial encoding from off-centre sources. Ultimately, this will produces undesirable near field imaging artefacts. However, and as will be seen in chapter 7, a set of near field corrections can be implemented to mitigate these artefacts.

In addition, the use of a mosaic mask is another option to solve the problem as it projects the entire mask pattern onto the detector, but with different pattern shifts depending on the source position. This ensures that all point sources at the edges of the fully coded FoV project the same pattern as the rest of point sources. However, the detector needs to be large enough to ensure that at least one basic pattern of the mask is fully projected onto the detector.

3.5.2 Near Field Coded Aperture System Design Issues

Having outlined the possible CA camera configurations, the discussion that follows falls into two main parts; the mask characteristics and the CA camera geometric parameters. The former considers the parameters of the mask such as size, thickness, material, pattern open fraction and type, and the number of basic patterns used in the mask if mosaics were to be considered. The geometric parameters on the other hand include the FoV and the geometric resolution. These together provide the design procedures and principles for CA imaging. Ultimately these have important consequences on the efficiency and on the resolution of the CA imaging device.

The Mask Parameters & Physical Considerations

As described earlier the MURAs and NTHT-MURAs families of CA patterns have ideal imaging properties. These patterns are the best available patterns that suit the proposed application. The MURAs have an open fraction of $\approx$ 50% and the NTHT-MURAs provides $\approx$ 12.5% open fraction. Both have significantly higher transmission capability than the parallel-hole collimators that allow 0.01-0.1% transmission. The choice of the mask parameters is a compromise and is governed by the object size, and the distances between mask and object and the mask and detector. Thus, the physical mask size and the FoV depend on these parameters.

In addition, the mask thickness is another important parameter for imaging. Binary masks produce ideal imaging properties i.e. allow a perfect decoded image with noise-free

data. To replicate the same performance in real imaging, the mask has to be infinitely thin and at the same time perfectly opaque in those areas designed to block the incident flux. In practice, these γ-rays have a finite probability of passing through the mask. The best material to be used as a mask is the one having minimum thickness for a given attenuation.

The above discussed arrays are of two types non-self-supporting masks and self-supporting pattern. In the latter case, all opaque areas are connected at least along a line. However, in practical terms, the non-self supporting array is also not a problem to construct, as it can be made as a supported mask at the design stage with appropriate use of modern materials. This achieved by putting a thin low atomic number (Z) but supportive grid between adjacent open holes. The most obvious material is carbon fibre but other materials can also be used. This however, may cause a loss of throughput and potential increase in scatter particularly for low energy photons.

The Geometric Parameters

There are several important parameters when considering CA for imaging. Apart from the intrinsic imaging characteristics, other geometrical factors are important and crucial for imaging. These include the physical detector size, the number of detector pixels, and the distances between the mask and the object, and between the mask and the detector. The choice will usually be governed by the desired FoV size and imaging resolution [99].

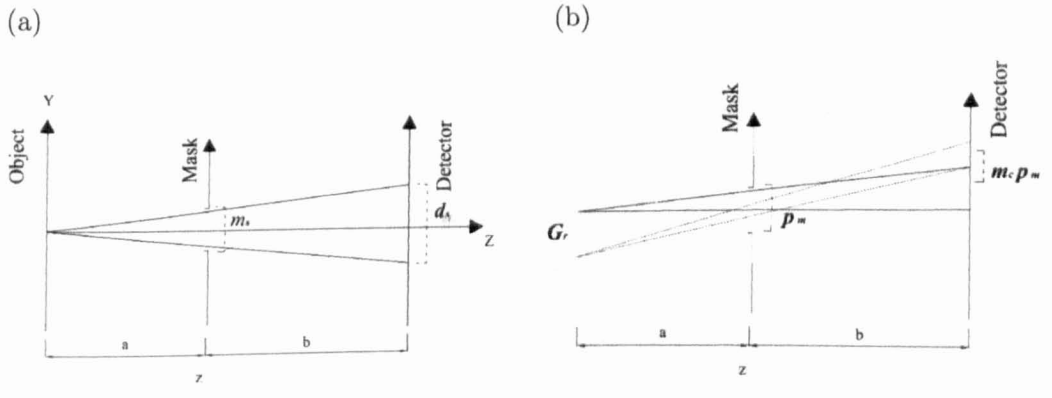

Figure 3.19: Coded aperture geometric parameters: (a) determining the magnification coefficient , (b) determining the mask geometric resolution, G_r.

In near field geometry the magnification coefficient, m_c is always greater than one. This is also called the scaling coefficient and is defined as the ratio of the size of mask shadowgram on the imaging detector to the physical size of the mask. For a mask of size m_s, the magnification coefficient is purely geometric and with reference to Fig. 3.19 (a) can be obtained from:

$$\frac{d_s}{m_s} = \frac{z}{a}$$

$$m_c = \frac{m_s(\frac{a+b}{a})}{m_s} = 1 + \frac{b}{a} \tag{3.24}$$

where a is the object-to-mask distance and b the mask-to-detector distance as demonstrated in Fig. 3.15. It is important that the magnification coefficient should not be confused with the object magnification, O_m. The later can be defined as the ratio of the size of the projected object to the actual size of the object itself. This can be obtained from a simple geometry as:

$$O_m = \frac{b}{a} \tag{3.25}$$

This indicates that the projected object is re-scaled. If $a>b$ this mean that the mask is closer to the detector and thus, the projected object is minified. On the other hand, if $a<b$, the projected object is magnified. Both object magnification and magnification coefficient are related to each other so that:

$$m_c = O_m + 1 \tag{3.26}$$

One parameter of great importance in CA near-field design is the geometric resolution. The geometric resolution is the resolution of the system due to its geometric design. With reference to Fig. 3.19 (b) and considering an ideal detector the mask geometric resolution, G_r, can be obtained from [110]:

$$G_r = \frac{m_c \times p_m}{b} \cdot a = \frac{m_c \times p_m}{m_c - 1} \tag{3.27}$$

where p_m is the size of a mask hole.

Equation 3.27 suggests that the mask geometric resolution is largely affected by the aperture-hole size and the magnification coefficient. In practice, the image obtained from

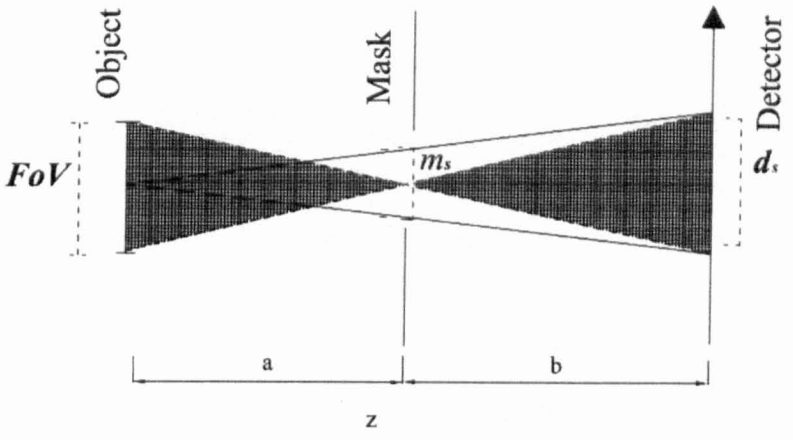

Figure 3.20: Determining the imaging FoV from a simple geometry.

real CA imaging system has a somewhat worse resolution and called the system resolution, due to other confounding factors (e.g. intrinsic camera resolution, statistical noise etc).

Another important parameter in CA imaging design is the FoV or the size of object to be imaged by the CA. The size of the FoV is governed by the magnification coefficient and the detector size, d_s, and with reference to Fig. 3.20 geometrically can be defined as:

$$FoV = \frac{d_s}{m_c - 1} \tag{3.28}$$

The FoV is closely related to the mask geometric resolution. This means that to improve the geometric resolution, by using a higher magnification, the FoV is actually reduced. The ratio between the two can be obtained from:

$$\frac{FoV}{G_r} = \frac{d_s}{m_c p_m} \tag{3.29}$$

Based on Eq.3.29 the trade-off between the mask element and the FoV for a mask pixel, p_m , of arbitrary selected size 2 mm, can be seen in Fig. 3.21 (a). The relationship between the geometric resolution as a function of magnification coefficient is given in Fig. 3.21 (b). This suggest that the resolution is the same as the size of the hole magnified by the factor m_c assuming ideal detector. However, in practice in a real CA system other parameters such as intrinsic resolution and detector sampling must be considered.

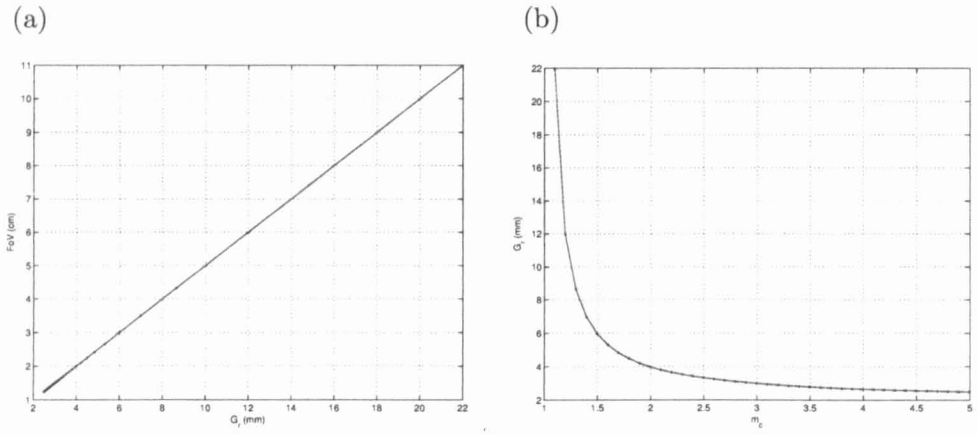

Figure 3.21: Coded aperture geometric parameters: (a) trade-off between resolution and FoV, also reducing the FoV improves magnification, (b) the geometric resolution against magnification coefficient, illustrates that after $m_c > 4$ there is a very small improvement.

3.6 The Decoding Methods

As discussed before, CA is a two-step image formation device. First, it encodes the source information by casting a shadow of the CA pattern onto the imaging detector. Second, the recorded image must then be reconstructed by some form of decoding techniques to recover the original source object. This process is designed to give the spatial information and the intensity of the source object located within the FoV. Thus, the reconstructed image become as similar as possible to the original source object.

There are several reconstruction technique proposed in the literatures for image decoding. The choice for a certain method depends on the application, the type of patterns used, and the available resources. The most widely used methods are the correlation analysis methods and the iterative reconstruction technique [109]. The correlation methods are fast, the iterative methods may generate slightly better reconstructed images but albeit requiring longer execution time. All these methods reconstruct the object in the focused plane, but can not completely remove the influence of over/underlying planes.

This work focuses on the correlation technique because it provides the highest sensitivity for point-like object [109]. The following subsection provides a brief summary of the correlation methods used in this thesis. The discussion also include sampling approach to

avoid artefacts in the decoded image.

3.6.1 Correlation Techniques

The correlation approach involves decoding the CA projected image with some array function of the mask pattern. The correlation process can be easily calculated via the inverse-transform of the product of the Fast Fourier Transform (FFT) of the two arrays. In modern computers this process can take few seconds. The early method of decoding was based on "matched filter" array [95]. This means that the postprocessing array (i.e. array of 1's and 0's) is the mask, A, itself. This correlation process is called auto-correlation and an example of the matched decoding can be found in Fig. 3.3.

Another decoding method proposed by Brown [95] is refered to as the "mismatched filter" array. The only difference between these two decoding methods is that in the mismatched decoding the 0's in the array, A, are substituted with -1's. Thus, the resulting array are now called, G and if correlated with the binary array A, it produces an ideal peak (impulse like) with zero side lobes. This is because the mismatched filtering suppress the pyramid of the autocorrelation function. This decoding method is called the mismatched cross correlation function. Fig. 3.22 compares the system PSF of the random array obtained with matched decoding with that obtained with mismatched filtering. In the first case the decoded image is the response function convolved with a pyramid Fig. 3.22 (b). The side-lobe value in this case can be given by $(r.s+1)/4$ with $r.s$ representing the array dimension [68]. The decoded image improves with mismatched method as demonstrated in Fig. 3.22(d). This is because the zeros in the decoding array having been replaced with negative terms (-1s) and thus, the artefacts removed or subtracted off while decoding [68].

Mismatched decoding method is also refered to as "balanced correlation" [68] analysis. This is because the post processing array, G, of such patterns contain +1's and -1's and the negative terms balance the positive terms of array, A, to a δ function once both arrays are correlated.

In the case of mosaic arrays the correlation process is called periodic correlation. In this case the recorded pattern is also correlated with a cyclic postprocessing array. One of the advantages of imaging with mosaic pattern is that if the object is in the centre of the mask, and the projected image takes less than the whole imaging detector area, then a central area equivalent to the basic pattern is enough for decoding. In other words, this

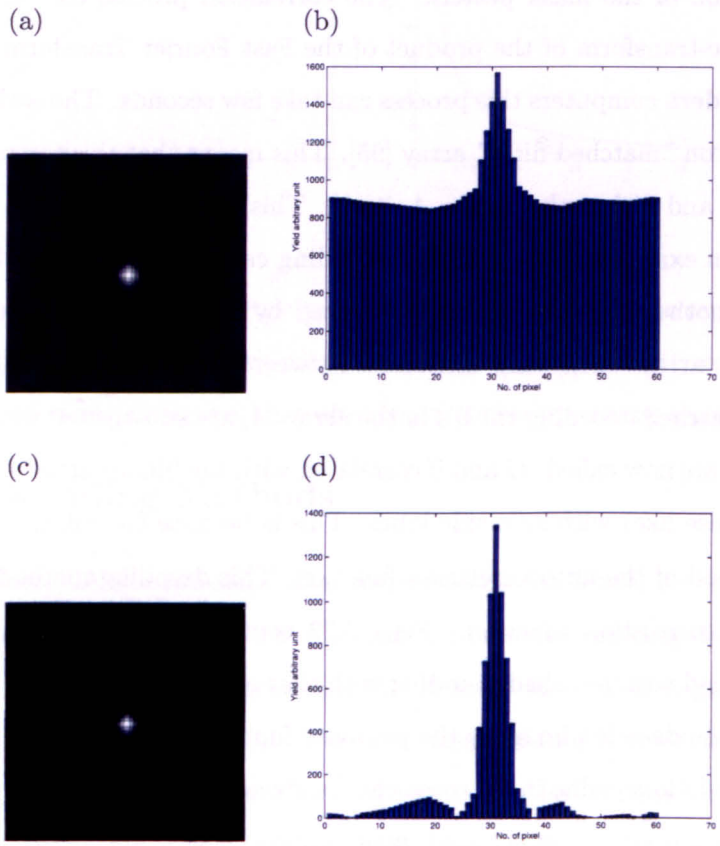

Figure 3.22: The random array and its response function using matched analysis compared with mismatched correlation: (a) The decoded image of the random array using matched filtering, (b) vertical bar plot of the decoded image showing a peak on top of pyramid shape, (c) The decoded image of the random array using mismatched decoding, (d) vertical bar plot of the decoded image using mismatched decoding.

central area contain all the object information needed to reconstruct the image. In this case, the postprocessing array needs to be of similar size to the projected image. If then correlated with the selected central area of the recorded pattern it will recover the object. It is worth noting that zero padding are not necessary if both the projected image and the postprocessing array are appropriately scaled. In fact, with the periodic correlation, mosaicking the postprocessing array, G, is also not necessary.

On the other hand, the mask camera arrangement shown in Fig. 3.18 b provides non-periodic projections. This is because one basic pattern is used to provide image magnification. In this case, particular care must be taken to ensure that the projection of the pattern is of similar size to the postprocessing array. If not, then the scaling or zero padding is needed to ensure that both arrays are of the same size. This is to ensure that the reconstructed image is not affected by edge boundary effect. It is worth noting that the decoding process with periodic or non-periodic correlation maintains an ideal PSF.

In near-field digital decoding process, it is important that the projection is sampled appropriately to avoid artefacts. This is because in the selected geometry the projection of each mask hole is sampled on the detector more than once. This is of course dependent on the chosen magnification coefficient,m_c. The projection of each CA hole can be represented as $\alpha \times \alpha$ square of square pixels. The sampling strategies or concepts in this case depend on the following equation [110]:

$$\alpha = \frac{m_c p_m}{p_d} \tag{3.30}$$

where p_m is mask pixel size and p_d is the size of the detector pixel. This is an important equation and valid for all CA arrays involving the correlation analysis. This means that if a mask of size $r \times s$ is used for imaging a point source then the projected image is simply $\alpha r \times \alpha s$ pixels. The $\alpha \times \alpha$ square is filled with 1's or 0's according to the relevant position on the mask. If the chosen CA imaging geometry ensure that $\alpha > 1$ then this called fine sampling [70]. It simply mean that the shadow cast of the aperture hole covers more than one detector pixel. Another important issue with decoding is to ensure that the mask shape is matched at the decoding stage. The postprocessing array, G, has also to be extended from $r \times s$ to $\alpha r \times \alpha s$ in order to perform the correlation. The arrays new locations must then be filled using either of two ways:

- (i) First, by using the same scaling factor of the original postprocessing array. The

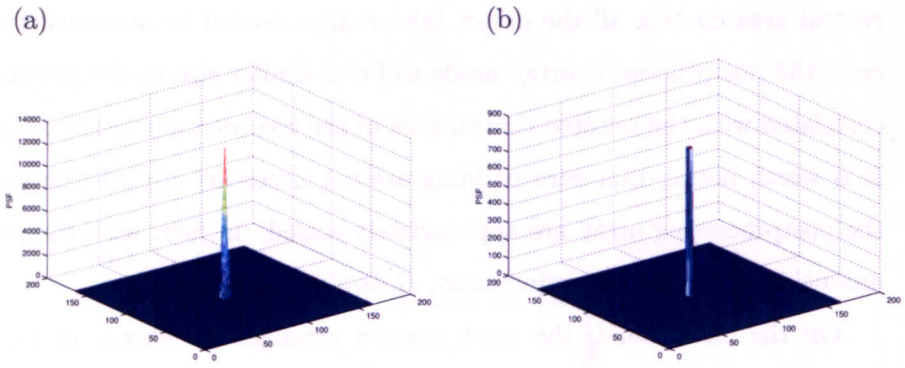

Figure 3.23: The system PSF for binary MURA mask using two decoding method: (a) using fine sampling , (b) using δ-decoding. Both methods were demonstrated with scaling factor of 4.

filling here is with 1's and -1's in a similar fashion to the original decoding array elements. The system PSF for the binary MURA using this fine sampling method is given in Fig. 3.23 (a)

- (ii) Second, by using 0's. This means that all the new locations are filled with 0's. Fenimore [70] called this method a δ-decoding. The system PSF for the binary MURA using this method is given in Fig. 3.23 (b)

To understand the principle of delta decoding consider imaging a point source the produced (recoded) image is blurred. A second blur also comes from decoding the projected image with the G function. According to Fenimore [70] δ-decoding can mitigate the blur of the reconstruction process i.e. the secondary blurring. In this case both the projected image and the decoding array, G, are finely sampled. The G array containing a δ functions for each CA-holes. This may slightly improve the resolution capability of the system in the case of isolated point-like objects with no background. Figure 3.24 show two profiles taken through the centre of the decoded images of a binary mask correlated using delta decoding and fine sampling respectively. This demonstrates that delta decoding have a slightly better resolution compared to the fine sampling mismatched decoding. However, fine sampling provides a higher sensitivity for such point-like object. Therefore, the vast majority of the CA data used in this thesis are based on fine sampling and with mismatched correlation analysis.

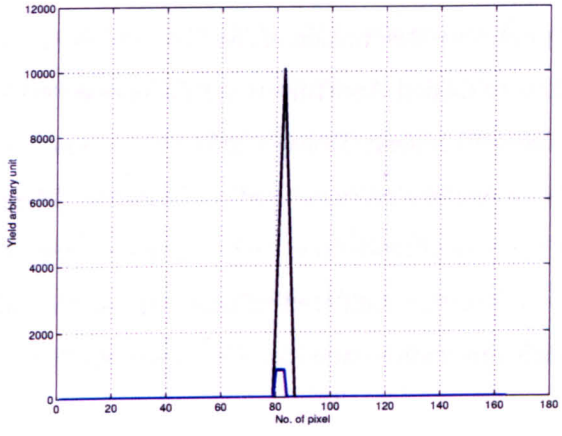

Figure 3.24: Profiles taken through the centre of the decoded images (system PSF) of a MURA of 41×41 for fine sampling decoding (black solid line) and delta decoding (blue solid line) respectively.

Chapter 4

Methodology

This chapter provides a description of the three different methods undertaken to investigate the applications of Coded Aperture (CA) for breast tumour imaging. The initial method is based on the well known Monte Carlo Simulation (MCS) approach. This begins by describing the simulation package used in this work. Then in brief, describes the MCNPX input file and the way of modelling the imaging detector. Then the modelling steps and the validation process of the simulated camera against the full-size clinical gamma camera is described. Such verification steps are important and provide confidence to the simulation work.

The other two methods of investigation are non-Monte Carlo and were particularly used for CA imaging investigations. The first of these is based on a simple approach called Binary Mask Shift (BMS) representing the action of a distributed source in the projective CA imaging geometry. This is attractive because it allows us to study these artefacts without the effect of $\Omega(\vec{r_o}, \vec{r_i})$ term of Eq. 3.13. The second method is based on Pseudo-Ray Tracing (PRT). This is based on purely calculating the angle of incidence of each point in the object that successfully strikes an open aperture element and then hits the detector element. Interestingly, these non-Monte Carlo methods yields similar results but takes less computing power, than using a full MCS approach.

4.1 Monte Carlo Simulations

This section describes the central methodology used in this thesis: it describes the design and the development of the MCS method. It is basically divided into four main parts.

The first part provides an overview of the MCS technique and the different simulation packages for photon transport. The second part describes the structure of the simulation code system. The third part of this section present the simulation method and code verification for modelling the imaging detector. The final part of this section highlights the different geometries used in this work for modelling the exemplar Toshiba gamma camera used here. It also provides a description of the verification process.

4.1.1 Introduction

MCS is a computational technique that attempts to model a real physical system. This statistical calculation method is based on the technique of random variable sampling that utilizes sequences of random numbers [111]. For instance in the case of γ-ray transport problems, individual photons are tracked from point of origin to removal from the system (either by escape or by absorption), while interacting in a random way, as determined by the cross sections. Anger was the first to use this technique for simulating the physical response of his gamma camera. Since then, the technique has gained wide spread for many nuclear medicine applications. This may include the optimization of new cameras (detector or collimator) and the evaluation of the correction and the reconstruction techniques [112, 113].

There are a wide variety of simulation packages that are commercially available in practice. Codes such as SimSET [112], GATE [114], GEANT4 [115] and SIMIND [112] are dedicated codes and thus used for specific geometries and applications where as codes such as EGS4 [112] and MCNP [116, 111] are considered general-purpose codes. MCNP stands for Monte Carlo N-Particle and is a well established general-purpose code. It supports 34 particle (or coupled particles) types and has many cross section libraries for different physics models. The latest release is MCNP5 but MCNPX (stands for MCNP eXtended) is the one that was locally available. The main difference between the two codes is that MCNPX5 has many new additional features such as new source options, improved variance reduction technique and improved parallelism support. The latter feature can be achieved using parallel virtual machine and message passing interface which cluster to speed up calculation. Unfortunately MCNP5 did not become available in the department until 2006, but has yet to be validated.

Among the above mentioned Code MCNPX code was chosen because most of the above

dedicated codes employ large approximations on the interaction process particularly on the collimator model [112]. MCNPX however, models the physics of photon transport of the imaging system in a more accurate way. It is also more user friendly in term of geometrical and materials control and it does not require any programming.

4.1.2 MCNPX Code Description & Concepts

MCNPX (version 2.4.0) code was used in this work because it explicitly models the transport and the details physical interaction of photons within the geometries simulated. The code was written in Fortran-90 and Fortran-70, runs on PC Windows, Linux, and Unix platforms. It has powerful source definitions, a large collection of data libraries and good geometry plotting capabilities. It allows the user to build complicated geometries and to simulate the radiation transport within the geometries.

The input file requires specifying the materials, geometry, radionuclides and their energies. As well as the user need to determine what he needs to calculate from the geometry. The interactions of every primary and all subsequent photons and particles are tracked until they are either stopped, absorbed or leave the detection system. In other words, histories were terminated when the photon escapes from the detector or when its energy dropped to the energy cut-off (1 keV). Although MCNPX has a large collection of variance reduction techniques, these were avoided for two reasons. First, due to the reasonably good speed of the available computers it was decided to keep the physics of photon transport to ensure preserving the stochastic (isotropic) nature of photon imaging. Second, most of variance reduction techniques involve using tallies (the calculations required) alone and that was not the case in all the simulated data presented in this thesis. In fact a performance increase was achieved by eliminating tallies and thus variance reduction technique.

The Use of MCNPX

The objective of this part is to simply give an overview of the structure of the MCNPX input file. For details of how to use and run the input files see the user manual [116]. In brief, the MCNPX input file contains the 3D geometry of the simulated problem including the material and source definition. A simple example of the structure of the input file is given in Appendix B. The cell cards section (a legacy aspect from using Fortran)

collectively gives the geometry of the system modeled. Each cell is preceded by number and followed by its material number and density. Each cell is also composed of bounding surfaces. These surfaces are defined in the surfaces card section and always commenced by a surface number. In the surface card each surface is also given an alphabetic mnemonic to indicate the surface type e.g. CY mean Cylinder on the Y axis. The final cell geometry is defined by union, intersection and complement of the listed regions bounded by the surfaces.

In the data card section the card name must be the first entry. The type of particle is given in this section in the MODE card with the letter "P" stands for photon and "E" stands for electron transport. The "IMP" card is also used to determine the locally active particles transport. The data card section also contain the source specification cards that define the starting points for particle transport, and the material cards including the nuclide identification numbers. It also contain cell and surface parameters cards if they have not been specified in the cell and surface sections. For example the universe or "U" card is used to defines a universe number. This is considered as a self-contained cell e.g. a sphere or a box. A "FILL" card may be used to fill a subsequent cell of that universe using a specified universe number. The "LAT" card may also be used to create a repeated lattice structure of the relevant cell. The "TRCL" card provides a co-ordinate transform and may be used to shift or rotate the cell [116].

The final and the most important part of this section contain the physics model and the tally specification card i.e. the calculations that needed. The physics model is selected as either "simple physics" model or "detailed physics" model. The former does not take into account coherent scatter and the latter does and is the one used in this study. The last card in this section is the "NPS" which is the total number of histories used to terminate the simulation. Alternatively, the "CTME" card may be used that terminates the simulation by setting the total simulating time in seconds.

Monte Carlo Basic Concepts

Having described the layout of the input file the MCNPX code, then the package reads the file of the specified geometry and desired calculations. It then simulates individual particle histories and records the requested information. It basically allows the representation of all aspects of physical data with no approximations or averaging. This means that the

individual probabilistic events subject to statistical processes during interactions with various media are simulated sequentially.

The MCNPX code uses a built in pseudo-random number generator. MCNPX code uses the linear congruential of Lehmer [116] but it has been modified in such way so that it can take into account different computer platform. The pseudo-random number generator supplies a unique sequence of numbers having an initial value called seeds. If the same seed is used it will generate the same sequence of random number. The pseudo-random number generator has also a random number stride (period or jump). This is basically the number of random numbers between any two consecutive particle histories. The code has a default pseudo-random number stride but it can be changed on the "RAND" card so that the stride is not exceeded. As with most codes MCNPX code deal with binary numbers. A pseudo-random sequence of integers I_n is generated by:

$$I_{n+1} = mod(R_m I_n, n^{48}) \tag{4.1}$$

Where R_m is the random number multiplier and 48 bit integers and 48 bit floating point mantissas are assumed. The default value of R_m is 5^{19}. The pseudo-random number is then given by:

$$R_n = (2^{-48} I_n) \tag{4.2}$$

The starting pseudo-random number of each history is:

$$I_{n+1} = mod(M^s, I^n) \tag{4.3}$$

Where s is the pseudo-random number stride. The default value of s is 452525_8. This number ensures that the bit pattern will change when the stride is multiplied by almost anything. The period P of the MCNP algorithm is:

$$P = 2^{46} \approx 7.04 \times 10^{13} \tag{4.4}$$

4.1.3 Modelling the Imaging Detector

Most γ-ray imaging detectors normally operate in pulse mode [117]. This mean that each detected photon is represented as a pulse and the final image is produced from a narrow window of particular amplitudes corresponding to a particular range of deposited energy. Thus, to simulate and accurately model the imaging detector, using the MCNPX code,

one needs to know the energy deposition, process by the detector as well as the spatial information that gives the exact location of photons. This can be achieved by combining the use of tally F8 as well as the use of a feature of the MCNPX code refered to as Particle Track Output Card (PTRAC). The former gives the energy deposition of number of pulses recorded by the detector where as the latter gives detail interactions including the photon locations as well as their energies deposition. Both utilities provide accurate and detailed physics simulation for the imaging detector.

The following subsection provides a description of the steps undertaken to model the γ-ray imaging detector in a realistic way using the MCNPX code. This should also include the effects of limiting energy and spatial resolution on the projected images. These effects have been accounted for using a post simulation utility written using Matlab. The model then validated with experimental results so that it can be used as a platform with any image formation systems. Before describing the post-simulation program a description of the PTRAC is given here. In brief the use of PTRAC card in the simulation geometry of the MCNPX code produces a large output data file on particles trajectories. This single output list file, referred to as a PTRAC file has specific format. A summary of the format, the contents and the features of the PTRAC file is given in Appendix C. The PTRAC file needs to be sorted out first for further processing and image construction.

Post Simulation Program

To read the simulation data file a simple in-house post-processing program was written [118] to extract all histories from the PTRAC ASCII file corresponding to photons which interacted in the gamma camera's NaI crystal. The code then increments the image from these data file. The main disadvantages of this code is the limited imaging geometry and the long processing time. Further details of the code structure is available in [118] and references therein.

To achieve better efficiency the code has been slightly modified to suite different source geometries and simulation set-ups. The main structure and the theoretical principle of the original code remains the same. A flow chart of the modified matlab code is given in Fig. 4.1. The code accumulate the spatial information of photons and their energies that have been finally deposited in the detector lattice. The effective position of a photon within the detector is calculated as the weighted average of the energy lost within the

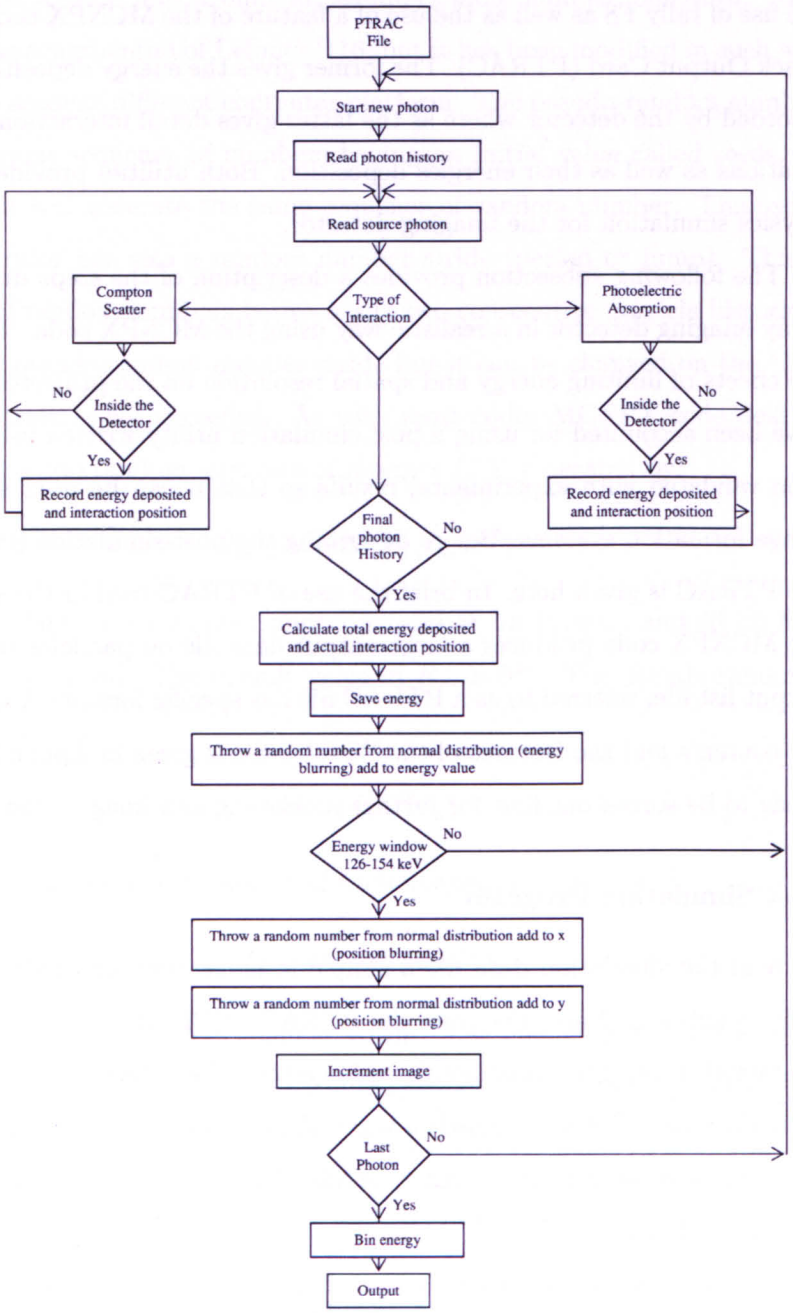

Figure 4.1: Flow chart for the post simulation code

scintillation crystal. This is achieved by following each individual event over the position of the respective interaction using the centre-of-mass principle for the calculation. The total energy deposited within the detector is obtained by summing all the energies lost by the photon.

The imperfections arising due to statistical uncertainty in position read out and in the recorded energy deposition process were also simulated using the same Matlab code. This was achieved by sampling a Gaussian distribution. Both the energy deposited by the photon and the X and Y position information are convoluted with a random noise from a zero mean values normal distribution. This process will simply blur both the spatial information and the energy deposition. Then the code uses a specified energy window to determine whether a particular event is accepted or ignored. Thus, all the major physics aspects of the imaging system are considered. The final part of the code is to divide the detector up into a matrix of pixels to produce a 2D projected image. The code also produces simulated energy histogram.

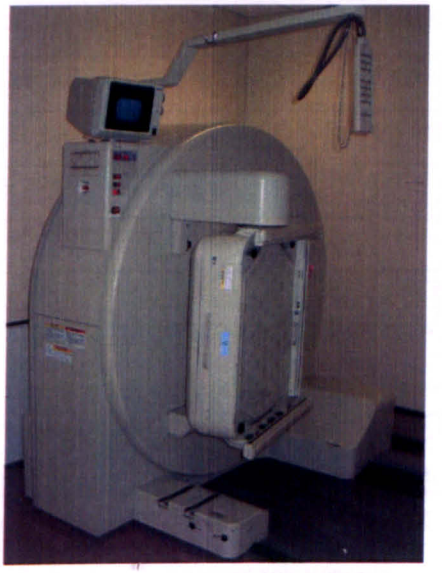

Figure 4.2: The Toshiba single headed gamma camera.

4.1.4 The Toshiba Gamma Camera

Figure 4.2 shows the imaging detector used in the majority of the simulated data. This is a Toshiba (GCA-7100A) single headed gamma camera based in Royal Surrey County

Hospital (RSCH) nuclear medicine department. The camera specifications obtained experimentally as well as by the manufacturer's are summarised in table 4.1 and table 4.2 respectively. The imaging detector is a single block rectangular object whose size is 55×40 cm^2. The scintillator (crystal) is of thickness 0.95 cm and provides an experimentally (by the manufacturer) verified spatial resolution of ≈0.37 cm FWHM. The later value is the system PSF measured at the center of the crystal with an idealised point source. This means that an idealised point source is seen not as a point but as a blur or spot. In practice, the use of some form of collimation is necessary to form the image, which further degrades resolution (see chapter 2).

Table 4.1: The main parameters of the Toshiba (GCA-7100A) single head system gamma camera. All the physical parameters are obtained using ^{99m}Tc point source and with its photon energy 140 keV with the LEHR collimator in place.

Main Parameters	**Values obtained**
Sensitivity (cpm/kBq)	4.6
Field of View (mm)	550×400
Photomultipliers	49 tubes×76 mm diameter
Scintillator	NaI (Tl) crystal
Crystal thickness	9.5 mm thickness
Collimator mass (kg)	65
Overall resolution (mm)	4.2 (at 0 distance)

Table 4.2: The Detector performance (manufacturer's specification). The physical measurements are obtained with ^{99m}Tc point source having 140 keV.

Main Parameters	**Manufacturer's Specification**
Energy range	50 - 400 keV
Field of view (mm)	550×400
Intrinsic resolution	3.7 mm FWHM (Central FoV)
Uniformity	3.3 % (Central FoV)
Linearity	0.2 mm (Diff)
Energy resolution	10.0% (Useful FoV)
Max count rate	230 kcps (20% windows)

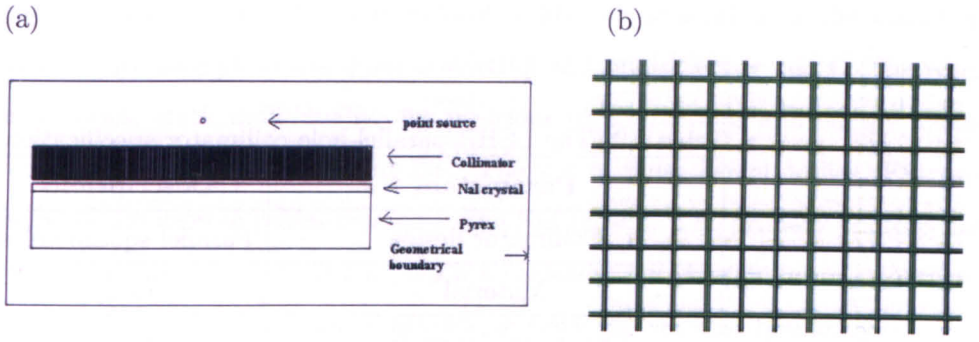

Figure 4.3: The MCNPX geometrical model of the gamma camera: (a) a side view , (b) a top view (not to scale) demonstrating the geometry of the LEHR parallel-hole collimator plotted from the MCNPX code.

Geometry

In this part a description of the imaging geometries, collimator and the camera over all design is provided. The camera was modeled following an approach suggested by DeVries and Moore [119]. The first and the most important component of the camera is the collimator (see 4.3 (a)) and was geometrically modeled as a parallel-hole having square holes (see 4.3 (b)) [119]. The simulated collimator was of LEHR type as such collimator is mainly used for imaging 140 keV photons. The main parameters or specifications of such collimator is given in table 4.3. The imaging detector consists of a 0.95 cm NaI scintillation detector with density 3.67 g/cm^3. The simulated detector is of size 40 cm $\times$40 cm and defined by 128^2 pixels, each 0.3125$\times$0.3125 cm^2. The backscatter from the Photo-Multiplier Tube (PMT) array is approximated by simulating a 6.8 cm thick slab of Pyrex following the method recommended by [119]. This homogenous block of Pyrex has 66% of the density of normal Pyrex to accurately simulate the PMT array glass material. The Pyrex was positioned directly behind the camera imaging detector. Thus, all the camera components were modelled, with MCNPX code, using sets of simple geometric primitives with various materials assigned to these shapes. Finally, all the camera geometries including the source should be within a sphere used in all simulations to limit the area in which transport take place as shown in Fig. 4.4.

In all simulations carried out in this thesis the sources are emitted isotropically in

Table 4.3: The LEHR parallel-hole collimator specifications.

Parameters	**Descriptions**
Collimator design	Parallel square holes
Material	Lead
Septa thickness (t)	0.02 cm
Hole size (d)	0.15 cm
Hole length (l)	4.00 cm
collimator to detector distance (e)	0.575 cm

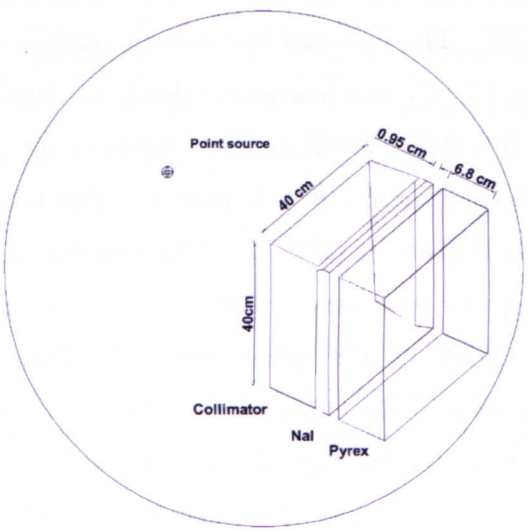

Figure 4.4: The MCNPX model of the LEHR parallel-hole collimator gamma camera including the geometrical boundary.

all directions of the geometry. The simulated photons generated in the object under study are mainly subject to Compton scattering and photoelectric effect. The resulting photon histories, track individually, the positions of interactions and energy losses are then recorded in the PTRAC output file. The use of pulse height tallies (F8) provide the energy distribution of pulses created in the NaI crystal. The primary photons and all subsequent photons and electron particles are considered in the simulation. All these are tracked until they are either stopped entirely or leave the detector boundary.

For accurate and more realistic simulation of the Toshiba gamma camera, each photon must be then subject to the effects of limited photoelectron statistics reflected in the finite energy and spatial resolution. To account for these effects, specific values were utilized derived from a-priori experiments on an actual Toshiba clinical gamma camera. The use of these detector imperfection processes in the simulation is discussed in the following section.

Verification of the Simulation

In order to validate the simulation data, an accurate and detailed knowledge of the Toshiba gamma camera response function is required. This is important to have a good faith that the geometry and the results from the simulation are correct. To simulate the response function of the gamma camera detector, first the resolution function of the camera needed to be modeled. Both the energy deposition and the spatial resolution function of the gamma camera were assumed to be closely approximated by a Gaussian response. This meant that to simulate a physical γ-camera both Gaussian energy blurring and Gaussian spatial blurring are required.

Firstly, the limited spatial resolution encountered in real imaging situations, the recorded (X, Y) spatial information are blurred. The spatial blurring was achieved by sampling a Gaussian distribution with FWHM=0.37 cm, corresponding to the intrinsic resolution as determined by the camera's manufacturer. In the real gamma camera, this effect is due to incorrect image recording by the PMT. For the simulated data the true (X, Y) spatial information is blurred by a Gaussian with σ=FWHM/2.35=0.1574.

Similarly, recording of the energy deposition process is also subject to Gaussian broadening by sampling a Gaussian with energy dependent FWHM. The FWHM energy dependence was determined experimentally, using derived spectra from the aforementioned

Toshiba gamma camera. Various mono-energetic gamma sources (^{201}Tl, ^{57}Co, ^{99m}Tc and ^{51}Cr) ranging from 72-320 keV peak energies were experimentally imaged in air with no scattering material. The FWHM values of these energy spectra were fitted to a function [120] relating the energy deposited with the FWHM of the energy response [121, 120]:

$$FWHM = n_1 \times E^{1-n_2} \tag{4.5}$$

where n_1, n_2 are values representing the best fit to the experimental data and the simulated results from the MCNPX, and E is the energy deposited. The above functional model is used in the Matlab code for blurring the energy deposited. Based on the the above energy spectra measurements, using the actual Toshiba gamma camera, and using Eq.4.5 the best fit was found with n_1=0.35 and n_2=0.23 as demonstrated in Fig. 4.5.

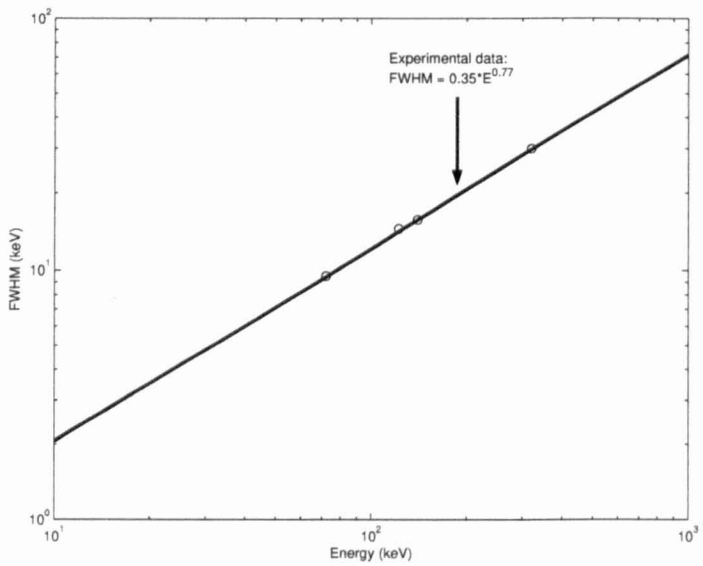

Figure 4.5: The relationship between the full energy peak FWHM and the energy deposited in the detector. Unfilled circles represent the experimental data.

The γ-ray photons used in nuclear medicine usually suffer from Compton scattering as they travel through the scattering medium. As a result of this interaction process a photon loses energy. In addition, the NaI detector has an imperfect response to the incoming pulse. Thus, the energy deposition in the NaI crystal should be subjected to an acceptance window defined by 20% ($\pm$ 10%) about the full energy peak. Because this symmetrical window is set around the full energy peak it is often called the photopeak window. For

^{99m}Tc, having gamma emission of 140 keV, the window is typically set between 126-154 keV. Photons which fall outside this window are rejected and do not contribute to the final image. In reality, the final projected image contains some proportion of scattered photon in the photopeak, due to statistical broadening.

Having constructed, tested the simulated geometry of the aforementioned Toshiba γ-camera, the initial step to be taken now is verify the simulation. This can be obtained by determining the simulated system Point Spread Function (PSF) and the energy spectra and comparing it with the experimental data.

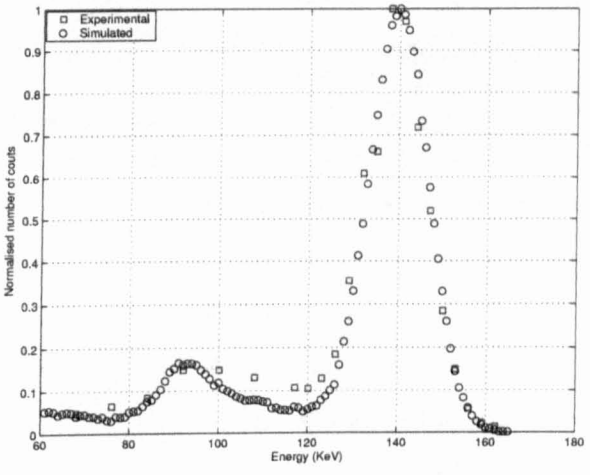

Figure 4.6: Comparison between the simulated and the experimental energy spectra for ^{99m}Tc of an small point source in air. The slight discrepancies between the two spectra are within the acceptable marginal error (i.e. 2-5 % of the FWHM).

(a) Energy Spectra

Using the PTRAC utility the simulated energy photopeak for a point source in air was first obtained and then compared with the the corresponding experimental data obtained from the Toshiba γ-camera. In both cases the incident radiation was mono-energetic (^{99m}Tc) at energy 140 keV. Figure 4.6 demonstrates the energy photo-peaks obtained from both the simulated data and the experimental data.

(b) System Spatial Resolution

The PSF is usually obtained from the 2D projected image of a point source in air. It

can also be theoretically determined using the collimator equation and expressed as the FWHM. A set of MCS experiments of a point source in air located at various distances, (f), from the LEHR parallel-hole (of square-hole) were conducted. The chosen distances were 2 cm, 5 cm, 10 cm, 25 cm, 50 cm and 75 cm and the number of histories simulated in each of these simulated work was 10^8. These were performed to investigate the spatial resolution as a function of distances from the γ-camera collimator. The same experiments were *a-priori* performed using the aforementioned Toshiba clinical imaging system that coupled to an hexagonal-hole LEHR collimator. Exemplar plots of the response from a point source in air at 25 cm distance obtained from both the MCS and the simulated data are shown in Fig. 4.7. Figure 4.8 (a) and (b) shows the image profiles from both experiment and simulation of a point source in air separated by 10 and 50 cm from the collimator respectively. These demonstrate that simulation is in good agreement (i.e. $\pm$ 2%) with the experimental data.

The spatial resolution expressed in FWHM were calculated from the simulated data and then compared with both the experimental data and the theoretical predictions. The theoretical resolution predictions were based on the collimator geometric spatial resolution equations proposed by Anger [77] and Webb [65] respectively. According to Anger the geometric resolution of the parallel hole collimator in terms of FWHM can be expressed as:

$$FWHM = \frac{d(l + f + e)}{l} \tag{4.6}$$

where d is the hole diameter and f is the source-to-collimator distance and e is the distance between collimator and the centre of the detector (commonly e=0.575 cm), finally l is the collimator length or depth. Now if the parameters of Eq. 4.6 are replaced with the values shown in table 4.3 then the equation becomes $FWHM = 0.038f + 0.172$. Similarly, Webb [65] suggested a similar equation but he ignored the e term as:

$$FWHM = \frac{d(l + f)}{l} = 0.038f + 0.150 \tag{4.7}$$

The above theoretical equations defined by Webb and Anger suggest that the spatial resolution of the parallel-hole collimator can be improved by placing the source closer to the collimator. Thus, both equations seem to have a linear relationship [65].

Using the least square error line fit to the experimental and simulated data gives this equation $FWHM = 0.038f + 0.210$ as plotted in Fig. 4.9. This also shows the variation

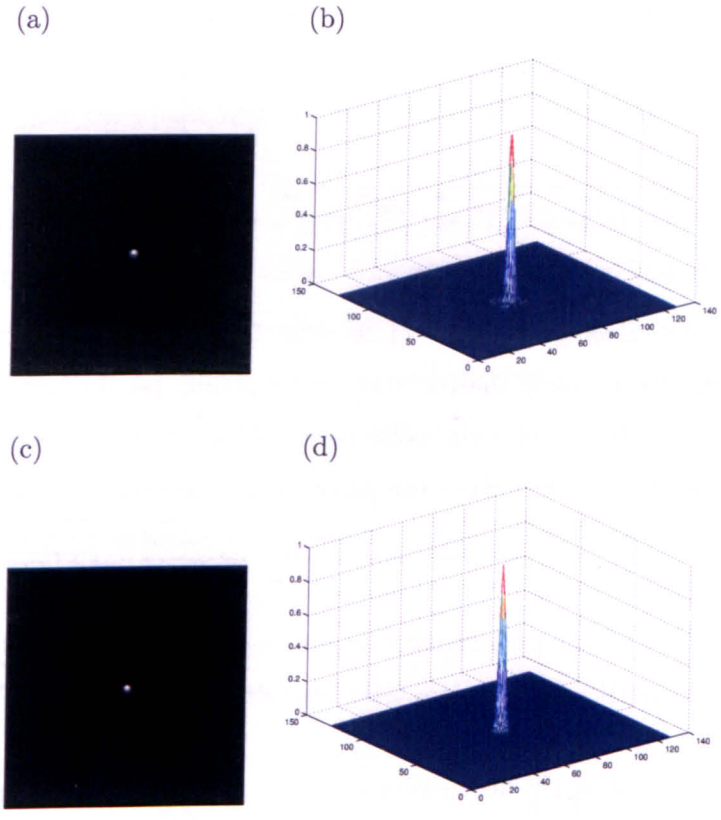

Figure 4.7: Exemplar plots of the response from a point source at 25 cm from the collimator face: (a) the image obtained experimentally using the Toshiba γ-camera, (b) the corresponding 3D plot of the image, (c) The simulated image and finally (d) the corresponding 3D plot of the simulated image. These demonstrate that the simulated results agree with the experimental data.

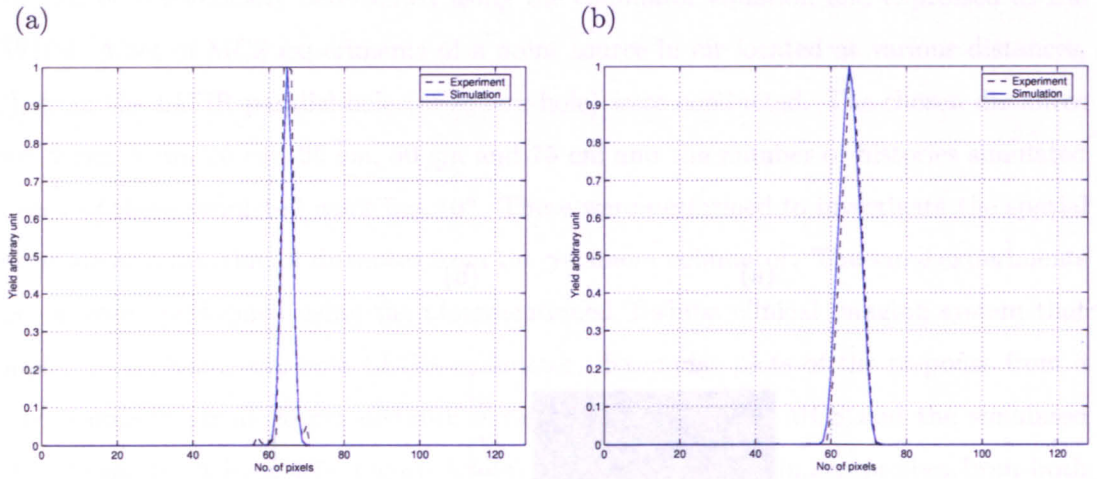

Figure 4.8: Exemplar profiles of the PSF from a point source obtained using MCS and real experiment using the the Toshiba γ-camera: (a) the point source located at 10 cm from the collimator, (b) the point source separated from the collimator by 50 cm. This demonstrates that the closer the point source from the collimator the sharper the PSF.

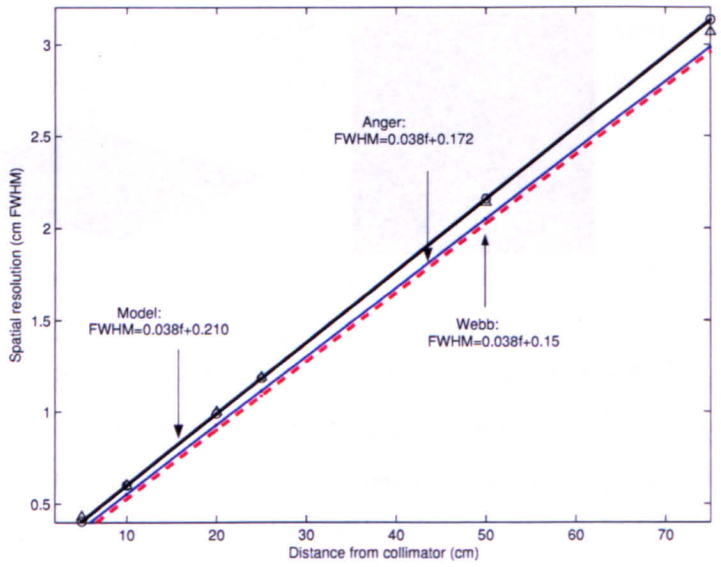

Figure 4.9: The spatial resolution in terms of the FWHM of an infinitesimally small point source of ^{99m}Tc in air versus imaging distance for experimental (unfilled triangle) and simulated results (unfilled circle) compared with theoretical models proposed by Anger and Webb.

of the spatial resolution in term of the FWHM for the LEHR parallel-hole collimator. The presented results are for the simulated and experimental data compared with the Anger and Webb theoretical equations. These demonstrated the fall off of the spatial resolution with increasing the distance of the source from the collimator. Figure 4.9 demonstrates good agreement between the simulated and experimental data although the simulated collimator had a square hole compared with the hexagonal hole in the case of experimental data. This is also confirmed and agrees with that concluded by DeVries [122] that on average both the square hole and the hexagonal hole approximately give the same result.

Figure 4.9 also show sthat the model used for the experimental and the simulated data also agree with Webb and Anger Model. The slight differences (less than 5%) between the model used here and the Webb and Anger models are expected. This is because both theoretical models given by Anger and Webb are geometrical models and neglects any thing else. However the model used for the experimental and simulated data are more realistic as it includes the degradation effect of the camera physics. This is because in both cases the imaging detector was based on NaI and this is responsible for worsening the spatial resolution.

This simulated camera model was used as a benchmark for the subsequent work with CA. The same camera model has been used after replacing the LEHR collimator with CA.

4.1.5 Implementation of Coded Aperture for Simulation

Having described the Monte Carlo (MC) method and the validation procedures, this section describe the MC implementation of CA pattern. To do so one first need to establish the relationship between the mask parameters including mask-to-detector-distance and source-to-mask distance. These parameters are important as it determines the system spatial resolution and needs to be established first. Before the MC coded images were undertaken, simple calculations were carried out to determine the suitable mask thickness and material. From Beer's Law, the attenuation or fractional loss of γ-ray photons stopped in a material is given by the formula for linear attenuation coefficient:

$$1 - \frac{I_T}{I_0} = 1 - \exp^{-\mu x} \tag{4.8}$$

where I_T is the transmission intensity after passing through material, I_0 is the initial

incident intensity, μ is the attenuation coefficient (cm^2/g) at the energy of interest and finally x is the density thickness (density thickness) g/cm^2.

The fraction of γ-rays passing through a material positions is called mask transmission or transparency, t, and is given by:

$$t = \exp^{-\mu x} \tag{4.9}$$

where ρ is the density of the mask material g/cm^2.

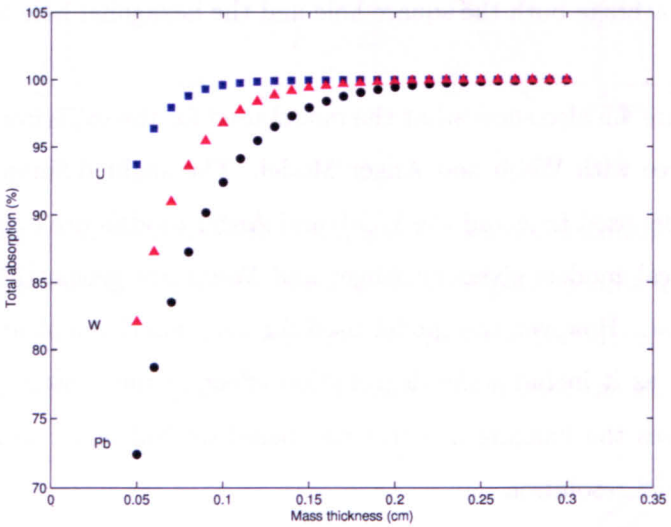

Figure 4.10: The calculations of the total absorption as a function of materials thickness. The materials used in the calculations were uranium (U), tungsten (W) and lead (Pb). The simulated CA mask was tungsten sheet of thickness 1.5 mm as this will attenuate 99.4% of the incident photons of energy 140 keV.

The best material to be used as a mask is the one having minimum thickness for a given attenuation i.e. with the maximum product $\mu \times \rho$. At 140 keV the values of μ were calculated, using the XCOM programme [123], for three materials; uranium, tungsten and lead. The mass absorption coefficient for these three materials as a function of thickness is illustrated in Fig. 4.10. Of these investigated materials, uranium (48.97 cm^{-1}) is the best material, followed by tungsten (30.5 cm^{-1}) and then lead (22.96 cm^{-1}). However, it was decided to use tungsten with 1.5 mm thickness because practically it is the most suitable material. Tungsten has a density of 19.3 g/cm^3 and its linear attenuation coefficient at 140 keV is 1.76 cm^2/g. For the chosen mask thickness of 1.5 mm and based on eq. 4.8,

the mask transmission is $t = 0.006$ or 0.6%. This means that it allows less than 1% penetration of that introduced into the image and contributes to the deterioration of its quality and contrast.

Basic Mask Design for Scintimammography

In the particular case of scintimammography, the imaged region can be approximated to be a uniform volume of tissue with approximately uniform background activity, superimposed upon a small region of enhanced activity which is usually attributed to a lesion or disease presence. This target area is typically smaller than the sensitive imaging area provided on a clinical gamma camera. The displacement of the CA and the gamma camera away from close proximity to the breast means that shielding can be introduced to mitigate the effects of unwanted cardiac, liver, and bladder tracer uptake. In practice, the standard clinical gamma camera detector is limited in dimension to $\sim 1/2$ m^2. Taken together with the need to shield the detector from non-specific (non-breast) activity means that the use of a mosaic mask may be impractical [124].

In addition, since the size of the breast is usually smaller than the γ-camera imaging detector, the second CA camera arrangement, Fig. 3.18 (b), is examined. This geometry allows a basic mask pattern to be projected onto the imaging detector. However, there are some constraints imposed by the detector. For instance, the allowed distance between the object and the CA mask, the size of the object or the FoV and the chosen image magnification. The latter is limited by the size of the object and more importantly by the size of the detector and its resolving capability. Finally and importantly the detector sampling so that the image produced not be distorted by the artefacts.

Several masks have been investigated in this study; 41×41 MURA (symmetric mask) and 82×82 NTHT-MURA. Several geometrical configurations has also been considered. In additions, small investigations were carried out using 31×31 MURA (antisymmetric mask) and mosaic pattern arrangement based on either 41×41 MURA masks. The main parameters of these masks are summarised in table 4.4. It is worth noting that the smaller the CA-hole the higher the image resolution but fewer photons reach the detector. In this study realistic aperture sizes of 2mm and 1mm were used in the simulations because it may be difficult in practice to design aperture-holes smaller than 1mm.

Table 4.4: The main parameters for the masks used geometry in CA imaging investigations.

The Mask	A	B	C
Mask pattern	MURA 41×41	NTHT MURA 82×82	MURA 31×31
Open fraction	50%	12.5%	50%
Mask symmetry	symmetric	antisymmetric	anti-symmetric
Material	Tungsten	Tungsten	non
Mask pixel size	2 mm	1 mm	2 mm
Magnification coefficient	4	4	4
Geometric resolution	2.6 mm	1.6 mm	2.6 mm
FoV	8.2 cm	8.2 cm	6.2 cm
Mask thickness	1.5 mm	1.5 mm	Perfect

4.2 Non-Monte Carlo Methods

The main problems with MCS is that it takes very long execution time due to its intensive calculations. To obtain sufficient statistics the simulation can takes several weeks and produce huge output PTRAC files particularly with CA simulation. Two non-Monte Carlo methods, taking much less computation time, were developed to investigate and understand the performance of CA for imaging various source objects. The first method is referred to as the Binary Mask Shift (BMS) whereas the second method is referred to as Pseudo-Ray Tracing (PRT). These methods are discussed in the following subsections.

4.2.1 Binary Mask Shift (BMS) Method

This method was initiated using the projected image array of a perfect MURA (or pattern based on MURA) binary mask generated by an on-axis point source. Then using assumed knowledge of the shape of the distributed source to be imaged, the projected pattern was systematically shifted according to the projected point source pattern that would be obtained by every non-zero element in the object. The result of each single or "binary shift" of the projected pattern is then summed with the preceding projection pattern. For illustration consider a binary mask that has been first shifted to the left then right and then up and down and finally summed.

$$\begin{pmatrix} 0 & 0 & 0 & 0 \\ 0 & 1 & 1 & 0 \\ 0 & 1 & 1 & 0 \\ 0 & 0 & 0 & 0 \end{pmatrix} \begin{pmatrix} 0 & 0 & 0 & 0 \\ 1 & 1 & 0 & 0 \\ 1 & 1 & 0 & 0 \\ 0 & 0 & 0 & 0 \end{pmatrix} \begin{pmatrix} 0 & 0 & 0 & 0 \\ 0 & 0 & 1 & 1 \\ 0 & 0 & 1 & 1 \\ 0 & 0 & 0 & 0 \end{pmatrix} \begin{pmatrix} 0 & 1 & 1 & 0 \\ 0 & 1 & 1 & 0 \\ 0 & 0 & 0 & 0 \\ 0 & 0 & 0 & 0 \end{pmatrix} \begin{pmatrix} 0 & 0 & 0 & 0 \\ 0 & 0 & 0 & 0 \\ 0 & 1 & 1 & 0 \\ 0 & 1 & 1 & 0 \end{pmatrix}$$

$$\begin{pmatrix} 0 & 1 & 1 & 0 \\ 1 & 3 & 3 & 1 \\ 1 & 3 & 3 & 1 \\ 0 & 1 & 1 & 0 \end{pmatrix}$$

The summed shifted copies were then decoded with the usual post-processing, G function (an inverse filter of A). This binary mask displacement method represents a far-field approximation and is also given by using Eq. 3.13 but with a constant $\Omega(\vec{r_o}, \vec{r_i})$ term. This noise-less composite method was used to demonstrate the effect of artefacts from planar objects or displaced (shifted) sources. Mask transparency, finite mask thickness and statistical noise is not considered in this approach. But the projection data were convolved with a 2D Gaussian of standard deviation, $\sigma = 1.57$ mm, to simulate the intrinsic PSF blurring of the gamma camera. As will be demonstrated in the next chapter, this simple BMS approach could be used to predict the source and the background pattern produced by uniform 2D object. This initial approach lead to the development of the Pseudo-Ray Tracing (PRT) method [124].

4.2.2 Pseudo-Ray Tracing (PRT) Method

This method has been used to investigate the background distortion observed when imaging planar and 3D source phantoms. The images obtained from the PRT are divided into two groups these generated from a phantom containing lesion and those generated from a phantom without a lesion. In all the projections of a CA-hole cast by a point on the object falling on the detector grid these are represented by Eq. 3.13 and is calculated using purely geometric formulae. Simple in-house code was written to do this calculation based on calculating the fractional solid angle [125] subtended by each element of the mask whose shadow projected along the flux direction is intercepted by the detector. An accurate knowledge of the solid angle presented by the source to the mask is essential for calculating the projection.

The solid angle, Ω, (in steradian) is generally defined by an integral over the surface

(a) (b)

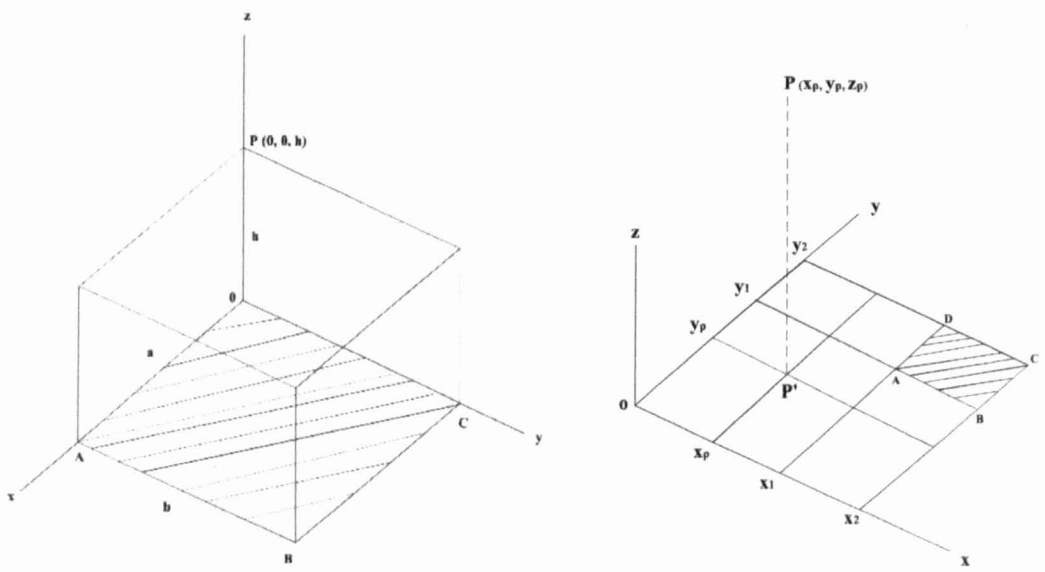

Figure 4.11: Schematic diagrams used to define the solid angle for a point P: (a) a geometry for a solid angle subtended by the shaded rectangle 0BCD , (b) a geometry for a solid angle subtended by the small shaded rectangle ABCD at the point P. Both geometrical diagrams were adapted from [125].

that faces the source. The calculation here is based on calculating the fractional solid angle subtended by a rectangle shape [125]. To illustrate this consider the schematic diagram of Fig. 4.11 (a) the fractional solid angle, Ω, subtended by the rectangle 0BCD at point P is represented by:

$$\Omega = h\int_0^a dx \int_0^b \frac{dy}{(x^2+y^2+h^2)^{\frac{3}{2}}} \tag{4.10}$$

As will be seen in Appendix B the above equation with the double integration can be solved and the result is:

$$\Omega = \arctan \frac{ab}{h\sqrt{a^2+b^2+h^2}} \tag{4.11}$$

To illustrate how the fractional solid angles for each open element of the mask is calculated consider the schematic diagram of Fig. 4.11 (b). The rectangle in this case is enclosed by the four straight lines $x=x_1$, $x=x_2$, $y=y_1$ and $y=y_2$ and the coordinates of the observation point P are (x_p, y_p, z_p). For the small shaded area ABCD (see Fig. 4.11 (b)) the fractional solid angles, Ω, is represented by four solid angles subtended by rectangles:

$$\begin{aligned}\Omega = &\arctan \frac{(x_2-x_p)(y_2-y_p)}{z_p[(x_2-x_p)^2+(y_2-y_p)^2+z_p^2]^{\frac{1}{2}}} \\ &- \arctan \frac{(x_1-x_p)(y_2-y_p)}{z_p[(x_1-x_p)^2+(y_2-y_p)^2+z_p^2]^{\frac{1}{2}}} \\ &- \arctan \frac{(x_2-x_p)(y_1-y_p)}{z_p[(x_2-x_p)^2+(y_1-y_p)^2+z_p^2]^{\frac{1}{2}}} \\ &+ \arctan \frac{(x_1-x_p)(y_1-y_p)}{z_p[(x_1-x_p)^2+(y_1-y_p)^2+z_p^2]^{\frac{1}{2}}}\end{aligned} \tag{4.12}$$

Equation 4.12 has been used to calculate the fractional solid angle subtended by each opening of the mask at an arbitrary point. To calculate the projection for a 2D or 3D object the solid angle calculations requires *a priori* knowledge of the source distribution. In SM this is not a major issue as the breast is commonly compressed to a known thickness, and the 2D projection can be obtained from a simple optical camera. The code finds the center of the projection of the mask-hole by ray-tracing.

To simulate a continuous distribution in the case of 2D or 3D objects, the phantom is divided into 3D volume elements or voxel of 1 mm^3. Attenuation in the phantom, mask transparency, finite mask thickness and statistical noise are not considered in this simple model. The projection data were convolved with a 2D Gaussian of standard deviation, σ

= 1.57 mm, to simulate the intrinsic PSF blurring of the gamma camera. The CA camera performance has been judge based on its ability to detect a variable spherical lesion located at different positions and different Tumour-Background-Ratios (TBRs).

Chapter 5

Pilot Simulations Using a MURA Coded Aperture for Near Field Imaging

Having described the main methods developed for Coded Aperture (CA) imaging investigations in the previous chapter, the results from a preliminary study are given here. This chapter presents the near-field investigations of a CA coupled to conventional γ-camera using some relatively simple imaging geometries. These highlight the differences between the imaging geometries in previously reported [96] astronomical applications and that of using CA imaging in nuclear medicine environment [74, 76]. In presenting these results this chapter is divided into four main sections. The first section describes the main investigations obtained with the simple case of imaging a point source in air. The second section presents the effect of multiple-sources and imaging at multiple-depths. These intended to demonstrate the effect of multiplexing on the decoded images. The third and the fourth sections discuss the main investigations carried out with 2D and 3D source objects respectively.

5.1 Introduction

Using the MURA CAs in the far-field geometry with low noise applications produces artefact-free images when imaging point-like objects. In such far-field imaging problems

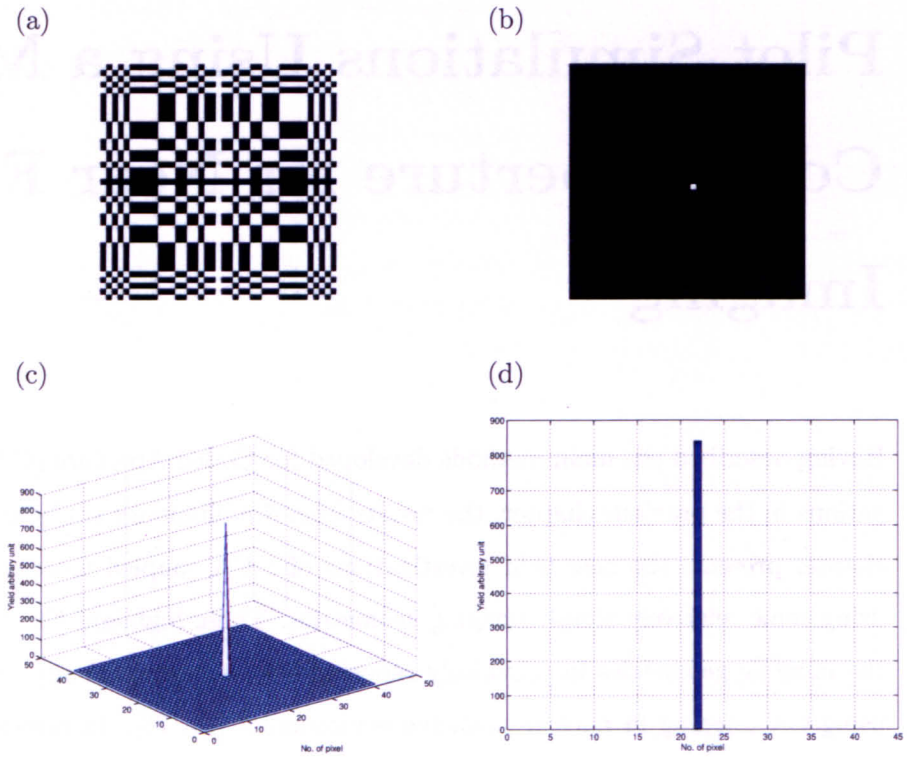

Figure 5.1: The response function (PSF) of an: (a) ideal (no noise) binary mask, (b) ideal decoded image i.e. the cross correlation of (a) with its G function produces sharp point with zero side-lobe, (c) 3D plot of the ideal decoded image and finally (d) a vertical profile.

applications, an object characterised as being made of isolated point sources (at infinity) distributed over a mainly dark background. These conditions provide the basis of artefact-free and high Signal-to-Noise-Ratio (SNR) imaging. Theoretically and as explained in chapter 3 in such low noise stellar applications [96] the $\Omega(\vec{r}_o, \vec{r}_m)$ factor of Eq. 3.13 is constant (i.e. $\cos^3(\theta) \cong 1$). This means that the imaging process can be considered to utilize a far-field geometry providing artefact-free images. Fig. 5.1 (a-d) demonstrates that in such situation the binary MURA produces a perfect correlation properties with zero side-lobes. In addition, to demonstrate the performance of the binary MURA CA of exemplar size 41×41 the Modulation Transfer Function (MTF) can be calculated. The MTF is a useful measure as it tell us about the quality of the imaging system and how it is susceptible to noise. There are various functions used to derive [126] the MTF and the one used here is defined as the absolute value of the Fast Fourier Transform (FFT) of the PSF and is given as:

$$MTF(u, v) = |H(u, v)| \tag{5.1}$$

where $H(u, v)$ is the FFT of the system PSF

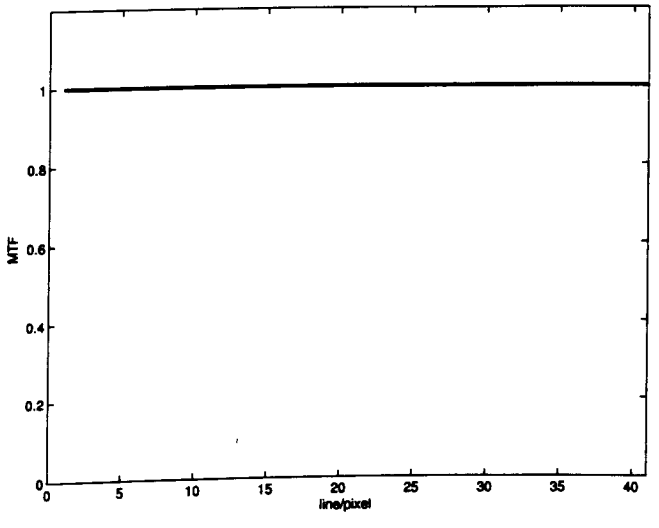

Figure 5.2: The MTF of the MURA-CA as a function of frequency demonstrating how efficient is the MURA in passing frequency information.

Figure 5.2 demonstrates that the MTF for the binary MURA-CA system has one value at all frequencies [126]. Thus, this represents the ideal case with no blurring or noise effect.

In practice, due to the finite size of the mask holes the CA imaging system can have several MTF values.

5.2 Near-Field MURA Coded Aperture Imaging

In contrast to the astronomical applications, this thesis is concerned with the near-field imaging as the source is placed at close distance (40 cm) from the detector to maximise the efficiency by collecting acceptable number of photons. In this case the far-field approximation breaks down and the incident photons are no longer parallel. This is a challenging task as the incident photons in near-field imaging geometries produce serious artefacts. A combination of Monte Carlo method and two other iterative methods have been conducted to illustrate the performance of CA imaging system and the quality of the reconstructed images. Fortunately a number of methods [104, 76, 124] have been suggested to mitigate these near-field effects (see chapter 7).

In all investigations carried out in this study only static projection images (planar images) were considered i.e. data collected from a single angle. This is because multiple view CA imaging has been demonstrated [75] to add structured noise (from the out-of-focus planes) to the decoded images.

5.2.1 Imaging with a Point Source

This section represent the various investigations obtained with a point source using the aforementioned methods. The effect of placing the point source off the central axis is investigated demonstrating the effect of partial encoding. In addition, the effects of out of focus decoding is also investigated. Finally, in placing the point sources in water, this showed a relatively small effect on the decoded image, albeit with some loss of statistics. The main findings are highlighted and discussed in the subsequent sections.

(a) On-central axis point source

Figure 5.3 shows the schematic setup of the near-field imaging geometry for an idealised point source in air on the central axis. This imaging geometry ensures a magnification coefficient, (m_c), of four. This geometry setup is an ideal case for a point source in air and is used as a reference for the subsequent point source imaging results. In this case,

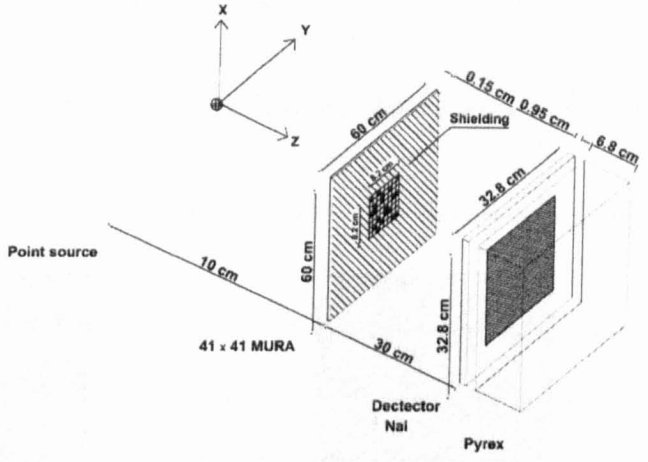

Figure 5.3: Schematic diagram of the MCS using MURAs-CA, in the near-field imaging geometry, with a ^{99m}Tc photon energy (140 keV) point source. The imaging detector consist of 0.95 cm NaI scintillation detector defined by 164^2 pixels each of 0.2^2 cm^2. The physical dimension of the mask is 8.2 cm^2. The source-to-mask-distance is 10 cm^2 and the mask-to-detector-distance is 30 cm^2.

the projected shadowgram of the mask is completely covered by the whole detector area. This projected "image" does not produce the object directly (see Fig.5.4 (a)) and needs to be decoded with the postprocessing array, G. This however, produces the intrinsic response function image from a point source for this particular arrangement. The point source decoded image produced from a CA camera is also referred to as the Point Source response Function or Point Spread Function (PSF). Fig.5.4 (b-d) illustrates the results of imaging the aforementioned point source with imaging geometry shown in Fig. 5.3. Note, the small cross-shaped side-lobes observed in Fig. 5.3 is due to the variation in the incident angle of γ-rays i.e. solid angles effect, as will be seen later in chapter 7. The observed results from this on central axis geometry is near perfect because the correlation process of the projected image and the G function is complete and acts over all elements in the mask and detector.

Having obtained the correlated image from an on-central axis point source, the effect of photon statistics can be established. In this case and for a set of point sources in air the total number of simulated photons were systematically varied. Then the peak value plotted as a function of photon statistics is given in Fig. 5.5 (a). From the point source

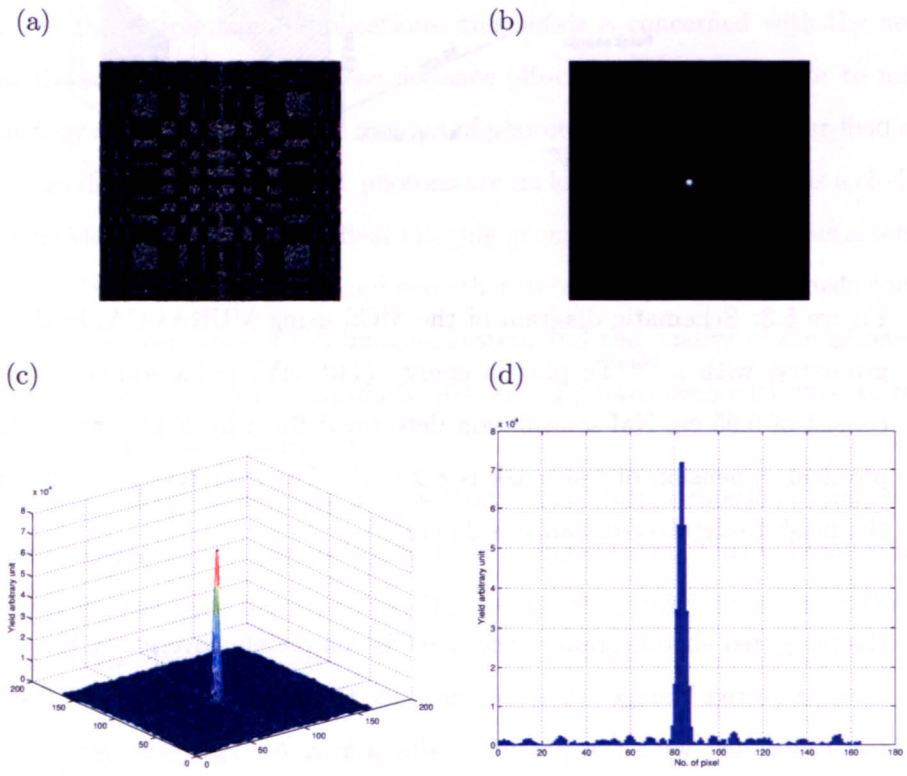

Figure 5.4: The MCS of system response from an idealised point source in air in the central axis shown in Fig. 5.3: (a) shows the appearance of the mask shadow i.e. the projected image , (b) the decoded image, (c) the 3D plot of the decoded image, and finally (d) a vertical profile taken through the centre of the decoded image. Note for this simulation $\approx$ 7.5 Million photons were simulated and $\approx 1.6\times10^5$ detected by the detector. The decoded image instead of a sharp point image there is a blurred spot. This latter effect is principally due to the simulated γ camera's finite PSF as well as object magnification.

in air investigations as a function of the simulated photons it was concluded that there only starts to be a significant drop in image quality when the total photons detected drops below $\sim$ 150k. This corresponds to a detected photon density of 10-100 photons cm^{-2}.

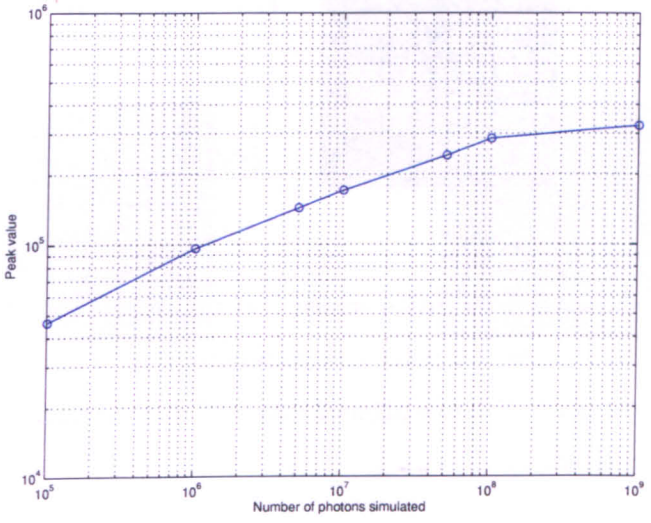

Figure 5.5: The effect of photon statistics a plot of the peak value as a function of counting statistics. This show that further increase in the simulated number of photons produce no significant increase in the peak value.

(b) System Spatial Resolution

One of the preliminary investigations with MURA-CA was to evaluate the spatial resolution by simulating two idealised point sources of ^{99m}Tc in air separated by 6 mm. The geometrical configurations for this simple experiment is the same as demonstrated in Fig. 5.3. The decoded image and the corresponding vertical profile taken through the centre of the decoded image is illustrated in Fig. 5.6.

(c) Off central axis point source displacement

A series of MCS experiments, using a point source (140 keV) in air, were carried out to investigate the peripheral point source response function. In each case, the point source was displaced by a 1 cm along the horizontal (Y axis of Fig. 5.3) about the centre of the FoV corresponding to a breast phantom that is 10 cm wide. The projected images were considered and then correlated with the post-processing array, G, corresponding to the

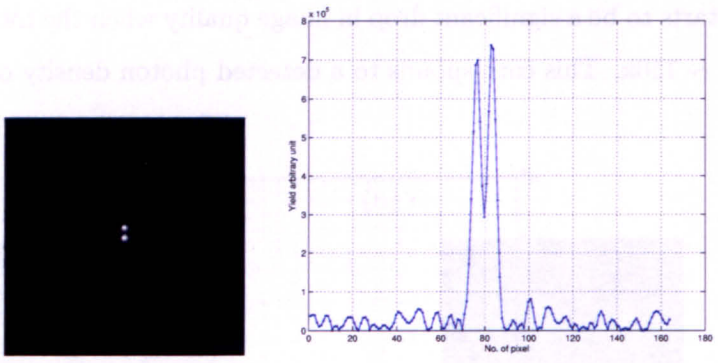

Figure 5.6: Spatial resolution image: (a) the decoded image result from the two point sources, (b) Profiles of 2 point sources separated by 6 mm, in air with the full-width-half maximum 4 pixel. NB: one pixel=2 mm, and due to imaging geometry a magnification of 3 is also present.

central source.

Fig. 5.7 and 5.8 show exemplar plots of the point source response function, of 3 and 5 cm point source displacement respectively. These two off-central-axis sources project only part of the mask onto the detector with respect to the full-field projection seen in Fig. 5.4 (a-d). The resulting decoded source locations in the decoded images were, unsurprisingly, shifted accordingly. This results in a lower peak point response value due to sensitivity (solid angle) loss. In addition, the side lobes clearly observed in the decoded image demonstrates enhanced magnitude with source displacement.

To investigate this further, a set of point source response functions from the MCS data and the theoretical calculation were compared. An accurate knowledge of the fractional solid angle Ω subtended by each opening of the mask to the source is essential for this theoretical calculation. The fractional solid angle Ω is generally defined by an integral over the surface that faces the source; and for the mask is calculated from Eq. 4.12 considering the same geometrical configuration of the MCS. For a particular position of the source, the subtended fractional solid angle of each opening of the mask was calculated using the Eq. 4.12 then multiplied by the fractional area of projected shadow (illumination). This fractional area is equal to the covered area of the shadow by the detector divided by the

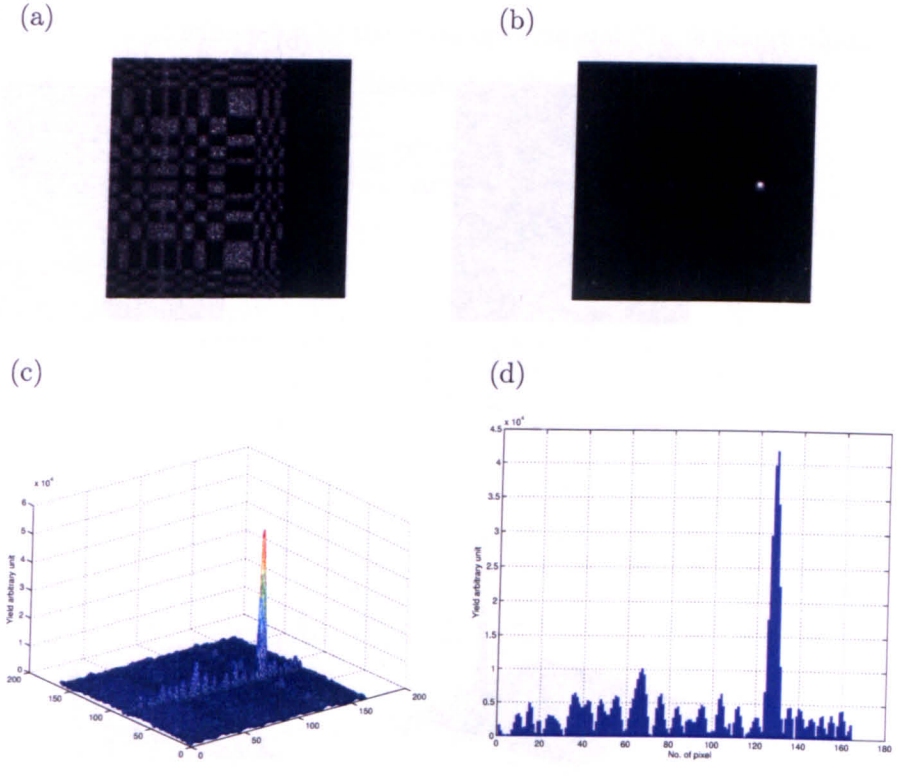

Figure 5.7: Exemplar plots of the response from a point source displaced by 3 cm from the central axis obtained from MCS: (a) the projected image which is simply a shadow of part of the mask, (b) the corresponding decoded image, (c) a 3D plot of the decoded image and finally (d) a horizontal profile through the decoded image. Note that (c) and (d) illustrate the "cross-like" side-lobes that occur due to imperfect imaging conditions associated with near-field geometry.

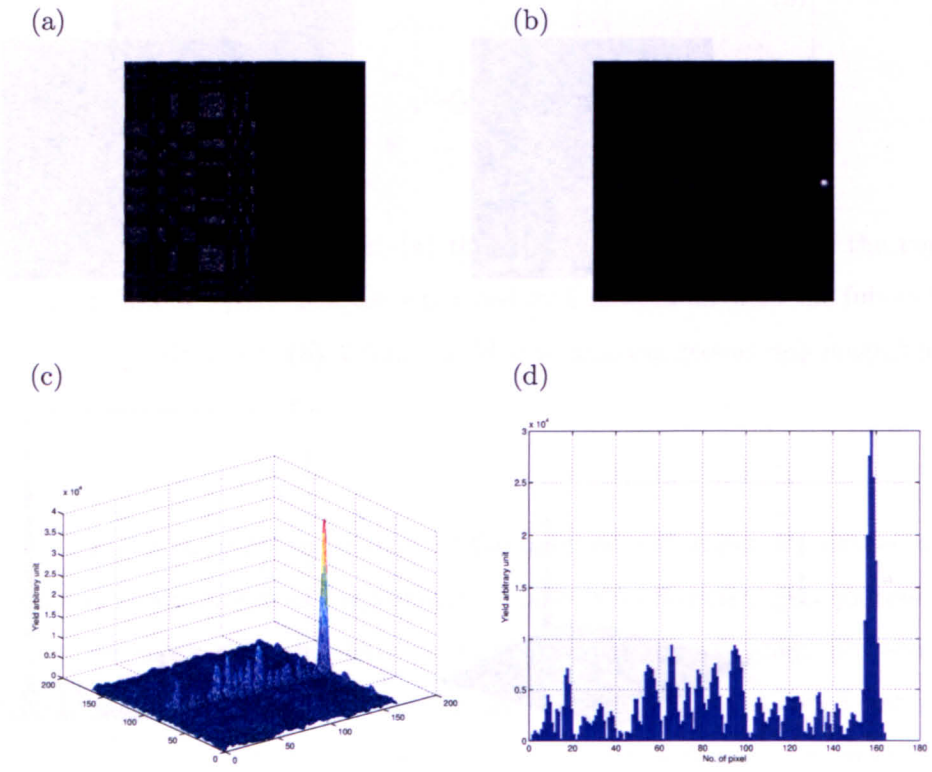

Figure 5.8: Exemplar plots of the response from a point source displaced by 5 cm from the central axis: (a) the projected image is simply a shadow of part of the mask, (b) the corresponding decoded image, (c) a 3D plot of the decoded image and finally (d) a horizontal profile through the decoded image. Once more, imperfect imaging causes an unwanted artefact in the image the magnitude of which increases with source displacement.

total area of the shadowgram. It is equal to one if the whole cast shadow is covered by the detector. Then this elemental solid angle is summed over all the mask opening as:

$$\Omega = \sum_i \sum_j \Omega_{ij}(\vec{r_0}) \times \xi 1_{ij}(\vec{r_0}) \tag{5.2}$$

where i,j represent the index of the mask opening and $\vec{r_0}$ is the source position, Ω_{ij} is the elemental solid angle subtended by the mask opening and $\xi 1_{ij}$ is the fractional area of the covered shadow by the detector as illustrated in Fig. 5.9.

$$\xi 1 = \frac{covered\,area}{total\,area} \tag{5.3}$$

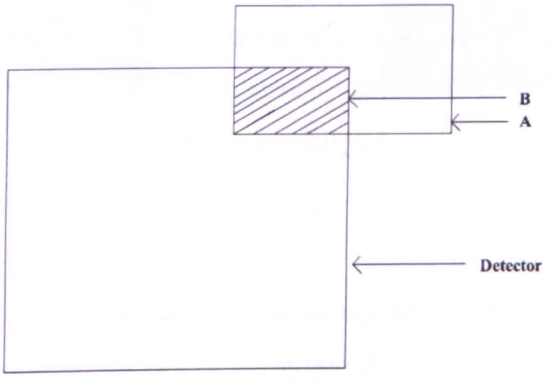

Figure 5.9: Schematic diagram showing fractional detected cast illumination of mask hole (shaded area) on the edge of the detector. In this case $\xi = \frac{B}{A}$ and $A=(p_m \times m_c)^2$, where: p_m is the mask pixel size.

The results of the source response function were represented in term of maximum (peak) value for each source as a function of point source displacement and is given in Fig. 5.10. From such a figure one can see that the simulated data is slightly larger compared to the theoretical calculation. This slight discrepancy in the results is believed to be due to practical considerations not implemented in the theoretical calculation such as mask penetration and the finite mask thickness. The results also demonstrates that for the particular geometry shown here (MURA of 41×41 elements, magnification of 4) the point source displacements across the FoV produces a maximum loss of 0.52 in sensitivity along the the central axis. This will be expected to produce quadratic combination of 0.52^2= 0.2704 at the corners.

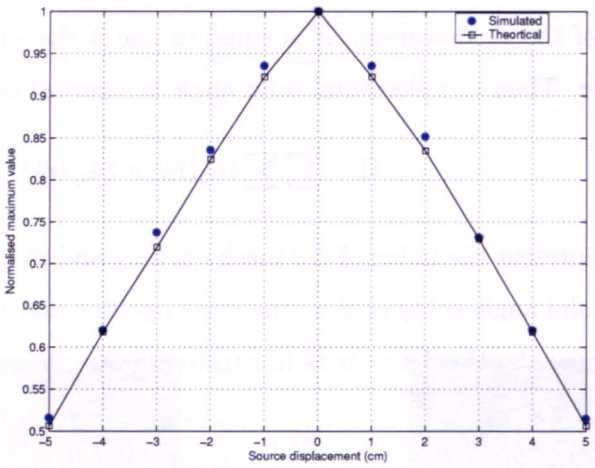

Figure 5.10: The maximum value of the decoded image as a function of an off cental axis point source displacement. The horizontal shifts about the centre of the FoV correspond to a 10×10 cm^2 FoV. Similar effects can be seen in the perpendicular direction. There is approximately a factor of 2 difference between the central and the edge (off-central axis) point source.

Further study of the spatial variation in sensitivity was initiated using Binary Mask Shift (BMS) of the MURA pattern of 41×41 elements after being scaled by 4 to have the same imaging geometry as the MCS. As discussed in the previous chapter, in the BMS method, the mask is basically shifted one pixel at a time to produce the required shifted point source. This noiseless composite mask was then decoded using the usual G function to demonstrate the intrinsic imaging properties of the MURA mask under consideration. Figure 5.11 show exemplar plots of the binary (ideal) response from a shifted mask pattern corresponding to a point source shifted by 3 cm.

For a realistic comparison of the BMS with MCS data each open hole of the shifted binary mask is then multiplied by 10^6 (representing the activity of the point source) and then convolved with a 2D Gaussian of standard deviation, $\sigma = 1.57$ mm, to simulate the intrinsic PSF blurring of the gamma camera. Then this is decoded using the usual G function to demonstrate the intrinsic imaging properties of the MURA mask under consideration. Herein, only the 3 and 5 cm were considered individually. Figures 5.12 and 5.13 show exemplar plots of the binary (ideal) response from a projected mask pattern, decoded images corresponding to a 3 cm and 5 cm source displacement respectively. This

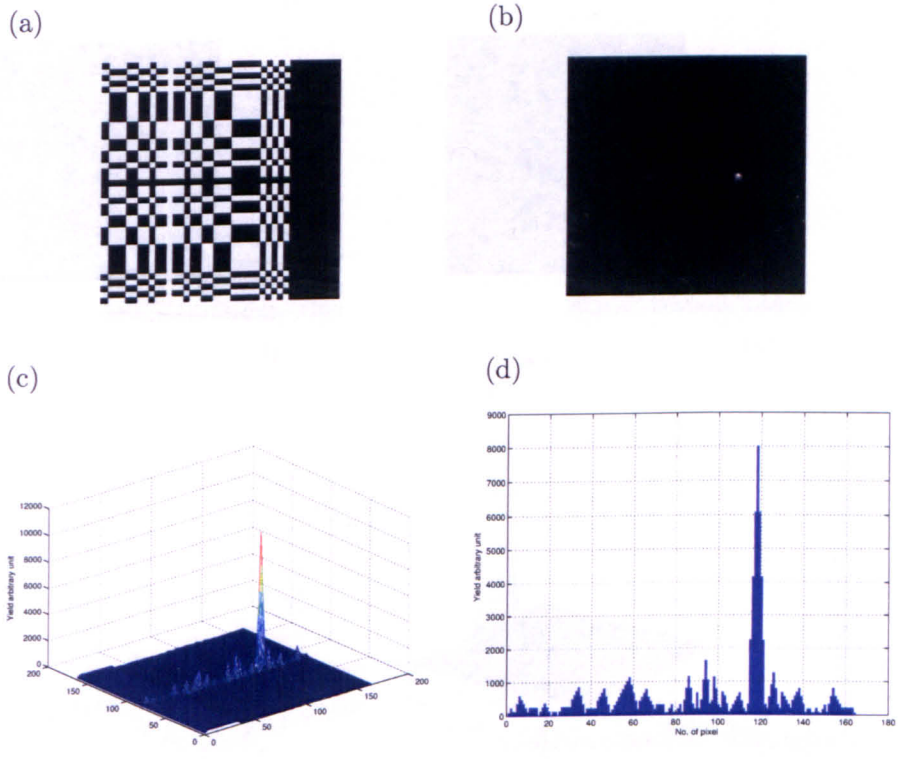

Figure 5.11: Exemplar plots of the BMS displaced by 3 cm: (a) shifted binary mask, (b) the corresponding decoded image, (c) a 3D plot of the decoded image and finally (d) a horizontal profile through the decoded image. This demonstrates the intrinsic imaging properties of the MURA mask.

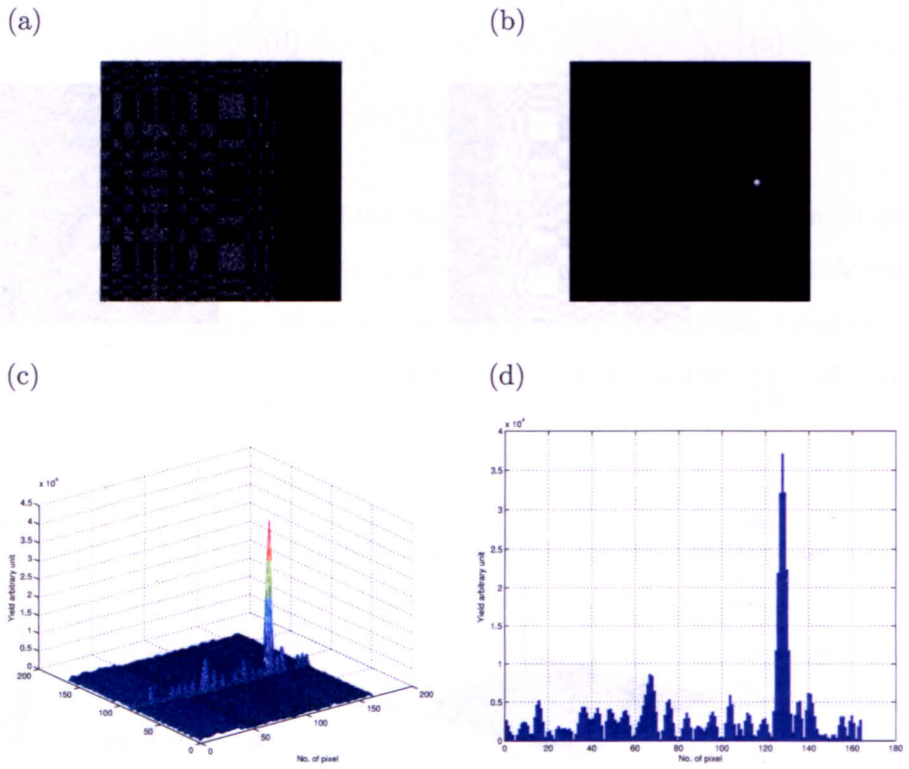

Figure 5.12: Exemplar plots of the response function from BMS displaced by 3 cm, that shown in Fig. 5.11, after adding spatial blurring: (a) shifted mask, (b) the corresponding decoded image, (c) a 3D plot of the decoded image and finally (d) a horizontal profile through the decoded image.

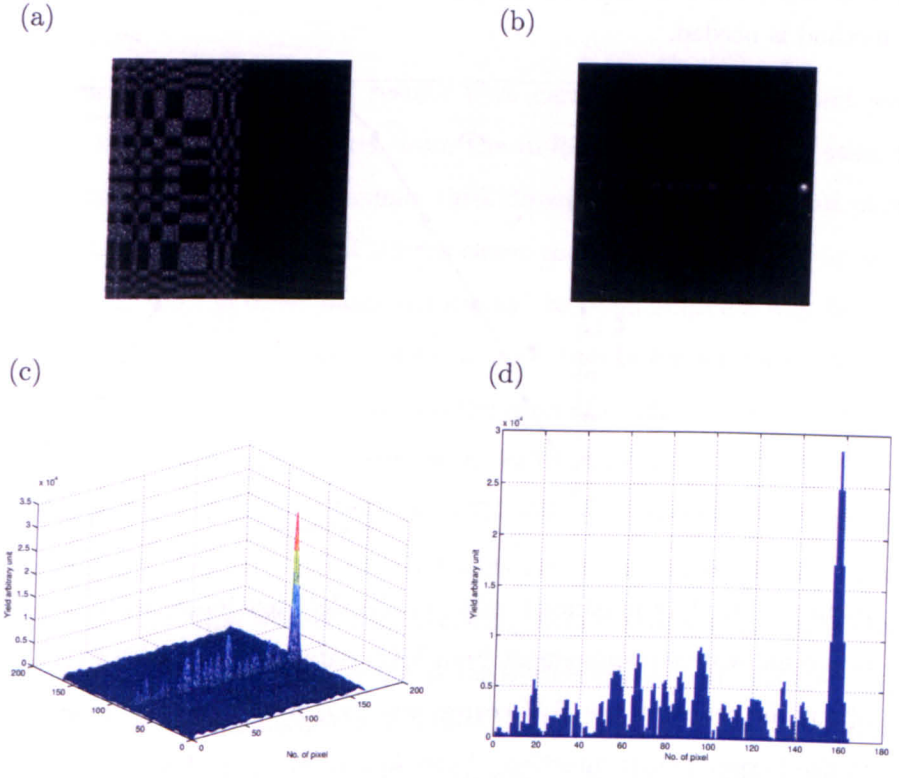

Figure 5.13: Exemplar plots of the response from a BMS displaced by 5 cm: (a) binary mask shift, (b) the corresponding decoded image, (c) a 3D plot of the decoded image and (d) a horizontal profile through the decoded image.

binary mask displacement produces a striking similar results to the MCS results shown in Figs.5.7 and 5.8. This suggests that the form of artefacts, in term of the shape and the magnitude of the side-lobes, arising from such imaging geometry can be predicted. The slight discrepancies in the BMS results compared to the simulated data is expected because in the BMS method there was no incident angle variation included i.e. solid angle effects were considered constant for all mask positions. To implement the variations in the angle of incidence for γ-rays at all mask locations and displacements, then the PRT method is needed.

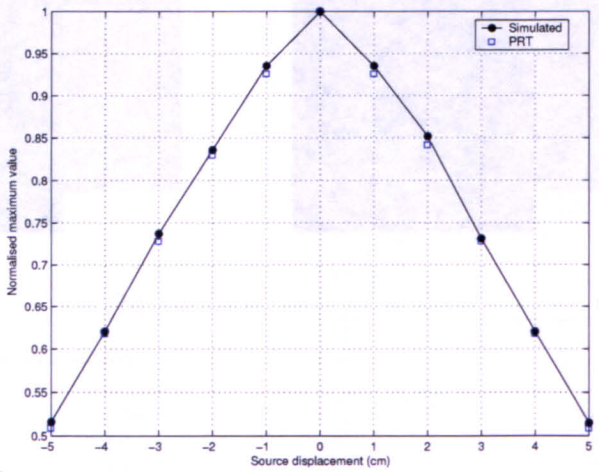

Figure 5.14: The maximum value of the decoded image as a function of an off cental axis point source displacement from MCS data compared with PRT. The horizontal shifts about the centre of the FoV correspond to a 10×10 cm^2 FoV. Similar effect can be seen in the perpendicular direction. There is a good agreement between the two methods.

Imaging a point source of similar configuration geometry to that shown in Fig. 5.3 but with an infinitely thin mask, using the PRT method has found to be almost identical to the MCS data of the same geometry. The shape and the magnitude of the small cross-shaped side-lobe artefact in the decoded image is observed clearly in both methods. Displacing the point source along the horizontal direction using the PRT method was compared with that obtained from the MCS data and the results are given in Fig. 5.14. The PRT displacements results produce almost identical results to the MCS data. A similar effect was seen in the perpendicular direction. The slight discrepancies between the MCS data and PRT is believed to involve some issues such as mask penetration and the finite mask

thickness that have not been consider in the PRT method.

(d) Out of Focus Source Displacement

The correlation of the projected image of a point source in air (on-central axis) and the postprocessing array G produces a delta function with a d.c. bias but no significant side-lobes for a point source in the desired decoding plane. However, this theoretically only holds true for a fixed source:CA distance, although this may be considered to be at infinity for large distances.

In contrast, a number of MCS results were carried out using a point source that is displaced, along the principal axis, from the in-focus plane. In each case, the point source is displaced by a 1 cm step, axially (in Z direction) from the in-focus plane of that shown in Fig.5.3. Moving the point source closer to the mask produces an increases in the magnification. On the other hand, displacing the point source a way from the mask reduces the magnification. Exemplar plots of these results are shown in the subsequent figures (5.15-5.20). The decoded images and the form of artefacts arising from the out-of-focus source displacement were compared with the in-focus plane of Fig.5.4.

The source displacement, obviously, reduces or enlarge the image magnification coefficient sm_c, and produces large complex artefacts structures. However, for these experiments, the same G function was used for decoding throughout, which represented a fixed magnification of 4 in order to observe the point source response at unknown depth, and using a simple central-plane decoding approach. Therefore, in these simulation experiments the influence of out-of-plane (axially displaced point source) activity in a near-field geometry was observed. It can be seen clearly that at a 1 cm source displacement, there is a clear point-source signature, with evidence of increased side-lobe artefact. However, at 2 cm displacement, this artefact approaches the magnitude of the original out-of-plane point source signature. In addition, the observed PSF width of the original out-of-plane source naturally increase/decreases according to the effective magnification coefficient, m_c, produced by its displacement.

The above results (5.15-5.20) demonstrate the severity of the out-of-focus artefacts. These demonstrate that different forms of highly distorted images are produce in each case. This out-of-focus confirms what was suggested by Barrett and Swindell [66]: that the off-focus planes produce non-uniform complex blurred background. Figure 5.21 graphically

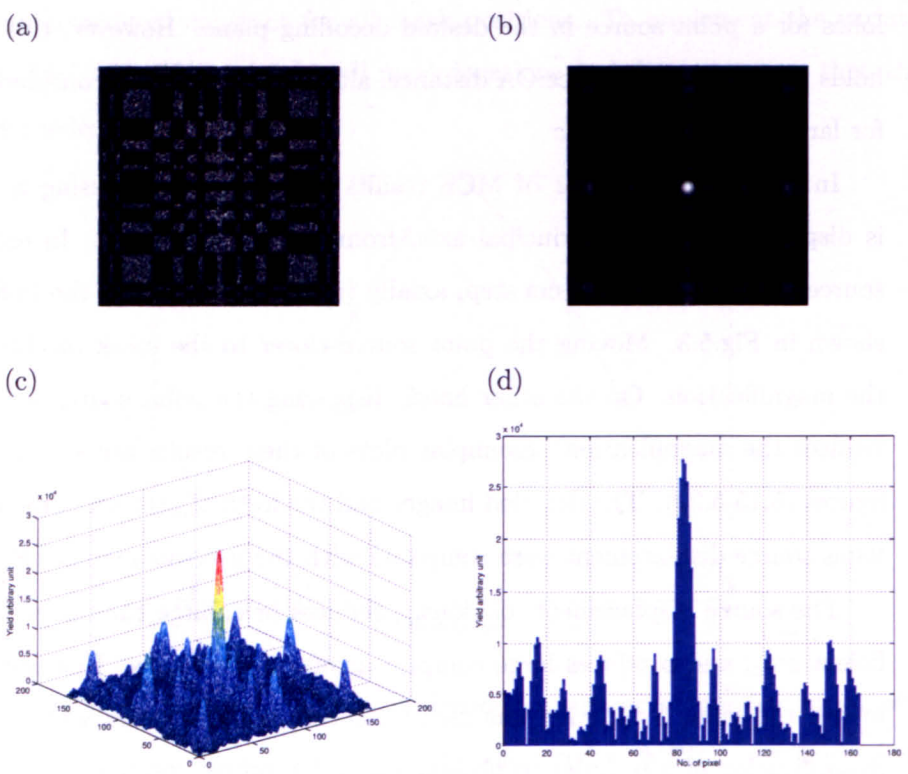

Figure 5.15: The MCS of system response from a point source displaced by 1 cm toward the mask: (a) the projected image which looks superficially similar to the usual CA pattern. There is, in fact, a loss of pattern around the perimeter due to the increased magnification. (b) the decoded image which has some unwanted artefacts due to imperfect correlation, (c) a 3D plot of the decoded image, and (d) a vertical profile through the centre of the decoded image, showing these effects in more details.

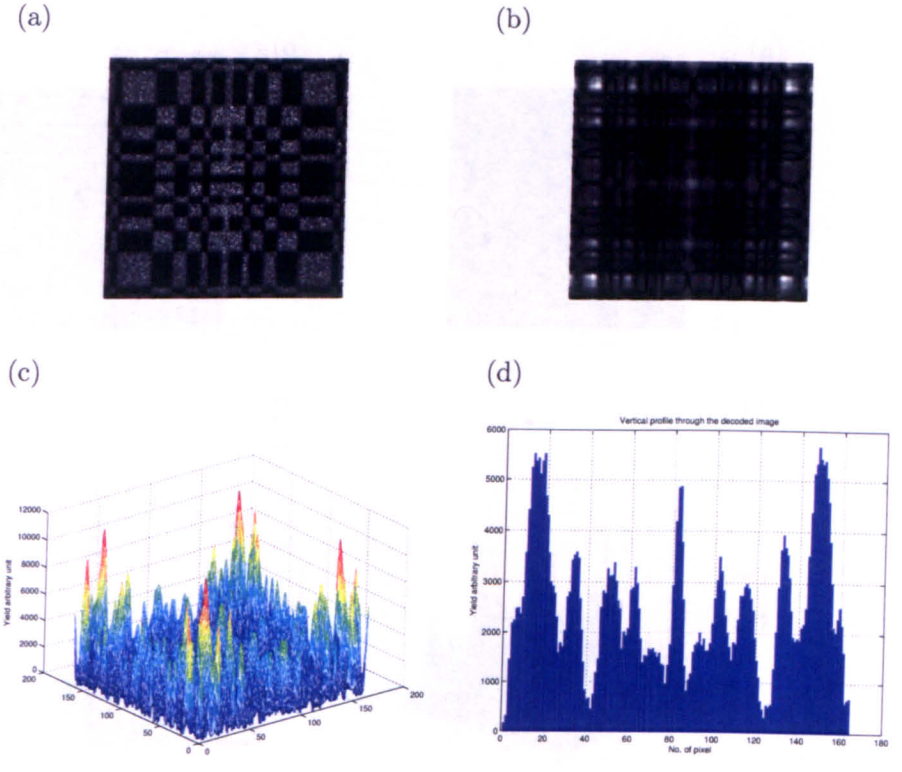

Figure 5.16: The MCS of system response from a point source displaced by 2 cm, from the in-focus, toward the mask with m_c=4.75: (a) the projected image exhibiting further loss of the mask pattern, (b) the decoded image, (c) a 3D plot of the decoded image, and (d) a vertical profile through the centre of the decoded image. This shows further deterioration in the image. However, it is worth noting the scale: in this case the artefacts are of similar or smaller magnitude compared to those seen in Fig. 5.15.

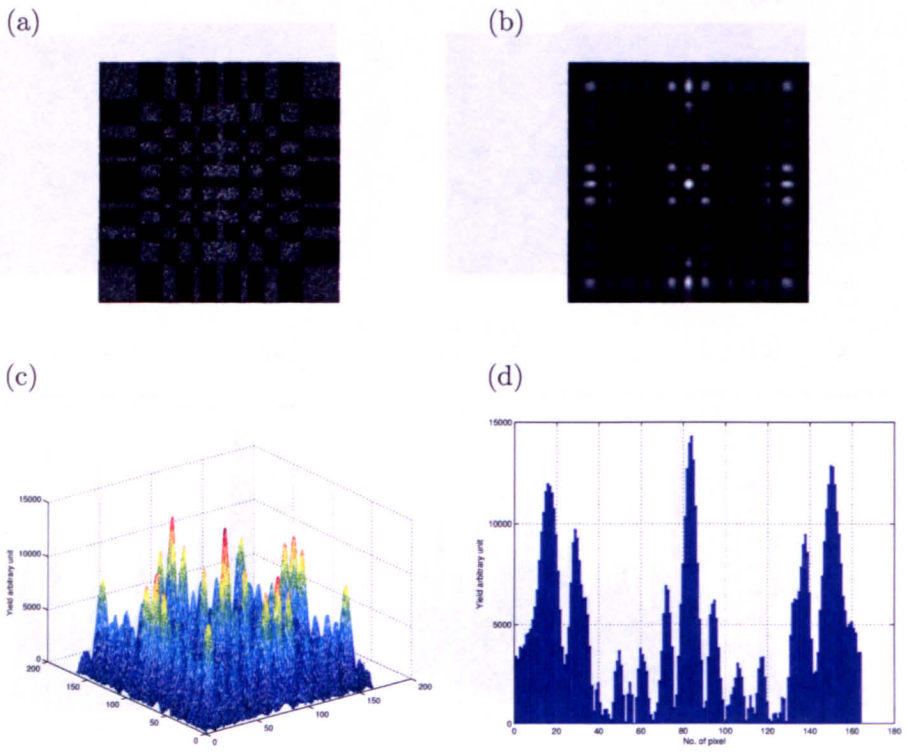

Figure 5.17: The MCS of system response from a point source displaced by 3 cm, from the in-focus, toward the mask with m_c=5.29: (a) the projected image, (b) the decoded image, (c) a 3D plot of the decoded image, and (d) a vertical profile through the centre of the decoded image. The peak magnitude of the artefacts here is about half the peak response seen in Fig. 5.15

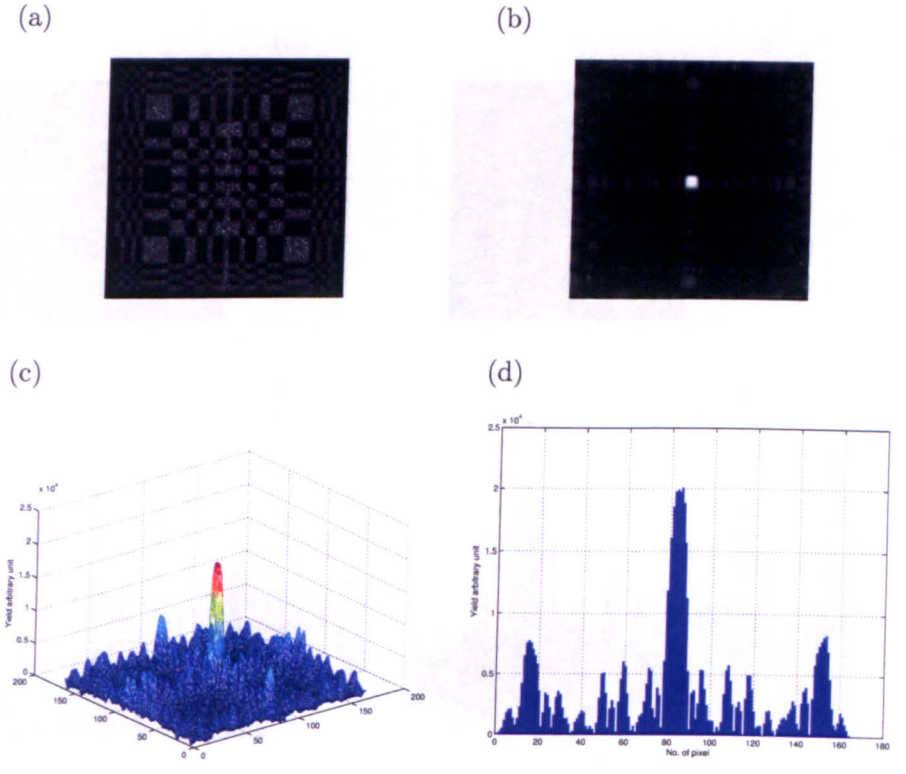

Figure 5.18: The MCS of system response from a point source displaced by 1 cm, from the in-focus, away from the mask with m_c=3.73: (a) the projected image, (b) the decoded image, (c) a 3D plot of the decoded image, and (d) a vertical profile through the centre of the decoded image. In this case a border can be seen around (a) corresponding to loss of magnification. This is imperfect correlation also enhances the cross-shaped side-lobes seen as a consequence of near-field imaging.

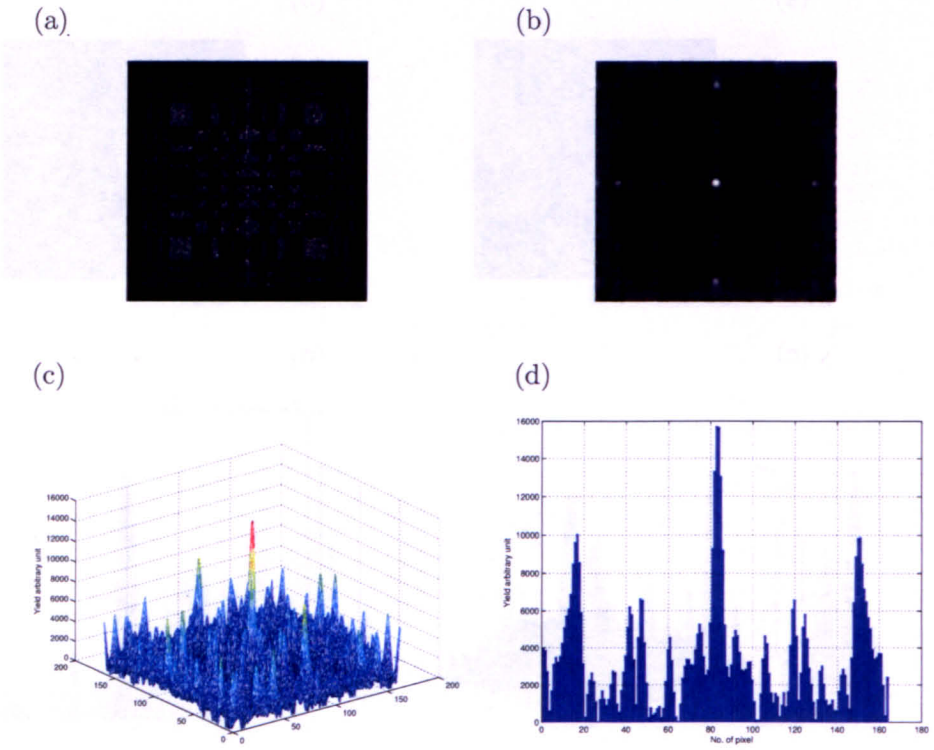

Figure 5.19: The MCS of system response from a point source displaced by 2 cm, from the in-focus, away from the mask with m_c=3.50: (a) the projected image, (b) the decoded image, (c) a 3-D plot of the decoded image, and (d) a vertical profile through the centre of the decoded image. Similar effects as for Fig. 5.18 are observed except that further "false peak" artefacts are also seen.

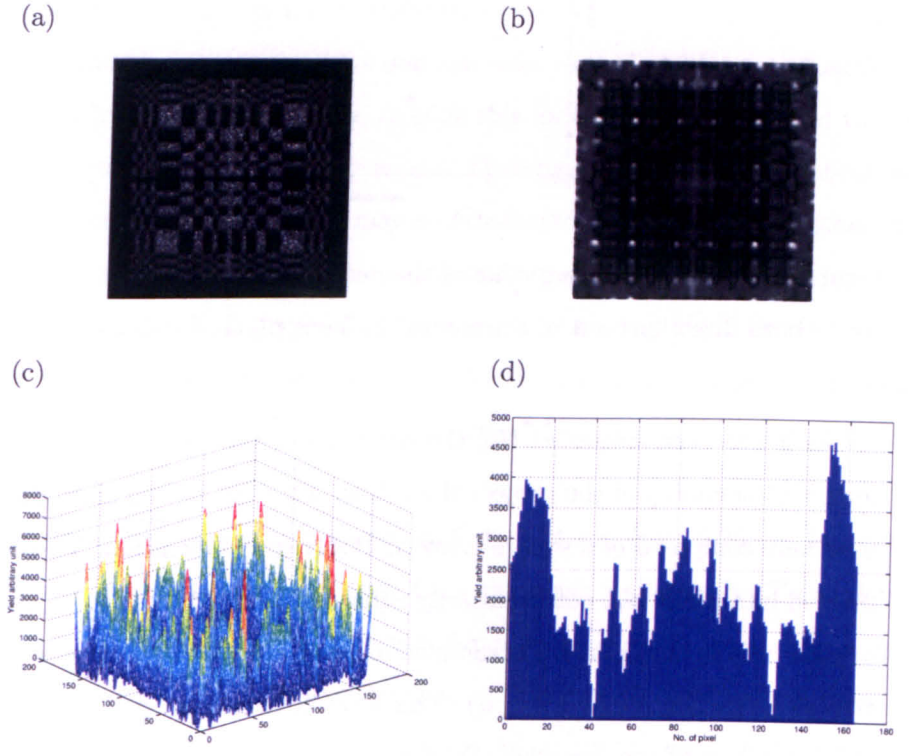

Figure 5.20: The MCS of system response from a point source displaced by 3 cm, from the in-focus, away from the mask with m_c=3.30: (a) the projected image, (b) the decoded image, (c) a 3D plot of the decoded image, and (d) a vertical profile through the centre of the decoded image. In this case the peak response from the point source is now lost in the broader artefacts. However, the magnitude of the artefact. However, the magnitude of the artefacts smaller than the peak response from the point source.

express this depth dependent effect.

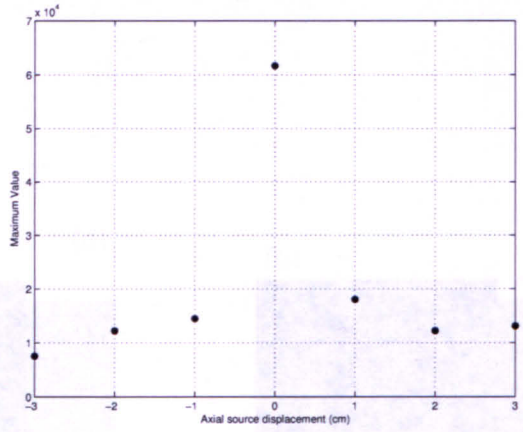

Figure 5.21: The maximum value of the decoded image as a function of the axial shift in cm in both directions out of the central in-focus plane.

As it has been suggested [70] the out-of-focus artefacts are believed to be due to the imperfect sampling of the projected shadow. This can be explained considering the mask used here composed of a square array of 41×41 (p×q) elements. The detector is similarly divided into pixels but not necessarily equal to the size of the mask pixels. The projection of each hole in the aperture is sampled as an $\alpha \times \alpha$ set of the square pixels depending on the magnification coefficient (m_c). This leads to an important equation that relates m_c to the projection of the mask-hole [110] as:

$$\alpha = \frac{m_c p_m}{p_d} \tag{5.4}$$

where p_m is mask element size and p_d is the size of the detector pixel. The above equation suggests that if α is integer then the projection of a point source covers exactly a square of $\alpha \times \alpha$ pixels. This will then provides a perfect reconstructed image. This only exists for a specific position of the point source in the object and in practice this not the case. Thus, in the case the mask projection not matching the detector pixel i.e. α is having non-integer value then the constructed image is affected and the undesirable artefacts appear in the image. The severity of the artefacts increases as the matching of the projection and the detector pixel decreases.

To investigate the effect of non-integer values of α in the decoded image, BMS method was used. This method was used to eliminate the near-field and the statistical noise effect.

The decoded image of a point source projected for different value of α ranging from 3.9-4.2 was simulated. Figure 5.22 and Fig. 5.23 demonstrate that the intrinsic response function image of a MURA mask of 41×41 pattern is seriously affected by the small difference in the α value. It is worth noting that in all these different data the decoding was performed in the same depth. Thus, focusing the CA camera properly and decoding at the right depth minimises these out-of-focus artefacts.

From all the above investigations one can infer that all sources at a particular depth are decoded correctly, but all others, outside this focal plane, are not, and therefore may contribute artefacts to the focal plane image. This suggests that for SM applications, where point-like objects are anticipated, it may be possible to apply a set of scaled decoding steps to seek out limited depth information as one can expect to see the highest intensity at the correctly decoded depth, dependent on the noise in the actual data. Attempts were made to decode the above results (i.e. Figs. 5.15-5.20), of a point source at different depths, in the right focal plane by applying a set of scaled decoding steps to seek out the correct plane.

The resulting decoded images shown in Fig. 5.24 and Fig. 5.25 are for only a point source moved by 3 cm toward and away from the mask respectively. These demonstrate that it is possible to recover the response function of a single point source located at different depth. Note, the presence of artefacts in these decoded images particularly in Figs. 5.24. This is because the point source has been moved closer to the mask and thus, the magnification coefficient, m_c, is greater than 5. Thus, in these particular geometries and due to the limited size of the imaging detector parts of the projected shadowgram of the mask are missing. This is believed to be the main cause of such imaging artefacts. From these investigations one can infers that the ideal geometry when imaging a thick object is to ensure that the maximum magnification coefficient at the front face of the object.

(e) Depth of Focus

From the above discussion one can see that the postprocessing array (G function) must be scaled so that it match the dimensions of the projected image. This is necessary to produce a perfect reconstructed image as imperfect matching distorts the resulting response function image. The aim of this section is to investigate the performance of the intrinsic response function image of a point source in air as a function of depth i.e. to

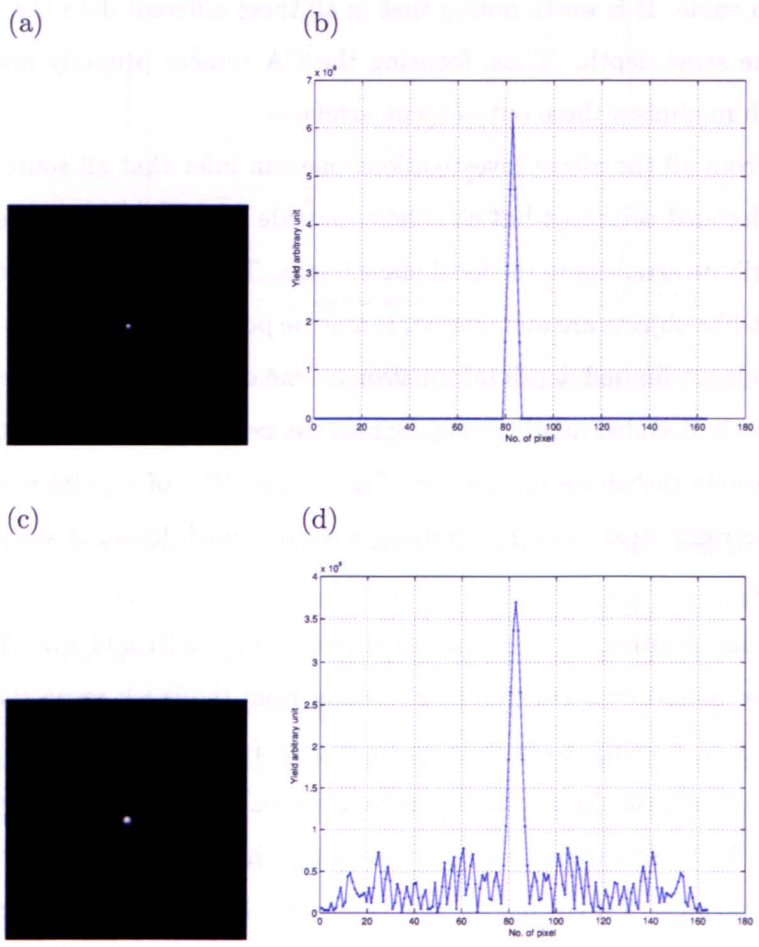

Figure 5.22: The effect of non-integer value of α on the PSF of a point source projected using BMS: (a) the decoded image for α=4 showing the ideal case of PSF, (b) a profile through the centre of such decoded image, (c) the decoded image for α=3.9, (d) and a vertical profile through the centre of the decoded image. This demonstrate that small change in α is responsible for the loss in the peak value of (b) by $\approx$ 42%. Note that the mean side-lobe is $\approx 0.5\times10^8$.

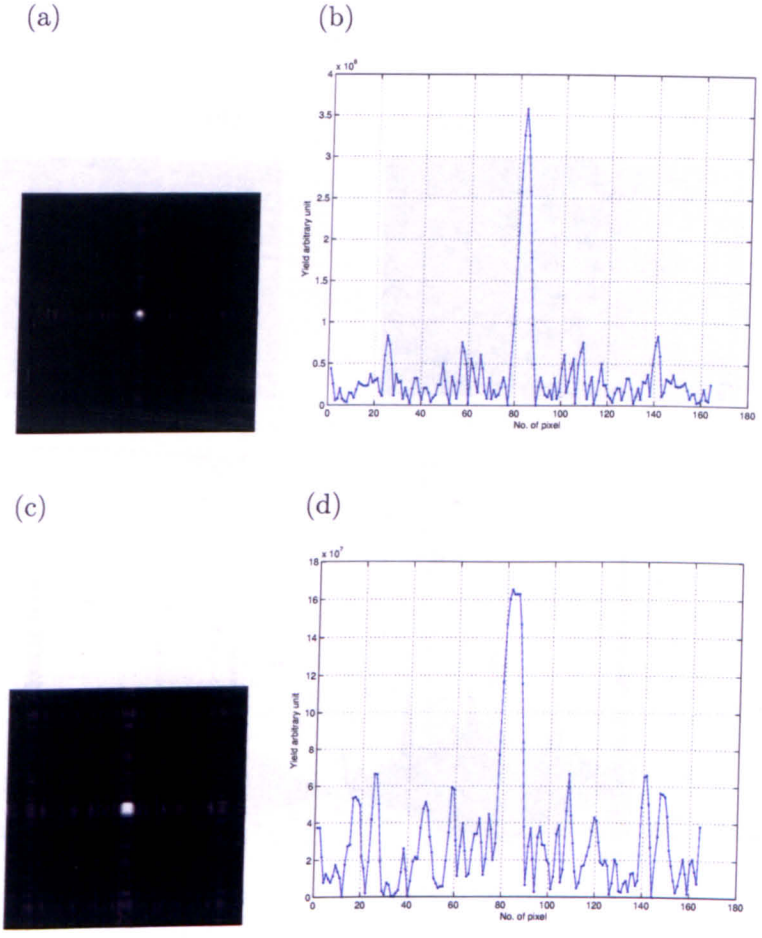

Figure 5.23: The effect of non-integer value of α on the response function of a point source projected using BMS: (a) the decoded image for α=4.1, (b) a profile through the centre of such decoded image showing that the small change in α is responsible for the loss in the peak value by $\approx$ 43% compared with Fig. 5.22 (b) and the mean side-lobe is 0.5×10^8., (c) the decoded image for α=4.2 and, (d) a profile through the centre of such decoded image. Similarly the loss in the peak value is $\approx$75%. The mean side-lobe is $\approx 0.5\times10^8$.

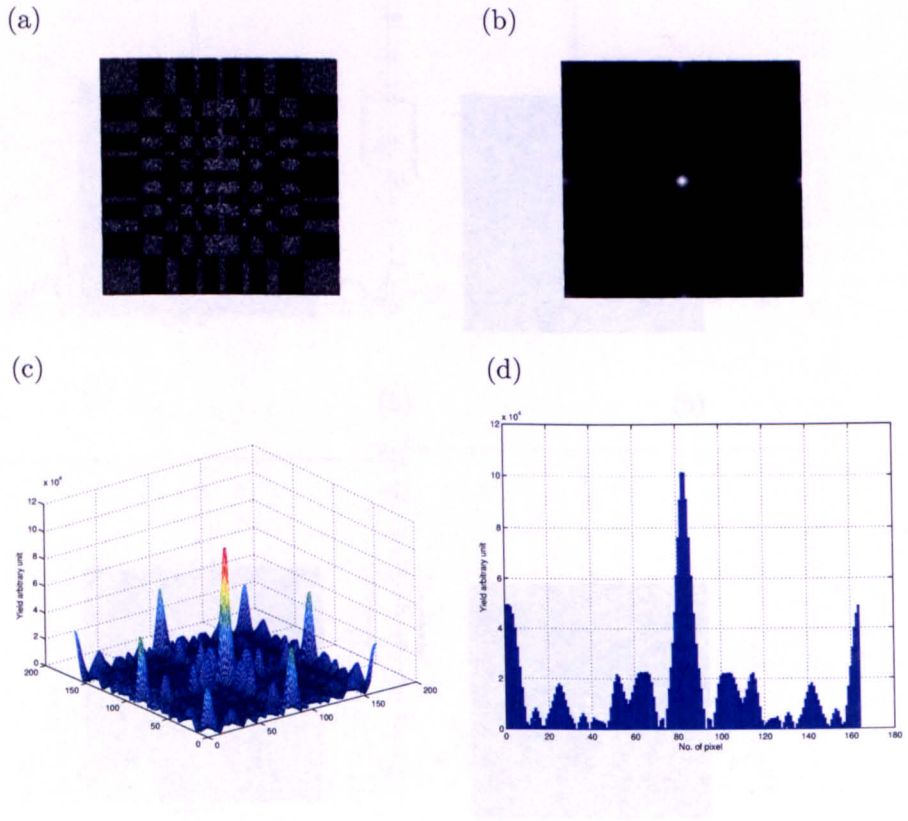

Figure 5.24: The MCS of system response of a point source displaced by 3 cm, from the in-focus, toward the mask with m_c=5.29: (a) the projected image results from decoding (a) with the equivalent scaled G function, (b) the decoded image, (c) a 3D plot of the decoded image, and (d) a vertical profile through (b). This should be compared with Fig. 5.17

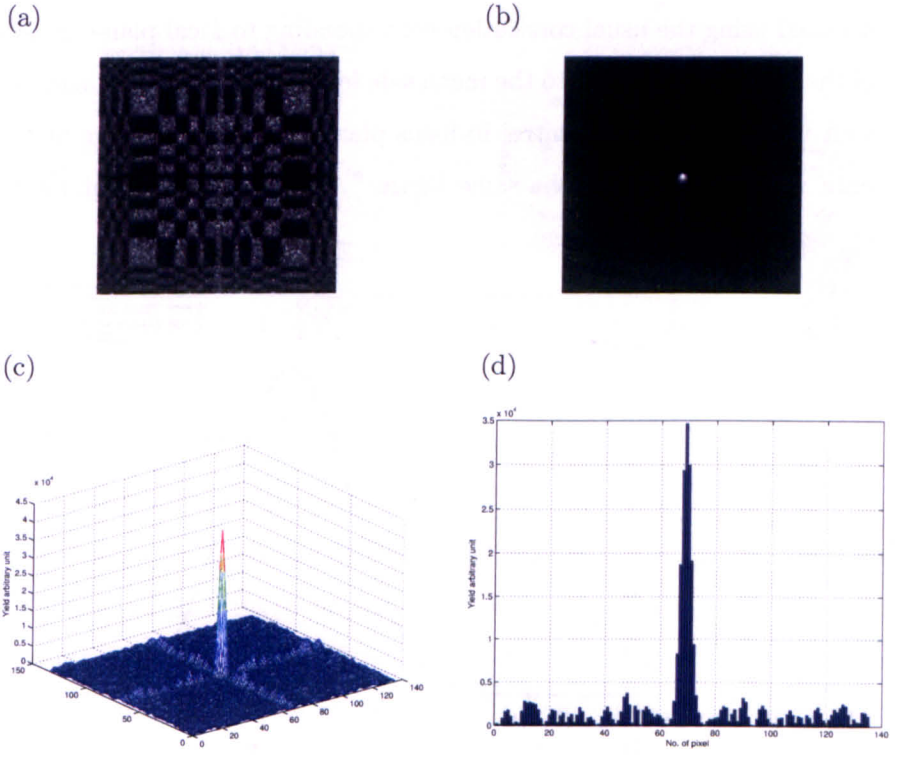

Figure 5.25: The MCS of system response of a point source displaced by 3 cm, from the in-focus, away from the mask with m_c=3.30: (a) the projected image, (b) the decoded image results from decoding (a) with the equivalent scaled G function, (c) a 3D plot of the decoded image, and (d) a vertical profile through the centre of (b). This plot should be compared with Fig. 5.20

measure the depth of focus. The depth of focus is usually defined as the Full-Width-Half-Maximum of the PSF measured at different depth. A set of MCS experiments imaging an idealised point source in air was first carried out using the geometry depicted in Fig.5.3. Then in each simulation the point source was displaced by 1 mm (in the Z directions of Fig.5.3) step from the in-focus plane. This mean that the projection is changing due to the changes in the object-to-detector distance. Note that in each case the projected image is decoded using the usual correlation corresponding to focal plane. Figure 5.26 show a plot of the ratio of peak value to the mean side lobe of all decoded images as a function of axial shift in mm, about the central in-focus plane. A Gaussian curve fit to the demonstrated data was also shown in the same figure. A small displacement form the focal plane is enough to distort the image.

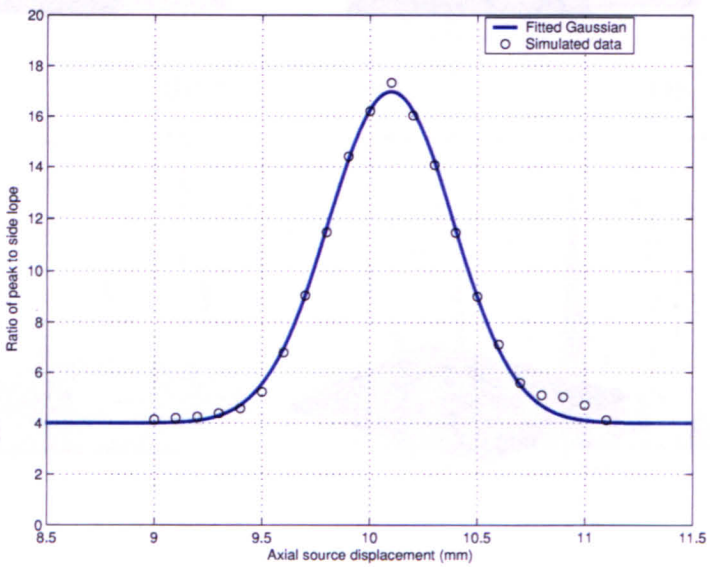

Figure 5.26: Plots of the depth of focus: the ratio of peak to the mean side lobe of the decoded image as a function of axial shift in mm, about the central in-focus plane with Gaussian fit. The FWHM=0.6826 cm and this represent half of the in focus point source.

5.2.2 Multi-source & Multi-depth Decoding

Having considered the effects of a single point source at different depths, in the next set of MCS the effects of >2 sources at different depths is investigated. In each case 10^8 photon histories were simulated.

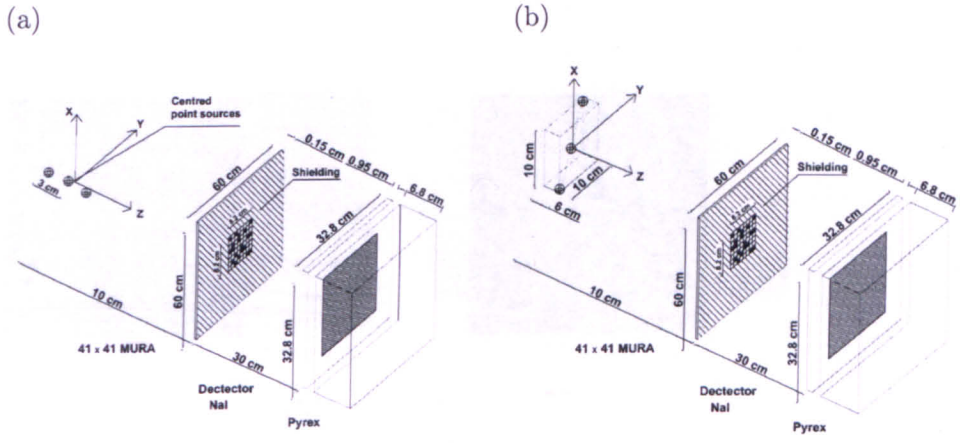

Figure 5.27: Schematic diagram of the simulated geometry: (a) 3 point sources in air with the central source at the focal plane and the other two sources separated by 3 cm in front of and behind the middle source, (b) 3 point sources in air at different depths separated diagonally by X cm. The parallelepiped of $10\times10\times6$ cm^3 test volume was drawn to clearly identify the locations of the point sources.

(a) Imaging On Axis Point Sources Located at Multi-depth

First three point sources in air were placed along the principle axis with the central source at the focal plane and the other two (out-of-focus) sources separated by 3 cm in front of and behind the middle source as shown in Fig. 5.27 (a). The aim was to observe the potential artefacts from each source and to see whether the use of a set of scaled decoding steps are able to successfully construct all these sources. Initially the projected image was decoded in the central plane and the results are shown in Fig.5.28 demonstrating a slight side-lobe corruption from the other two planes in the projected image. However, the image is dominated by the central target source.

To recover the other two sources one needs to know the plane (depth) of the target

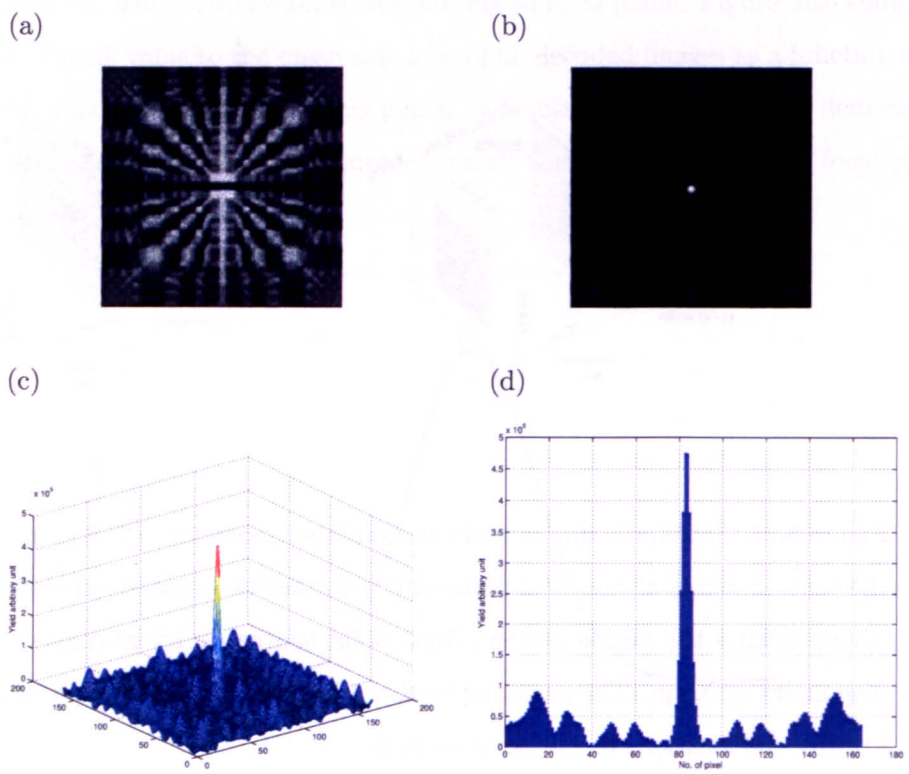

Figure 5.28: Exemplar plot of 3 point sources in air at different depths separated by 3 cm: (a) the projected image, (b) the decoded image of the central plane, (c) a 3D plot of the decoded image, (d) a vertical profile through the centre of the decoded image.

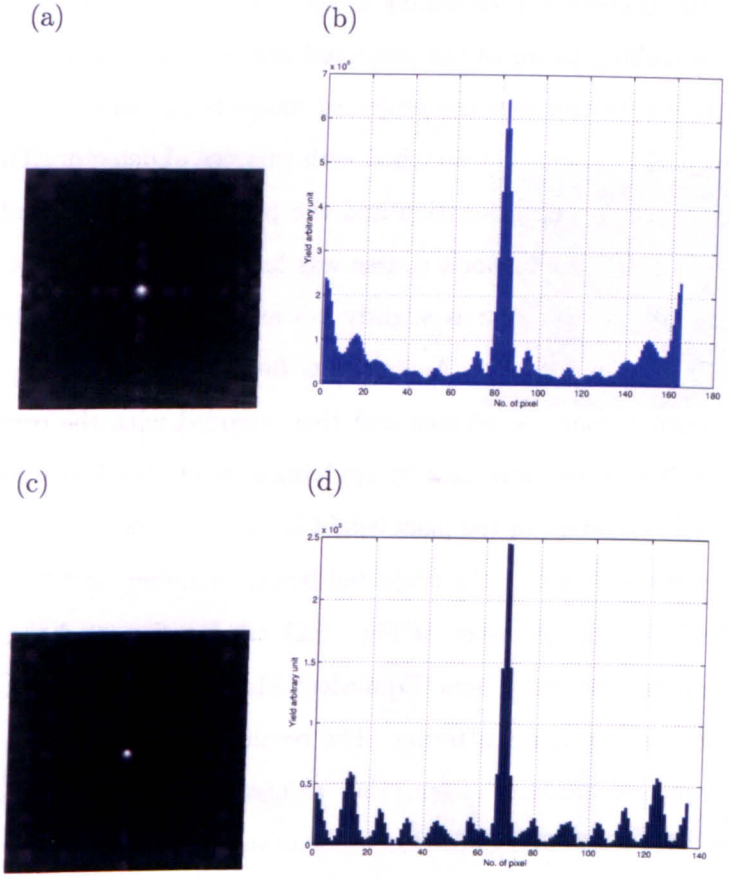

Figure 5.29: The MCS of system response using scaled decoding steps to recover the other two point sources of Fig. 5.28: (a) the decoded image of the first source, note that the point source is magnified by ≈4.3 (b) a diagonal profile taken from the upper right corner through the centre of the decoded image, (c) the decoded image of the second point source with magnified by ≈2.3, (d) a diagonal profile taken from the upper right corner through the centre of the decoded image.

object. If no *a priori* information is available then from the geometrical set-up all the distances between the mask and the detector and the mask and the the front face of the imaged object should be considered. In this particular example (Fig.5.28) and for the first point source that has been placed closer to mask, the projected mask pattern provides a magnification coefficient or scaling factor >5. Then the decoding function, G, scaled by the same scalling factor of the projected image. Since the imaging detector is of known size 164×164, in this case the projected image is correlated with only the central part of the scaled G function that matched with this size of detector. This is necessary to ensure that both the decoding function and the projected image are of the same size. On the other hand, the second point source was located at the farthest distance from the mask so that the scaling factor is slightly >3 and thus, the projected image is now smaller than the imaging detector. Again the G function has to be similarly scaled. In this case the projected image is selected and then decoded with the correctly scaled G function. Figure 5.29 demonstrates that by applying a set of scaled decoding both point sources are recovered. Variation in the peak height between sources can be compensated by applying zero order correction to the projected before decoding (see chapter 7).

Similarly, the geometry of Fig. 5.27 (a) was repeated, but in this case using cold (i.e. non-radioactive) Tissue Equivalent Material (TEM) to introduce the effect of photons attenuation and scattering. The result is shown in Fig. 5.30 demonstrates a slight appearance of "leakage" from other planes. The slight difference between Fig.5.28 and Fig. 5.30 is attributed to photon attenuation and scattering. Attempts were also made to recover the other two point sources using a set of scaled decoding steps and the result is presented in Fig. 5.31.

(b) Imaging Off Axis Point Sources Located at Multi-depth

The following set of MCS investigations combine the effect of both off-central axis and multi-depths point sources decoding. Thus, the response function from these investigations is the product of the off-central axis and the out-of-focus effect that has been separately demonstrated in the previous experiments. The aim was to demonstrate the system's ability in resolving these sources as well as to demonstrate the effect of multiplexing on the projected images. Four MCS experiments of point sources in air at different depths have been undertaken with sources placed along the major diagonal. All have the same

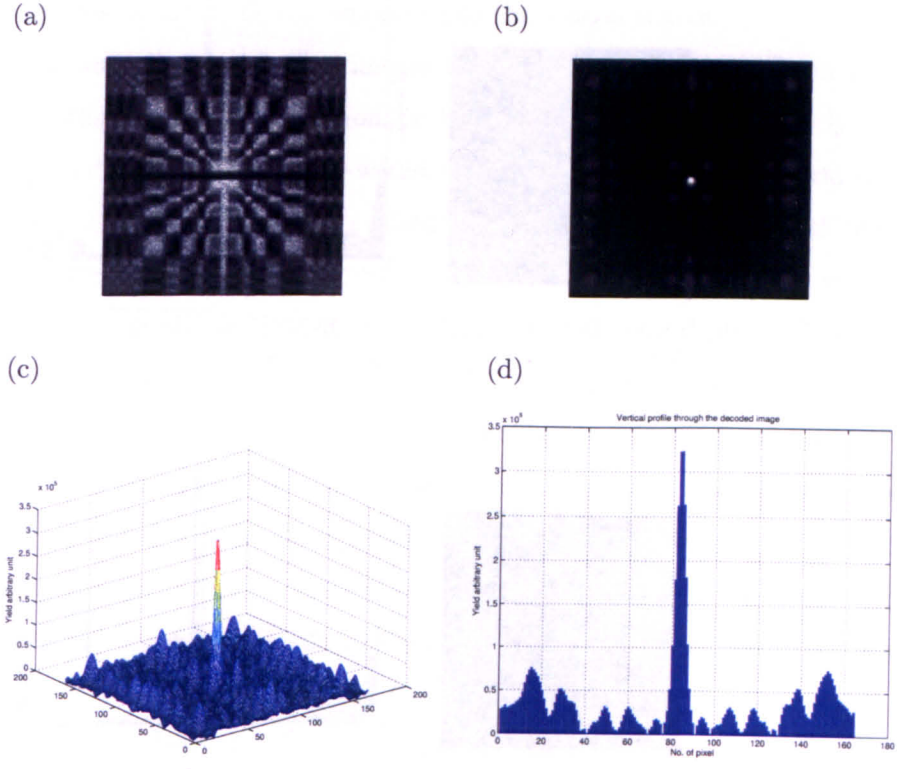

Figure 5.30: Exemplar plot of 3 point sources in TEM at different depths separated by 3 cm: (a) the projected image, (b) the decoded image of the central plane, (c) a 3-D plot of the decoded image, (d) a vertical profile through the centre of the decoded image. This demonstrates similar behavior to Fig.5.28, except that the peak has been attenuated

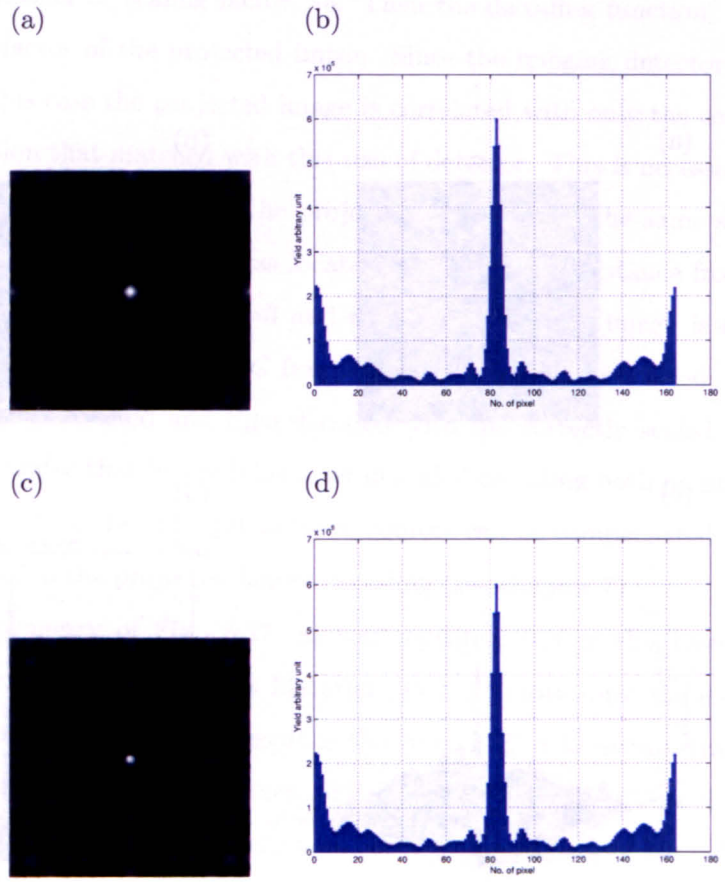

Figure 5.31: The MCS of system response using scaled decoding steps to recover the other two point sources in TEM of Fig. 5.30: (a) the decoded image of the first or front-most source, note that the point source is magnified by ≈4.3 (b) a diagonal profile taken from the upper right corner through the centre of the decoded image, (c) the decoded image of the second point source with magnified by ≈2.3, (d) a diagonal profile taken from the upper right corner of the decoded image through the centre.

experimental set-up as demonstrated in Fig. 5.27 (b) but with different numbers of point sources. It is worth noting that in each experiment the position of the central point source is the same placed on the central axis and giving an object magnification factor of 3. The point sources located closer to the mask provides higher object magnifications where as the point sources located further from the mask provides lower object magnifications. Initially, the projected images from these point sources were considered and then correlated with the post-processing array, G, corresponding to the central source.

The first and the second experiments are for only 3 point sources in air placed at different depths and separated diagonally by 7.68 and 1.22 cm respectively. In the first experiment and after decoding one would expect to see mainly the central point source as the two out-of-plane sources are placed at the far diagonal edges of the image as demonstrated in Fig. 5.32. In the second experiment the point sources were separated by 1.22 cm and initially correlated in the demonstrated central plane. The results from these experiments are presented in Fig. 5.33. These demonstrate the increased effect of artefactual leaks from other planes as the diagonally measured distance between two point sources decreases i.e. separation is less than 1 cm. Note also the initial indications of a non-uniform background associated with the multiple point sources in Fig.5.33. The slightly brighter patches seen in close to the edges of the image can be contrasted with the near uniform zero background seen in Fig.5.32. This effect is seen with greater clarity as the object moves from being point like to a distributed nature. A set of scaled decoding steps was used to recover the other two point sources is given in Fig. 5.34.

The third and the fourth experiments were for 5 (see Fig. 5.35) and 9 (see Fig. 5.36) point sources separated by 3.84 and 1.92 cm respectively. These distances were chosen to see the potential artefacts from such sources as well as to demonstrate the effect of multiplexing. More importantly to demonstrate whether the use of a set of scaled decoding steps is useful in resolving all the point sources separately. Initially, the two projected images shown in Fig. 5.35 (a) and Fig. 5.36 (a) were correlated in the demonstrated central plane in order to observe the effect of activity at out-off plane unknown depth. Figure 5.35 (d) demonstrates the locations of these 5 point sources with source number 1 being the closest to the mask and source number 5 is the farthest. Only two closest point sources to the focal plane can be clearly identified as a point sources. The other two point sources (1 and 5) were located at the two edges of the object FoV and thus, without

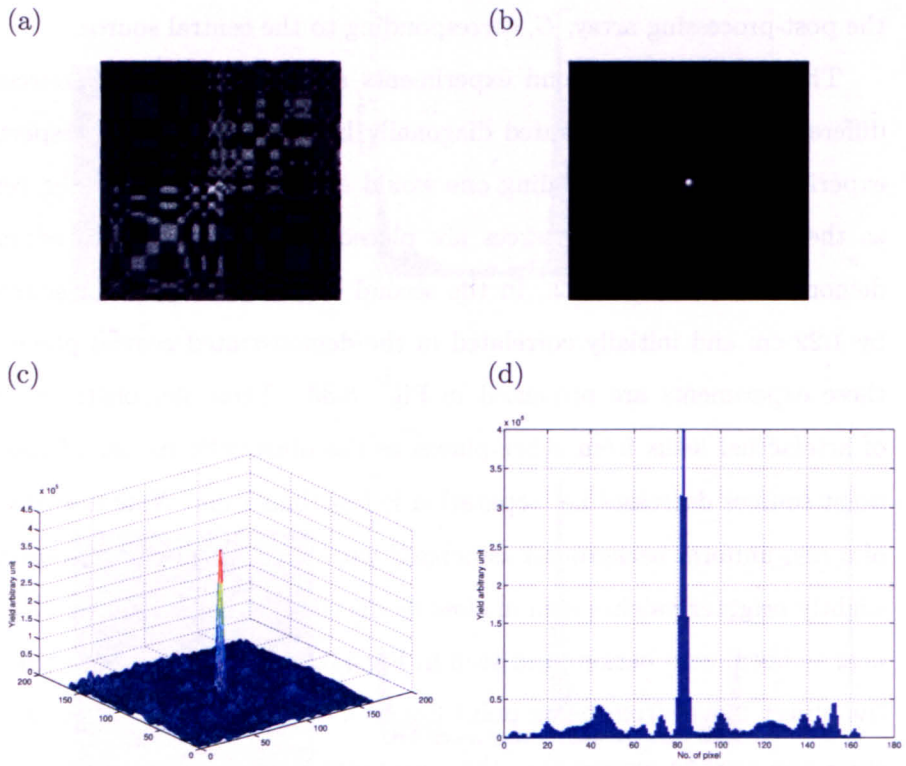

Figure 5.32: The MCS of system response for 3 point sources in air placed at different diagonal depths and separated by 7.68 cm: (a) the projected image, (b) the decoded image, (c) a 3D plot of the decoded image, (d) a diagonal profile taken from the top right corner of the decoded image.

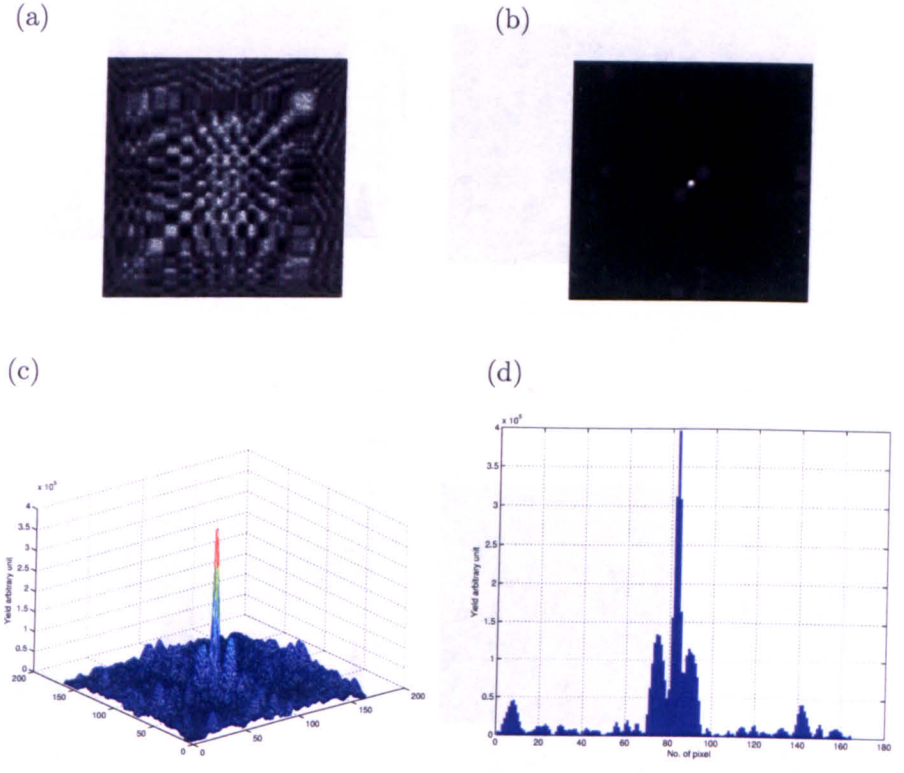

Figure 5.33: The MCS of system response for 3 point sources in air placed at different diagonal depths and separated by 1.22 cm: (a) the projected image demonstrating spill-over of depth dependent decoding into the central focal plane, (b) the decoded image, (c) a 3D plot of the decoded image, (d) a diagonal profile taken from the top right corner of the decoded image.

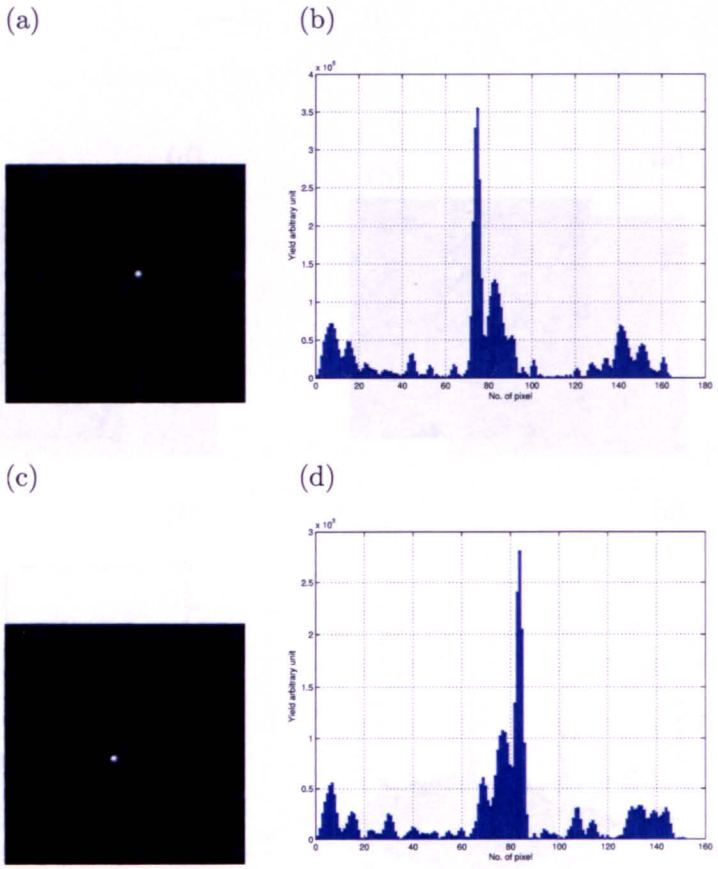

Figure 5.34: The MCS of system response using scaled decoding steps to recover the other two point sources of Fig. 5.33: (a) the decoded image of the first source, note that the point source is magnified by ≈3.3. This has been successfully recovered, but there is evidence of spill-over from the central plane, (b) a diagonal profile taken from the upper right corner through the centre of the decoded image, (c) the decoded image of the second point source with magnified by ≈2.7, (d) a diagonal profile taken from the upper right corner of the decoded image through the centre. Again a similar spill-over effect from the central plane can be seen.

prior knowledge were difficult to be identified from the side-lobes artefacts. This again show the drop-off in sensitivity with depth, although because of different magnification, this drop-off is not symmetrical about the focal plane.

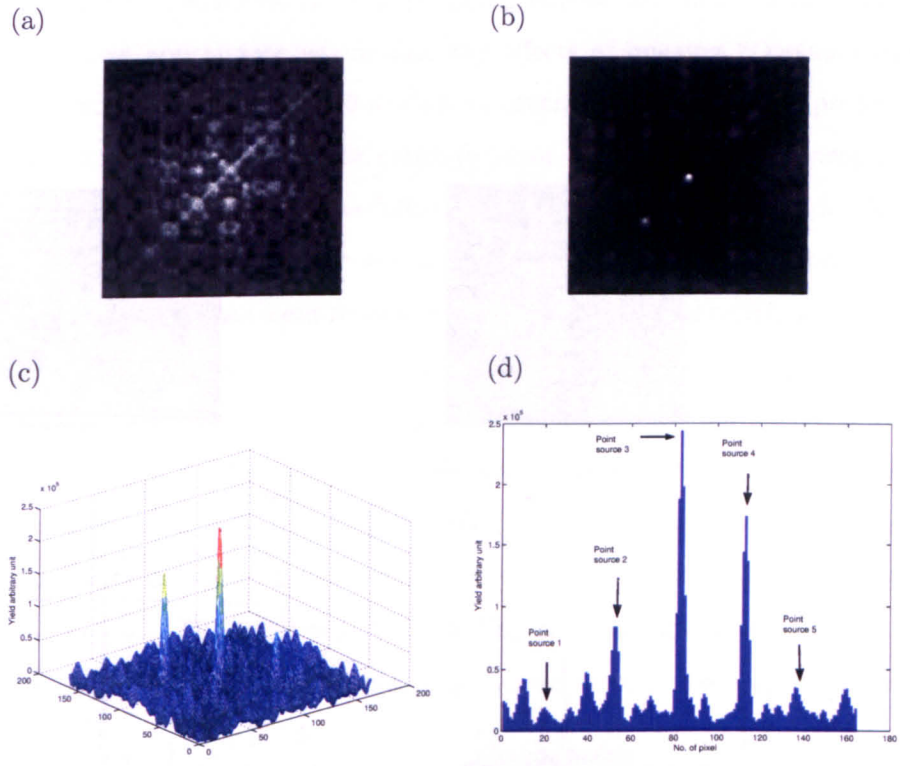

Figure 5.35: Exemplar of 5 point sources in air placed in the major at different axial depth separated diagonally by 3.84 cm: (a) the projected image, (b) the decoded image, (c) a 3D plot of the decoded image, and (d) a diagonal profile through the decoded image. Note that source 1 and 5 were identified through a set of scaled decoding steps.

A set of scaled decoding stages with a 1 mm step was used through the entire depth of the point sources. This is achieved through using the usual correlation method in order to recover the remaining two sources of Fig. 5.35 i.e. point sources number 1 and 5. This is because the other three central point sources can be easily identified with this step decoding. Figure 5.37 show that with a set of scaled decoding it is possible to separately recover both point sources but with significant artefacts. However, from these decoding steps one can infer that once the point sources exceeded 5 point and thus the depth spacing between these point sources are small it is difficult to successfully recover all the point

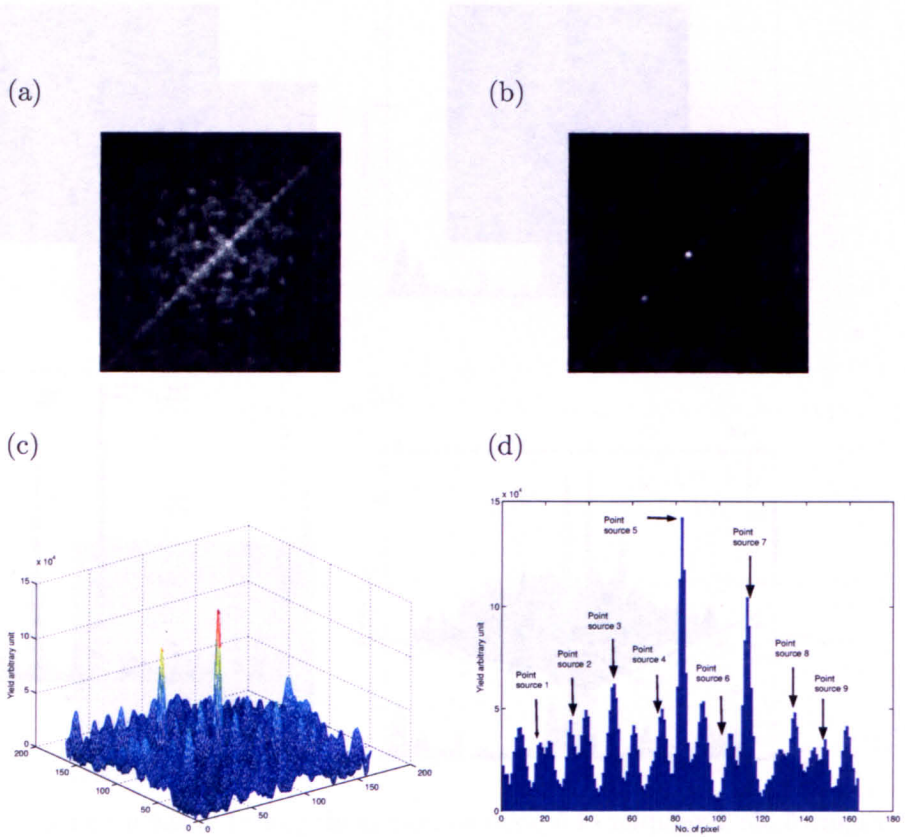

Figure 5.36: Exemplar plot of 9 point sources in air at different diagonal depth separated by 1.92 cm: (a) the projected image, (b) the decoded image, (c) a 3D plot of the decoded image, and (d) a diagonal profile through the decoded image. Note that planes at different depths contribute to artefacts in the decoded image (b).

sources.

5.2.3 Imaging a 2D Uniform Object

Having considered the geometric and decoding effects associated with multiple point sources, it is now appropriate to consider the effects of imaging 2D planar distributed source. The geometry seen in Fig. 5.3 of an on-central axis point source projects a shadowgram of the mask that covers the entire detector area. It is more appropriate to use a very large imaging detector in the following investigations but it was decided to limit the detector size to a more realistic size as may be found with a conventional γ-camera. The MCS experiments used here represent approximately planar (2D) square objects of 0.1 cm thickness and different sizes ranging from (1^2-12^2 cm^2) using the same mask camera configurations as demonstrated in Fig. 5.38. In each case approximately 10^9 photon histories were simulated. In these cases each point source of the object produces its own projected shadow of the CA. The coded image (2D distribution shadowgram) is the sum of each of these point source projections. Two exemplar planar object phantoms of size 1×1 cm^2 (see Fig. 5.39) and 5×5 cm^2 (see Fig. 5.40) are given here. In Fig. 5.41 the decoded images obtained from systematically increasing planar source are shown. Other exemplars of different object size are given in the next section.

The results from such investigations suggest that the distributed source artefacts appear very clearly for object larger than 1×1 cm (see Fig. 5.39). Due to the finite size of the detector different object sizes produce different artefact shapes (i.e. re-enforced with object size) in the reconstructed images. Thus, one tends to gradually lose the decoded objects completely as the artefact dominates the image for larger planar source distributions (see Fig. 5.41).

To initially investigate the background distortions, of a planar distributed object, appearing in the reconstructed image the BMS technique was used. This method produces a background distortion artefact that is due to the finite size of the object (off-axis sources) but ignoring other artefacts due to $\Omega(\vec{r_o}, \vec{r_i})$ term or variations in the incident γ-rays. Exemplar images of the predicted flat field distortion from the BMS method of a planar square source of 1 cm^2 and 5 cm^2 are given in Fig. 5.42 and Fig. 5.43 respectively. This shows that the intrinsic distributed nature of the source and the multiplexing that produces leads to a particular type of artefact that can be easily predicted. Although the

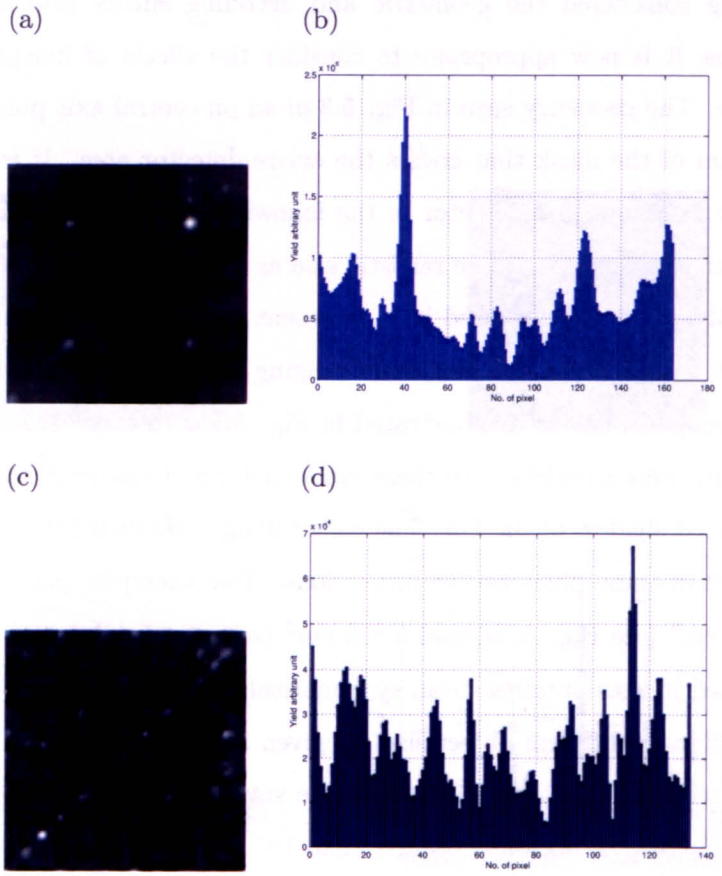

Figure 5.37: MCS of system response using scaled decoding steps to recover the other point sources of Fig. 5.35: (a) the decoded image of the first source, note that the point source is magnified by ≈4.2. The other 'ghost' sources also occur due to the imperfect decoding. (b) a diagonal profile taken from the upper right corner through the centre of the decoded image, (c) the decoded image of the fifth point source with magnified by ≈2.2, (d) a diagonal profile taken from the upper right corner of the decoded image through the centre.

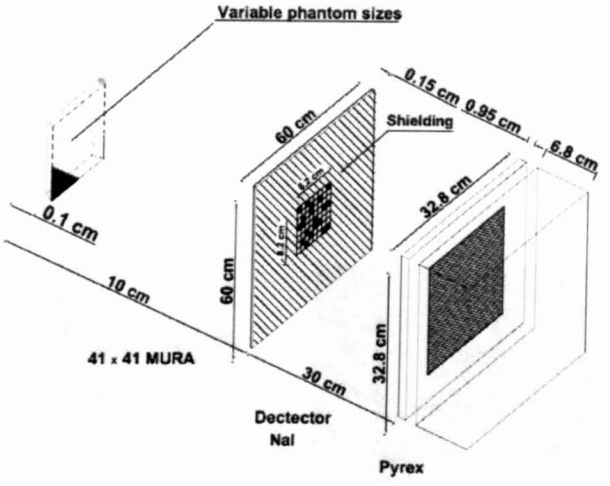

Figure 5.38: Schematic diagram of the flood field of variable phantom sizes showing the basic elements of the complete geometry simulated of thin phantom.

overall images and their corresponding surface plot from using the BMS method are similar to that produced from MCS, the BMS ignores solid angle effects. Therefore, to better reproduce and predict the shape of these artefacts, the PRT technique was employed, as this incorporate the solid angle effect that are particularly important in imaging with a near field geometry.

Thus, to consider the effects of all these geometrical artefacts, similar sized planar square objects were studied using the PRT method (see Fig. 5.44). The reconstructed image from such square source shown in Fig. 5.44 was compared to the corresponding from the BMS (see Fig. 5.42) and MCS data Fig. 5.39. Both methods successfully predicted the flat field background distortion artefacts of the uniform 2D object imaged. With the PRT and MCS methods the radiation intensity reaching the detector are not uniform (solid angle effect) and this causes a sensitivity dip toward the centre. Exemplar vertical profiles of predicted flat field distortion of 2D square source object of size 1×1 cm^2 and 3×3 cm^2 from PRT method compared with the corresponding produced from MCS data is shown in Fig. 5.45 (a) and (b) respectively. This show that the PRT method

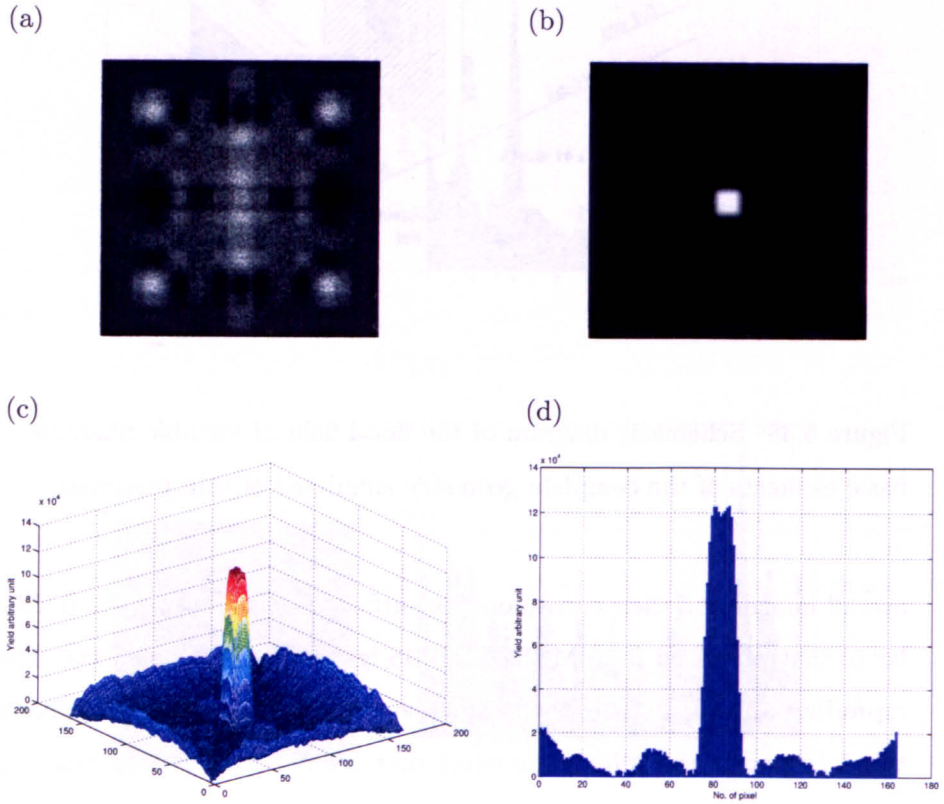

Figure 5.39: Exemplar plot of the MCS of a planar phantom of a $1 \times 1 \times 0.1$ cm^3: (a) the projected image, (b) the decoded image, (c) a 3D plot of the decoded image, this demonstrates the effect of the solid angle factor as it causes a sensitivity dip toward the centre, (d) a vertical profile taken through the centre of the decoded image.

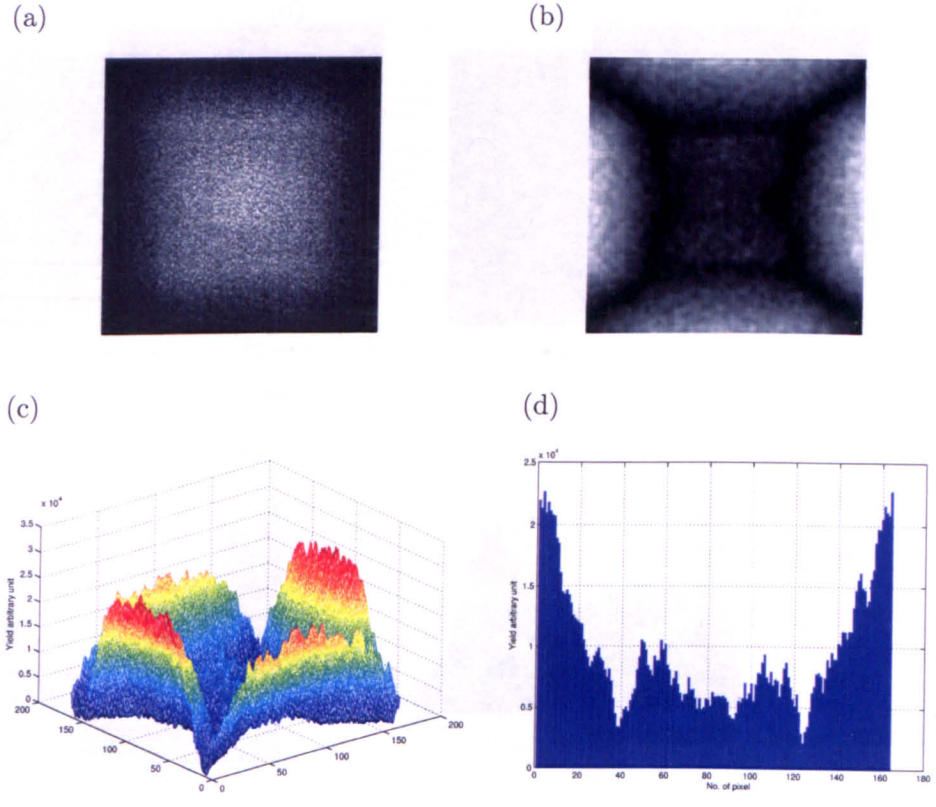

Figure 5.40: Exemplar plot of MCS of planar square source of 5×5×0.1 cm^3, (a) the projected image, (b) the decoded image, (c) a 3D plot of the decoded image, and (d) a vertical profile taken through the centre of the decoded image.

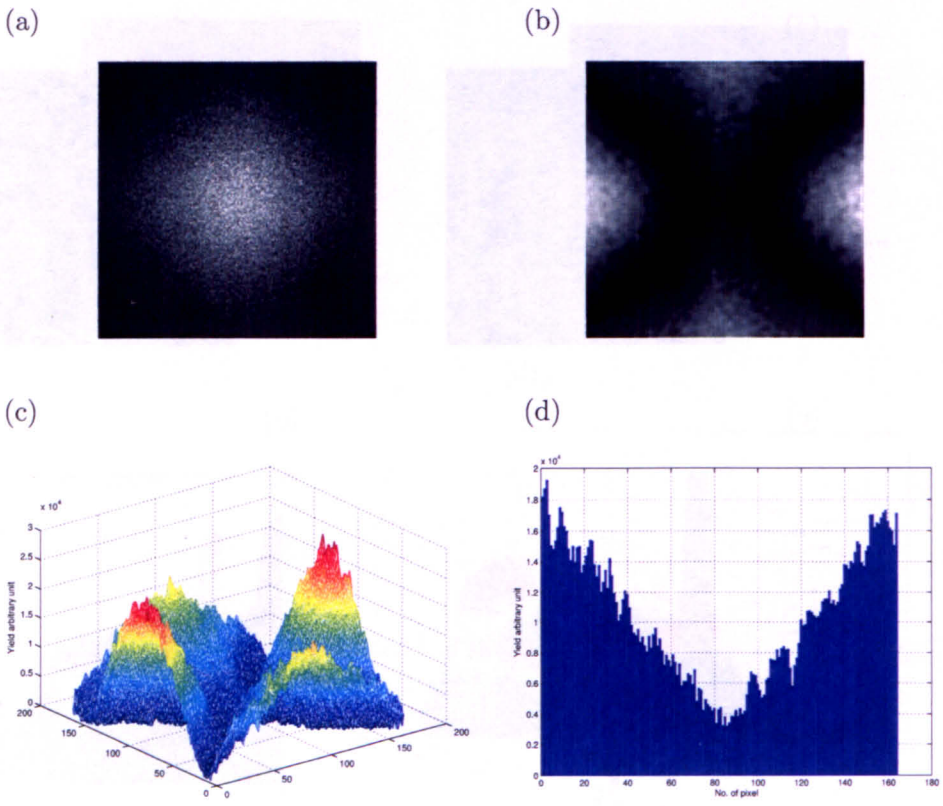

Figure 5.41: Exemplar plot of MCS of planar square source of $10\times10\times0.1$ cm^3, (a) the projected image, (b) the decoded image, (c) a 3D plot of the decoded image, and (d) a vertical profile taken through the centre of the decoded image.

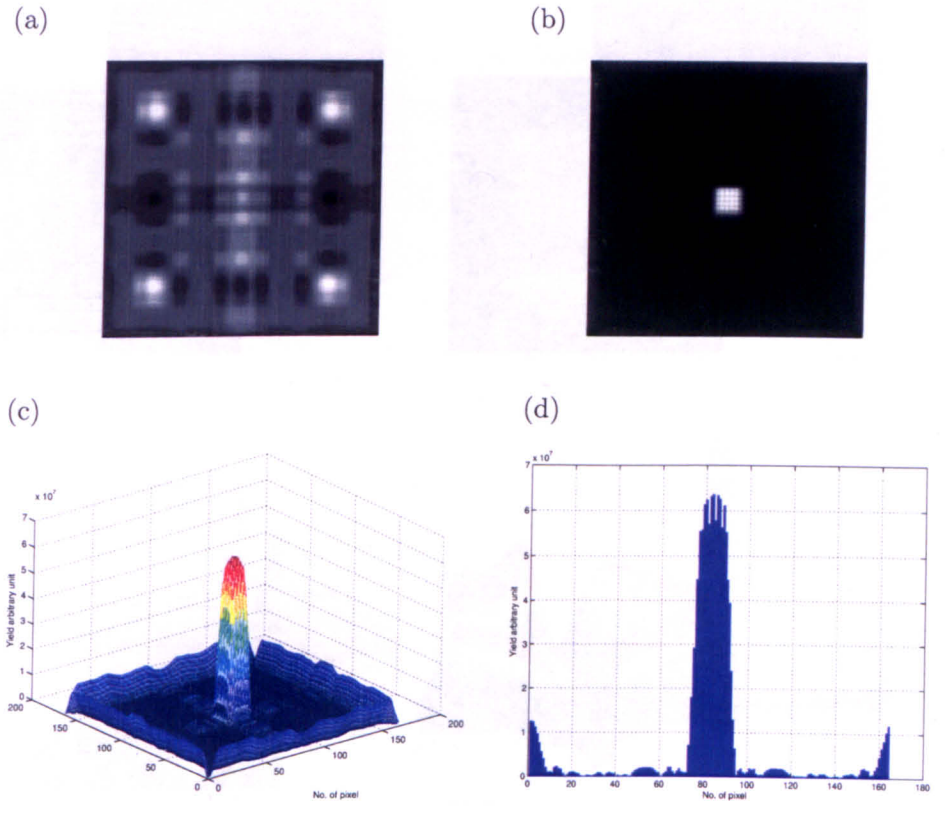

Figure 5.42: Exemplar plot of synthetic BMS equivalent to 1×1 cm^2 square source: (a) the projected image, (b) the decoded image, (c) a 3D plot of the decoded image, and (d) a vertical profile taken through the centre of the decoded image. This should be compared with 5.39

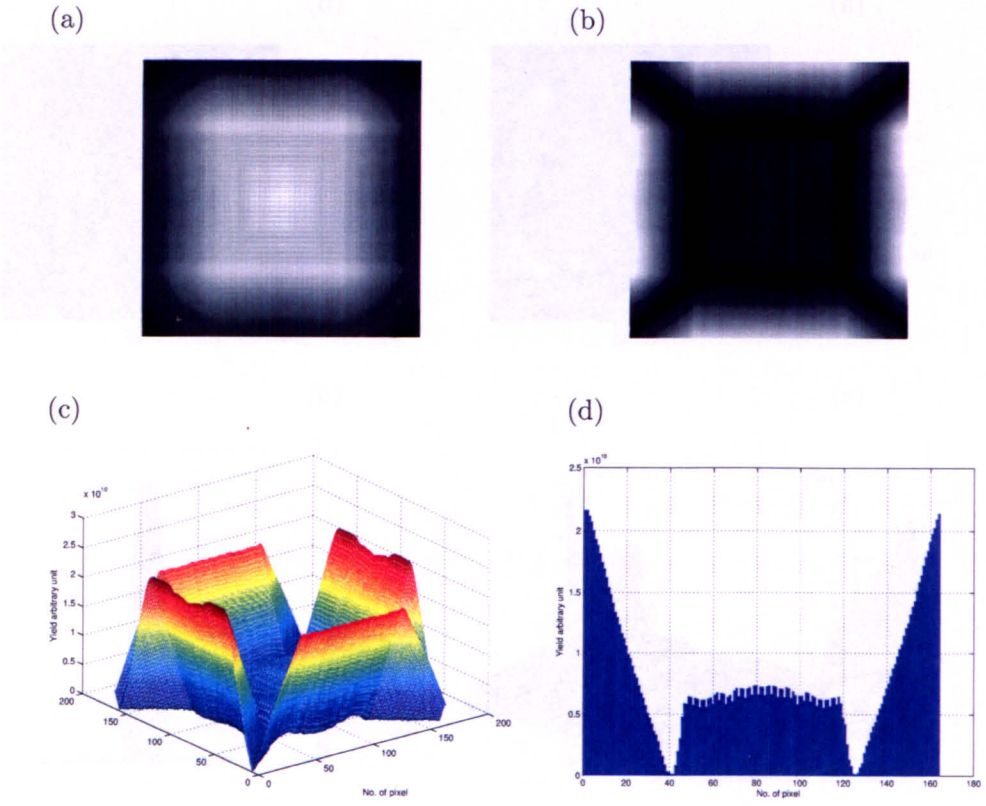

Figure 5.43: Exemplar plot of BMS equivalent to 5×5 cm^2 square source: (a) the projected image, (b) the decoded image, (c) a 3D plot of the decoded image, and (d) a vertical profile taken through the centre of the decoded image.

was found to produce flat field distortions that is almost identical to the MCS data. The slight discrepancies remaining are due to photon statistics and MCS geometry specific effects such as mask thickness. More results that compare the PRT and MCS methods are presented in Appendix E.

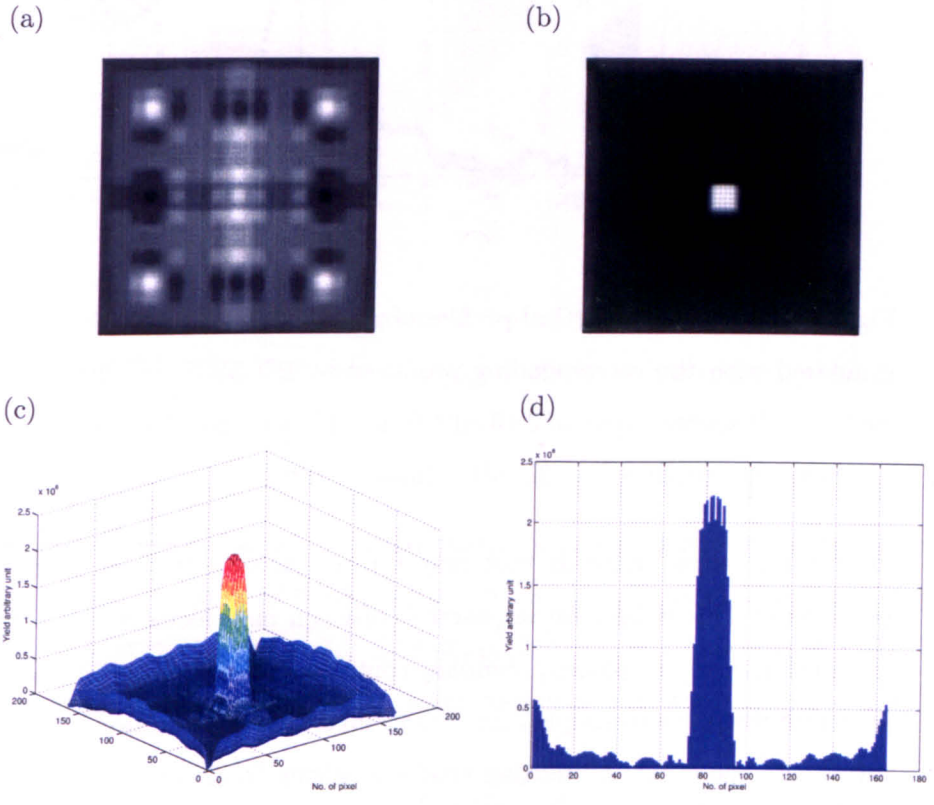

Figure 5.44: Exemplar plot of PRT of 1×1 cm^2 square source: (a) the projected image, (b) the decoded image, (c) a 3D plot of the decoded image, and (d) a vertical profile taken through the centre of the decoded image. This should be compared with Fig. 5.39 and Fig. 5.42. This technique successfully predicts the intrinsic flat field distortion caused by a distributed planar source.

5.2.4 Imaging a 3D Uniform Object

Having observed the in-plane artefacts produced by a 2D distributed source, and learnt how to predict and corrected these, a more realistic 3D object distribution was considered. Extending from 2D planar to 3D volumetric source objects means that Eq. 3.13 is now

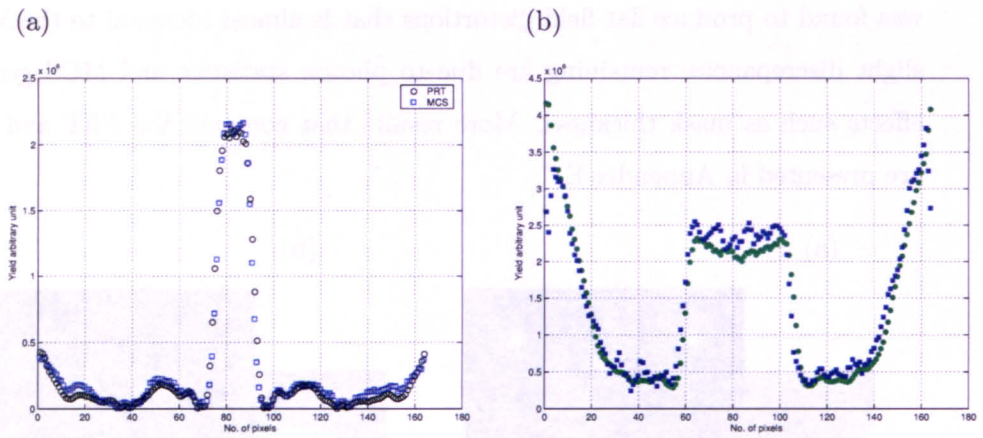

Figure 5.45: Exemplar vertical profiles of predicted flat field distortion from PRT method compared with the corresponding produced by 2D MCS: (a) 2D source object of 1×1 cm^2, (b) 2D source object of 3×3 cm^2 from PRT method (filled circle) compared with the corresponding produced by 2D MCS (filled square).

extended to triple integrals that may further increase the complexity of the decoding procedure. This is because in practice, one can only focus in one plane and the other underlying/overlying planes potentially contribute to blurred out-of-plane artefacts, as was seen with the previous simple point source investigation in section (5.2.1 (d)). This section investigate the effects of imaging artefacts arising from 3D "flood field" uniform objects using PRT and MCS method. The aim was to generate a prediction of the unwanted background structure by simulating a uniform 3D object of similar size to a compressed breast.

The geometrical set-up of the MCS is shown in Fig. 5.46. Different target volumes of fixed thickness (6 cm) ranging from 6-864 cm^3 were imaged. In each case approximately 10^9 photon histories were simulated. Figure 5.47 and Fig. 5.48 show two exemplar of the predicted flat field distortion from MCS method of a 3D source of 1×1×6 cm^3 and 5×5×6 cm^3 respectively. The results from these investigations suggest that the artefact appear very clearly for object larger than 1 × 1 cm and increase with source object size. For larger source object > 4 cm the decoded images show 2 arc-shaped valley in each side of the image. The effect of the volumetric source is clearly demonstrated in Fig. 5.47(a) compared with that produce from the planar source but having the same size shown in

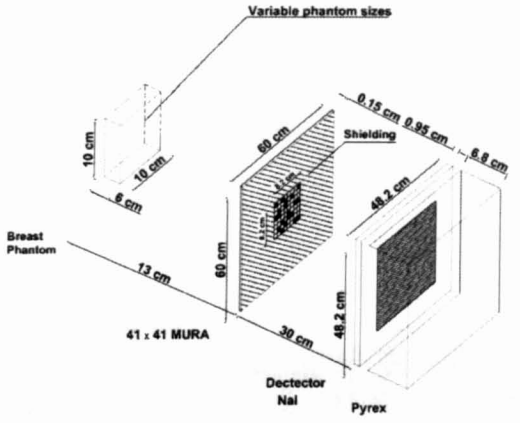

Figure 5.46: Schematic diagram of the flood field of variable phantom sizes (having fixed thickness of 6 cm) showing the basic elements of the complete geometry simulated.

Fig. 5.39 (a).

Now the PRT method is used to demonstrate the predicted flat field distortion obtained for different target volumes of fixed thickness (6 cm) ranging from 6-864 cm^3. Figure 5.49 show exemplar of the predicted flat field distortion from PRT method of a 3D source of $1\times1\times6$ cm^3 demonstrating a slightly larger distortion artefacts compared with the 2D source object.

To consider the difference between a full 3D prediction of the background compare to just considering 2D in-plane effects, a high statistics PRT method was used. Fig. 5.50 shows exemplar (few more results are shown in appendix E) profiles of the decoded image of the predicted flat field distortion obtained from the PRT method for 2D planar and 3D volumetric source objects. The imaging profiles taken through the centre of the decoded images demonstrate that the flat field distortion artefacts from 3D volumetric source objects appear some how similar to that observed when imaging a 2D planar object. It is also worth showing the decoded images resulting from these 2D planar and 3D volumetric source objects. This is clearly demonstrated in Fig. 5.51 showing that the flat field distortion artefacts from 3D appear some how similar to that observed when imaging a 2D planar object. This suggests that the source of gross artefacts is largely attributed to the effect of in-plane distributed radioactivity and the effect of incomplete (partial coding)

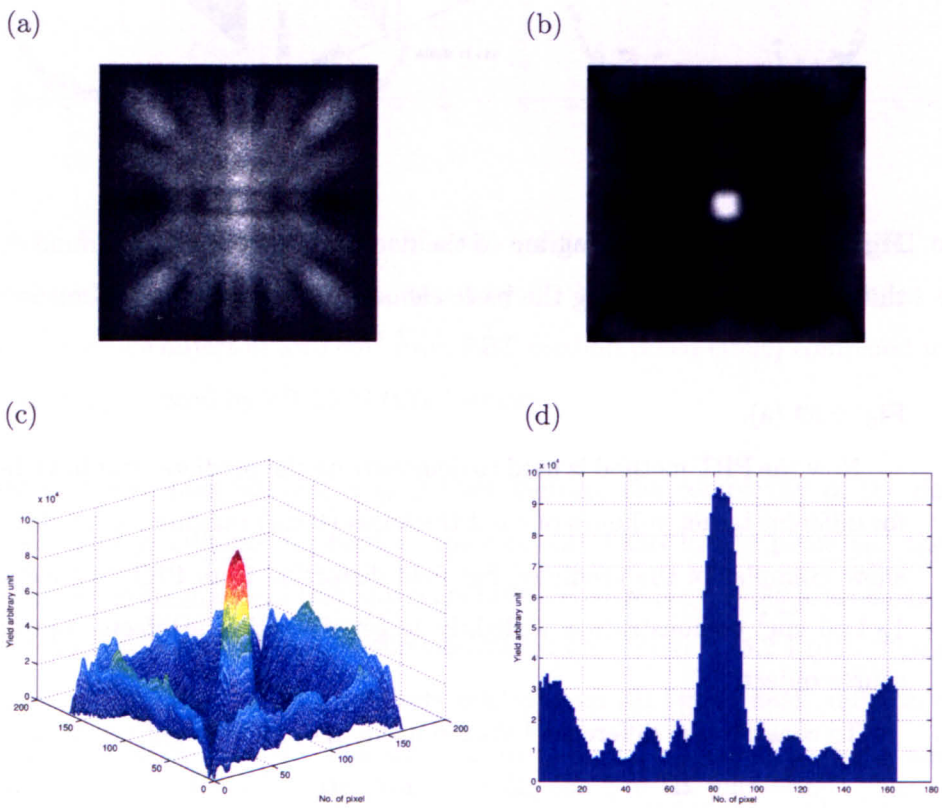

Figure 5.47: Exemplar plot of MCS of 3D square source of $1\times1\times6$ cm^3: (a) the projected image, (b) the decoded image, (c) a 3D plot of the decoded image, and (d) a vertical profile taken through the centre of the decoded image.

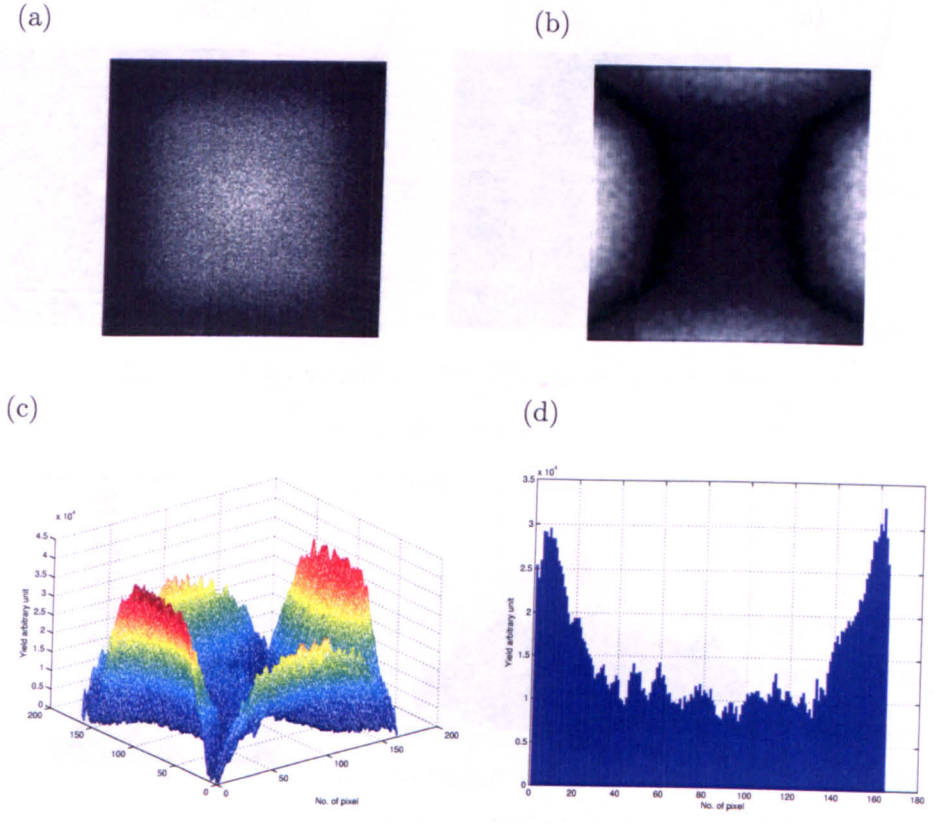

Figure 5.48: Exemplar plot of the simulated 3D phantom of a $5 \times 5 \times 6$ cm^3: (a) the simulated image, (b) the decoded image, (c) a 3D plot of the decoded image, and (d) a vertical profile taken through the centre of the decoded image. The effect of limited photon statistic is clearly demonstrated.

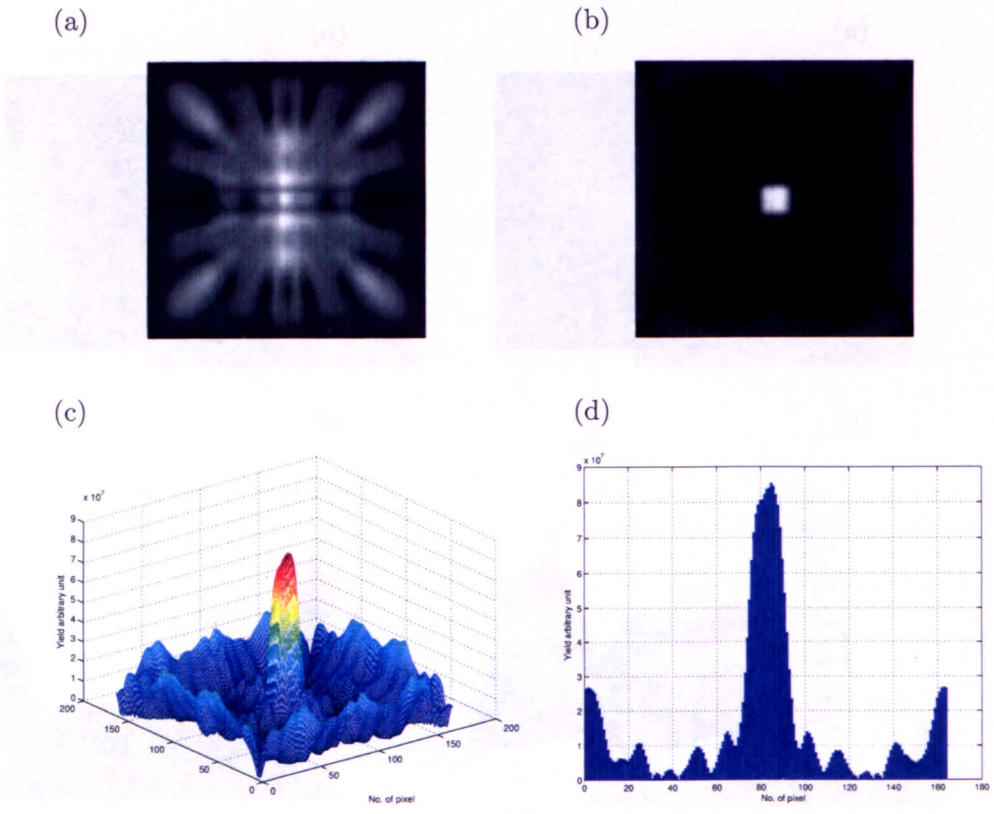

Figure 5.49: Exemplar plot of PRT of 3D square source of 1×1×6 cm^3: (a) the projected image, (b) the decoded image, (c) a 3D plot of the decoded image, and (d) a vertical profile taken through the centre of the decoded image. This should be compared with Fig. 5.44.

of the mask pattern due to off-axis sources.

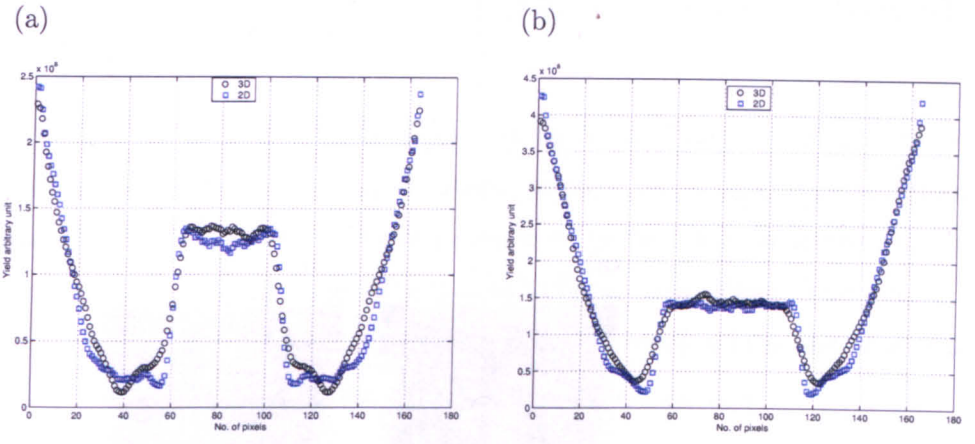

Figure 5.50: Exemplar vertical profiles of predicted 2D flat field distortion from the PRT method for a planar source compared with 3D source object after least squares fit to normalise the distribution: (a) planar square object of size 3×3 cm^2 compared with 3D object of 3×3×6 cm^3, (b) planar square object of size 4×4 cm^2 compared with 3D object of 4×4×6 cm^3.

The 3D set of investigations suggests that the main cause of the distortion artefacts, in near-field geometry, is the finite distributed size of the source object mainly from within the focal plane. It also suggests that the form of the artefact, in terms of the shape and the magnitude of the side-lobes, arising from such imaging geometry can be predicted. These are encouraging results and suggest that the MURAs-CA near field distortion observed with distributed 3D source object, as might be found in SM, can be easily predicted and corrected (see chapter 7).

5.2.5 Conclusions from the Pilot Simulation Study

From the above investigations one may draw the following conclusion:

1. The MURA pattern for imaging a point-like object in the near field geometry has good performance with zero side lobes. However, image artefacts are intrinsic to CA imaging when using near-field geometry even when imaging small point like objects.

2. The non-Monte Carlo methods i.e. the BMS and the PRT methods produce compa-

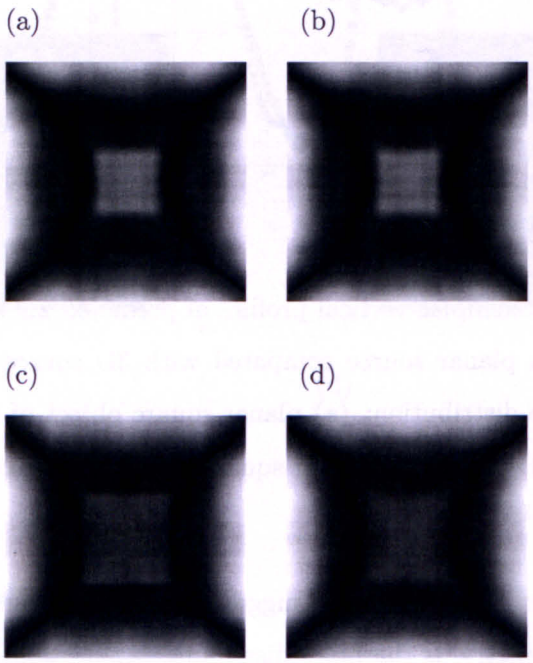

Figure 5.51: The decoded images from PRT method for 2D and 3D source object: (a) the decoded image from 2D source object of size 3×3 cm^2, (b) the decoded image from planar source of size 4×4 cm^2, (d) the decoded image from planar source of size 4×4×6 cm^2. These reconstructed images demonstrate that the predicted flat field distortion obtained from the PRT method for 2D planar and 3D volumetric source objects are almost the same.

rable results to using MCS. Both methods successfully predict the form of artefacts, in term of the shape and the magnitude of the side-lobes that is due to the off-centre source displacement.

3. It should be noted that by even removing the effect of varying the incident γ-ray or solid angle effect (when using the BMS method), the artefacts are still present in the decoded image. These artefacts accounted for the effect of source displacement result in losing information by not covering the whole image. This suggests that for high resolution near-field imaging one ideally needs a large detector that fully samples the mask patterns for all the sources within the FoV.

4. In the case of a single point source in air located at different depths, decoding is not a problem as it can be obtained by applying a set of scaled decoding steps to seek out limited depth information, where the highest intensity is seen at the correctly decoded depth.

5. One of the observation demonstrated with MURA-CA investigations is that the out-of-focus behaviour of reconstruction have complex non-uniform structure. These investigations suggest that 3D imaging with CA is not the best option as the out of focus planes produces highly distorted images with severe artefacts.

6. The multi-source & multi-depth decoding investigations demonstrate the effect of multiplexing on the projected image particularly as the complexity of the object increases. In addition, once the complexity of the object increases i.e. for more than 5 sources and the spacing between them are less than 0.5 cm FWHM, then it becomes difficult to faithfully recover the true distribution due to the presence of artefacts.

7. Distortion artefacts appear in the image with large magnitude once the geometry starts to become more complicated (distributed) and the FoV increases. These were visualized for objects larger than 1×1 cm^2. The source of background distortion artefacts appear when imaging 2D and 3D object are believed to be due to a combination of several factors: 1) Due to finite size of the detector the off-axis sources cause incomplete (partial coding) of the mask pattern. 2) The inherent non-linearity in the photon flux impinging on the detector.

8. The non-Monte Carlo methods successfully predict the form of artefacts arising from imaging extended objects of 2D shape. The BMS method predicted the shape of artefacts that are due to off-axis sources and finite size of the object (extended sources) but ignores the effect of varying the angle of incidence of the gamma-rays. However, for PRT and MCS methods the near field effect cause non-uniform radiation intensity to reach the detector and thus another form of artefacts appear in the image.

9. The background artefacts produced by uniform 2D and 3D source objects of different sizes using the PRT method compared with the corresponding data obtained with the MCS method suggests that the PRT method produces striking similarities to the MCS data. These results are encouraging and thus, the so-called near field distortion observed with distributed planar and 3D sources, as might be found in SM using coded apertures, can be easily predicted and corrected.

Chapter 6

Monte Carlo Simulation of Breast Tumour Coded Aperture Imaging

Having previously considered the effects of decoding point sources and establishing an approprite CA imaging geometry for SM, this chapter now considers the simulation issues needed for representing finite-sized lesions in a clinically realistic imaging situation. Thus, this chapter describes the geometric model of the 3D phantom and the method of calculating the activities for the breast tumour imaging used in these investigations are described. Then the quantitative parameters used to assess the different image formation methods investigated in this thesis. The emphasis is on presenting the main MCS investigations carried out with CA breast tumour imaging. First to be investigated were the effects of adding a hot background to assess the system behavior to various background sources. More importantly, the effect of unwanted cardiac uptake on the decoded images, and how this might affect tumour imaging was considered. Then the need to shield the camera from unwanted cardiac/torso uptake was studied. Finally qualitatively comparison is made of the performance of CA for detecting lesions of various sizes and Tumour-to-Background-Ratio (TBR) before and after shielding.

6.1 Breast Tumour Imaging

This section first provides a description of the 3D breast phantom MCS geometry used for SM imaging. Then the way of calculating the activity is described, used in a realistic clinical simulation, to estimate the total photon flux emitted from the source. Then the

application of MURA-CA coupled to conventional γ-camera after removing the collimator for breast tumour imaging is investigated.

6.1.1 Geometric Model & 3D Phantom

Due to the lack of availability MCNPX data of a female anthropomorphic phantom, it was decided to use a model of simplified geometries to describe the upper part of the body or torso. Thus, the geometries discussed herein are designed to be nonetheless representative of a realistic SM imaging situation. The different elements of the complete 3D geometry studied under MCNPX include: source(s), torso phantom, breast, tumours. Uniform isotropic point-like sources of ^{99m}Tc emitting 140 keV photons are located inside the breast compartment, with or without background activity assigned to the surrounding media. The breast is schematized as a parallelepiped of $10 \times 10 \times 6$ cm^3. The body or torso compartment was simulated by a parallelepiped of ($40 \times 20 \times 20$ cm^3). The heart was simulated as a sphere of 8 cm diameter having an uptake:background concentration ratio of 10:1 s assumed based on Ref. [127]. All tissue atomic compositions and material densities were obtained from the ICRU report 44 [128].

A breast thickness of 6 cm was chosen based on the assumption of light breast compression. This assumption is used to emulate SM where the breast is immobilized to provide a more uniform background in the resulting image. It has been suggested [13] that breast compression increases the lesion delectability. The density of the breast phantom is similar to that found in the uncompressed breast. In this way one is able to consider the effect of the adjacent surrounding scattering material in isolation whilst neglecting any effects from the non-specific uptake in the torso. The lesion(s) was simulated as spheres of variable sizes but always positioned at 3 cm depth from the surface of the breast. Photons are then generated either in the background object or the lesions under study. These were first estimated by calculating the activity of a given dosage used clinically a realistic SM imaging condition.

6.1.2 Activity Calculation

In order to emulate clinically realistic SM imaging in cranio-caudal view, the number of simulated γ-rays must be matched to that found in a clinical imaging situation. As have been reported in the literature [83, 34] the patient is usually injected with arround 555-740

MBq of ^{99m}Tc-sestamibi and imaged for 10 minutes. First, it was assumed the radiotracer is uniformly distributed in the torso.

For a dosage of 555 MBq the integrated number of photons generated in patient during SM scans is $\sim 5.55 \times 10^8$ photons/seconds. For these, activity calculation a corrective factor of 0.89 (the branching ratio for ^{99m}Tc), which represents the proportion of 140 keV photons emitted for each transition, ignoring the small loss to the radioactivity before scan and the decay loss during the scan. As well as adjusting the emitted photons during scan for the patient of (128000 cm^3) for omissions in the phantom geometry (e.g., it has no liver, lungs, legs, head, or bladder) then the total number of emitted photons within the upper torso compartment used in the simulation is assumed to be $\sim 10^{10}$ photons. This is the total simulated photons and are distributed based on the total volume of the source and the Tumour activity-to-Background Ratio (TBR).

The breast and the torso should have the same ratio radioactivity concentration values to obtain clinical images with about a 1:1 torso: breast ratio. The heart is well known to produce a significantly higher activity concentration than most other non-tumour tissues. This is due to its substantial blood supply and because ^{99m}Tc sestamibi was originally developed as a heart perfusion agent. A heart-background-ratio of 10:1 is assumed based on values taken from [127]. The tumour activity concentration in the simulations is then varied ranging from 3:1 up to 100:1 for the 2, 4, 6 and 10 mm diameter tumours. Table 6.1 shows a summary of lesion diameters and the estimated integrated flux for various tumour diameters simulated. This demonstrates the extremely low integrated flux available for small lesions at low TBR.

Having estimated the integrated flux the entire Monte Carlo code geometries are verified to ensure accurate source distribution. This is achieved by looking carefully at the performance of individual sections of the code. Then the location and direction of simulated photons are plotted to ensure that each source is uniformly distributed, and ensure that the photons/volume are as desired for all sources and as adjusted by the TBR concentration.

The simulation time spent calculating the huge background photon contribution, in the 3D phantom, is large (few weeks) compared to the time spent generating photons originating in the lesion. To reduce subsequent computational time, for required background photons, the energy, position, and direction of the gamma photons that successfully

Table 6.1: Summary of lesion diameters (mm) and the simulated photons for different tumour-background-ratio of tissue uptake.

TBR	10:1	20:1	40:1	50:1	60:1	80:1	100:1
Lesion diameter (mm)	γ	γ	γ	γ	γ	γ	γ
2	2.9E+4	5.9E+4	1.2E+5	1.5E+5	1.8E+5	2.3E+5	2.9E+5
4	2.3E+5	4.7E+5	9.4E+5	1.2E+6	1.4E+6	1.9E+6	2.3E+6
6	7.9E+5	1.6E+6	3.2E+6	4.0E+6	4.7E+6	6.3E+6	7.9E+6
8	1.9E+6	3.8E+6	7.5E+6	9.4E+6	1.1E+7	1.5E+7	1.9E+7
10	3.6E+6	7.3E+6	1.5E+7	1.8E+7	2.20E+07	2.9E+7	3.7E+7

reached the detector with energy 126-154 keV were then saved in list mode from the resulting MCNPX PTRAC file. For the lesion component different simulations were run by systematically increasing the lesion size with different TBR. The lesion PTRAC data were then added to the background torso data. This removed the need to generate separate torso data for each simulation. All these simulation consists of tracing the path of gamma photons (^{99m}Tc isotropic sources emitting 140 keV photons) through tissue equivalent scattering material, through the image formation method until detected in the detector.

6.1.3 Quantifications of Planar Tumour Images

In order to compare tumour images from different simulations, three fundamental parameters values are quantified: the observed tumour spatial FWHM and the observed tumour visibility contrast and the contrast-to-noise ratio. These are discussed in the following subsections.

Tumour Spatial Resolution

Tumour spatial resolution is expressed as FWHM and is of interest as it reveals how much the spatial resolution of the camera spreads out the tumour dimensions in the 2D planar image. The tumour spatial FWHM was calculated by taking a profile through the centre of the tumour of the detected lesion in a row of pixels after a gaussian curve fit, using Matlab 6.5. The calculated values are the average of four such FWHM values for each

tumour, using one along each of the x, y, and two 45^o diagonal directions.

Lesion Contrast

The observed tumour contrast was calculated to quantify the lesion visibility. The lesion contrast, C, was defined as:

$$C = \frac{S - B}{B} \tag{6.1}$$

where S representing the tumour signal and B representing the background.

The signal was obtained by first defining a region of interest (ROI) around the tumour at the modeled depth. This ROI is a square area and was defined by the FWHM i.e. the tumour signal in this case is twice the FWHM to ensure that all tumour events are included. Then integrate all the tumour event and divided by the number of pixels (area) of that ROI. The background was defined similarly but in this case a square area that is six times the FWHM excluding the area that contains the tumour signal.

Contrast-Noise-Ratio (CNR)

The CNR was computed with the aim to quantify how visible a lesion would be against the local background. This is important as it allows for the comparison of images taken with different imaging conditions. The CNR is defined as:

$$CNR = \frac{|\mu h2 - \mu h1|}{\sigma 1} \tag{6.2}$$

where: $\mu h2$ is the mean signal, $\mu h1$ is the mean background values and $\sigma 1$ is the standard deviation in the background.

6.2 Imaging with a Coded Aperture

This section contains the various investigations carried out with MURA-CA and are thus, divided into two main subsections. The first subsection initially investigates the effect of imaging a small hot lesion in air without scattering material. This represents a highly idealised case as it neglects any surrounding tissue scatter or non-specific tracer uptake. Then the effects of scatter by imaging a lesion in Tissue Equivalent breast Material (TEM) is considered. The second subsection demonstrates the effects of non-negligible background

activity both within the breast and emanating from the torso. It also includes the effects of cardiac uptake, the limited photon statistics and the effects of open field geometries. In all these cases the projected images were decoded with the post processing array, G, using the fine sampling cross-correlation method (see chapter 3).

6.2.1 Imaging a Lesion in Air & in Tissue Equivalent Material

Before considering the effect of imaging a lesion in a hot background, a spherical lesion in air and in cold TEM were initially investigated using MCS. Note for these simulations $\approx$ 7.5 Million photons were simulated. Figure 6.1 show exemplar plot of the decoded images of a 10 mm lesion in air and in TEM of size $10\times10\times6$ cm^3. The slight difference between the two profiles of Fig. 6.1 (b) and (d) is due to the photon attenuation and scattering present in the case of lesion TEM. These results should be compared with that which might be found in perfect imaging conditions where the source is an infinitely small point (see Fig. 5.4).

6.2.2 Imaging a Lesion in 3D Warm Background

In the particular case of SM (see Fig. 6.2), the target region can be considered approximated to be a uniform volume of tissue with approximately uniform background activity, superimposed upon which small regions of enhanced activity are usually attributed to lesions or disease. This target area is typically smaller than the sensitive imaging area provided on a clinical gamma camera. Displacement of the camera from the breast allows the projected flux to fill the camera field of view and thus, produce a magnified image. Solid angle losses in photon flux, which might otherwise occur if a collimator were used, are countered by the inherent wide angle acceptance of CA imaging, and the high open area ($\sim$50%) when MURAs-CA are used.

Having demonstrated the effects of imaging a lesion in air and in a cold scattering medium corresponding to breast tissue, the effects of adding activity (hot background) to the surrounding breast tissue is considered. In addition, the effect of activity in the adjacent torso or the target region is also considered. These were necessary to realistically assess the systems behaviour to the various background intensities.

Before investigating the performance of the CA imaging system for SM, the effect of background activity from the hot 3D phantom geometries is considered. These are

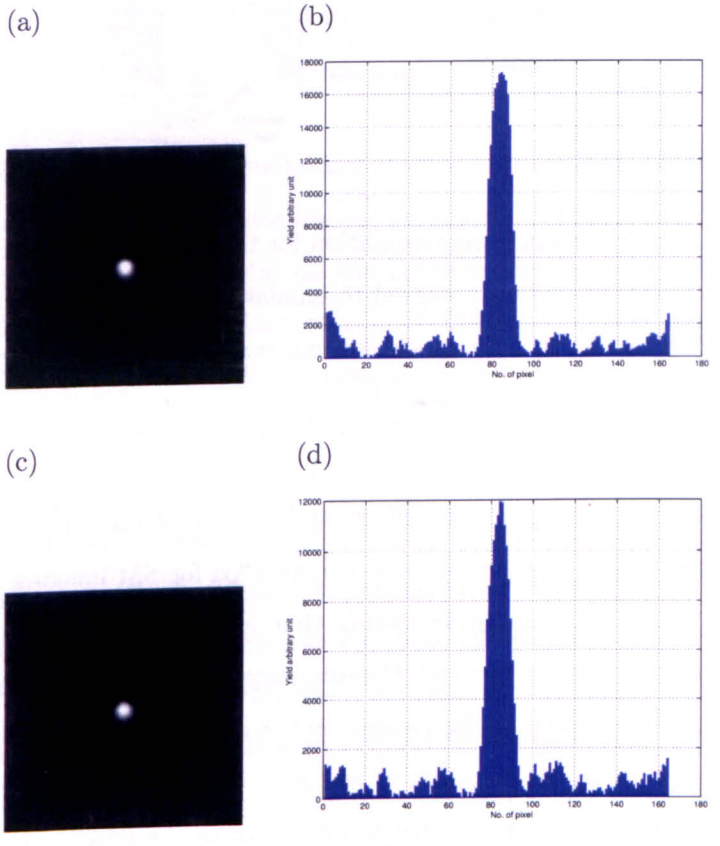

Figure 6.1: Exemplar MCS plot of the decoded images of 10 mm diameter lesion in air and in TEM: (a) the decoded image of a 10 mm diameter in air, (b) vertical profile through the decoded image of (a), (c) the decoded image of a 10 mm diameter lesion in TEM, (d) a profile through the centre of (c).

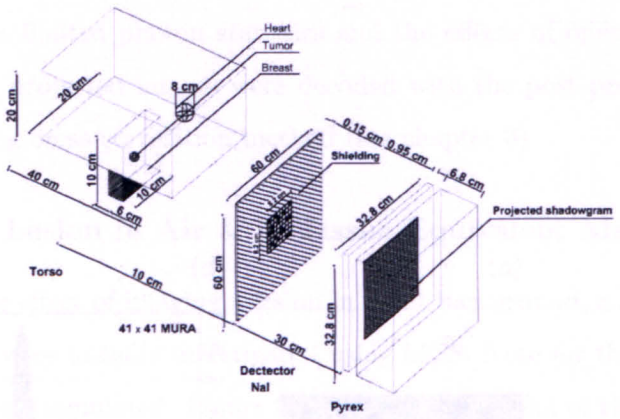

Figure 6.2: A schematic representation for the 3D torso phantom and MURAs camera for Monte Carlo simulation designed to emulate scintimammography. The frame surrounds the CA is made of 1.5 mm thick tungsten to minimises detection of oblique photons arriving from outside the breast FoV.

responsible for photon attenuation and scattering and thus, affects the quality of the projected image. For the 140 keV energy used for SM imaging the more commonly form of scattering is Compton scattering that arises as the γ-ray travel through the tissue. Both photon attenuation and Compton scattering limits any quantitative measurement performed with the imaging system. In CA imaging the scattered photons are expected to arise from within the phantom as well as from the CA-camera imaging system itself. The following subsection is intended to demonstrate the effect of the background and scatter activity from the unwanted uptake on the CA imaging system, and address whether this will reduce the diagnostic accuracy and the image contrast.

Effect of Local Scatter & Background Activity

The CA imaging system is particularly sensitive to stray photons from outside the target ROI compared to collimator-based imaging. The aim of this section is to demonstrate the background arises from the presence of heart and torso in the 3D phantom. All the Monte Carlo generated images are obtained from 3D phantoms using the imaging geometries shown in Fig. 6.2.

Since the activity concentration in the heart is ten times the background this may

Table 6.2: The total number of detected photons form each source for different heart:background ratios.

Sources	Heart ratio 1	Heart ratio 10
Torso	867672	868104
Tumour	1192	1311
Heart	24190	243915
Breast	403011	403231

suggest that the contribution of activity and cardiac scatter from the heart could play a major role in the quality of the decoded image. To explore this more clearly two simulation studies were generated with 10^8 total photon histories simulated in each case using the geometry shown in Fig. 6.2. In the first simulation the heart activity was set equal to the background activity concentration in the torso and breast phantom where as in the second simulation the heart activity concentration was ten times greater than the background. The second case mimics the clinical situation in which the concentration in myocardium is 10 times the normal breast tissue. The total number of detected photons from each source in the 3D phantom geometries in each case are shown in table 6.2. The deposited energy spectrum from each simulation is shown in Fig. 6.3. These give an indirect measure of the effect of scatter on the energy spectra, which also include the effect of the camera energy resolution. These clearly demonstrate the contribution of scatter and direct radiation from the heart and other sources in the 3D phantom. It shows that the major contributions (scatter and direct radiation) are from the torso and the heart.

Despite the use of 1.5 mm thick tungsten frame surrounding the CA (see Fig. 6.2) to minimises detection of oblique photons arriving from outside the breast breast FoV, there was also background contribution from the heart and the torso. Figure 6.3 (b) clearly show the effect of the heart on the decoded image and is mainly created by the wide open geometry of the CA imaging. To demonstrate this, the full energy photo-peak of the 3D phantom shown in Fig. 6.3 (a) and (b) were compared as shown in Fig. 6.4. For this particular geometry the background contribution of the heart to the left breast This shows the contribution of scatter and direct radiation from the heart. In addition, the response of the detector to the incoming radiation is not perfect due to in ability of the proposed system to separate nearby transitions (represented by the energy resolution).

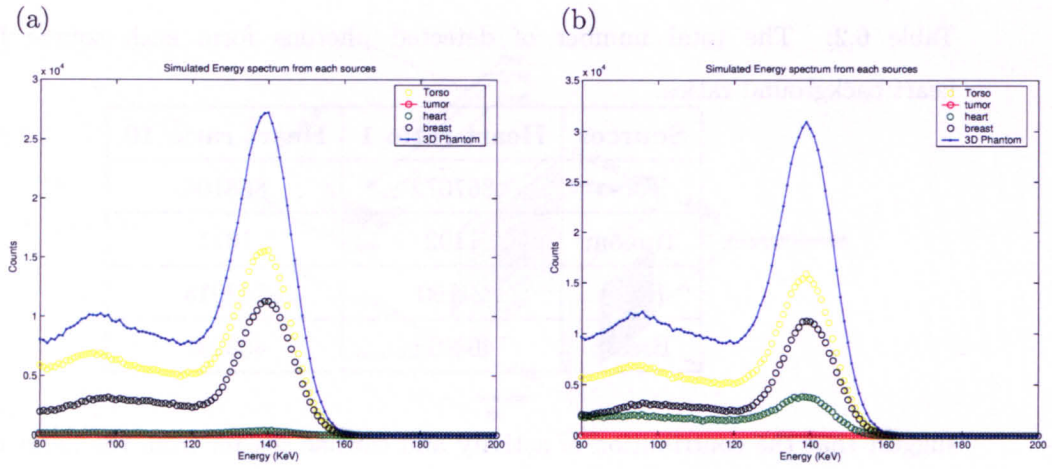

Figure 6.3: The simulated full energy photopeak generated using the geometry depicted in Fig. 6.2: (a) the heart activity concentration is equal the background (b) the heart activity concentration is 10 times the background. In both cases a 10 mm lesion with TBR of 10:1 was placed at a depth of 3 cm.

These together will impose a severe limitation on the ability of the system to characterize, detect and quantify the activity contained in a small lesion in the breast. Furthermore, the larger the volume of the non-target object compared to the lesion causes blooming of the apparent source size as well as a loss of sharpness of object.

The above investigations suggest that the open field geometry associated with MURA-CA imaging requires correcting the non-specific background tracer uptake. This is mainly due to both scattered photons (within torso, heart and non-tumour breast tissue) as well as the emitted radiation from the non-zero background activity of 3D phantom geometries. The displacement of the CA and the γ-camera away from the close proximity to the breast means that shielding can be introduced to mitigate the effects of unwanted cardiac/torso uptake. Although, the contribution of scatter can be reduced by using a 20%, "energy window", on the photo-peak energy of the recorded events, further reduction could be obtained by the use of proper geometric shielding.

To investigate the effect of shielding a 1.5 mm tungsten sheet was used to reduce the contribution of the heart and the torso. This has been achieved by shielding the CA and camera from the background torso/cardiac flux by placing 1.5 mm tungsten sheets on

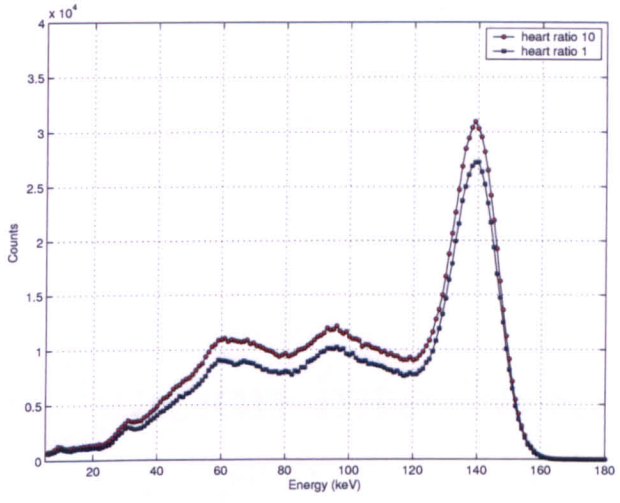

Figure 6.4: Two Monte Carlo generated energy spectra using the imaging geometry shown in Fig. 6.2 with heart activity equal background (filled circle) and with heart activity 10 times the background (filled circle).

the off-side of the breast, and around all surfaces which could geometrically emit photons through to the CA. This effectively removes most of the unwanted torso/cardiac flux. Figure 6.5 show exemplar plots of the decoded image after shielding for the 3D phantom geometries shown in Fig. 6.2 with a 10 mm lesion having a TBR of 40:1 (see table 6.1).

Despite the use of shielding the appearance of a large artefact (two arc-shaped valleys in each side of the image) in the decoded image causing subsequent loss in visualising the target lesion. This suggest that post-simulation corrections are necessary to correct for the near field distortion observed from the 3D distributed. These near-field corrections are necessary to accurately assess the performance of the CA-SM imaging system. In order to remove the effect of volumetric background corruption caused by systematic decoding artefacts and thus, to improve the lower limit on tumour detection, in terms of contrast and resolution these near-field corrections are presented in the next chapter.

(a) (b)

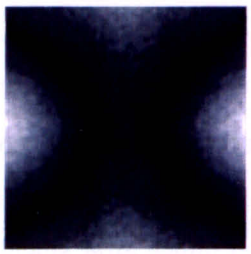

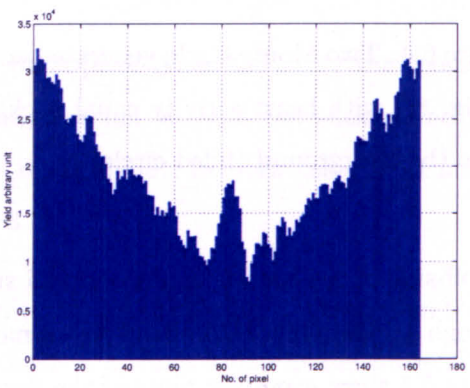

Figure 6.5: The MCS decoded image of the 3D phantom geometries using the geometry shown in Fig. 6.2. after shielding the camera by placing the 1.5 mm tungsten sheets on the off-side of the breast, and around all surfaces which could geometrically emit photons through to the CA.

Chapter 7

An Investigation into Near Field Image Artefacts

This chapter describe the near-field artefact corrections that have been developed and then applied to the CA-SM data to remove or minimise the corruption artefact arising in the decoded image of such 3D source object. The main aim is to correct the effects of non-ideal imaging conditions and to investigate how these post-acquisition methods of image correction can improve object detection.

7.1 Near Field Artefacts Corrections

As has been demonstrated in chapter 6 near-field CA imaging presents a number of problems when imaging an extended object (a lesion) surrounded by a noisy background activity from normal tissue of the breast. In these non-ideal imaging conditions, imaging artefacts arise as the imaging geometry deviates significantly from ideality i.e. is not any more a point-like object. There are many factors that may be attributed to this deviation including the finite object thickness and the intensity variation across the projected image. The latter is due to angular variation in the incident γ-rays falling on the detector i.e. the incident γ-rays are no longer parallel. Other possible effects that cause degradation in the decoded image are the geometry of the mask, incomplete (partial) projection and background contributions outside the target detection plane [129]. These sources of image artefact significantly affect the decoded image and thus, obfuscate the analysis of underlying diagnostic information.

Previous studies [104, 76] in CA imaging have explored and implemented different solutions to alleviate the artefacts induced by the inherent near-field geometry. Accorsi and Lanza suggested [104] that factors such as variation in the incident angle of γ-rays, which adds an intensity modulation to the projection of the mask pattern, finite thickness of both the object and the mask are the most serious causes of artefacts when imaging a planar object. Thus, they also looked at the consequence of the $\cos^3(\theta)$ factor of expression 3.13 and mathematically expanded this consequence into a Taylor series to second order [104]. Each of these expansion terms contributes various artefacts arising from the imaging geometry whose shape has been mathematically predicted [104]. To illustrate the above discussion in a mathematical way one needs first to recall the following expression from chapter 3:

$$D(\vec{r}_i) = \int\int_{\vec{r}_o} O(\vec{r}_o) A(\frac{a}{z}\vec{r}_i + \frac{b}{z}\vec{r}_o)\Omega(\vec{r}_o, \vec{r}_i) d^2\vec{r}_o \tag{7.1}$$

where: $D(\vec{r}_i)$ is the recorded counts in the detector at position $\vec{r}_i$ and

$$\Omega(\vec{r}_o, \vec{r}_i) = \frac{p_m^2}{a^2}\cos^3(\theta) \tag{7.2}$$

where: $\theta = \arctan(|\vec{r}_i - \vec{r}_o|/z)$ and all other symbols are given in chapter 3.

Accorsi and Lanza [104] define some of the symbols presented in Eq. 7.1 as:

$$\xi = -\frac{b}{a}\vec{r}_o$$
$$O'\vec{r} = O(-\frac{a}{b}\vec{r})$$
$$A'\vec{r} = A(\frac{a}{z}\vec{r})$$

where: O' and A' are, respectively, a rescaled and reflected (negative sign mean the object is inverted) form of the object and a rescaled version of the mask pattern. It is worth noting and as been stated before that the scaling coefficient for O' is not the same as scaling coefficient for A'. Now Eq. 7.1 become:

$$D(\vec{r}_i) \propto \int\int_{\vec{\xi}} O'(\vec{\xi}) A'(\vec{r}_i - \vec{\xi}) \cos^3[\arctan(\frac{|\vec{r}_i + \frac{a}{b}\vec{\xi}|}{z})] d^2\vec{\xi} \tag{7.3}$$

From the theory presented in chapter 3 the reconstructed image I can be obtained by correlating D with the properly scaled postprocessing function, G', as:

$$I = D \otimes G' \tag{7.4}$$

In far field geometry the imaging process provides artefact-free images because $\cos^3(\theta) \cong 1$. This is because the object is effectively located at infinity, so that $|\vec{r}_i - \vec{r}_o| << z, \forall(\vec{r}_o, \vec{r}_i)$. Thus, Eq. 7.3 become in the form of convolution so that:

$$D = O' * G' \tag{7.5}$$

In contrast in the near-field geometry the object is placed at a close distance from the detector so that $|\vec{r}_i - \vec{r}_o|$ has almost similar value to z. Thus, the effect of the near-field is a modulation by $\cos^3(\theta)$. Following Accorsi and Lanza [104] is suggested mathematical expansion of $\cos^3(\theta)$ term in Eq. 7.3 into a second order Taylor series with centre $\vec{r}_i$, and with the use of $\cos(\arctan(x)) = \frac{1}{1+x^2}$, the result is:

$$\cos^3\left[\arctan(\frac{|\vec{r}_i + \frac{a}{b}\vec{\xi}|}{z})\right] \cong \cos^3\left[\arctan(\frac{|\vec{r}_i|}{z})\right]$$
$$\left\{1 - \frac{3/z^2}{(1+\frac{|\vec{r}_i|^2}{z^2})}\left[\vec{r}_i \circ \frac{a}{b}\vec{\xi}\frac{1}{2}\frac{a}{b}|\vec{\xi}|^2 - \frac{5/2z^2}{1+\frac{|\vec{\xi}|^2|}{z^2}}(\vec{r}_i \circ \frac{a}{b}\vec{\xi})^2\right]\right\} \tag{7.6}$$

where $\circ$ indicates a scalar product. This expansion is more accurate with high magnification geometry where the object is placed very close to the detector. In such cases the near field effect is large as:

$$\frac{|\frac{a}{b}|\vec{\xi}}{\vec{r}_i} = \frac{|\vec{r}_o|}{|\vec{r}_i|} < 1 \tag{7.7}$$

As demonstrated above Eq. 7.6 breaks $\cos^3(\theta)$ into zero, first and second order terms of a Taylor series. Each of these expansion terms contributes various artefacts arising from the near-field imaging geometry as summarized here, details appear elsewhere [104]. From Eq. 7.6 one can see that the zero order does not depend on $\vec{\xi}$ and is obtained as:

$$\cos^3\left[\arctan(\frac{|\vec{r}_i + \frac{a}{b}\vec{\xi}|}{z})\right] \cong \cos^3\left[\arctan(\frac{|\vec{r}_i|}{z})\right] \tag{7.8}$$

If 7.8 is substituted with 7.3 then this give the following equation:

$$D(\vec{r}_i) = \cos^3\left[\arctan(\frac{|\vec{r}_i|}{z})\right] \int\int_{\vec{\xi}} O'(\vec{\xi})\ A'(\vec{r}_i - \vec{\xi}) d^2\vec{\xi} \tag{7.9}$$

In this case, as Eq. 7.9 demonstrated, the projected image, D, is no longer in the form of a convolution (or correlation) due to the near-field term. Thus, correlating D with the correctly scaled G' will not produce a perfect reconstruction to the object. However, if the near-field effect stopped at zero order then this effect can be easily compensated (see section 7.1.1).

According to Accorsi and Lanza [104] the first order artefacts can be corrected by placing the object and the mask in the centre of the detector. From Eq. 7.6 the expression that indicates the first order is given as:

$$\cos^3\left[\arctan(\frac{|\vec{r}_i+\frac{a}{b}\vec{\xi}|}{z})\right]\Big|_I \cong -\cos^3\left[\arctan(\frac{|\vec{r}_i|}{z})\right]\frac{3/z^2}{\left(1+\frac{|\vec{r}_i|^2}{z^2}\right)}\left(\vec{r}_i\circ\frac{a}{b}\vec{\xi}\right) \tag{7.10}$$

Now substituting in Eq. 7.3 after zero order correction leads to the following:

$$D(\vec{r}_i)=\frac{\vec{r}_i}{z^2+|\vec{r}_i|^2}\circ\int\int_{\vec{\xi}}\vec{\xi}O'(\vec{\xi})A'(\vec{r}_i-\vec{\xi})d^2\vec{\xi} \tag{7.11}$$

A' is the aperture transmission function and if the object is uniform and centred in the FoV then the result is not a strong function of shift and thus the first order artefacts are eliminated [104]. Now only second order artefacts still remain and thus, are a cause of image corruption. These artefacts can be corrected by using the mask/antimask technique. By first substituting in Eq. 7.3 and from Eq. 7.6 one can see that the second order terms are given as:

$$\begin{aligned}\cos^3\left[\arctan\left(\frac{|\vec{r}_i+\frac{a}{b}\vec{\xi}|}{z}\right)\right]\Big|_{II} \cong \cos^3\left[\arctan(\frac{|\vec{r}_i|}{z})\right]\frac{3/z^2}{(1+\frac{|\vec{r}_i|^2}{z^2})} \\ \times\left[\frac{1}{2}\frac{a}{b}|\vec{\xi}|^2-\frac{5/2z^2}{(1+\frac{|\vec{r}_i|^2}{z^2})}(\vec{r}_i\circ\frac{a}{b}\vec{\xi})^2\right]\end{aligned} \tag{7.12}$$

Having summarised the consequence of $\cos^3(\theta)$ term the following subsections describe the near-field corrections methods that have been applied to the SM data to correct for the CA artefacts. These methods are zero order correction, mask/anti-mask correction and background subtraction (subtracted flat field correction). The mask/anti-mask technique is equivalent to a second order correction as referred to in ref. [104]. Since the mask pattern has been centred and the object also been placed in the centre of the FoV then this mean all the presented result has been first order corrected. The main aim from these corrections was to demonstrate how post-acquisition methods of image correction can improve object detection for the SM data.

7.1.1 Zero Order Correction

Near field CA imaging geometry causes variations of the incident γ-ray flux on the detector. This modulation of the intensity of the projection of the mask on the detector is dependent

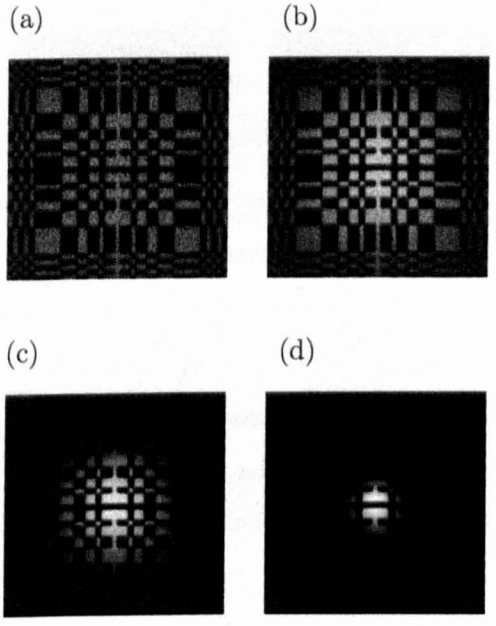

Figure 7.1: The effect of $\cos^3(\theta)$ factor on the projected images as a function source-to-detector distance, z: (a) the projected image with z=40 cm, (b) the projected image with z=20 cm, (c) the projected image with z=10 cm, (d) the projected image with z=4 cm. In all the above imaging geometries a magnification coefficient of 4 was used.

on the position of the source as it projects photons through the aperture. This modulation in the intensity is of course due to the $\cos^3(\theta)$ factor, as described in chapter three. The effect of $\cos^3(\theta)$ factor on the projected image as a function of object-to-detector distance, z is demonstrated in Fig. 7.1. It is worth noting that all projected images are obtained with the same magnification coefficient.

Each projected image demonstrated in Fig. 7.1 can be corrected and the above demonstrated near field effect can be compensated from the knowledge of the distance of the object from the detector, z. This can be achieved if the projected image, D, is divided by $\Omega(\vec{r_o} = 0, \vec{r_i})$ as:

$$I_c = \frac{D(\vec{r_i})}{\cos^3(\arctan(\frac{\vec{r_i}}{z}))} \tag{7.13}$$

where I_c is the corrected image and $\vec{r_i}$ (pixel coordinate) with respect to the centre of the image i.e. (i0,j0)=(n/2, n/2) is given by:

$$|\vec{r_i}| = \sqrt{[((n/2 - i) \times p_m)^2 + ((n/2 - j) \times p_m)^2]}$$

where n is equal the size of the image and p_m is the mask pixel size.

Equation 7.13 only corrects the incident solid angle of gamma-ray photons seen by a source at the centre of the mask i.e. as if the reconstruction was focused at the center of the FoV. Applying this correction to the projected images shown in Fig. 7.1 i.e. dividing each projected image by $\Omega(\vec{r_o} = 0, \vec{r_i})$ using Eq. 7.13 produces the results shown in Fig. 7.2. The zero effect is reduced and the projection is now a convolution as in the case of far field geometry.

It is worth noting that imaging an idealized point source centred on-axis of the FoV and then applying this correction to the projected image before decoding will flatten the field. If the corrected image were then decoded with the post-processing array, G, it would produce a perfect response function image with reduction in the cross-shaped side-lobes (see Fig. 7.3). This is the ideal response from a point source and thus can be said to be analogous the far-field case. This near-field correction (pre-correlation) is valuable as it flattens the field. Figure 7.4 (a) and (b) demonstrates the projected images of planar square source of size 4^2 cm^2 before and after zero order correction. The corresponding decoded images of the predicted flat field distortion of planar square source of size 4^2 cm^2 before and after zero order correction are shown in Fig. 7.5.

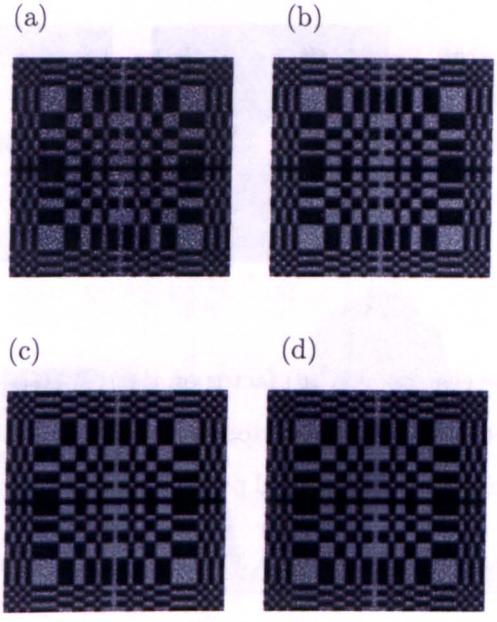

Figure 7.2: This demonstrates that applying a zero order correction to the projected images shown in Fig. 7.1 minimises the effect of $\cos^3(\theta)$ factor: the corrected projected image with (a) z=40 cm, (b) z=20 cm, (c) z=10 cm, (d) with z=4 cm.

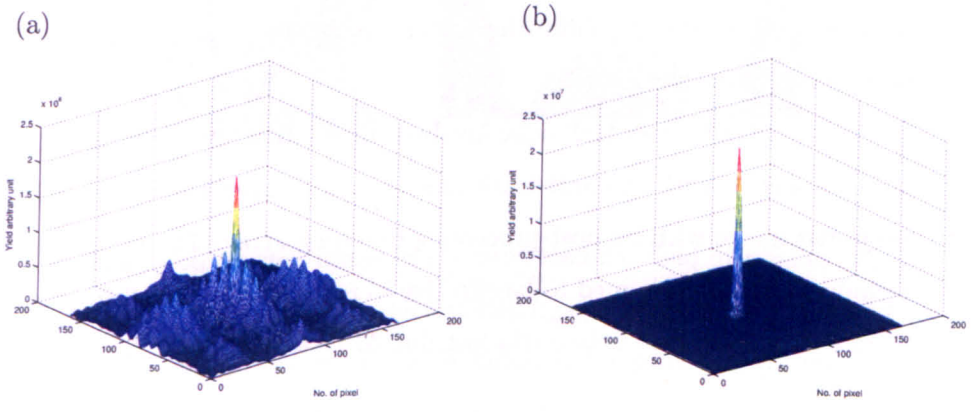

Figure 7.3: The reconstructed image of an on-axis point source in air from PRT: (a) with no zero order correction , (b) with zero order correction demonstrating the slight removal of the cross shaped side lobe. The noise effects and the effect of mask thickness are demonstrated in both case.

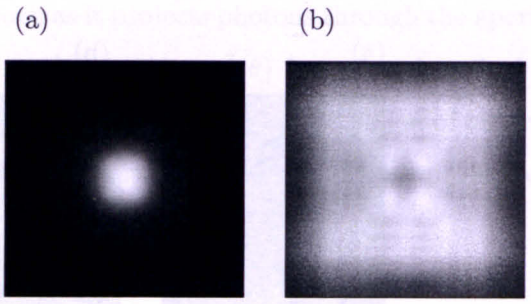

Figure 7.4: The effect of $\cos^3(\theta)$ factor on the projected image of a planar square source of size 4×4 cm^2 with source-to-detector distance, z=4 cm: (a) with no zero order correction , (b) with zero order correction. All projected images were obtained from the PRT method.

7.1.2 Mask/Anti-Mask Correction

All the masks investigated in this thesis have an interesting property that one can generate the mask and its negative (anti-mask) along with the decoding patterns, G, for each one. The anti-mask is given by interchange of the opaque and transparent the mask elements. Figure 7.6 show an exemplar of mask and the anti-mask patterns of MURA. Such mask pattern possesses a 90^o antisymmetry about its centre. This means that the anti-mask can be obtained by simply rotating the mask by 90^o. Thus, the use of such mask patterns reduces the cost and simplifies the associated moving mechanisms if such masks were to be physically constructed [108].

The mask anti-mask technique involves taking two separate images: one with the mask and the second with the anti-mask and then add these two images after decoding each projected image with its post-processing decoding array. The use of the mask/anti-mask technique has been claimed to be effective in reducing the near field artefacts [104] as well as recovering signal-to-noise-ratio lost due to systemic non-uniformity in the background [108, 76].

To demonstrate the performance of this technique for SM imaging a cube lesion of size 1×1×1 mm^3 (with TBR equivalent to 100:1) embedded in a hot 3D phantom of 2×2×2 cm^3 produced from the PRT method was investigated. Two separate images were simulated one with the mask (A^+) and the second with the anti-mask (A^-) in each case as demonstrated in Fig. 7.7. The first projected image from the mask reconstructed by

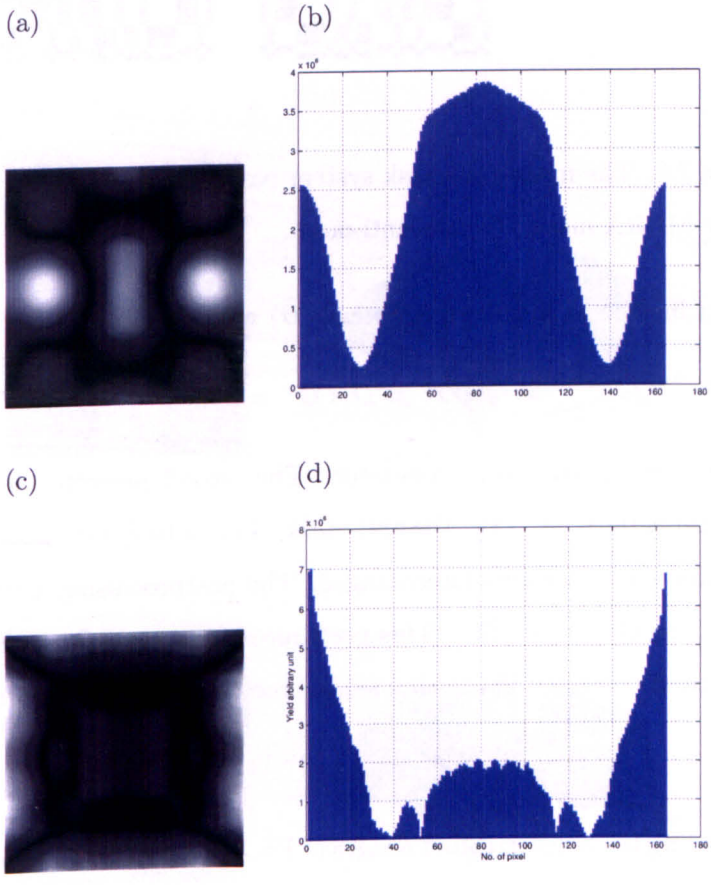

Figure 7.5: The reconstructed image of the predicted flat field distortion of planar square source (of 4×4 cm^2) using PRT: (a) the decoded image (obtained from Fig. 7.4 (a)) before zero order correction, (b) a vertical profile through centre of (a), (c) the decoded image after zero order correction (obtained from Fig. 7.4 (b)), (d) vertical profile through the centre of the corrected decoded image.

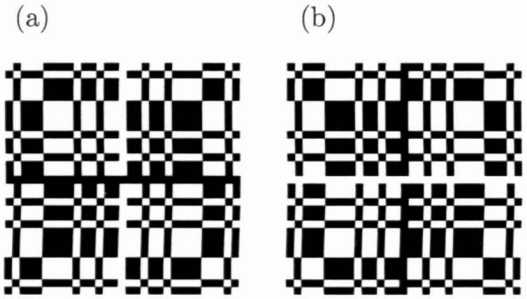

Figure 7.6: The mask anti-mask system based on MURA of 31×31 matrix: (a) antisymmetric MURA mask , (b) the anti-mask.

correlating the mask projected image (D) with the postprocessing array G^+

$$I^+ = D \times G^+ = O \times G^+ \times A^+ \tag{7.14}$$

where $\times$ is the correlation operator. The second projected image is with the negative aperture pattern (A^-) i.e. the anti-mask. This is basically the same as the mask but with open and close elements interchanged. The postprocessing array G^- is a complement of the G^+ i.e $G^- = (-1)G^+$. This postprocessing array, G^-, must be used for correlating the second projected image so a second reconstructed image is now given by:

$$I^- = D \times G^- = O \times G^- \times A^- \tag{7.15}$$

Adding the two correlated images of Fig. 7.7 produced the result given in Fig.7.8. This shows that some the artefacts may be reduced by using the mask/antimask correction technique. This is because by adding Eq. 7.14 and Eq. 7.15 one obtains:

$$I = O \times G^+ \times A^+ + O \times G^- \times A^- \tag{7.16}$$

According to [76] $A^+ - A^- \equiv G^+$ and thus Eq. 7.16 become:

$$I = O \times [G^+ \times A^+ + G^- \times A^-] \tag{7.17}$$

But $G^- = (-1)G^+$ and thus, Eq. 7.17 become:

$$I = O \times [G^+ \times A^+ - G^+ \times A^-] = O \times G^+ \times [A^+ - A^-] \tag{7.18}$$

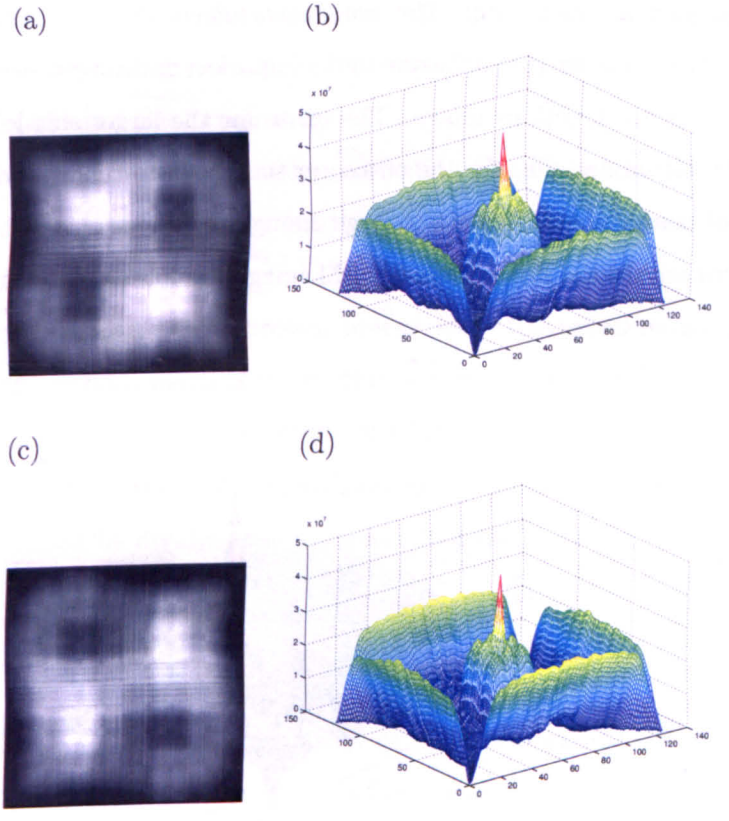

Figure 7.7: The performance of the mask-anti-mask technique: (a) the projected image using the mask, (b) 3D plot of the decoded image of the mask, (c) the projected image using the anti-mask and finally (d) 3D plot of the decoded image using the anti-mask.

But $A^+ - A^- \equiv G^+$ and thus, the final image from the mask/antimask technique is equivalent to [76]:

$$I = O \times G^+ \times G^+ \tag{7.19}$$

This mean that the decoding technique uses the correlation of G with itself. This produces a delta function with side-lobes equal to -1 and thus, reduces the non-uniform background artefacts [76]. The imaging artefacts that are still present in the decoded image of Fig.7.8 are primarily due to the imperfect decoding process, which do not properly produce delta functions image. The cause for the larger side-lobes is believed to be due to the partial decoding for the off-center sources from the extended source object. This is also because the detector is not large enough to fully samples the mask patterns from all sources within the FoV. Thus, for SM imaging another correction method is needed and can do even better.

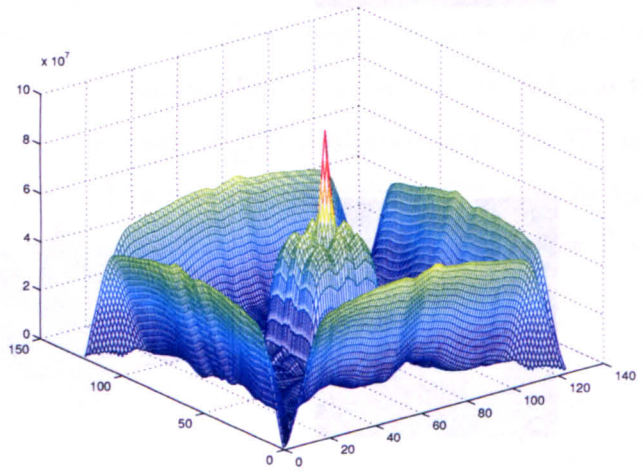

Figure 7.8: A 3D surface plot of the reconstructed image obtained by adding the correlated images obtained from the mask and anti-mask that shown in Fig. 7.7. It should be noted that the mask/anti-mask method provides a slight improvement by a factor of $\sqrt{2}$. Note that it also reinforces the side-lobes.

7.1.3 Background Subtraction

As demonstrated in the previous chapter once the object distribution moved from being point-like to an extended object, as is the case of non-specific uptake in normal breast tissue

imaging, artefacts will arise. This suggests that the raw projection images of the 3D CA-SM data need to be corrected from the effect of unwanted volumetric background artefacts. These background corruption artefacts are object-dependent and a *priori* knowledge is needed to subtract and remove these artefact contributions to the target objects (lesion). Luckily, the unwanted background from non-specific uptake can be predicted and thus, its effects minimized to keep the target object alone. One way to achieve this is through using the PRT method, the other through using the MCS method assuming prior knowledge of the object. Both methods give close representation of the shape and the form of these background artefacts but the former is faster.

To apply the background subtraction correction the shape and the thickness of the breast needs to be identified. In practice the thickness of this is known from the amount of compression used, typically 6 cm. The shape could then be easily captured from an optical image acquired from above compressed breast. Once this information is available then MCS or the PRT method, which is faster, can be used to produce a prediction of the expected background distributed radioisotope distribution. In order to match this predicted background artefact with the observed distribution, first, an 2D initial normalisation factor, N_f, was obtained by dividing the observed data image, O_d by the background data image, B_d, as:

$$N_f(i,j) = \frac{O_d(i,j)}{B_d(i,j)} \tag{7.20}$$

Then the mean value over i and j, M_v, of N_f was obtained. An interval of value containing the "M_v" value was used to calculate the Mean Square Error (MSE) between the observed data (O_d) image and the normalised background data image (B_d) as:

$$MSE = \frac{\sum_{i=1}^{N1}\sum_{j=1}^{N1}[O_d(i,j) - \alpha 1 B_d(i,j)]^2}{N1 \times N1} \tag{7.21}$$

where $N1$ is the size of the image, $\alpha 1 \in [M_v - \beta, M_v + \beta]$ in step of 0.01 and β is set to a value big enough such that the MSE plot respect to $\alpha 1$ would show the minimum. A simple background subtraction technique is performed to remove the resulting scaled background.

To demonstrate this correction method an attempt was made to correct the non-specific uptake associated with imaging a bright lesion (uptake ratio 10:1) in a non-zero

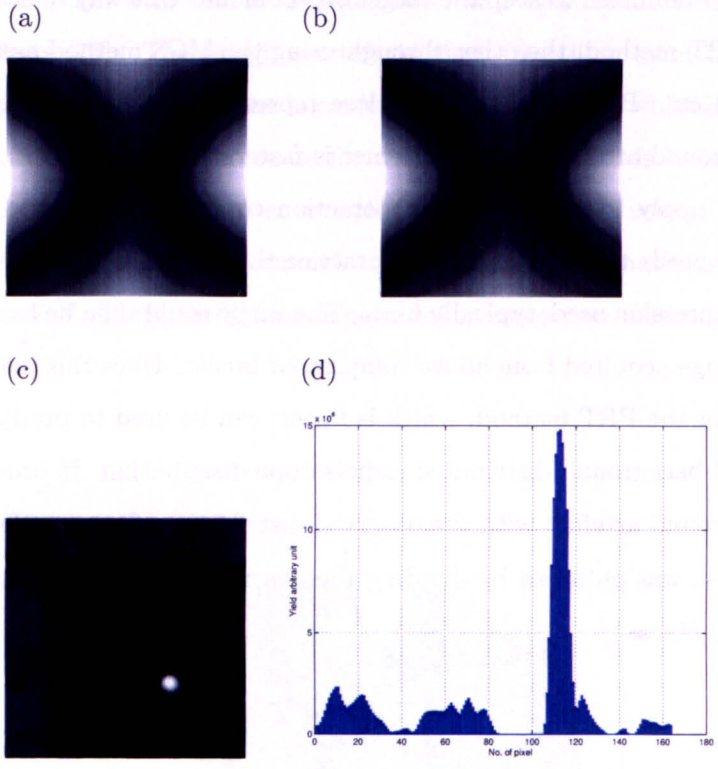

Figure 7.9: The reconstructed image of 3D object of size 10×10×6 cm^3 with off-axis 10 mm diameter sphere (uptake 10:1) placed at depth of 3 cm: (a) raw decoded image from PRT method containing the lesion, (b) the predicted background of similar size phantom, (c) the subtracted image with some background artefacts, (d) diagonal profile through the the subtracted image.

noisy background using the PRT method. In this case a 10 mm spherical lesion was displaced from the centre of the FoV by 2 cm in both the X, Y positions and placed at a depth of 3 cm from the surface of a uniform phantom with size 10×10×6 cm^3. The mask used in this investigation is an MURA of 41×41 elements and the aim was to determine the performance of the MURA camera system in resolving such a lesion. Figure 7.9 demonstrates that the appearance of a large artefact (two arc-shaped valleys in each side of the image) in the decoded image causing subsequent loss in visualising the target lesion. The cause of these gross artefacts are the background contributions from activity above/below and within the decoded plane under consideration. The use of a background subtraction technique is necessary to remove the effect of volumetric background corruption and to resolve the target object as shown in Fig. 7.9 (c). For this particular example the MSE (see Eq. 7.21) as a function of scaling factor is demonstrated in Fig. 7.10 (a) and the figure also illustrates a profile through the centre of the observed data and the scaled background (see Fig. 7.10 (b)).

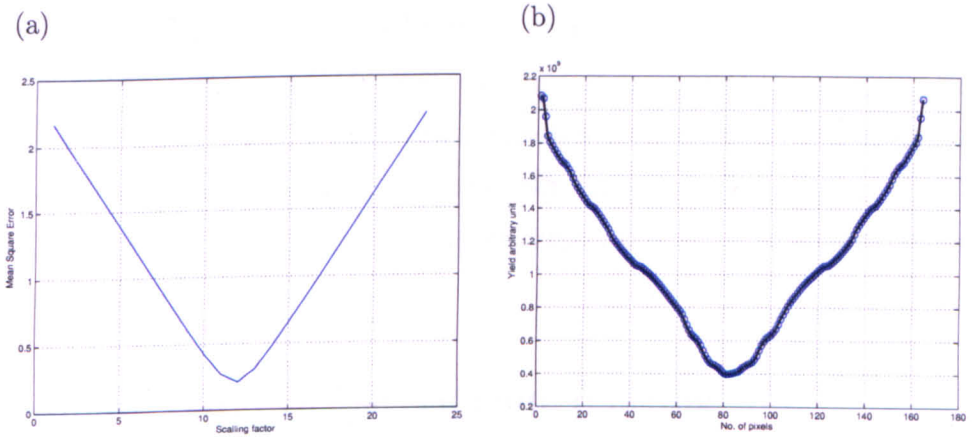

Figure 7.10: Illustration of the method of performing background subtraction: (a) a plot of the MSE as a function of the scaling factor which gives a unique minima for matching the predicted background with the observed data, (b) profiles through the decoded image of the observed data (solid black line) and the scaled background (un-filled circle) demonstrating the excellent fit between the two. Continuous line represents observed data whilst the open circles represent scaled background.

Having demonstrated the near field effect and the imaging artefacts arising when us-

ing MURAs-CA, in the near-field imaging geometries, for breast tumour imaging. Then present and demonstrate how to implement the near-field correction methods in order to alleviate these imaging artefacts and improve the quality of the decoded image. These set of near field artefact corrections are then applied to all the 3D data of a hot lesion in warm background presented in the next chapter.

Chapter 8

Assessment of Coded Aperture for Breast Tumour Imaging

This chapter is divided into three main sections. The first section describes the various investigations carried out with Monte Carlo Simulation (MCS) to assess the performance of a MURA-CA imaging system for breast tumour imaging. The effectiveness and the performance of the CA imaging system was first assessed after the near-field artefact corrections and then compared with two collimator-based systems. The second section presents the various investigations obtained with the Pseudo-Ray-Tracing (PRT) non-Monte Carlo method. The final section in this chapter provides a summary discussion to the main outcome.

8.1 Monte Carlo Breast Tumour Imaging

Using MCS the applications of MURA-CA for breast tumour imaging was first assessed and then compared with two collimator-based image formation methods. These image formation methods are parallel hole collimators namely the Low Energy High Resolution (LEHR) collimator and the Ultra-High Resolution (UHR) collimator. The aim was to assess and evaluate the effectiveness and the performance of these image formation methods under a variety of clinical imaging situations. These image formation methods were quantitatively assessed in term of lesion contrast and lesion resolution.

8.1.1 Coded Aperture Breast Tumour Imaging

The current MCS investigations consider the MURA-CA SM imaging using a standard clinical gamma camera (without a collimator). All the CA-SM results presented in this section have been corrected from the near-field artefacts as described in chapter 7. To assess the CA imaging system this section is divided into two subsections: the first subsection present the CA-SM results obtained from whole body torso phantom. The second subsection present the CA-SM results obtained from isolated breast phantom. In all craniocaudal projected images were simulated as a function of Tumour-Background-Ratio (TBR) but with different lesion sizes placed at fixed depth (3 cm).

Imaging using 3D Body Torso Phantom

As demonstrated in chapter six, the imaging geometry shown in Fig. 6.2 requires first proper shielding from non-specific background tracer uptake and then corrections from the near-field imaging artefacts (see chapter 7). The former is necessary due to the open field geometry associated with the MURA-CA to shield the CA-camera from the torso and the heart. The latter is the main source of background noise due to its high level of radiotracer concentration. This has been achieved by shielding the CA and camera from the background torso/cardiac flux by placing 1.5 mm tungsten sheets on the off-side of the breast, and around all surfaces which could geometrically emit photons through to the CA. This effectively removes most of the unwanted torso/cardiac flux as demonstrated in Fig. 6.5. Before presenting the results the CA-SM MCS, data have been first corrected for the near field distortion described in section 7.1. These post-simulation corrections were necessary to remove the effect of volumetric background corruption caused by systematic decoding artefacts and thus, to improve the lower limit on tumour detection, in terms of contrast and resolution. In here only zero order correction, first order correction and background subtraction corrections are considered. Second order correction (mask/antimask technique) was only applied for particular cases.

(a) The Effect of Finite Lesion Size

Initially, the effect of finite lesion size is also investigated by measuring the tumour visibility in the decoded image as a function of TBR, ranging from a TBR of 5:1 to a highly

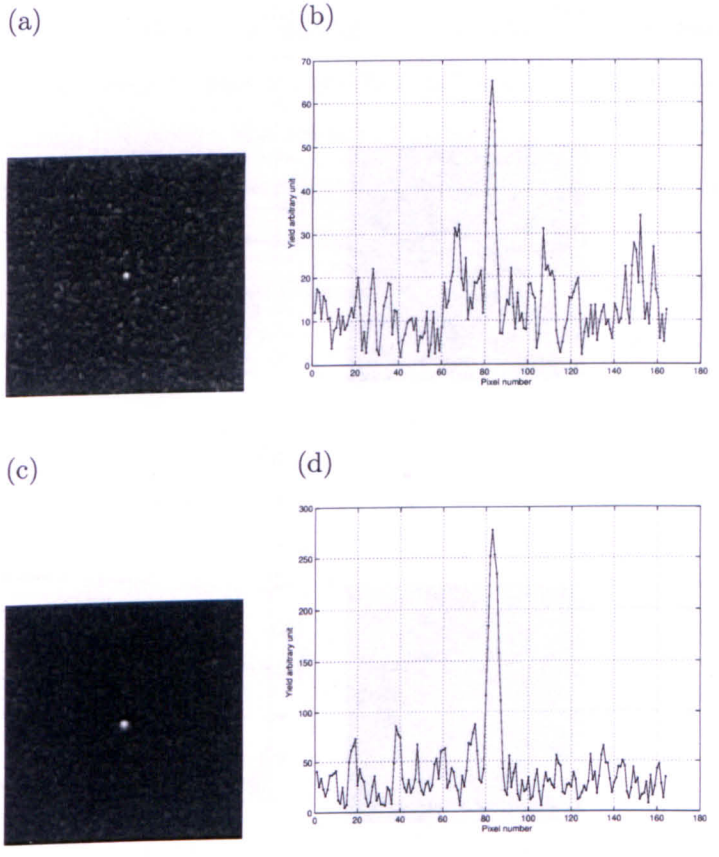

Figure 8.1: A plot of the decoded images obtained from the geometry shown in Fig. 6.2 of a 2 and 4 mm diameter lesion respectively: (a) the decoded image of a projected image of 2 mm diameter lesion with TBR 5:1, (b) the horizontal profile through the centre of (a), (c) the decoded image of a projected image of 4 mm diameter lesion with TBR 5:1, (d) a horizontal profile taken through the centre of (c). Note the camera has been shielded as described in the text and the post simulation corrections include zero order, first order and background subtraction corrections.

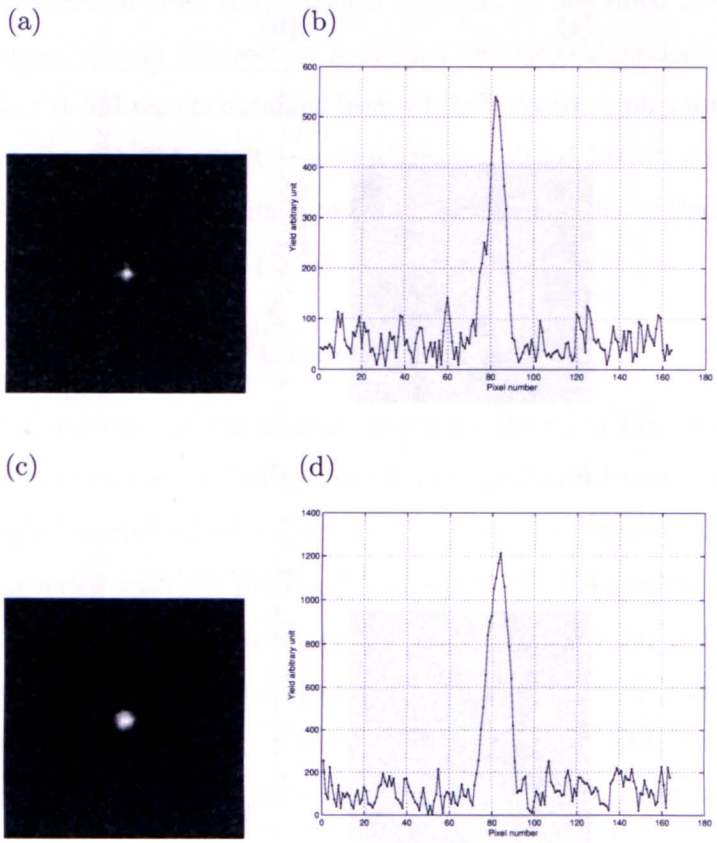

Figure 8.2: A plot of the decoded images obtained from the geometry shown in Fig. 6.2 of a 6 and 10 mm diameter lesion respectively: (a) the decoded image of a projected image of 6 mm diameter lesion with TBR 5:1, (b) the horizontal profile through the centre of (a), (c) the decoded image of a projected image of 10 mm diameter lesion with TBR 5:1, (d) a horizontal profile taken through the centre of (c). Note the camera has been shielded as described in the text and the post simulation corrections include zero order, first order and background subtraction corrections.

idealised case of TBR of 100:1. The aim was to analyze the detectability as a function of the tumour size, by varying the diameter and hence the In all simulated data the tumour was located at the centre of the breast phantom at a depth of 3 cm. Figures 8.1 and 8.2 show exemplar plot of the decoded images and the corresponding image profiles of 2, 4, 6 and 10 mm lesions with uptake ratio of 5:1. The quality of the decoded images are slightly affected by the limited photon statistics that has an effect on the image contrast and spatial resolution. However, the results of these simulation studies show that with the shielding and the near field corrections and with a TBR ratio as low as 5:1, all lesions have been clearly visualized. These are encouraging results as it demonstrates that the MURA-CAs coupled to conventional γ-camera may have a good performance in breast tumour imaging application.

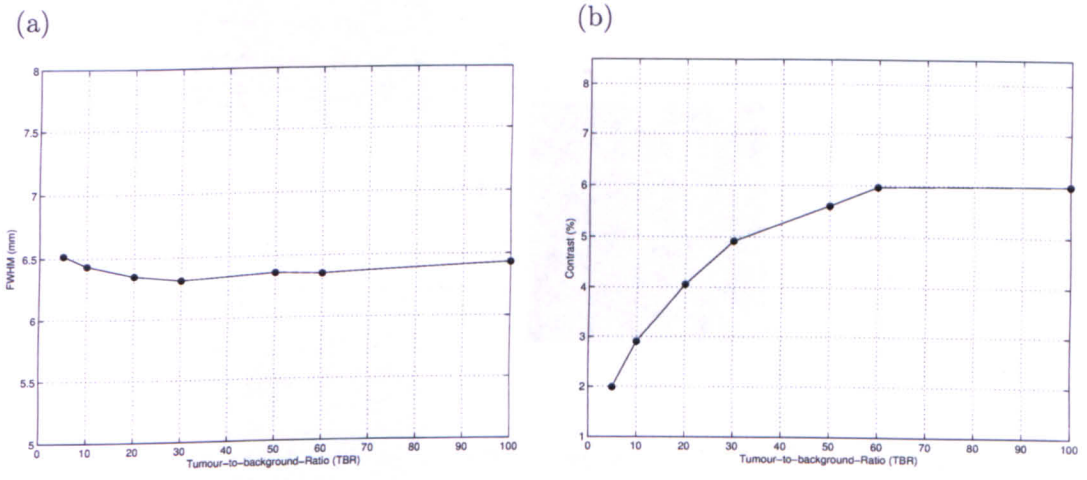

Figure 8.3: Quantification of the MCS data of MURA-CA camera in detecting a signal in a hot background: (a) the tumour FWHM as a function of TBRs. Values calculated from data images of 10 mm lesions, (b) tumour contrast as a function of TBRs for 10 mm lesion. Values shown are calculated from Eq. 6.1.

To demonstrate this further the effectiveness of the MURA-CA imaging system need to be quantitatively assessed. This was achieved by calculating the lesion spatial resolution, in term of Full-Width-Half-Maximum (FWHM), and lesion contrast as a function of TBR. Figure 8.3 (a) and (b) show the calculated FWHM and contrast for a 10 mm diameter lesion using the full 3D torso phantom simulation geometry. Due to the limited photon

statistics and the partial volume effect, the observed tumour FWHM values are smaller than the actual size of the lesion.

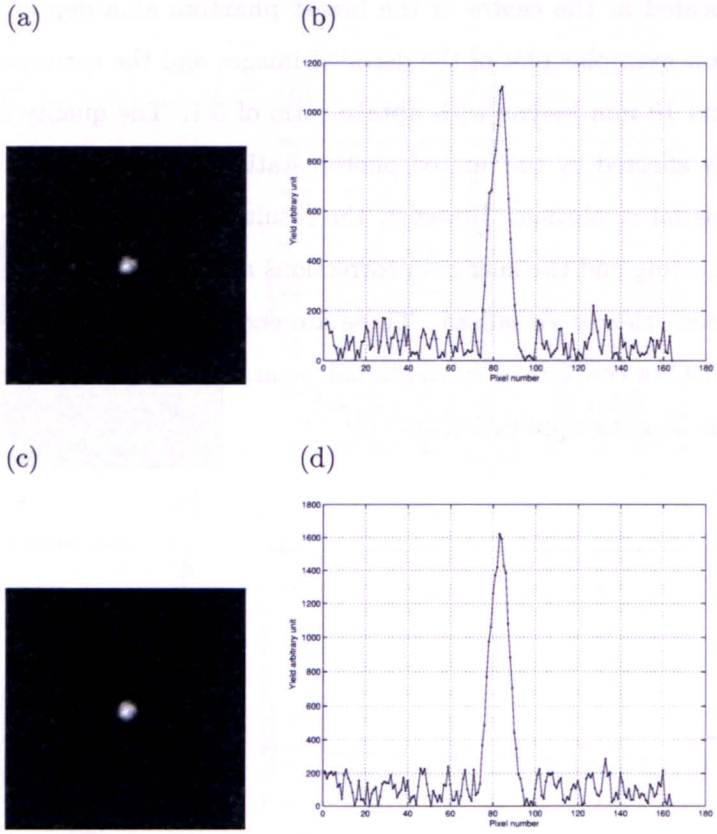

Figure 8.4: The decoded images and the corresponding profiles obtained from the MCSs of a 3D phantom containing a 10 mm diameter lesion: (a) the decoded image with TBR of 3:1, (b) a horizontal profile taken through the centre of (a), (c) the decoded with TBR of 5:1, (d) a horizontal profile through the centre of (c).

Imaging a Tumour in Isolated Breast Phantom

he MCS geometry is the same as shown in Fig. 6.2 but with no torso and heart i.e. no shielding is required. Thus, this imaging geometry only considers a spherical lesion impeded inside the breast of $10\times10\times6$ cm^3 at 3 cm depth from the surface of the breast. A breast thickness of 6 cm was chosen based on the assumption of light breast compression emulating SM in the cranio-caudal view . The detector is a planar block 32.8×32.8 cm^2

by 0.95 cm thick of NaI at a distance of 30 cm from the coded mask. Since the overall spatial resolution of a CA camera is predominantly affected by the detector intrinsic spatial resolution (3.7 mm in this case) the chosen geometry provides an object magnification of 3. The mask is based on a 41×41 MURA pattern and composed of 2×2 mm^2 tungsten elements with a thickness of 1.5 mm, providing ≈ 99.4% photon attenuation for 140 keV photons at normal incidence.

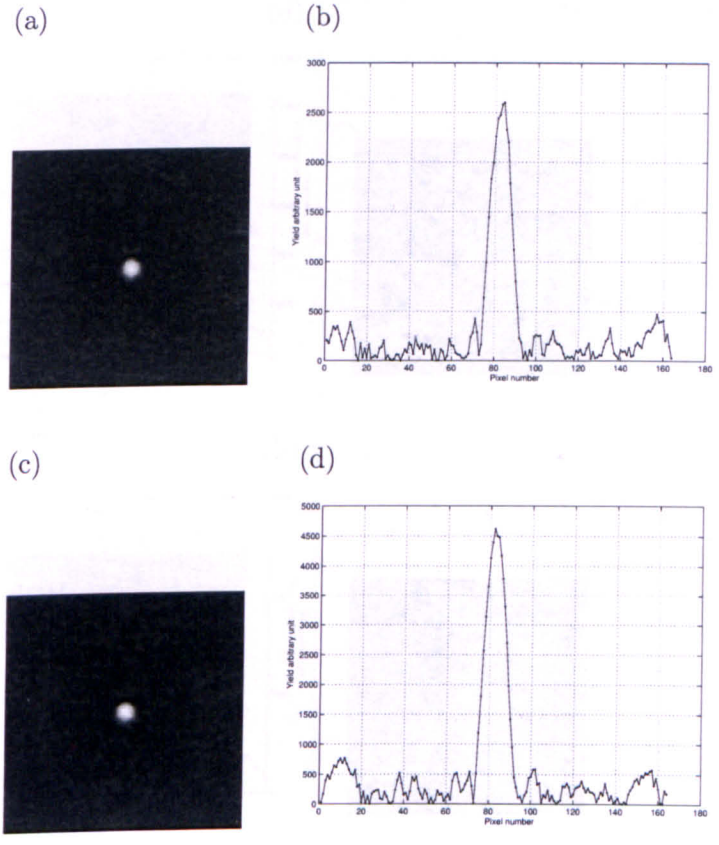

Figure 8.5: The decoded images and the corresponding profiles obtained from the MCSs of a 3D phantom containing a 10 mm diameter lesion: (a) the decoded image with TBR of 10:1, (b) a horizontal profile taken through the centre of (a), (c) the decoded with TBR of 20:1, (d) a horizontal profile through (c).

The background radiation simulated from the breast was 2×10^9 photons. A variations in lesion sizes and TBR concentration were simulated. The TBR value was calculated by dividing the number of photons from the tumour per cm^3 by the number of photons from

the background per cm^3. Two post-simulation near field artefacts corrections (zero order correction and background subtraction) have been applied to all CA-SM data. Initially, the effect of TBR improvement on the quality of the decoded image and on lesion detectibility was investigated. The results from these investigations are shown in the subsequent Figs. 8.4- 8.7. These demonstrate the SM imaging characteristic of the MURA-CA imaging system.

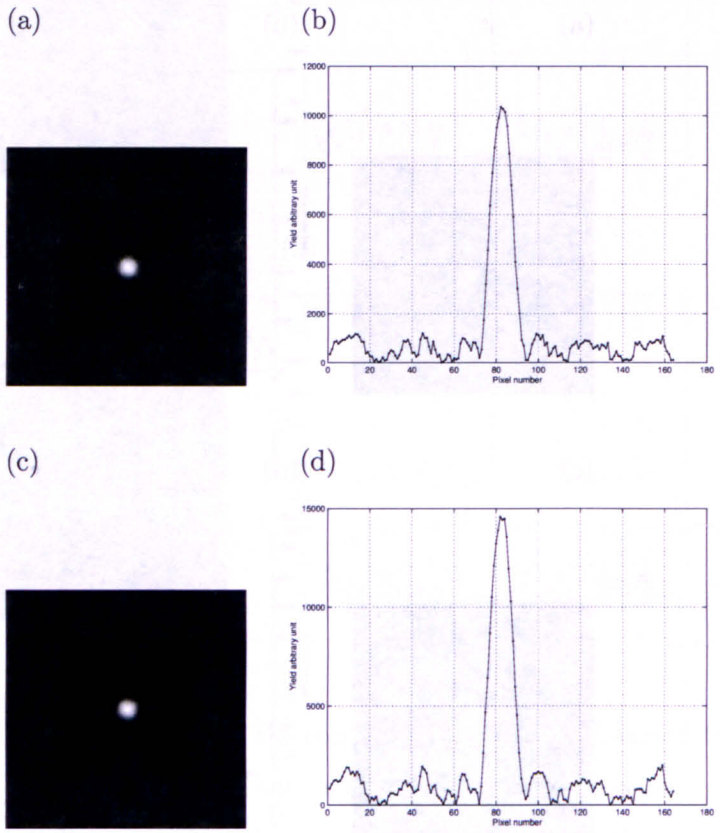

Figure 8.6: The decoded images and the corresponding profiles obtained from the MCSs of a 3D phantom containing a 10 mm diameter lesion: (a) the decoded image with TBR of 40:1, (b) a horizontal profile taken through the centre of (a), (c) the decoded with TBR of 60:1, (d) a horizontal profile through (c).

To evaluate the tumour detectability the MURA-CA breast tumour imaging approach needs to be assessed. This is acheived by quantitative calculation of the lesion contrast, FWHM and the detected tumour event under a variety of clinical imaging situations. In

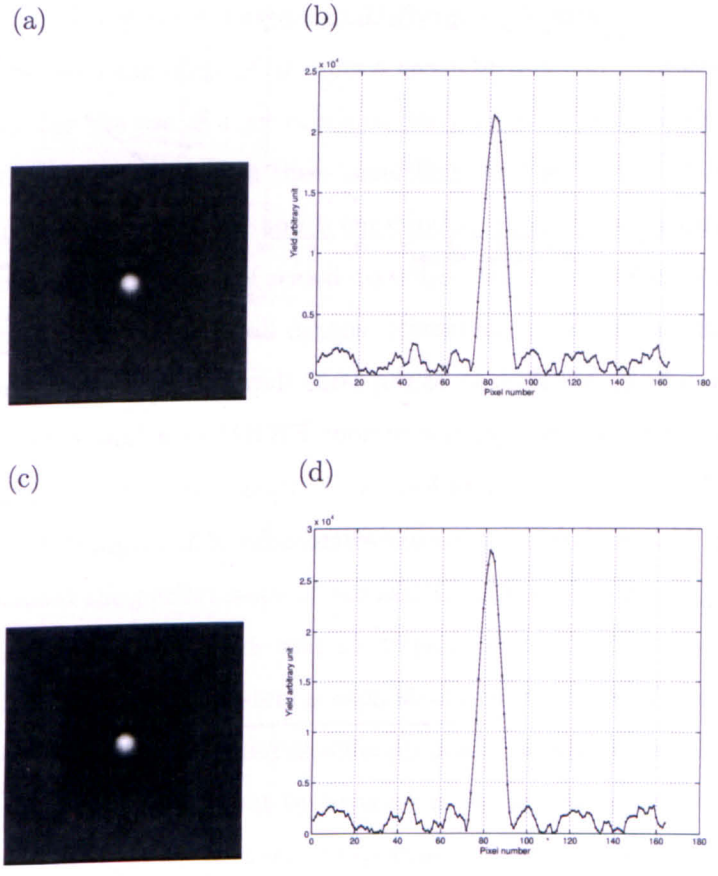

Figure 8.7: The decoded images and the corresponding profiles obtained from the MCSs of a 3D phantom containing a 10 mm diameter lesion: (a) the decoded image with TBR of 80:1, (b) a horizontal profile taken through the centre of (a), (c) the decoded with TBR of 100:1, (d) a horizontal profile through (c).

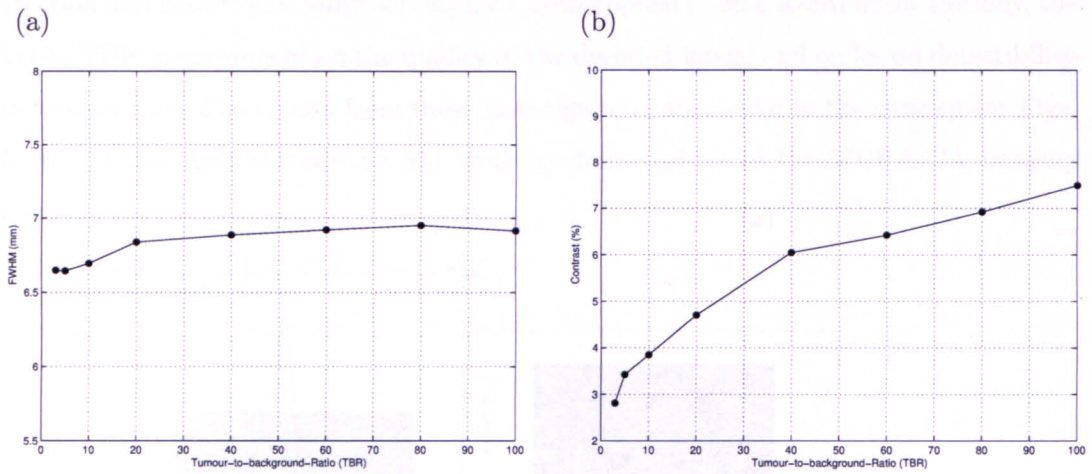

Figure 8.8: Quantification of the MCS data of MURA-CA camera in detecting a signal in a hot background: (a) the tumour FWHM as a function of TBRs. Values calculated from data images of 10 mm lesions, (b) tumour contrast as a function of TBRs for 10 mm lesion. Values shown are calculated from Eq. 6.1.

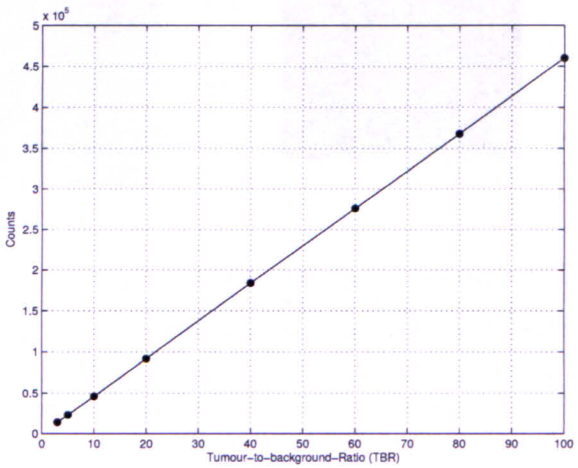

Figure 8.9: The number of tumour detected photon from a 10 mm diameter lesion using the MURA-CA camera coupled to full-size standard γ-camera as a function of TBR.

here the results from the 10 mm diameter lesion placed at a fixed position with 3 cm depth are presented. Tumour FWHM and contrast obtained by the MURA-CA camera are drawn as a function of TBR as in Fig. 8.8 (a) and (b) respectvely. The number of tumour detected photons from the MURA-CA as a function of TBR is shown in 8.9.

(a) The effect of Imaging a Lesion at Different Depths

This section investigate the effect of imaging a lesion at different depths. The aim was to demonstrate whether the use of a set of scaled decoding steps are capable of detecting a lesion placed at unknown depth. In these investigations the 10 mm diameter lesion was systematically placed at 3.5, 4, 4.5 and 5 cm depths. From these investigations and for all TBRs studied, the use of a set of scaled decoding steps for each MCS data are able to successfully construct the lesion at all depths. Exemplar plots from 4 different MCS data for a 10 mm diameter lesion (uptake of 10:1) placed at different depths are shown in 8.10 and 8.11.

(b) The effect of Imaging Mutiple lesions

Having demonstrated the performance of the MURA-CA system in detecting a spherical lesion positioned on the central axis and at different depths, this section demonstrates whether the MURA-CA imaging system is capable of detecting one or more lesions located off-central axis i.e. the lesion(s) placed at different positions within the phantom. Two set of MCS experiments were carried out by imaging a 10 mm diameter lesion(s) with TBR of 5:1 but at fixed depth. In the first set of experiments only one lesion is simulated where as in the second set of experiments 2 and 3 spherical lesions were simulated respectively. These experiments were designed to demonstrate the effect of both off-central axis lesion decoding. Figure 8.12 shows the decoded images of 10 mm diameter lesions (uptake 5:1) placed at different positions within the phantom. This demonstrates that with only zero-order correction and background subtraction even the off-central lesion can be clearly visualised. In an attempt to further enhance the lesion and reduce the side-lobes artefacts shown in Fig. 8.12 the mask/antimask correction technique (see section 7.1.2) was used. The result from this double simulations is shown in Fig. 8.13. This technique slightly smooth the decoded image but the image may further enhanced by the use of image processing techniques.

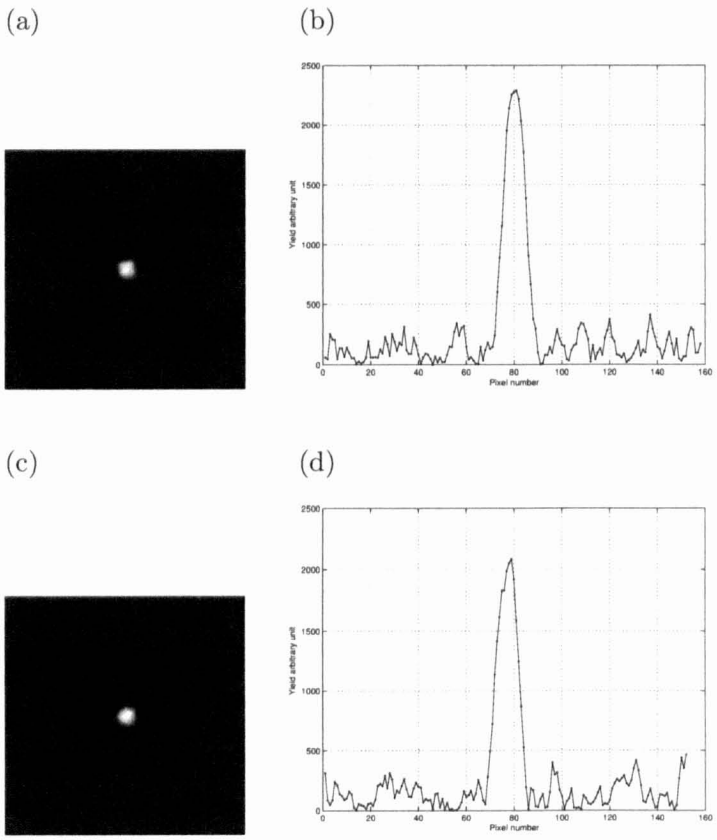

Figure 8.10: The decoded images and the corresponding profiles obtained from the MCSs of a 3D phantom containing a 10 mm diameter lesion at different depths but with uptake of 10:1: (a) the decoded image with the lesion placed at depth 3.5 cm, NB: $\approx$ 41k photons detected by the detector, (b) a vertical profile taken through the centre of (a), (c) the decoded with the lesion placed at 4 cm, NB: $\approx$ 36k photons hit the detector, (d) a vertical profile drawn through the centre of (c).

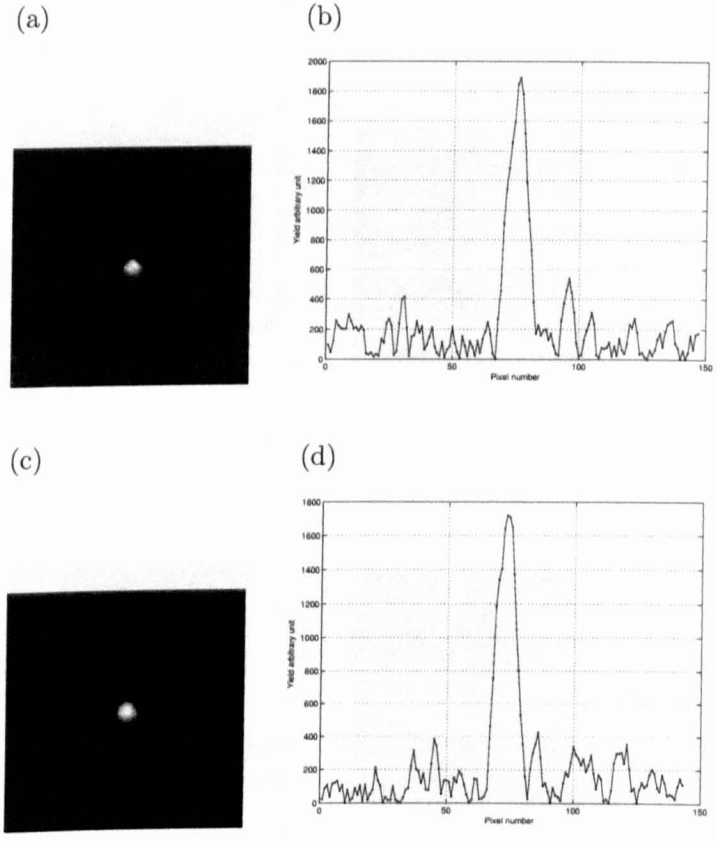

Figure 8.11: The decoded images and the corresponding profiles obtained from the MCSs of a 3D phantom containing a 10 mm diameter lesion at different depths but with uptake of 10:1: (a) the decoded image with the lesion placed at depth 4.5 cm, NB: $\approx$ 32k photons detected by the detector, (b) a vertical profile taken through the centre of (a), (c) the decoded with the lesion placed at 5 cm, NB: $\approx$ 28k photons detected by the detector, (d) a vertical profile drawn through the centre of (c).

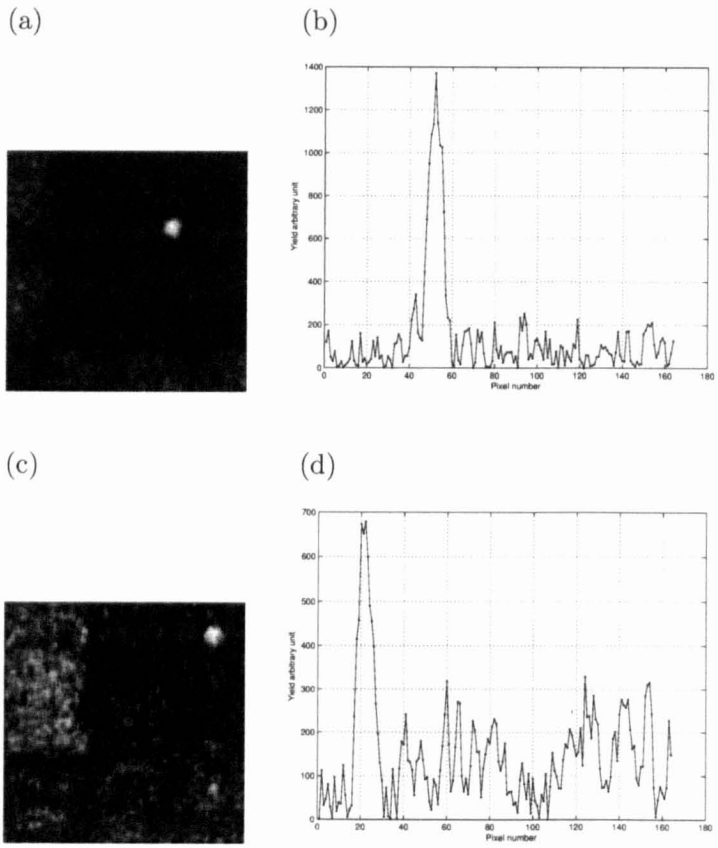

Figure 8.12: The decoded images and the corresponding profiles obtained from the MCSs of a 3D phantom containing a 10 mm diameter lesion: (a) the decoded image with a TBR of 5:1 (lesion was displaced from the centre of the FoV by 2 cm along both the horizontal and vertical directions), (b) a diagonal profile through (a), (c) the decoded image with TBR of 5:1 (lesion was displaced from the centre of the FoV by 4 cm along both the horizontal and vertical directions), (d) a diagonal profile through (c).

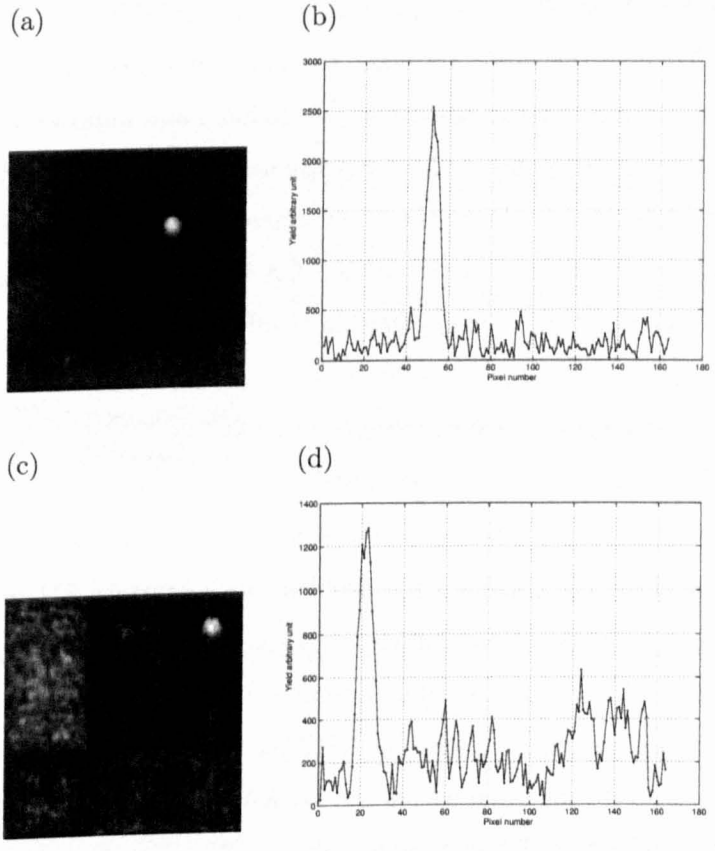

Figure 8.13: The decoded images using the mask/antimask technique and the corresponding profiles obtained from the MCSs of a 3D phantom containing a 10 mm diameter lesion: (a) the decoded image with a TBR of 5:1 (lesion was displaced from the centre of the FoV by 2 cm along both the horizontal and vertical directions), (b) a diagonal profile through (a), (c) the decoded image with TBR of 5:1 (lesion was displaced from the centre of the FoV by 4 cm along both the horizontal and vertical directions), (d) a diagonal profile through (c).

Having demonstrated the effect of off-centra axis lesion on the decoded image and lesion detectibility, in here the effect of multiple lesions are demontrated. Figure 8.14 shows exampler plot of the decoded images of 2 and 3 spherical lesions (of 10 mm diameter and uptake of 5:1) respectively. In the case of two lesions (Fig. 8.14 (a)), both lesions are clearly visualised. However, in Fig. 8.14 (c) the third lesion is hardly seen. Thus, for this particular case the mask/antimask technique was used in order to allivate some of the artefacts (caused by the off-central axis lesions) and improve image contrast. As demonstrated in Fig. 8.15 only a slight improvement has been achieved with the mask/antimask correction technique. From these investigations one can infer that with a larger imaging detector one would expect the MURA-CA imaging system to have a higher performance in detecting multiple lesions particularly off-central axis lesions.

(c) The effect of Imaging small Lesions

The above MCS results demonstrated in this section show that the MURA-CA imaging system coupled to the conventional γ-camera has a potential in detecting a 10 mm lesion down to TBR of 3. One of the problem of the current SM technique using a standard γ-camera with the LEHR collimator is the detection of lesion lower than 1 cm size [51, 89, 84, 93]. This simulated the development of a high resolution small FoV dedicated γ-camera that also equiped with the UHR parallel-hole collimator [50, 94, 46, 47, 45, 48, 49]. To demonstrate the capability of the MURA-CA in detecting small lesions two lesion sizes of 5mm and 8 mm diameter were selected. In each case two fixed TBRs of 5:1 and 10:1 were simulated and the results from these simulations are presented in Figs. 8.16 and Figs. 8.17.

To assess the CA-SM system performance one needs to compare the CA-SM data with the corresponding obtained from the LEHR collimator and the UHR collimator image formation methods. The aim was to assess each imaging system separately and to observe what factors that have an effect on lesion Note that all the MCS data were obtained under similar imaging conditions for true comparison with the MURA-CA.

8.1.2 Breast Tumour Imaging using LEHR Collimator

Planar Scintimammography (SM) is generally performed using a LEHR parallel-hole collimator coupled to full-size clinical γ-camera. This section evaluates the SM imaging

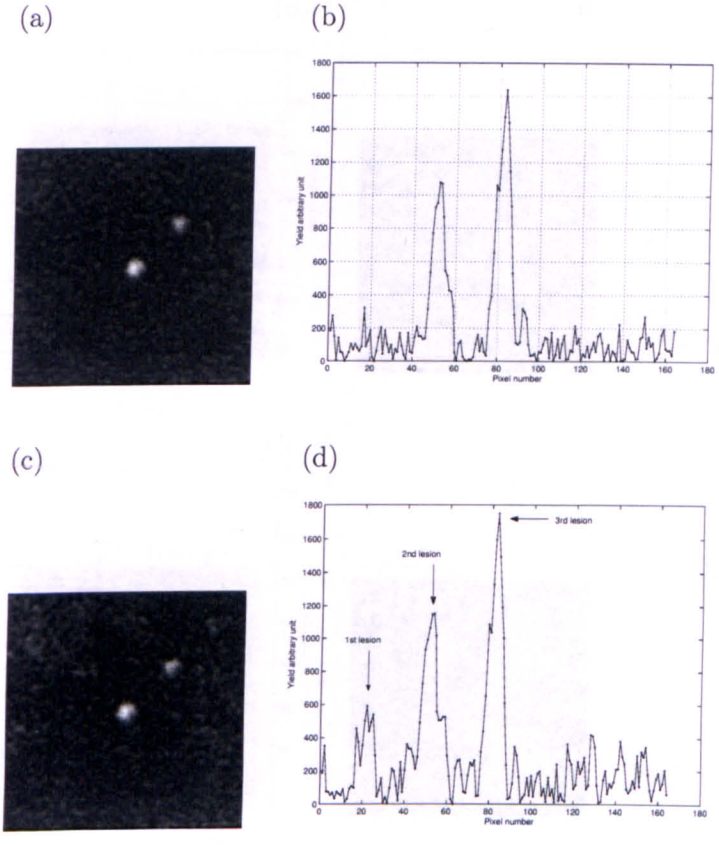

Figure 8.14: The decoded images and the corresponding profiles obtained from the MCSs of a 3D phantom containing 2 or 3 lesions: (a) the decoded image with two lesions with TBR of 5:1, (b) a diagonal profile through (a), (c) the decoded image with TBR of 5:1, (d) a diagonal profile through (c).

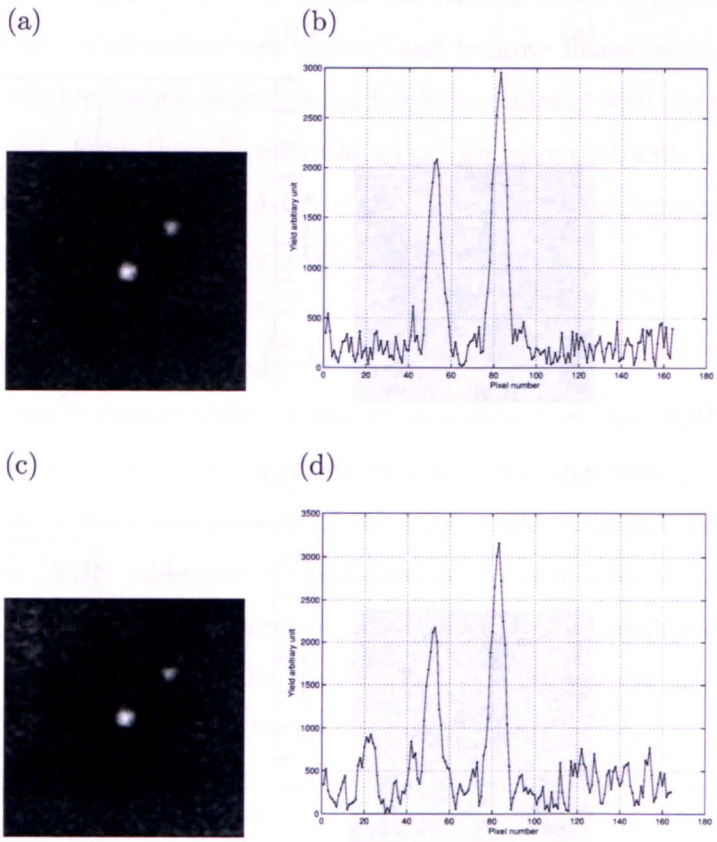

Figure 8.15: The decoded images and the corresponding profiles obtained from the MCSs of a 3D phantom containing 2 or 3 lesions using the mask/antimask technique: (a) the decoded image with two lesions with TBR of 5:1, (b) a diagonal profile through (a), (c) the decoded image with TBR of 5:1, (d) a diagonal profile through (c).

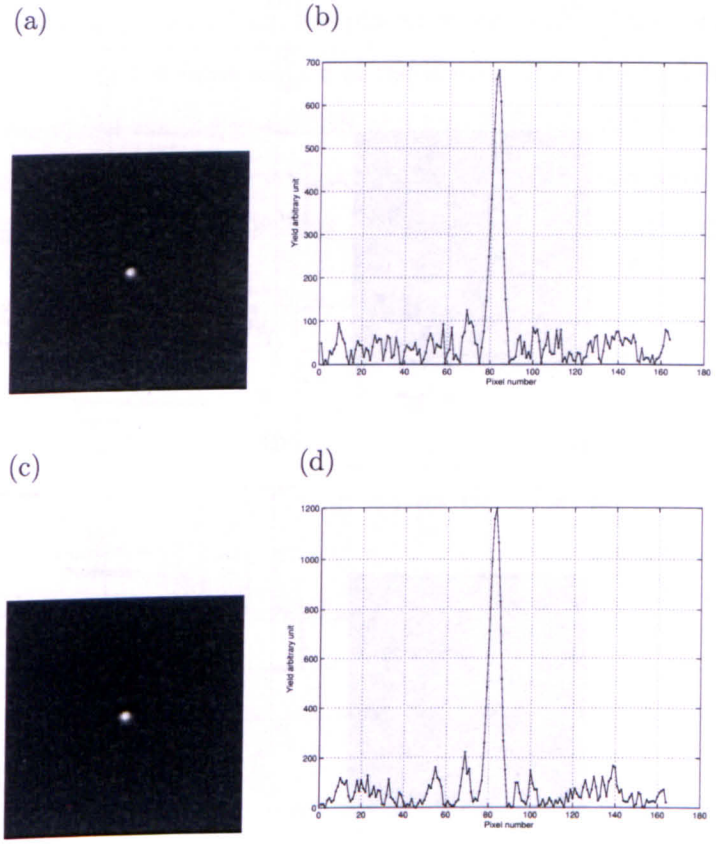

Figure 8.16: The decoded images and the corresponding profiles obtained from the MCSs of a 3D phantom containing a 5 mm diameter lesion: (a) the decoded image with TBR of 5:1 (NB: ≈3k photons detected by the detector) (b) a horizontal profile taken through the centre of (a), (c) the decoded with TBR of 10:1 (NB: ≈5k photons detected by the detector), (d) a horizontal profile through (c).

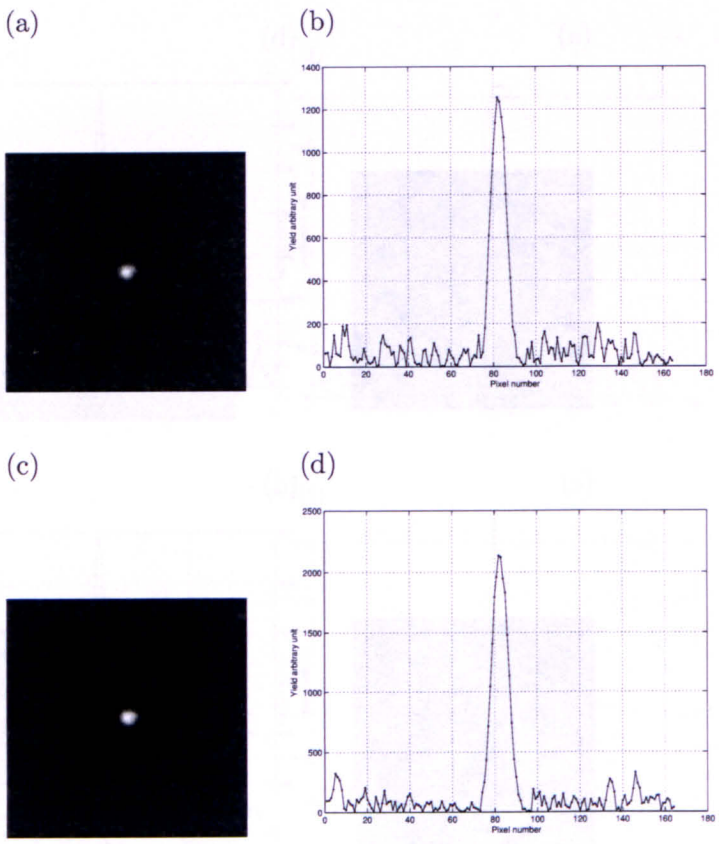

Figure 8.17: The decoded images and the corresponding profiles obtained from the MCSs of a 3D phantom containing a 8 mm diameter lesion: (a) the decoded image with TBR of 5:1 (NB: ≈11k photons get detected), (b) a horizontal profile taken through the centre of (a), (c) the decoded with TBR of 10:1 (NB: ≈23k photons detected by the detector), (d) a horizontal profile through (c).

characteristic of the LEHR collimator to compare it with that previously obtained with the MURA-CA. The simulated parameters of the LEHR collimator is given in Fig. 4.3. The simulated detector was a planar block 40×40 cm by 0.95 cm thick of NaI. A uniform hot breast of size 10×10×6 cm^3, separated from the LEHR collimator by 0.1 cm, was simulated. The background radiation simulated was 2×10^9 photons. A spherical lesion filled with soft tissue of diameter 1 cm was placed at the centre of the Field of View (FoV) at a depth of 3 cm from the front surface of the breast. The tumour level of activity i.e. TBRs values were varied ranging from TBR of 3:1 to TBR of 100:1. The simulated imaging geometry of a realistic phantom is shown in Fig. 8.18. The projected image produced from the simulation composed of 128×128 square pixels of sizes 0.3125×0.3125 cm.

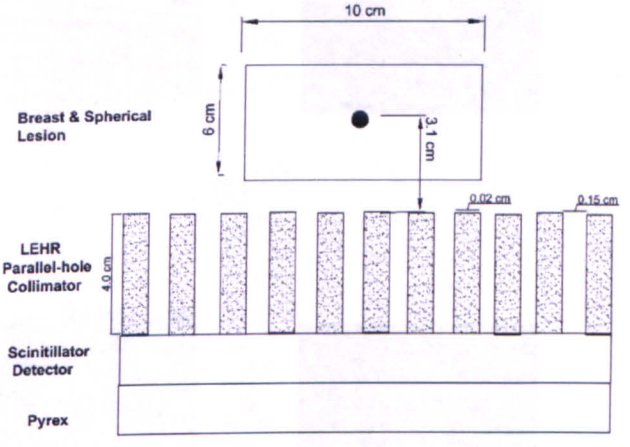

Figure 8.18: The simulated geometry set-up in a longitudinal view (not to scale). The breast phantom is almost touching the collimator and the lesion at 3 cm depth from the surface of the breast. Note that the distance between the centre of the lesion and the collimator surface is 3.1 cm.

Initially, the effects of an improvement on the quality of the projected image and lesion detectability as a function of TBR when imaging with a LEHR collimator was investigated. Figures 8.19-8.22 show the results of the SM imaging characteristic of the LEHR collimator for a 10 mm diameter lesion under different TBRs. The results demonstrate that the quality of the projected image is greatly affected by the TBR value. At low TBR values $\leq$ 5:1 the image is noisy and thus the lesion is hardly visualised. This is mainly due to the limited number of events detected from the tumour. In such case the main source of noise is the

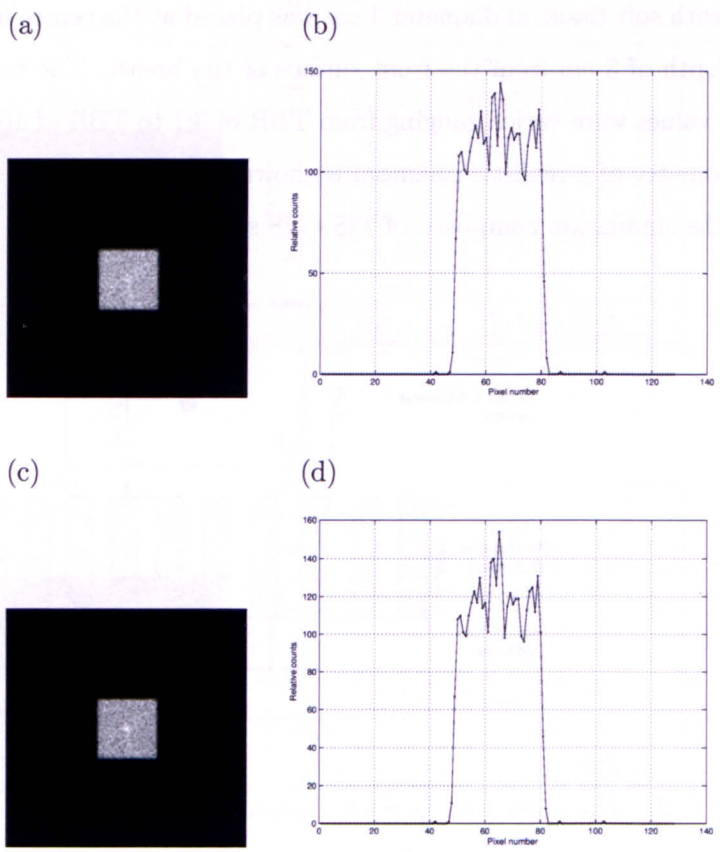

Figure 8.19: The MCS projeced images and the corresponding profiles obtained from 3D phantom containing a 10 mm diameter lesion: (a) the projected image with TBR 3:1, (b) a horizontal profile through the centre of (a), (c) the projected image with TBR of 5:1, (d) a horizontal profile taken through the centre of (c).

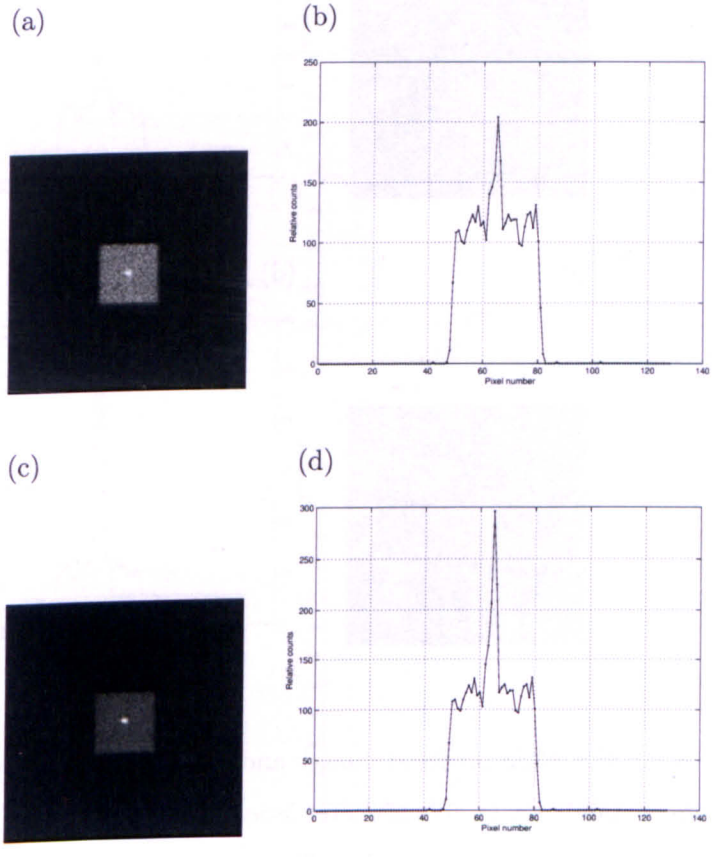

Figure 8.20: The MCS projeced images and the corresponding profiles obtained from 3D phantom containing a 10 mm diameter lesion: (a) the projected image of TBR 10:1, (b) a horizontal profile taken through the centre of (a), (c) the projected image with TBR of 20:1, (d) a horizontal profile taken through the centre of (c). All the images were acquired using the LEHR collimator coupled to the conventional γ-camera.

Poissons noise because the detection is governed by the statistical process.

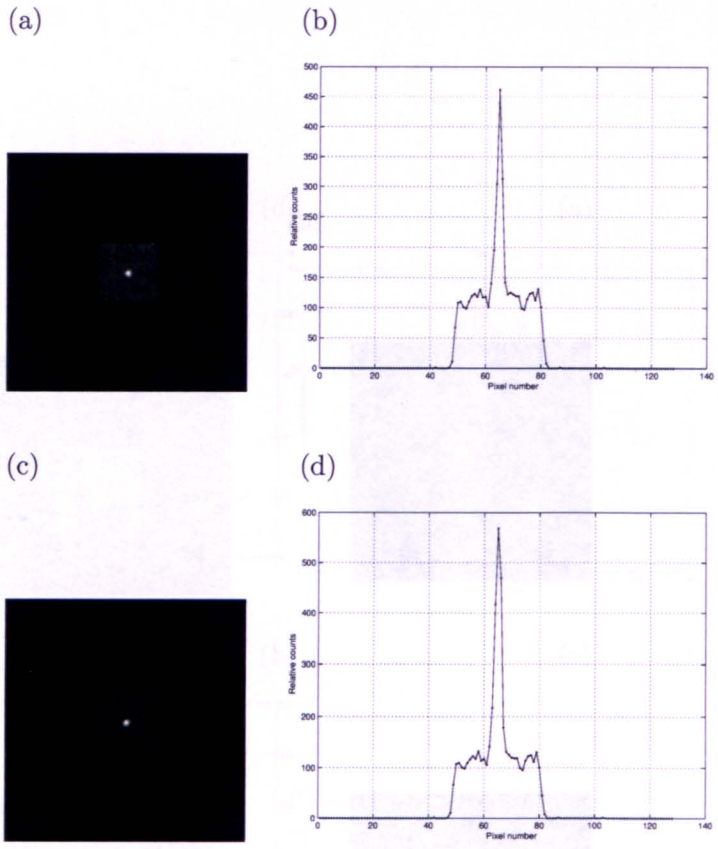

Figure 8.21: The MCS projeced images and the corresponding profiles obtained from 3D phantom containing a 10 mm diameter lesion: (a) the projected image containing a lesion with TBR of 40:1, (b) a horizontal profile taken through the centre of (a), (c) the projected image of TBR of 60:1, (d) a horizontal profile through the centre of (c).

Having demonstrated the projected images and the corresponding profiles acquired using the LEHR collimator coupled to conventional γ-camera as a function of TBR. In here the performance of such camera was evaluated quantitatively by calculating lesion contrast and Full-Width Half-Maximum (FWHM) as a function of TBR. Figure 8.23 (a) and (b) show the calculated FWHM and contrast respectively. Figure 8.23 (b) show that at lower TBRs the nonspecific breast activity significantly affects the observed lesion contrast. Note that for the LEHR collimator, the projeced image of a 10 mm diameter tumour with uptake of 3:1 both the lesion resolution and contrast were difficult to calculate

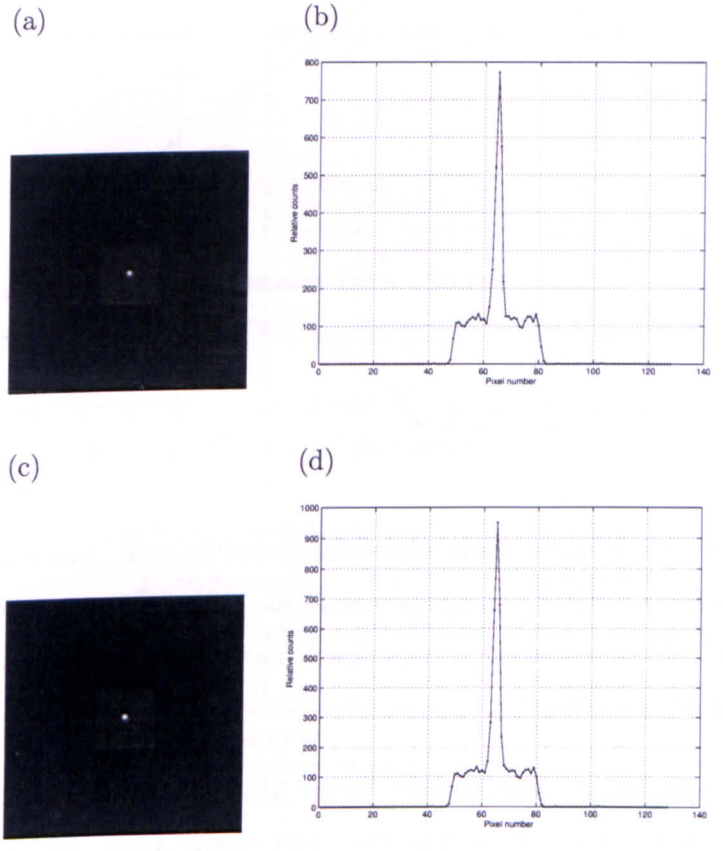

Figure 8.22: The MCS projeced images and the corresponding profiles obtained from 3D phantom containing a 10 mm diameter lesion: (a) the projected image contaning a lesion with TBR of 80:1, (b) a horizontal profile taken through the centre of (a), (c) the projected image containing a lesion with TBR of 100:1, (d) a horizontal profile taken through the centre of (c).

as the image is seriously affected by Poisson noise. The improvement, in contrast values demonstrated at TBR > 10:1 is due to the increase of tumour signal compared to the background. To demonstrate this the total number of detected photon from the tumour was plotted as a function of TBR as shown in Fig. 8.24.

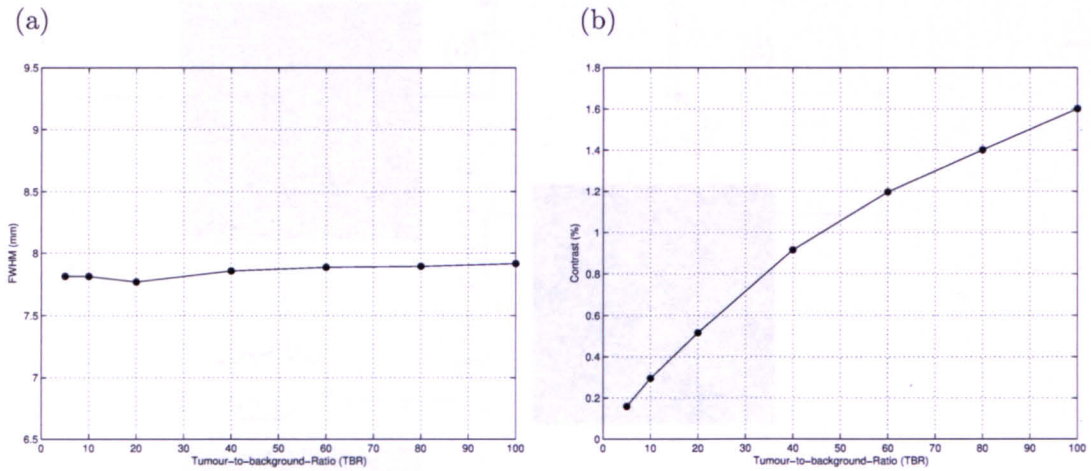

Figure 8.23: Quantification with γ-camera in detecting a signal in a hot background: (a) the tumour FWHM as a function of TBRs. Values calculated from data images of 10 mm lesions, (b) tumour contrast as a function of TBRs before for 10 mm lesion. Values shown calculated from Eq. 6.1.

To investigate the capability of the LEHR parallel-hole collimator in detecting small lesions with sizes less than 1 cm two lesion sizes of 5 mm and 8 mm diameter were selected. In each case two fixed TBRs of 5:1 and 10:1 were simulated and the results from these simulations are presented in Figs. 8.25 and Figs. 8.26. The data showed that due to the low detected photon from the tumour the 5 mm lesion is not visualised and a TBR of 10:1 or higher is required to clearly visualise the 8 mm lesion.

8.1.3 Breast Tumour Imaging using UHR Collimator

In recent years there are a large interest in dedicated γ-cameras for use in breast tumour imaging [130]. One of the commercially available cameras is the LumaGEM camera, *Gamma Medica, inc.*, Northridge [131]. This solid-state Cadmium Zinc Telluride (CZT) γ-camera is equipped with an ultra-high resolution collimator. The imaging FoV of such

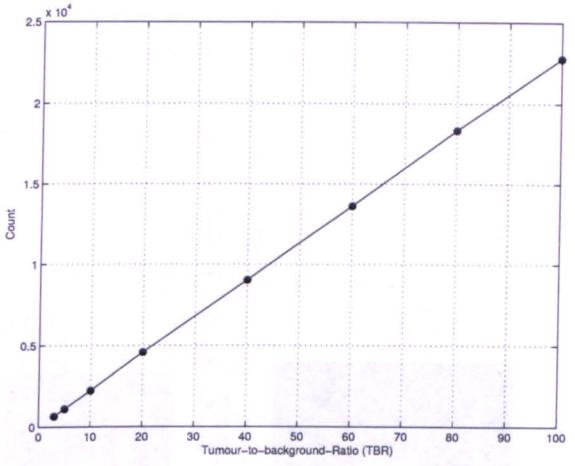

Figure 8.24: The tumour detected photon from a 10 mm diameter lesion as a function of TBR. Values acquired from the MCS of the LEHR coupled to the full-size γ-camera.

camera is 16×20 cm^2 with 2.5×2.5×5 mm^3 (see table 1.3).

Table 8.1: The UHR parallel-hole collimator specifications [131].

Parameters	**Descriptions**
Collimator design	Parallel square holes
Material	Lead
Septa thickness (t)	0.02 cm
Hole size (d)	0.122 cm flat-to-flat
Hole length (l)	2.54 cm
collimator to detector distance (e)	0.1 cm

This section presents the MCS work to the aforementioned CZT camera that utilises a parallel-hole UHR collimator with the parameters shown in table 8.1. The experimental set-up for the UHR parallel-hole collimator MCS work is shown in Fig. 8.27. This MCS set-up and the imaging conditions used here is exactly the same as the LEHR collimator investigations. For the simulated CZT camera size 20×20 cm^2 (80×80 pixels). The recorded (X, Y) spatial information was blurred by sampling a Gaussian probability function with FWHM=1.58 mm. The energy deposition process is also subject to Gaussian broadening with energy dependent FWHM values obtained from the published experimental data [131]. The camera was first validated using the validation steps described in

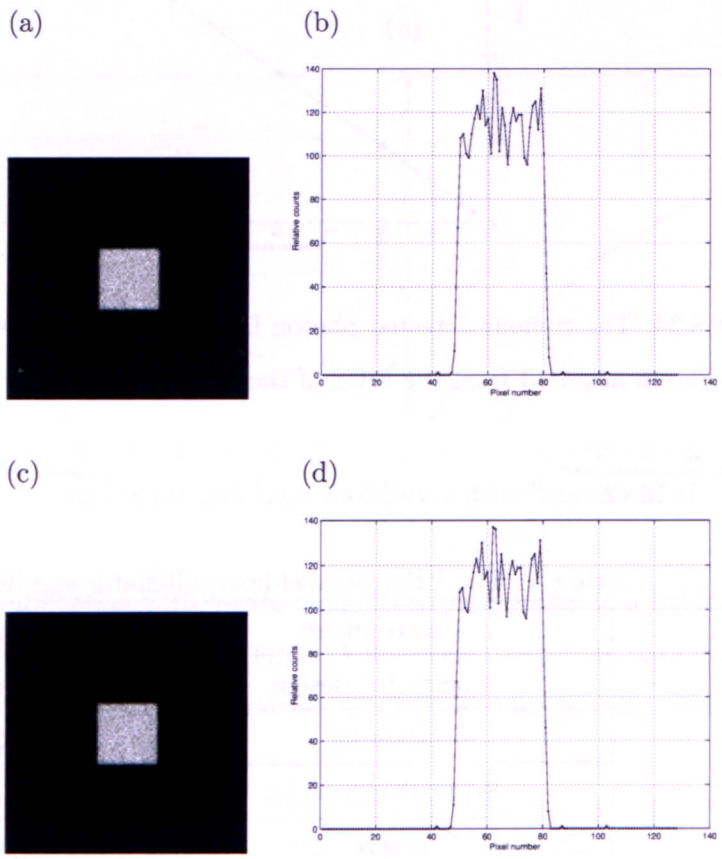

Figure 8.25: The MCS projeced images and the corresponding profiles obtained from 3D phantom containing a 5 mm diameter lesion: (a) the projected image of TBR 5:1 (NB: only 123 photons detected from the lesion), (b) a horizontal profile taken through the centre of (a), (c) the projected image with TBR of 10:1 (NB: 235 photons detected from the lesion), (d) a horizontal profile taken through the centre of (c). All the images were acquired using the LEHR collimator coupled to the conventional γ-camera.

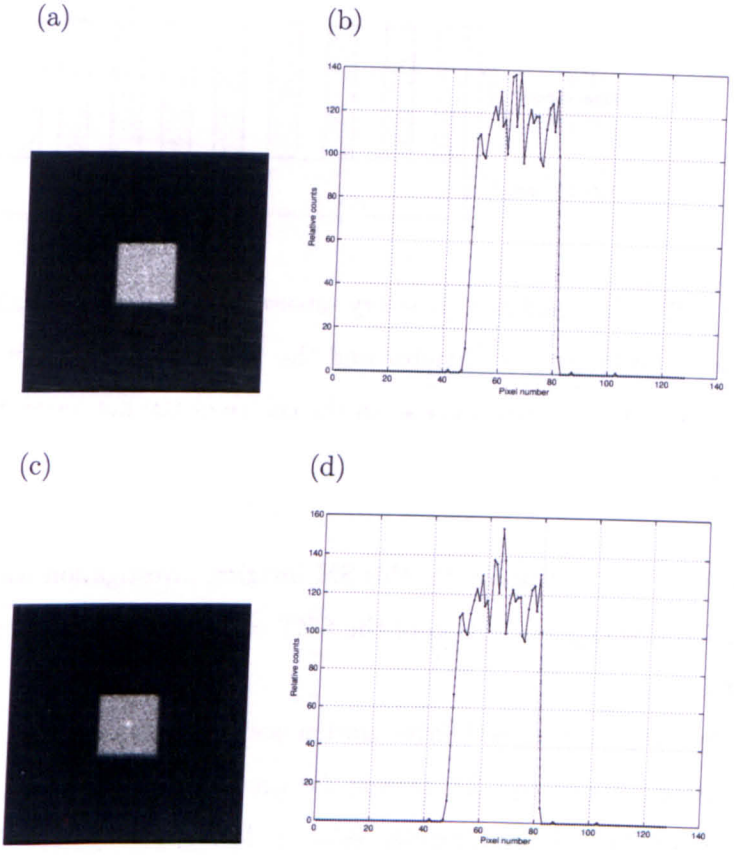

Figure 8.26: The MCS projeced images and the corresponding profiles obtained from 3D phantom containing a 8 mm diameter lesion: (a) the projected image of TBR 5:1 (NB: 536 photons detected from the lesion), (b) a horizontal profile taken through the centre of (a), (c) the projected image with TBR of 10:1 (NB: 1100 photons hit the detector), (d) a horizontal profile taken through the centre of (c). All the images were acquired using the LEHR collimator coupled to the conventional γ-camera.

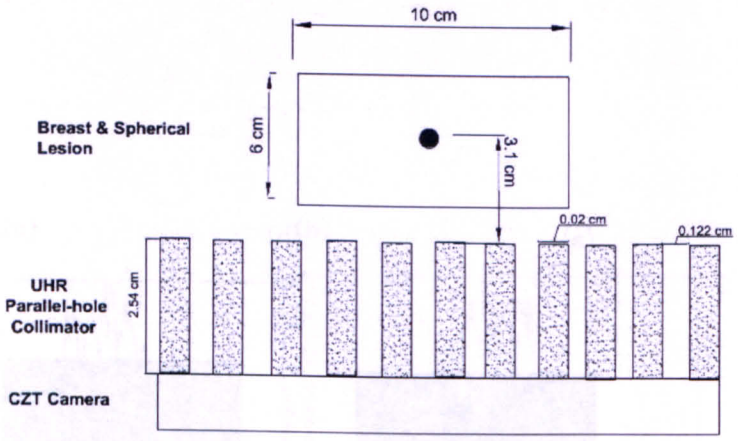

Figure 8.27: The simulated geometry set-up side view (not to scale). The breast phantom is almost touching the collimator and the lesion at 3 cm depth from the surface of the breast. Note that the distance from the centre of the hot lesion to the collimator surface was 3.1 cm.

chapter 3. The motivation for this SM imaging investigation was to utilise the enhanced spatial and energy resolution of the CZT camera compared to the full size conventional γ-cameras.

The subject of current investigation seeks to determine the performance of the UHR collimator coupled to CZT camera for breast tumour imaging. Figures 8.28-8.31 show the results for a l0 mm diameter lesion under different TBRs. These clearly demonstrate the influence of the TBR factor on the quality of the projected image and the lesion detectability. The effectiveness and performance of the CZT camera was then evaluated by quantitative comparison of lesion contrast and Full-Width Half-Maximum (FWHM) under a variety of clinical imaging situations. Figure 8.32 (a) and (b) show the calculated FWHM and contrast respectively. Figure 8.32 (a) demonstrates that the UHR collimator give more or less very similar results to the LEHR collimator in term of lesion resolution. Note however, that for the UHR collimator, the 10 mm diameter tumours with TBR of 3 is just abut visualized. Below the TBR of 3 the lesion visibility is seriously affected by Poisson noise. The number of tumour detected photons as a function of TBR is also plotted in Fig. 8.33.

To investigate the capability of the UHR parallel-hole collimator in detecting small

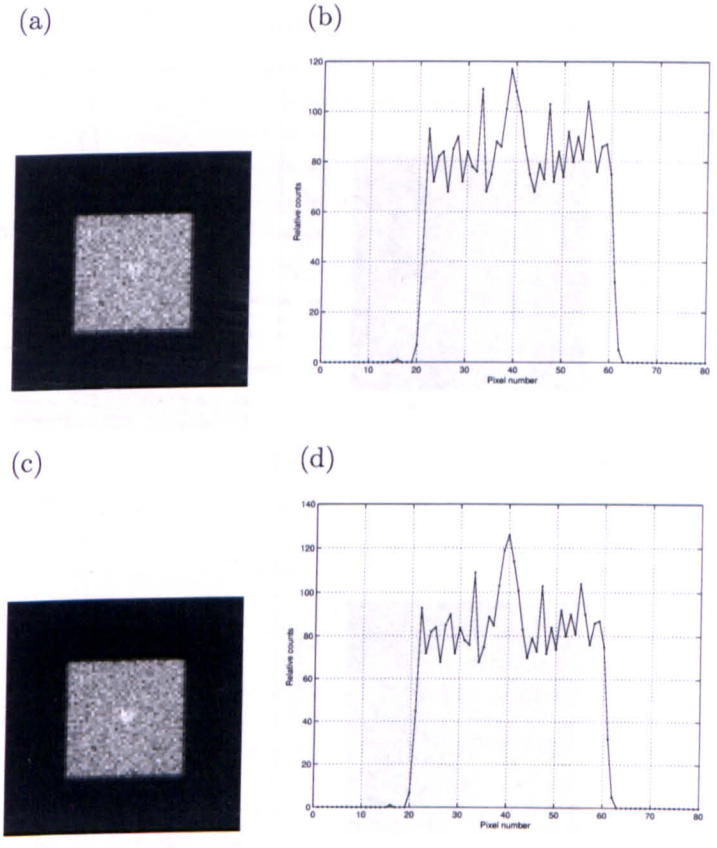

Figure 8.28: The MCS projeced images and the corresponding profiles obtained from 3D phantom containing a 10 mm diameter lesion: (a) the projected image of 10 mm diameter lesion with TBR 3:1, (b) a horizontal profile through the centre of (a), (c) the projected image containing 10 mm diameter lesion with TBR 5:1, (d) a horizontal profile through the centre of (c). All the images were acquired using the UHR collimator coupled to the CZT camera.

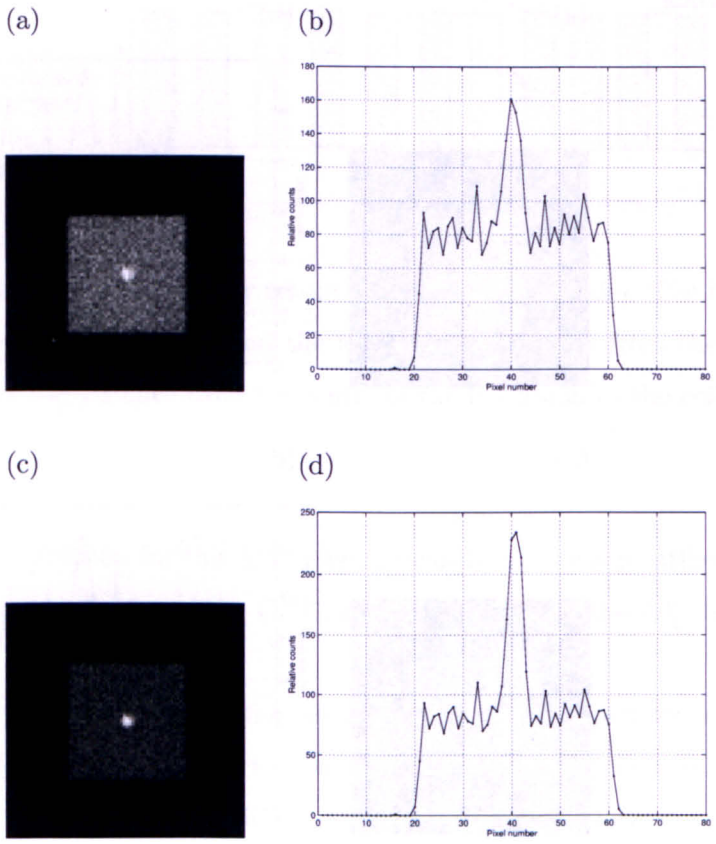

Figure 8.29: The MCS projeced images and the corresponding profiles obtained from 3D phantom containing a 10 mm diameter lesion: (a) the projected image with TBR of 10:1, (b) a horizontal profile taken through the centre of (a), (c) the projected image of TBR of 20:1, (d) a horizontal profile taken through the centre of (c). All the images were acquired using the UHR collimator coupled to CZT camera.

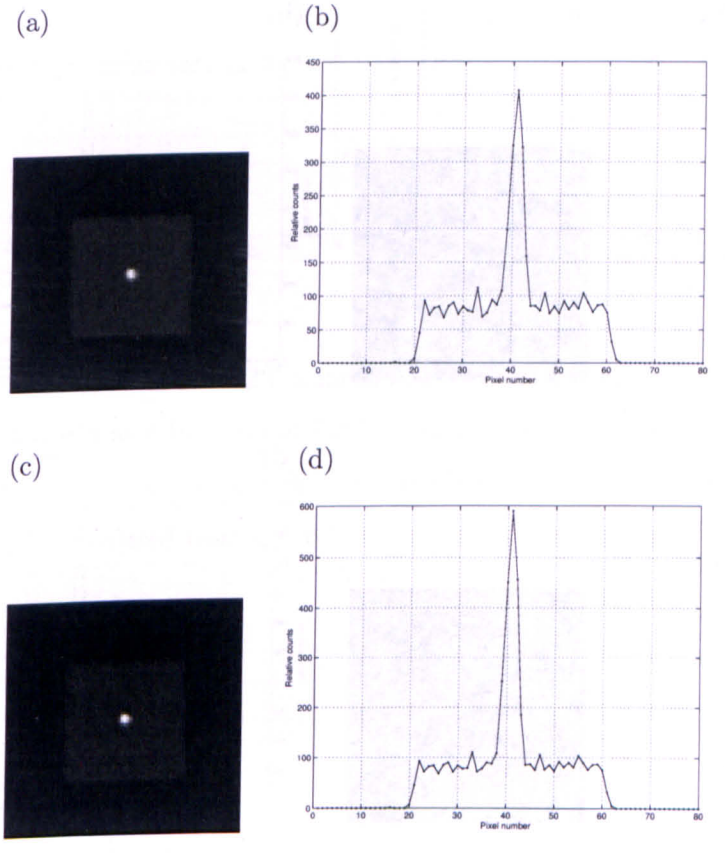

Figure 8.30: The MCS projeced images and the corresponding profiles obtained from the 3D phantom containing a 10 mm diameter lesion: (a) the projected image with TBR of 40:1, (b) a horizontal profile taken through the centre of (a), (c) the projected image with TBR of 60:1, (d) a horizontal profile taken through the centre of (c).

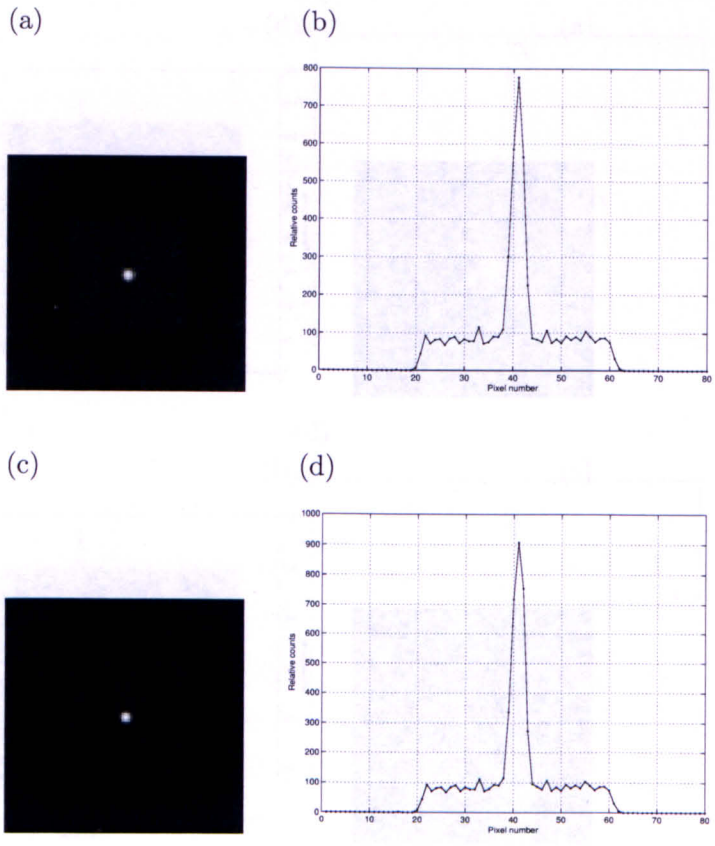

Figure 8.31: The MCS projeced images and the corresponding profiles obtained from 3D phantom containing a 10 mm diameter lesion: (a) the projected image with TBR of 80:1, (b) a horizontal profile taken through the centre of (a), (c) the projected image of isolated breast phantom of TBR 100:1, (d) a horizontal profile taken through the centre of (c).

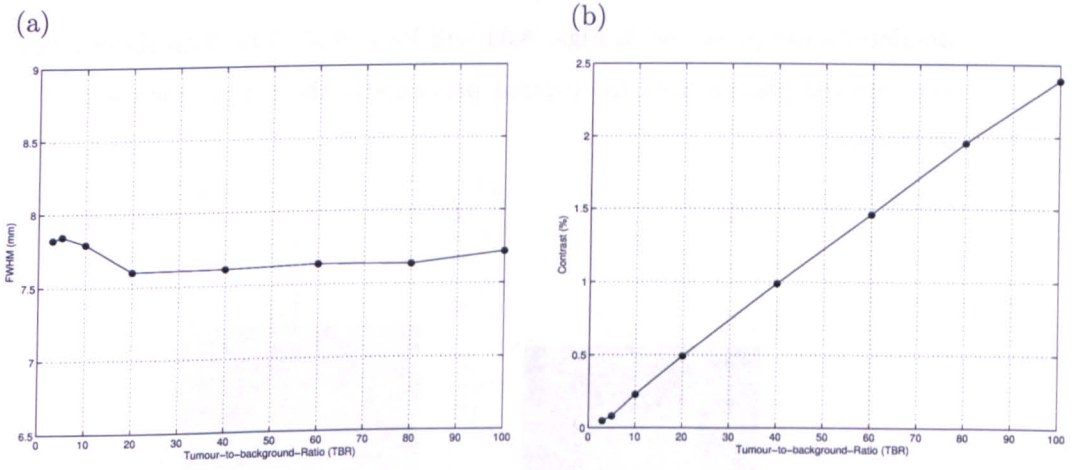

Figure 8.32: Quantification with CZT camera in detecting a signal in a hot background: (a) the tumour FWHM as a function of TBRs. Values calculated from data images of 10 mm lesions, (b) tumour contrast as a function of TBRs before for 10 mm lesion. Values demonstrated were calculated from Eq. 6.1.

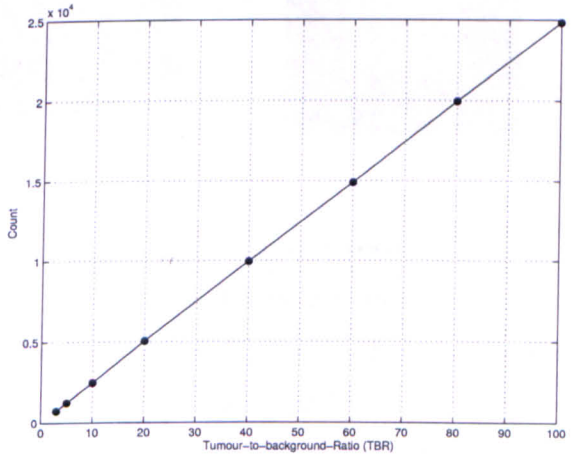

Figure 8.33: The tumour detected photon from a 10 mm diameter lesion using the UHR parallel-hole collimator coupled to the CZT camera as a function of TBR.

lesions with sizes less than 1 cm two lesion sizes of 5mm and 8 mm diameter were selected. In each case two fixed TBRs of 5:1 and 10:1 were simulated and the results from these simulations are presented in Figs. 8.34 and Figs. 8.35. The data showed that due to the low detected photon from the tumour particularly the 5 mm lesion with TBR of 10:1 is hardly seen.

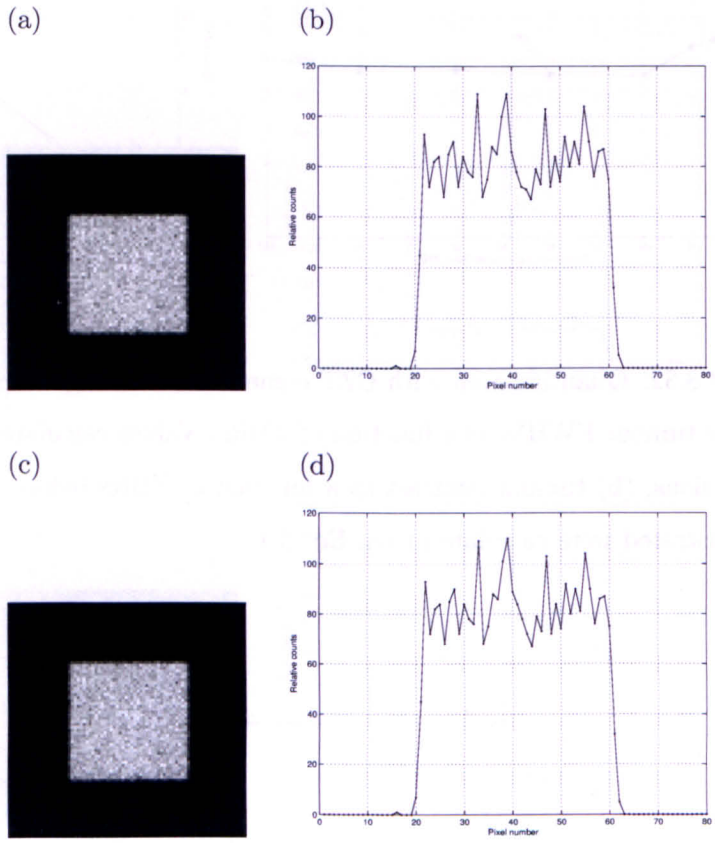

Figure 8.34: The MCS projeced images and the corresponding profiles obtained from 3D phantom containing a 5 mm diameter lesion: (a) the projected image with TBR of 5:1 (NB: 155 photons hit the detector), (b) a horizontal profile taken through the centre of (a), (c) the projected image of isolated breast phantom of TBR 10:1 (NB: 290 photons hit the detector), (d) a horizontal profile taken through the centre of (c).

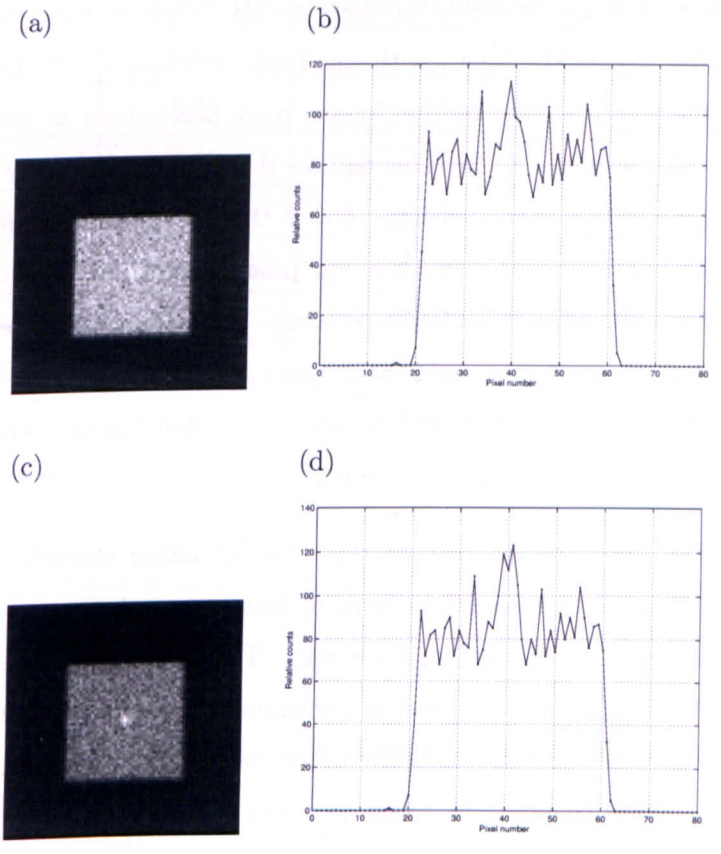

Figure 8.35: The MCS projeced images and the corresponding profiles obtained from 3D phantom containing a 8 mm diameter lesion: (a) the projected image with TBR of 5:1 (NB: 629 photons hit the detector), (b) a horizontal profile taken through the centre of (a), (c) the projected image of isolated breast phantom of TBR 10:1 (NB: 1257 photons hit the detector), (d) a horizontal profile taken through the centre of (c).

8.1.4 Conclusions from the Comparative Simulation Study

From the imaging characteristics of SM investigations using MURA-CA, LEHR and UHR parallel-hole collimators at different imaging conditions one may draw the following conclusions:

1. For all image formation methods the MCS data were generated from a 3D phantom that models the breast with small spherical lesion. The quality of these simulated images are limited by the Poisson noise particularly at low TBRs (i.e. low Signal-to-Noise-Ratio, SNR). This reduces the lesion detectability and the accuracy of any quantitative measurements. Other than image noise, photon scatter and photon attenuation are inherent physical process and thus, limit the precise quantification of source distribution in planar image. These seriously affect the lesion visibility and thus, the performance of the imaging system. In addition, statistical variations and partial volume effect tend to make calculated tumour fwhm values slightly smaller than the actual size of the lesion.

2. The above results demonstrate that all image formation methods produce more or less similar results in term of lesion resolution with a slightly lower values in the case of MURA (see table 8.2). This is beleived to be due to the effect of the decoding process involved in the case of the MURA-CA imaging system. The UHR collimator provides a slightly better peformance than the LEHR collimator in terms of image contrast. However, wih zero order correction and background subtraction the MURA-CA SM imaging approach provides significantly better performance in term of contrast (see table 8.3) than both collimator-based image formation methods.

3. The incomplete mask shadow (partial encoding) for the off-central axis lesions are the main cause that lower the performance of the CA imaging system particularly in the case of multiple lesions. These off-central axis lesions are responsible for a slightly imperfect decoding as each point source of the off-axis lesions produces sidelobes that lead to the degrdation of lesion visibility. As stated before an obvious way of solving this problem is to use a larger detector.

Table 8.2: The lesion resolution values (mm) for three image formation methods as a function of TBR.

TBR value	MURA CA	LEHR collimator	UHR collimator
3:1	6.65	-	7.82
5:1	6.64	7.81	7.84
10:1	6.69	7.77	7.79
20:1	6.84	7.86	7.61
40:1	6.89	7.85	7.62
60:1	6.92	7.89	7.64
80:1	6.95	7.89	7.63
100:1	7.92	7.92	7.72

Table 8.3: The contrast (see section 6.1.3) values (%) for three image formation methods as a function of TBR.

TBR value	MURA CA	LEHR collimator	UHR collimator
3:1	2.809	-	0.048
5:1	3.427	0.159	0.101
10:1	3.852	0.296	0.229
20:1	4.704	0.516	0.494
40:1	6.045	0.915	0.988
60:1	6.425	1.197	1.462
80:1	6.920	1.401	1.96
100:1	7.498	1.601	2.39

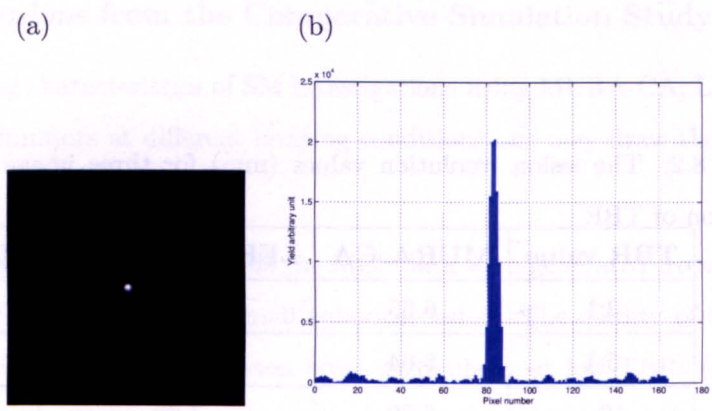

Figure 8.36: The system response from an idealised point source in air using the geometry shown in Fig. 5.3: (a) decoded image with FWHM=2.72 mm and a contrast value of 24.78, (b) a vertical profile taken through the centre of the decoded image (a). Note for this simulation $\approx$ 34k photons detected by the detector.

Having demonstrated the performance of the aforementioned image formation methods in breast tumour imaging, let us also determine the response function from all image formations systems. This was achieved by simulating a point source in air (with 10^7 photon histories) separated from the mask and the collimators by 10 cm. In the case of the MURA-CA the imaging geometry configuration ensure an object magnification of 3. The system response from an idealised point source for the MURA-CA, LEHR collimator and the UHR collimator are shown in the subsequent Figs. 8.36-8.38. The SNR (i.e. contrast multipled by the square root of the background [132]) for the simulted data produced from all image formation systems were calculated. The SNR for the MURA was the highest 323.75 where as for the UHR and LEHR collimators were 30.1 and 109 respectively.

8.2 Investigations using Pseudo-Ray Tracing

Having demonstrated in chapter five that the PRT method produces similar results to the MCS method, this section present the various investigations carried out with PRT to investigate the performance of different CA masks (see table 4.4) for breast tumour imaging. This is because the method is fast and requires less computation power than the

(a) (b)

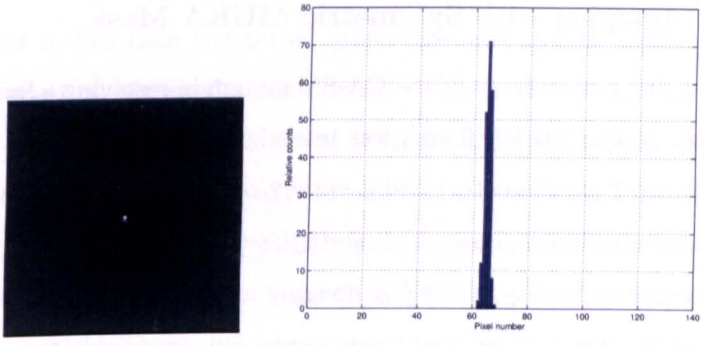

Figure 8.37: The system response from an idealised point source in air using the LEHR collimator: (a) projected image with FWHM=6.69 mm and a contrast value of 787.50, (b) a vertical profile taken through the centre of (a). Note for this simulation $\approx$ 1.1k photons detected by the detector.

(a) (b)

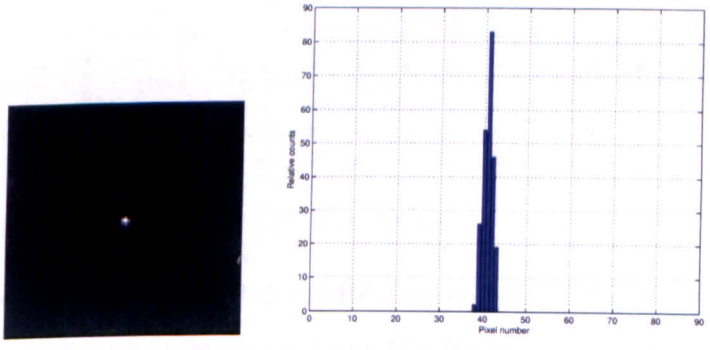

Figure 8.38: The system response from an idealised point source in air using the UHR collimator: (a) the projected image with FWHM=5.39 mm and a contrast value of 31.58, (b) a vertical profile taken through the centre of (a). Note for this simulation 1219 photons hit the detector.

MCS method. In all these investigations infinitely thin masks were used to eliminate the noise effects and other physical factor.

8.2.1 Imaging with Symmetric MURA Mask

The imaging performance of the CA-SM system in resolving a lesion embedded in a hot 3D phantom of size $10\times10\times6$ cm^3 was investigated using the PRT method. Different lesion sizes (0.5 & 1 cm diameter) and a variety of imaging TBRs conditions ranging from 5:1-100:1 are considered. These high statistics ($10^6/4\pi$ dis/mm^3) investigations demonstrate the intrinsic capability of the CA imaging in detecting a signal in a hot background. The aim was to demonstrate how post-acquisition near-field image corrections can improve object detection in terms of CNR and resolution. Note, the "noise" present arises due to systematic effects within the correlation process and due to the presence of artefacts in the decoded image.

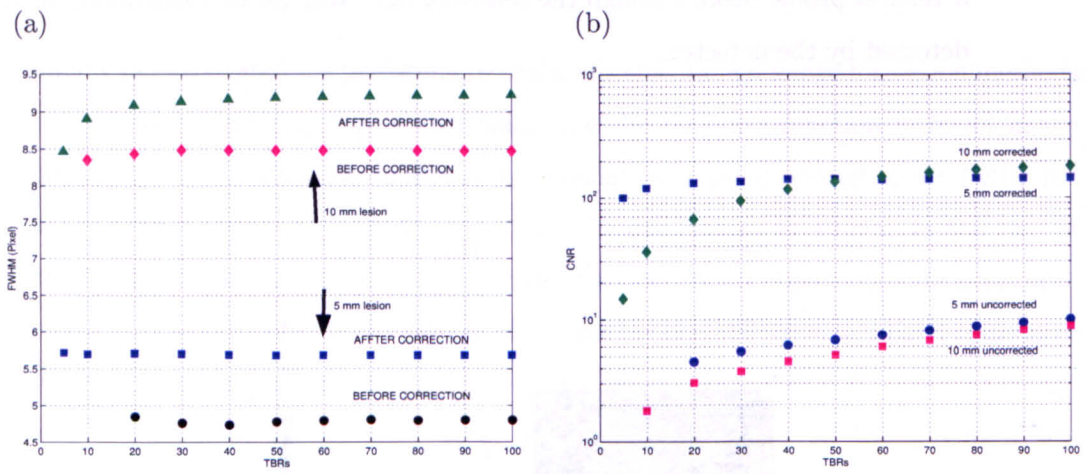

Figure 8.39: Quantification with MURA-CA imaging in detecting a signal in a hot background: (a) the tumour FWHM as a function of TBRs before and after near field corrections. Values calculated from the 3D data images of 5 and 10 mm lesions. NB: 1 pixel=2 mm, and due to imaging geometry a magnification of 3 is also present, (b) tumour CNR as a function of TBRs before and after near-field corrections for 10 and 5 mm lesion. Values calculated from Eq. 6.2 for images produced from PRT method.

The observed object size expressed in terms of FWHM of 5 and 10 mm diameter

lesions was quantified before and after the near-field corrections, with the results given in Fig. 8.39 (a). Values were averaged based on 4 profiles (horizontal, vertical and the two diagonal directions. Note that in each case, projection and partial volume effects reduce the measurement to less than the actual lesion size, and that it appears that TBRs has relatively little effect on observed resolution above TBR=20.

Figure 8.39 (b) illustrates the calculated CNR data, demonstrating that after the near-field corrections the lesion visibility of a 10 mm lesion down to a TBR of 5:1 and a 5 mm lesion down to TBR of 10:1. Note with near field corrections all lesions are visualised (not shown here) down to a TBR of 3:1. Prior to near field corrections the limits of visibility were at TBRs of 10:1 and 20:1 respectively. These data demonstrate that the use of near-field corrections in CA-SM system has relatively small effect on lesion resolution, but however, it does significantly improve the system contrast by approximately a factor of 10.

Having demonstrated the system contrast and resolution for a 10 mm lesion centred on the FoV, the following considers the off-axis lesion displacement. In each case, a 10 mm lesion with uptake ratio of 10:1 (at 3 cm depth) was systematically shifted by 1 cm along both the horizontal and vertical direction (X and Y axis) about the centre of the FoV corresponding to a breast phantom that is 10 cm wide. The decoded images were considered in each case after being corrected with background subtraction technique. Figure 8.40 (a) and (c) show exemplars of the subtracted images of off-axis lesion of 3 and 5 cm displacement respectively. In both cases the target object (lesion) is resolved but with the presence of background artefact.

8.2.2 Imaging with Mosaic MURA Mask

The use of mosaicking in CA imaging ensure complete encoding of the mask pattern but it requires a large detector. This is necessary to ensure that at least one complete basic pattern of the mask is fully covered in the detector. To demonstrate the effect of imaging with a mosiac mask a 2×2 of the basic MURA pattern with 41×41 were used. Figure 8.41 show exemplar plot of the PRT of planar phantoms with sizes 1×1×0.1 cm^3 and 5×5×0.1 cm^3. This demonstrates that the use of mosiac mask is not actually eliminating the imaging artefacts as it produces similar distortion artefacts when imaging a planar 2D uniform object (see section 5.2.3) if not worse.

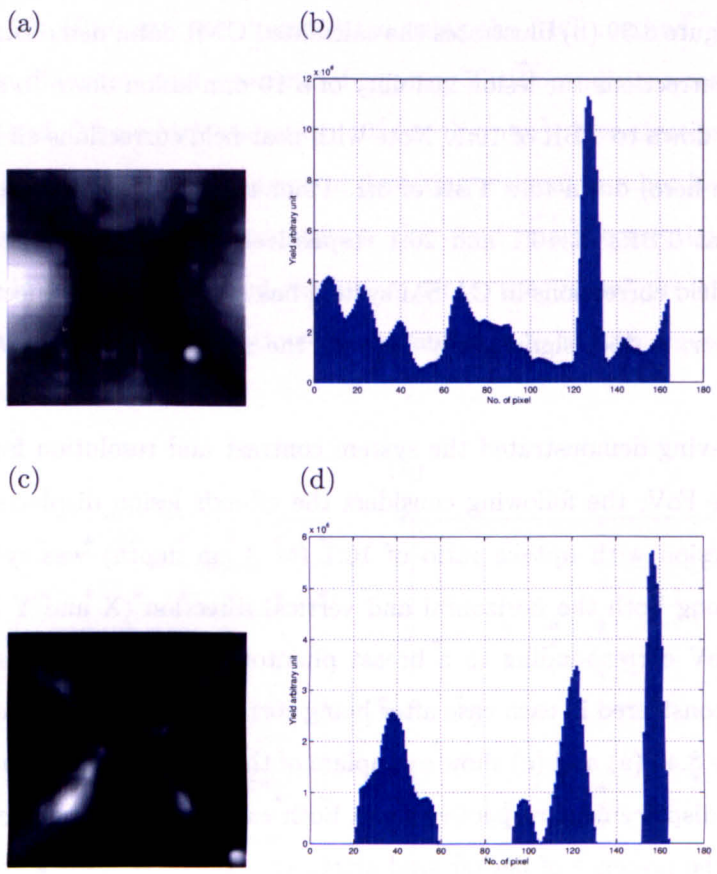

Figure 8.40: The reconstructed image of 3D object of size 10×10×6 cm^3 with off-axis 10 mm diameter sphere (uptake 10:1) placed at a depth of 3 cm: (a) raw decoded image from PRT method containing the lesion, (b) a diagonal profile through (a) phantom, (c) raw decoded image from PRT method containing the lesion, (d) a diagonal profile through (c).

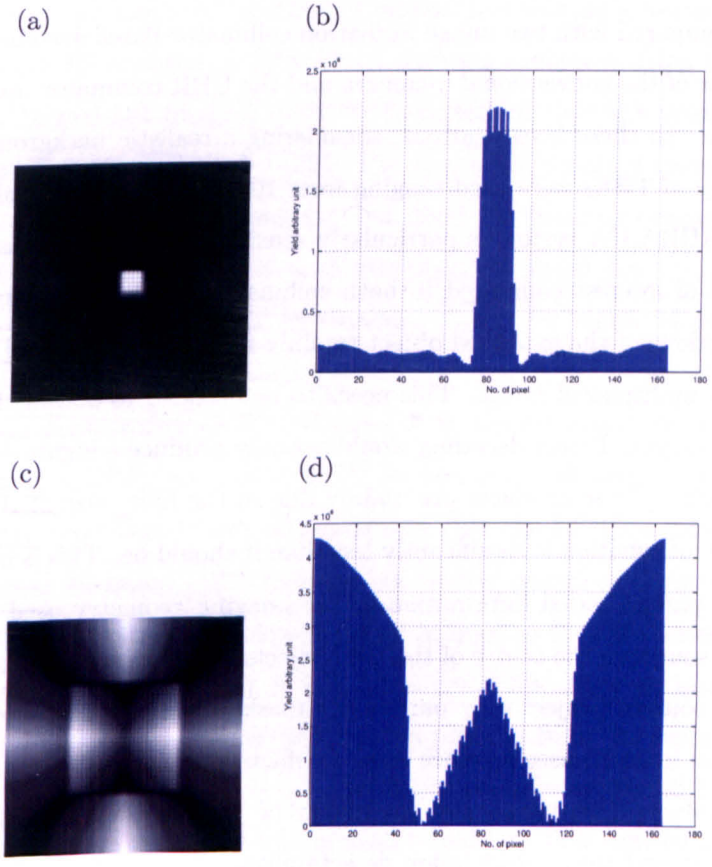

Figure 8.41: The reconstructed images of planar uniform object obtained from the PRT method: (a) the decoded image of a phantom of size 1×1×0.1 cm^3, (b) a vertical profile taken through the centre of (a), (c) the decoded image of a phantom of size 5×5×0.1 cm^3, (d) a vertical profile taken through the centre of (c). Note in this example only the central projected image of the mosaic (of size 164×164) was correlated with the corresponding decoding array.

8.3 Discussion

This chapter has demonstrated the application of different MURA-CA imaging systems for breast tumour imaging using MCS and PRT methods. First, the performance of the MURA-CA was assessed using the MCS method and then the effectiveness of the system was compared with two image formation collimator-based systems, namely the LEHR collimator of the conventional γ-camera and the UHR collimator used with a dedicated CZT camera. In these investigations, considering a realistic background activity distribution, a range of TBRs were used ranging from 100:1 to a more clinically realistic TBRs of 3:1. The MURA-CA system is particularly sensitive to stray photons from outside the target region of interest compared to both collimator-based imaging systems. In addition, the projections of the extended object (mainly from the background of the breast) produce a highly multiplexed image. This needs to be decoded to obtain the information contained in the object. Direct decoding would actually produce a highly distorted image with large artefacts. These artefacts are mainly due to the finite size of the detector the projected image information is significantly less than it should be. This is because the off-axis source cause partial coded information as the imaging geometry used here ensures that only a point source in the centre of th FoV projects an entire mask pattern onto the detector but other sources project only part of the mask pattern on the detector. Thus, the decoded process in such cases produce large artefacts that offset the performance of the CA imaging system. These mask out the ability of the CA imaging system to have a high image contrast and thus, affect lesion detectability.

To minimise these artefacts so that the MURA-CA in SM yields a higher overall performance than the collimator-based system a set of near field corrections is needed. First, zero order correction (see section 7.1.1) is need to correct the all the projected images (the image contain the lesion in a backgroud and the image contain the generated background) from the near field effect. Note that the predicted breast background can be generated using either accelerated MCS method or PRT method. Then a simple background subtraction (see section 7.1.3) is performed to remove the properly scaled background image. At this stage all the background is totally removed and now the projected image should only contain the lesion alone. Since CAs work well on imaging small objects and were originally developed for imaging point-like objects, this means that if the projected image

is then decoded with the usual G function it should then produce a lesion image. Thus, the smaller the source object the lower the sidelobe artefacts the better the performance of the CA imaging system. This improvement gradually decreased with increasing the object size i.e. once the source become extended.

The imaging performance of the CA-SM system in resolving a lesion of variable sizes embedded in a hot 3D phantom of $10 \times 10 \times 6$ cm^3 was evaluated using the MCS and the PRT methods. In real SM imaging with ^{99m}Tc-sestamibi (140 keV gamma emitter) the typical TBR is often as much as 9:1 [35]. The above MCS data demonstrate that with near near-field corrections the MURA-CA has good SM imaging characteristics. These data show that the lesion visibility for a 10 mm diameter lesion down to 3:1 and lesion as small as 2 mm with a TBR of 5:1 is also visible. This is far higher in performance than the current collimator-based SM imaging systems.

To assess the performance of the MURA-CA it was compared with the LEHR (see section 8.1.2) and the UHR (see section 8.1.3) parallel-hole collimators. For this particular imaging geometry used here it was demonstrated that the LEHR collimator coupled to the full-size clinical γ-camera yields more or less similar overall performance (albeit with reduced contrast), to UHR parall-hole collimator coupled to the CZT camera. The results data also show that the collimator is the main drawback of these imaging formation methods as only small fraction of the total emited photons from the lesion is detected i.e. the number of events detected in 10 minuest using the aformentioned image formation methods are small compared to the background radiation. This limited photon statistics affects the quality of the projected image as the observed number of counts are described by Poisson probability distribution. This make the detection of small lesion less than 8 mm in the case of the LEHR collimator and less than 5 mm in the case of the UHR collimator difficult. For accuretly visualzing a small lesion one needs a high TBR value (i.e.a higher SNR) higher than 10:1. The is necessary so that one can differentiate between the background region and the tumour region.

There are however, two problems associated with the near-field CA-SM imaging. The first problem is decoding at depth (plane) as in practice the location of lesion(s) is unknown. This is particularly true in the case of multiple sources i.e. more than 5 lesions separated by less than 1 cm. To recover the lesion one needs to know the depth of the target object. If no a *priori* information is available then from the geometrical set-up all

the distances between the mask and the detector and the mask and the front face of the semi-compressed breast should be considered. Note that the optimum imaging geometry is to ensure that the desired magnification coefficient, m_c, at the front face of the breast. This necessary so that with depth the m_c decreases and thus, the projected shadow from sources at depth which contain the sources information are covered by the detector. A set of scaled decoding is then used through the entire depth of the breast to recover the lesion(s) of unknown depth. From eq. 5.4 if α is integer then the projection of the mask-hole cover exactly a square of $\alpha \times \alpha$ pixel and thus, a perfect decoded image is produced. This only exist for a specific position of the lesion in the breast. If however α have non-integer value this mean that the G function is scaled with non-integer value as a result undesirable artefacts appear in the image (see section 5.2.1 (d)). To solve this problem and to see the lesion clearly and to eleminate these artefacts the only way is to ensure that in each depth (plane) that α is integer. With reference to eq. 5.4 for example if m_c=3.9, α=4 (chosen) and the mask element size p_m=2 then the size of the detector pixel is given as $p_d = p_m \frac{m_c}{\alpha}$=1.95. Another example if m_c=4.2, α=4 and the mask element size p_m=2 then p_d = 2.1 ans so on. This mean that for each non-integer depth then based on other parameters the size of the detector pixel p_d is chosen so that α is integer. If this can be achived off-line for such limited depth of simi-compressed breast then the artefacts arising from imperfect sampling can be either eleminated or minimised.

The second problem with the near-field CA-SM imaging is the off-central axis lesion particularly in the case of multiple lesions. The off-centre lesions contribute noise to the decoded image as these are responsible for the presence of side-lobe artefacts in the decoded image. These slightly offset the performance and the effectiveness of the system. An obvious way to solve this problem is to look up (by simulation) to the best geometrical set-up or to use a detector that is large enough to fully coded the object and cover the whole Field of View (FoV). Alternatively, give a larger activity (740 MBq [84] or 925-1110 MBq [49]) or image the the patient for more than 10 minutes. From the PRT high statistics ($10^6/4\pi$ dis/mm^3 photons was simulated) investigations the results demonstrate that the MURA-CA masks provide good performance and work well in the case off-central axis sources (see Fig. 8.39). From the above investigations one can infer that CA-SM would work even better with either a larger detector then used or with imaging for more than 10 minutes. The former is needed to cover the whole Field of View (FoV) of the object

and thus, fully coded the projected shadow pattern where as the latter is needed due to the presence of coding noise from the off-central axis sources.

Chapter 9

Summary & Conclusions

This chapter summarizes the main thesis outcomes that have been made and discusses the future directions for the continuation of this work.

9.1 Summary & Conclusions

Breast cancer is a major health problem affecting women in US, UK, and Western Europe. It also affects many other countries in Asia, and the third world. This study was aimed to join the battle against this aggressive disease by investigating the performance of Coded Apertures (CAs) in breast tumour imaging. After describing the problems caused by breast cancer an overview of the available literature was obtained covering the most currently used screening and diagnostic techniques of breast cancer. It also includes the recently developed dedicated camera designed for breast tumour imaging. Based on these literature it was found that the existing diagnostic techniques for evaluating breast cancer are a combination of imaging techniques and invasive breast biopsies. Among these imaging techniques is Scintimammography (SM) using a full size clinical γ-camera employing a Low Energy High Resolution (LEHR) collimator. This functional radionuclide technique offers information about the function of an organ and is a valuable diagnostic method particularly for evaluating dense breasts. However, the use of a physical collimator is a major disadvantage of such gamma camera SM imaging systems. It limits the performance of the imaging system and thus, exhibits a resolution-efficiency trade-off.

As an alternative, CA coupled to a standard clinical gamma camera, without a collimator was investigated in this thesis. This image formation technique is attractive for

imaging small sparse objects i.e. a small FoV object and thus, matches the imaging objective of SM. In addition, the recent advances in near-field artefacts correction have attracted us to investigate the CA imaging technique. The motivation for this study is that the use of CA for breast tumour imaging, using a standard γ-camera, may circumuent the need for high resolution dedicated systems. First, the most suitable CA patterns were explored including their generation role and correlation properties and with a review of the literature. This is important because the ideal reconstructed (decoded) image strongly depends on the choice of the aperture pattern. The current optimum mask patterns were found to be the Modified Uniformly Redundant Array (MURA) and the No-Two-Hole-Touching (NTHT) that is based on MURA. This is because the response function of such pattern is a δ-function with zero side-lobes. These patterns were particularly attractive as they combine the wide open area and the ability of obtaining a magnified image compared with the LEHR collimator. Following this, all the possible mask camera configurations, geometry and design for CA imaging were explored. It was pointed out that the mask camera design depends on the size and resolution of the detector as well as the size and the FoV of the object. Square mask elements were chosen to match the detector elements to make best use of the available detector area.

The original part of this work explores the application of CA imaging for breast tumour detection. Initially, these investigations were carried out using the well known Monte Carlo (MC) methods in imaging different phantom geometries. Before doing so and as a first part of this project, the MC methods and utilities were geometrically validated for accuracy. The validation was essential and was achieved by conducting an experimental study, at the Royal Surrey County Hospital, using a Toshiba (GCA-7200A) clinical gamma camera with a LEHR parallel-hole collimator imaging mono-energetic point sources having variable range of energies, as well as imaging a point source as different distances from the LEHR collimator.

After describing the MCS framework, the second and the most important part, involved the various investigations undertaken using a CA coupled to a full size standard γ-camera for imaging a point like source. 2D projected images were investigated after being decoded using the correlation analysis. To do so in-house code was written to reconstruct these projected images based on fine sampling cross correlation. In all planar images with an idealised point source no distortion or artefacts occur in the reconstructed

image except a small cross-shaped sides-lobe due to the near-field effect. These side-lobes can be minimised if the projected image are first corrected using a zero order correction. These results demonstrate the highest Signal-Noise-Ratio (SNR) for a source in the near-field geometry. However, these improvements for CA imaging tend to gradually decrease once the source becomes extended and its FoV increases unless use is made of a large detector that fully encodes all the source information. In this case artefacts (ghosts) of bright sources occur in the correlated image of distributed sources due to off central axis point sources. This is largely due to the multiplexing effect and the partially encoded information because the detector is not large enough to contain all the source information. From these investigations and for the particular imaging geometry used here it is clear that for the CA camera, the smaller the object the better the decoded image and thus, the greater the advantages of the CA system.

CA is a focusing technique and thus, demonstrates a tomographic capability from a single projection. This has been shown in the multi-source & multi-depth investigations. It has also been demonstrated that the out-of-focus planes produce non-uniform complex structural artefacts in the decoded image. This is because the projected image is not matched with the decoding array and thus, artefacts appear from the out-of-focus object plane. For faithful reconstruction one needs to properly focus in the desired decoding plane by using the appropriately scaled G function. Thus, if the sampling of the projection is perfect i.e. the mask projection matching the detector pixel then the distortion artefacts and structural noise are largely reduced. This only holds true for a fixed source:CA distance i.e. only exist for a specific position of the point source in the object. The imperfect detector sampling of the projection is because the mask projection does not perfectly match the detector pixel dimention i.e. α is having a non-integer value. Now scaling the decoding array G to a non-integer value means that the projected image is not matching with the decoding array. Despite this, one could still recover the object particularly for a limited depth, for a limited number of point-like objects.

To investigate the intrinsic contribution of non-specific or background artefacts from a uniform 2D and 3D source object the camera simulation physics were removed and an ideal plane detector was simulated. The results from such an ideal detector were found to be almost identical to the results obtained from the full camera simulation. This suggest that the problem is geometrical. Further investigations were carried out with CA imaging

and two non-Monte Carlo methods were developed. The first method is new but simple called Binary Mask Shift (BMS) and the second method is Pseudo-Ray Tracing (PRT). Both methods are capable of predicting the performance of CA for imaging a variable source object as well as the shape of artefacts that are due to off-axis sources and finite size of the object. However, BMS ignores the effect of varying the angle of incidence of the γ-rays and thus, can be said that it represent far field geometry for imaging an extended but uniform 2D source object.

On the other hand, the PRT method is far more realistic as it represents the near field imaging geometry. The background artefact pattern produced by uniform 2D and 3D source objects of different sizes using a PRT method were comparable with the corresponding data obtained with MCS. This suggest that both methods produce striking similarities and are almost identical. These results were encouraging and suggest that the so-called near field distortion observed with distributed 3D sources, as might be found in SM using CA, can be easily predicted and corrected. It was also found that the contribution of background artefact distortion is mainly from the in-plane activity.

To demonstrate the performance of CA for SM imaging pseudo-anthropomorphic phantom geometries containing torso, heart, breast and variable lesion sizes were first developed and then verified. Light breast compression has been assumed and the geometry chosen ensure craino-caudal imaging view. Various investigations were undertaken to evaluate the performance of the CA for the application of breast tumour imaging after image decoding. The performance of CA-SM was then evaluated by quantitative analysis of system resolution, contrast, and Contrast-Noise-Ratio (CNR) at different imaging conditions. Although a tungsten frame (1.5 mm thick) surrounding the CA largely minimises the detection of oblique photons arriving from outside the breast FoV, the open field geometry associated with the MURA-CA imaging is problematic. From such investigations it was found that proper shielding is required to shield the CA camera from the non-specific out-of-field background activities arising from the torso and the heart.

In addition, the non-specific background radiation from breast, photon scatter, source multiplexing and decoding process introduce noises to the decoded image. The multiplexing is an intrinsic property of the CA imaging system and is the cause that each point in the image is subject to the noise from other sources in the FoV. In other words each point in the image is subject to the noise from the rest of the detector plane. Due to

the limited size of the detector the presence of the breast background activities is the main contribution of imaging artefacts. These actually arise from the in-plane/out-plane activity as well as off-axis sources and are thus, responsible for the distorting quality of the decoded image.

For the CA to have competitive SM imaging characteristics the distortion artefacts need to be eliminated or minimised first to improve the image quality of the decoded image. To do so three near-field correction techniques were implemented to the CA-SM data. First the projected image needs to be corrected with the zero-order correction. Then a simple background subtraction should be performed to remove the effect of volumetric background corruption caused by scatter and systematic decoding artefacts. These two corrections are necessary and have to be applied to the projected images before decoding and in any order. Then the mask/antimask technique could be used if needed. Note that for the presented data in this thesis the mask/antimask technique was only used where specifically indicated.

After the near-field artefacts and for all lesions sizes that were investigated it was found that a minimal TBR of 3:1 is required for visualising any lesions. This is competitive with that observed clinically, typically 3:1 up to 9:1. For lesion resolution it was found that the values reported were less than the actual lesion size. This may be due to the projection and partial volume effects which contribute to the reduction of lesion resolution measurement. In addition, the artefact arising from the in-plane off-centre sources may further deteriorate the spatial resolution in the Z direction as well as in the X and Y direction.

To assess the performance of the CA-SM approach this was compared with a LEHR collimator placed on the the aforementioned camera. In addition, both image formation methods were also compared with the UHR parallel-hole collimator of the dedicated CZT camera. An important conclusion drawn from these simulation studies is that for these particular geometries the results were highly comparable in terms of spatial resolution. However, after the near-field correction the MURA-CA demonstrates superior performance in terms of contrast compared with both collimator-based systems. More importantly these collimator-based systems show poor detection efficiency particularly in the case of tumours less than 1 cm diameter.

One of the drawbacks of CA imaging is the complexity of the out-of-focus behavior of the decoding. Our investigations show that the out-of-focus planes do not necessarily blur

smoothly and continuously instead it produces sharp and complex structures. With these artefacts present it is not possible to unambiguously extract the object information and thus this seriously confuses the diagnostic process. However, in CA-SM imaging we are often after a small point-like object (lesion) and focusing properly on the right plane that contains the lesion is important and will provide evidence of lesion presence. Focusing on the correct plane at the target object can increase the SNR and this can be achieved iteratively by scanning (off line) over the different position of the object (the FoV). The main novel contributions of this work are the demonstration that CA-SM can provide higher contrast compared to collimator-based approaches and lesion as small as 2 mm with a TBR of 3:1 can be clearly visualised.

9.2 Future Work

The presented CA work has considered 2D projected images of ^{99m}Tc labelled sestamibi spherical lesions located at different positions of the pseudo-anthropomorphic phantom geometries. In such applications CA imaging technique showed good performance if both proper shielding and near-field artefact corrections are implemented. This opens new possibilities for future CA tumour imaging applications. One avenue of the possible further work in this area is to consider repeating the simulation work with a Zubal anthropomorphic phantom to investigate the optimum imaging geometries for the CA that consider a greater level of realism for non-specific background uptake. It would also be interesting to build a simple physical mask and repeat the MCS work experimentally. In addition, one of the problems of the CA-SM imaging is that the reconstruction at different planes as well as for off-central lesions multiple lesions with a set of decoding steps (scanning off line over the different plane of the object) introduces artefacts due to imperfect sampling. This 3D decoding technique needs further investigations with iterative reconstruction techniques suggested in [133, 134] in order to produce a cleaner image. This work can also be expanded for a 3D imaging i.e. looking at the possibility of a tomographic CA system that might rotate arround the breast. This should ensure a continous CA pattern, so that each projection is no longer cut short.

Another possible near-field applications for CA imaging would be sentinel node imaging, prostate imaging and thyroid imaging. Another possible and attractive application

would be small animal imaging. These are pseudo-planar objects (of small thickness), having small FoV and thus, represent point-like objects. In these small organs (small FoV) a high resolution image can be achieved by making the CA hole very small. This can be achieved by taking advantage of the large surface area of the conventional full-size γ-camera to achieve less than 2 mm spatial resolution. In addition, a high uniform sensitivity can be achieved compared to pinhole collimator. Thus, with proper shielding of the non-zero background arising from the surrounding organs of the area of interest and near-field corrections the MURA-CA imaging technique is capable of determining the location and the extent of the lesion. These suggested investigations could be carried out initially with MCS using more realistic anthropomorphic phantoms as it mimics the real situation in clinical practice.

Appendix A

Chapter three illustrate that the total photon distribution recorded at the detector when imaging with CA can be obtained by integrating over the object plane as:

$$D(\vec{r}_i) = \int\int_{\vec{r}_o} O(\vec{r}_o)\ A(\vec{r_m})\Omega(\vec{r}_o, \vec{r}_m)d^2\vec{r}_o \tag{9.1}$$

where:

$$\vec{r_m} = (\frac{a}{z}\vec{r}_i + \frac{b}{z}\vec{r}_o) \quad and \tag{9.2}$$

$$\Omega(\vec{r}_o, \vec{r}_m) = \frac{{p_m}^2}{a^2}\cos^3(\theta) \tag{9.3}$$

Equation 9.1 illustrates the basic mathematical formulation that describes the formation of the coded image when imaging a planar source.

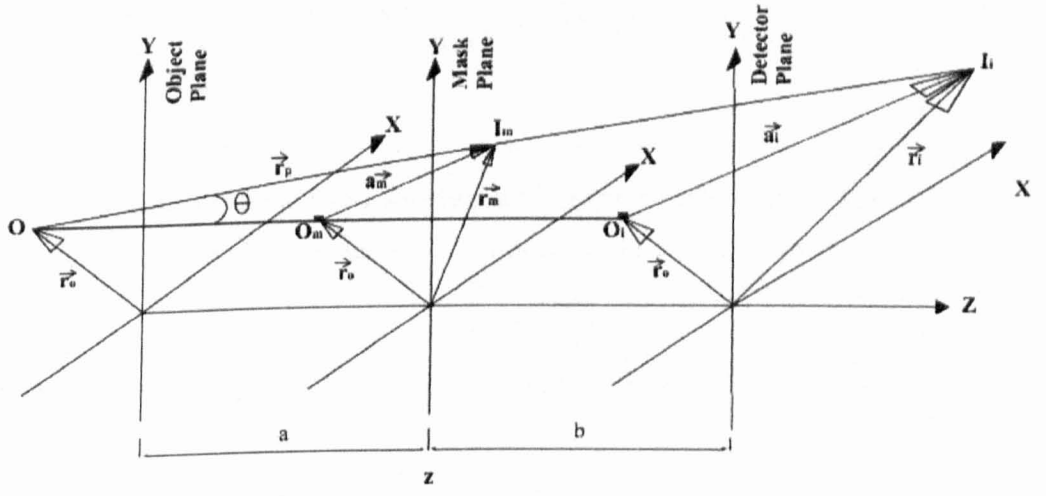

Figure 9.1: Coded aperture geometry showing the point of intersection with the ray going from $\vec{r_o}$ to $\vec{r_i}$ with illustration to all positions.

In the following we will try to prove equation 9.2 and 9.3 respectively. From the geometry of Fig. 9.1 one can see two similar right-angled triangles $(O\ O_m\ I_m)$ and $(O\ O_i\ I_i)$ so that:

$$\frac{\|\vec{a}_i\|}{\|\vec{a}_m\|} = \frac{O_iI_i}{O_mI_m} = \frac{OO_i}{OO_m} = \frac{a+b}{a} = \frac{z}{a}$$

$$\vec{a}_m = \frac{a}{z}\vec{r}_i$$

$$\vec{r}_m = \vec{r}_o + \vec{a}_m = \vec{r}_o + \frac{a}{z}\vec{a}_i$$

we know that $(\vec{a}_i + \vec{r}_o) = \vec{r}_i$

$$\vec{r}_m = \vec{r}_o + \frac{a}{z}(\vec{r}_i - \vec{r}_o)$$

since $z = a + b$

$$\vec{r}_m = \frac{b\vec{r}_o + a\vec{r}_i}{z}$$

Having proved Eq. 9.2, now we show (see Fig. 9.2) exemplar of some of the possible cases of the point of intersection with the ray going from $\vec{r_o}$ to $\vec{r_i}$ illustrating the positions of $\vec{r_m}$. that projected onto the detector plane.

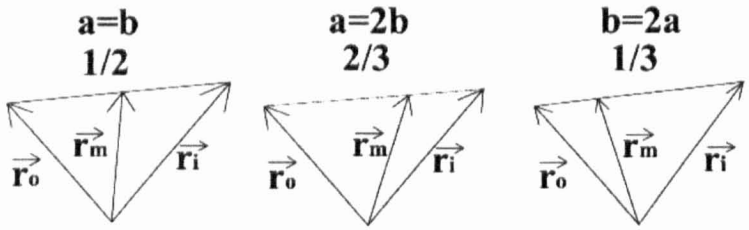

Figure 9.2: Exemplar of some of the possible cases of the point of intersection with the ray going from $\vec{r_o}$ to $\vec{r_i}$ illustrating the positions of $\vec{r_m}$ in each case. The illustration is projected onto the detector plane.

Now let us consider the term $\Omega(\vec{r}_o, \vec{r}_m)$ that given in Eq. 9.3. From Fig. 9.1 the $\Omega(\vec{r}_o, \vec{r}_m)$ can be obtained as:

$$\Omega(\vec{r}_o, \vec{r}_m) = \frac{{p_m}^2}{{r_p}^2} \times \cos\theta \tag{9.4}$$

where p_m is the side size of the square pixel of the mask and this approximation is valid since $r_p >> p_m$.

$$\Omega(\vec{r}_o, \vec{r}_m) = \frac{p_m^2}{a^2} \times (\frac{a^2}{r_p^2}) \times \cos\theta \tag{9.5}$$

From Fig. 9.1 we know that $(O\ O_m\ I_m)$ is a right-angled triangle at O_m, hence:

$$r_p = \frac{a}{\cos\theta} \Longrightarrow \cos\theta = \frac{a}{r_p} \Longrightarrow \cos^2\theta = (\frac{a}{r_p})^2 = \frac{a^2}{r_p^2}$$

Equation 9.5 becomes:

$$\Omega(\vec{r}_o, \vec{r}_m) = \frac{p_m^2}{a^2}\cos^3\theta \tag{9.6}$$

Appendix B: Example MCNPX input file.

```
c point source (12.5 cm dist.) in a cylinder of water
c detector cell cards
1 0 10                          imp:p=0    $ sphere void cell
2 1 -3.67 1 -2 3 -4 -5 6        imp:p=1    $ geometry parameters of Nai
3 2 -1.00 7 -8 -9 11            imp:p=1    $ water cylinder
4 4 -1.00 -11                   imp:p=1    $ tumour or lesion cell
5 3 -1.225E-3 -10 #2 #3 #4      imp:p=1    $ air around NaI and water cylinder
c end of cell card

c surface cards for detector
1 px -27.5                                 $ Rectangular detector
2 px 27.5
3 py -20
4 py 20
5 pz 0.0
6 pz -0.95
7 pz 10                                    $ bottom plane of water cylinder
8 pz 20                                    $ top plane of water cylinder
9 cz 2                                     $ radius of water cylinder
10 so 100                                  $ sphere
11 RCC 0 0 12 0 0 .005 .005                $ lesion inside cylinder
c end surface specifications

c Data Cards
SDEF pos=0 0 12.0025 par=2 erg=.14    $ source information
F8:P 1                                   $ energy distribution of pulses
F18:p 1                                  $ energy deposition tally
e0 0 1e-5 .001 250i .25                  $ energy bins
ft8 geb .00329 0.04191                   $ Energy broadening
MODE P                                   $ this is a photon problem
M1 11000 -.1534                          $ define NaI using Na and I atom fractions
```

```
53000 -.8466                          $ define NaI using Na and I atom fractions
c water in cylinder
M2 1001 -.66667                       $ water in cylinder
8016 -.33333                          $ define h2o using h and o atom fractions
c Air around the system
M3 7014 -.7809
8016 -.2095                           $ Air around the system
18000 -.0096
M4 1001 -.66667                       $ water in cylinder
8016 -.33333                          $ define h2o using h and o atom fractions
mplot                                  $ for plotting
nps 1000                               $ run 1000 photon histories in this calculation
print                                  $ print everything about the calculation
PTRAC file=asc event=src write=all max=1000    $ Max >=nps
c end data section
```

Appendix C PTRAC File

The two important parameters that determine the detection process when imaging with say ^{99m}Tc isotropic sources emitting 140 keV photons, are the energy contents of the photon and its position on the detector. The γ-ray photons generated from such a source are subject to Compton scattering, photoelectric effect and Rayleigh scattering. The resulting photon histories tracking individual the positions of interactions and energy losses are then recorded in a single output list file, referred to as a PTRAC file [116]. The use of the PTRAC command in the input file in the default mode produces unmanageable output data files on particles trajectories unless the number of histories are strictly limited. Thus, the use of PTRAC commands that link to the use of tally F8 are needed to filter out some of the unnecessary events information. This produce a relatively shorter PTRAC file and slightly reduces the computation time depending on the number of particles simulated. These commands instructs the code to only write specified events information to the file.

The PTRAC commands used in the majority of the simulations in this study are listed in table 9.1. Details discussion of these commands and PTRAC file format can be found elsewhere [111, 116]. Despite the use of these PTRAC command the majority of the simulated input files still produce very large output files (40-60 GB) particularly in the case of CA imaging geometries. This is because it provides a log of all events containing the 3D coordinates of their locations as well as the changes in the energy of the photons as they traverse through the imaging detector.

Table 9.1: The main parameters and commands used with the PTRAC are listed below. These instruct the code to write the event of interest such as scattering, collision and photoelectric absorption in an ASCII file.

Parameters	**Operation**
File	Write ASCII file (ASC)
Write	What need to be written (All)
Type	Type of event (Photon & Electron)
Tally	Tally F8

The PTRAC stored data generally has the same formate and possess the following features:

Table 9.2: The types of events most relevant to the gamma camera simulations. These events depend on the incident γ-ray photon, the atomic number and the size of the medium.

Event Code	**Event**
1000	Source
2009	Photon from double fluorescence
2016	Bremsstrahlung from electron
3000	Surface collision
4000	Collision inside the material
5000	Photoelectric absorption
9000	Particle termination

1. The first 10 lines of the PTRAC output file is refered to as header block and only provides information about the simulation set-up.

2. Records on particle histories appear on line 11 onward and in blocks. Each block contains new tracked particle. Every block begins with a line having 10 entries and the rest of lines are not. This is used to indicate the start of a new block and on the same time the end of the previous one.

3. The second line after the line of 10 entries is the event code i.e. the source information. This provides the type of the event that the particle undergoes. These are listed in table 9.2.

4. The first three entries on the second line of the block represent the 3D coordinates (x,y,z) of the event and the seventh entry represents the energy of the photon in MeVs.

5. The first entry of the third line of the block contains the code of the next event.

6. Line 4 is similar to line 2 as it contains the coordinates of the event and the energy content of the particle following the event.

7. The lines then continue to repeat as in (5) and (6) till the particle terminates or leaves the detector. The latter is another marks for the end of the block.

One of the main feature of PTRAC utility is the ability of recording the number or the percentage of scattering events separated from the Photo-electric event.

Appendix D

$$\Omega = h\int_0^a dx\int_0^b \frac{dy}{(x^2+y^2+h^2)^{\frac{3}{2}}} \tag{9.7}$$

Taking the second integration:-

$$\int_0^b \frac{dy}{(x^2+y^2+h^2)^{\frac{3}{2}}} = \frac{1}{(x^2+h^2)^{\frac{3}{2}}}\int_0^b \frac{dy}{(\frac{y^2}{x^2+h^2}+1)^{\frac{3}{2}}}$$

Now we assume the following:-

$$y = \sqrt{(x^2+h^2)}\tan\theta \tag{9.8}$$

$$dy = \sqrt{(x^2+h^2)}\frac{1}{\cos^2\theta}d\theta \tag{9.9}$$

when y=b $\Rightarrow$ θ=θ'

$$b = \sqrt{(x^2+h^2)}\tan\theta' \tag{9.10}$$

$$\Omega = h\int_0^a dx\int_0^{\theta'} \sqrt{(x^2+h^2)}\frac{d\theta}{\cos^2\theta}\cdot\frac{1}{[(x^2+h^2)+(x^2+h^2)\tan^2\theta]^{\frac{3}{2}}}$$

$$\Omega = h\int_0^a dx\int_0^{\theta} \frac{(x^2+h^2)^{\frac{1}{2}}}{(x^2+h^2)^{\frac{3}{2}}}\frac{d\theta}{\cos^2\theta}\cdot\frac{1}{(1+\tan^2\theta)^{\frac{3}{2}}}$$

We know that $1+\tan^2\theta = \frac{1}{\cos^2\theta}$

$$\Omega = h\int_0^a dx\int_0^{\theta'} \frac{1}{(x^2+h^2)}\frac{d\theta}{\cos^2\theta}\cdot\frac{1}{(1/\cos^2\theta)^{\frac{3}{2}}}$$

$$\Omega = h\int_0^a dx\frac{1}{(x^2+h^2)}\int_0^{\theta'}\cos\theta d\theta \tag{9.11}$$

$$\Omega = h\int_0^a dx\frac{1}{(x^2+h^2)}[\sin\theta]_0^{\theta'}$$

$$\Omega = h\int_0^a dx\frac{1}{(x^2+h^2)}\sin\theta' \tag{9.12}$$

We know that:

$$\cos^2\theta+\sin^2\theta = 1 \Rightarrow \frac{1}{tan^2\theta}+1 = \frac{1}{\sin^2\theta}$$

Also, from Eq. 9.10: $\tan\theta' = \frac{b}{\sqrt{x^2+h^2}}$

$$\frac{x^2+h^2}{b^2} + 1 = \frac{x^2+h^2+b^2}{b^2} = \frac{1}{\sin^2\theta'}$$

$$\sin\theta' = \frac{b}{\sqrt{x^2+h^2+b^2}} \tag{9.13}$$

From Eq. 9.13 into Eq. 9.12

$$\Omega = bh\int_0^a dx \frac{1}{x^2+h^2} \cdot \frac{1}{\sqrt{x^2+h^2+b^2}} \tag{9.14}$$

Now, we assume the following:

$$x = \sqrt{h^2+b^2}\tan\theta$$
$$dx = \sqrt{h^2+b^2}\frac{d\theta}{cos^2\theta}$$
$$when \quad x = a \Rightarrow \theta = \theta'' \quad then$$
$$a = \sqrt{h^2+b^2}\tan\theta''$$

$$\Omega = bh\int_0^{\theta''} \sqrt{h^2+b^2}\frac{d\theta'}{cos^2\theta'} \cdot \frac{1}{(h^2+b^2)\tan^2\theta' + h^2} \cdot \frac{1}{\sqrt{(h^2+b^2)\tan^2\theta' + h^2 + b^2}}$$

$$\Omega = bh\int_0^{\theta''} \sqrt{h^2+b^2}\frac{d\theta'}{cos^2\theta'} \cdot \frac{1}{(h^2+b^2)\tan^2\theta' + h^2} \cdot \frac{1}{\sqrt{(h^2+b^2)} \cdot \sqrt{1+\tan^2\theta'}}$$

We know the following:

$$1 + \tan^2\theta = \frac{1}{\cos^2\theta}$$

$$\Omega = bh\int_0^{\theta''} \frac{d\theta'}{\cos^2\theta'} \cdot \frac{1}{(h^2+b^2)\tan^2\theta' + h^2} \cdot \cos\theta'$$

$$\Omega = \frac{bh}{h^2}\int_0^{\theta''} \frac{d\theta'}{\cos\theta'} \cdot \frac{1}{(\frac{h^2+b^2}{h^2})\tan^2\theta' + 1}$$

$$\Omega = \frac{b}{h}\int_0^{\theta''} \frac{d\theta'}{\cos\theta'} \cdot \frac{1}{(1+\frac{b^2}{h^2})\tan^2\theta' + 1}$$

$$\Omega = \frac{b}{h}\int_0^{\theta''} \frac{d\theta'}{\cos\theta'} \cdot \frac{1}{(1+\frac{b^2}{h^2})\frac{\sin^2\theta'}{\cos^2\theta'} + 1} = \frac{b}{h}\int_0^{\theta''} \frac{d\theta'}{\cos\theta'} \cdot \frac{\cos^2\theta'}{(1+\frac{b^2}{h^2})\sin^2\theta' + \cos^2\theta'}$$

$$\Omega = \frac{b}{h}\int_0^{\theta''} \frac{\cos\theta' d\theta'}{(1+\frac{b^2}{h^2})\sin^2\theta' + 1 - \sin^2\theta'}$$

$$\Omega = \frac{b}{h}\int_0^{\theta''} \frac{\cos\theta' d\theta'}{\sin^2\theta' + \frac{b^2}{h^2} + 1 - \sin^2\theta'} = \frac{b}{h}\int_0^{\theta''} \frac{\cos\theta' d\theta'}{\frac{b^2}{h^2}\sin^2\theta' + 1} \tag{9.15}$$

For simplicity we will use $t = \theta''$ and for integration we assume that:

$t = \sin\theta' \Rightarrow dt = \cos\theta' d\theta'$

$$\Omega = \frac{b}{h}\int_0^{\sin\theta'} \frac{dt}{\frac{b^2}{h^2}t^2 + 1}$$

By taken another assumption:-

$$t = \frac{h}{b}\tan\theta'' \Rightarrow dt = \frac{h}{b}\frac{d\theta''}{\cos^2\theta''} \tag{9.16}$$

$$\Omega = \frac{b}{h}\int_0^{\theta''} \frac{h}{b}\frac{d\theta''}{\cos^2\theta''} \cdot \frac{1}{\frac{b^2}{h^2}\cdot\frac{h^2}{b^2}\tan^2\theta'' + 1} = \int_0^{\theta''} \frac{d\theta''}{cos^2\theta''} \cdot \frac{1}{1+\tan^2\theta''}$$

$$\Omega = \int_0^{\theta''} \frac{d\theta''}{\cos^2\theta''} \cdot cos^2\theta''$$

$$\Omega = \int_0^{\theta''} d\theta'' = \theta''$$

$$\Omega = \theta''|_0^{\sin\theta'}$$

$$\Omega = \sin\theta' \tag{9.17}$$

We know that:

$$\frac{1}{sin^2\theta} = 1 + \frac{1}{\tan^2}$$

$$a = \sqrt{h^2+b^2}\tan\theta'$$

$$\tan\theta' = \frac{a}{\sqrt{(h^2+b^2)}}$$

$$\tan^2\theta' = \frac{a^2}{(h^2+b^2)}$$

$$\frac{1}{sin^2\theta'} = 1 + \frac{1}{\frac{a^2}{(h^2+b^2)}} = 1 + \frac{h^2+b^2}{a^2}$$

$$\frac{1}{sin^2\theta'} = \frac{h^2 + b^2 + a^2}{a^2} \tag{9.18}$$

$$\sin\theta' = \frac{a}{\sqrt{h^2 + b^2 + a^2}} \tag{9.19}$$

From Eq.9.16 we know that:

$$\sin\theta' = \frac{h}{b}\tan\theta''$$

$$\frac{a}{\sqrt{h^2 + b^2 + a^2}} = \frac{h}{b}\tan\theta''$$

$$\Rightarrow \tan\theta'' = \frac{ab}{h} \cdot \frac{1}{\sqrt{h^2 + b^2 + a^2}}$$

$$\theta'' = \arctan[\frac{ab}{h} \cdot \frac{1}{\sqrt{h^2 + b^2 + a^2}}] \tag{9.20}$$

Appendix E

This appendix is divided into two main sections. The first section present the results that compare the MCS data of planar square objects with that from the PRT method. The second section present the results that compare the 2D object with the 3D object.

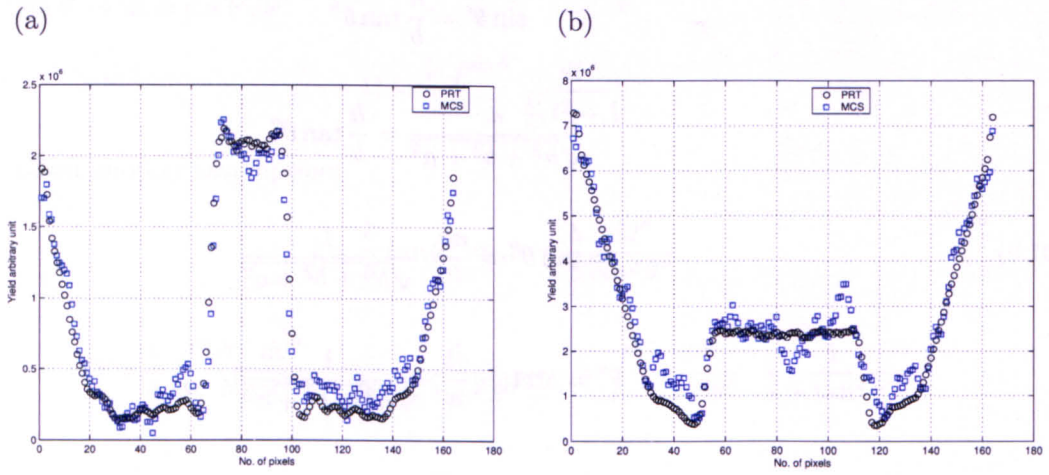

Figure 9.3: Exemplar vertical profiles of predicted flat field distortion from PRT method compared with the corresponding produced by 2D MCS data: (a) 2D source object of 2×2 cm^2, (b) 2D source object of 4×4 cm^2. The slight discrepancies remaining are due to photon statistics and MCS geometry specific effects such as mask thickness.

Imaging a 2D Uniform Object

The following set of results compared the predicted flat field distortion of 2D square source object. Figure 9.3 (a) and (b) present the predicted flat field distortion of size 2×2 cm^2 and 4×4 cm^2 from PRT method compared with the corresponding produced from MCS data. Figure 9.4 show another exemplar of the predicted flat field distortion of size 5×5 cm^2 and 10×10 cm^2 from PRT method compared with the corresponding produced from MCS data. The slight discrepancies remaining are due to photon statistics and MCS geometry specific effects such as mask thickness.

Imaging 2D & 3D Uniform Object

This section looked at the difference between the full 3D prediction of the background

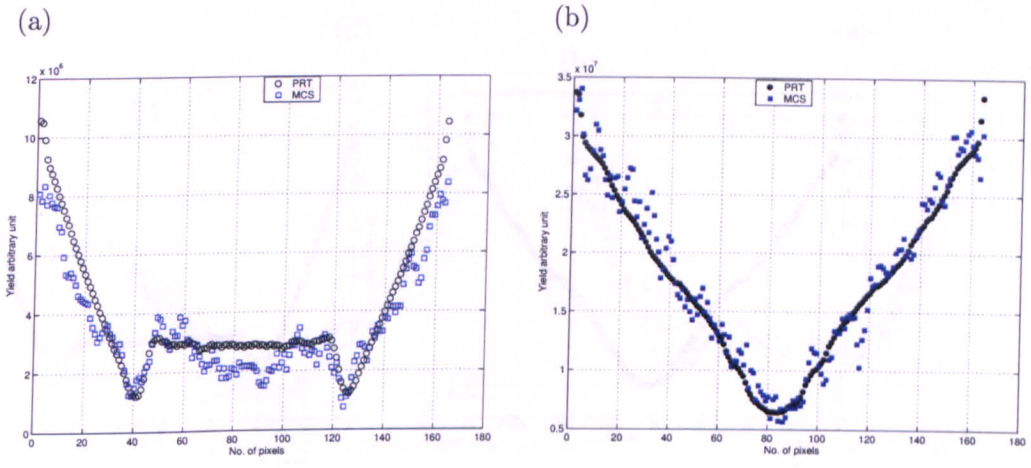

Figure 9.4: Exemplar vertical profiles of predicted flat field distortion from PRT method compared with the corresponding produced by 2D MCS: (a) 2D source object of 5×5 cm^2, (b) 2D source object of 10×10 cm^2 from PRT method (filled circle) compared with the corresponding produced by 2D MCS (filled square).

compare to just considering 2D in-plane effects from both the PRT as well as the MCS method. Exemplar vertical profiles through the decoded images of predicted 2D and 3D objects of different sizes obtained from the PRT method are shown in Fig. 9.5 and Fig. 9.6.

Having demonstrated that at a particular plane the predicted flat field distortion using the PRT method for a planar source is comparable to that obtained from the the 3D source object of similar size. The following set of results compare the flat field distortion of 2D square source object with the corresponding obtained from the 3D sourece object but with all data generated from the MCS. Exemplar vertical profiles through the decoded images oof planar object compared with 3D source object of different sizes are shown in Fig. 9.7 and Fig. 9.7. All data were obtained from the MCS method after least squares fit to normalise the distribution. The slight discrepancies remaining are due to photon statistics.

(a) (b)

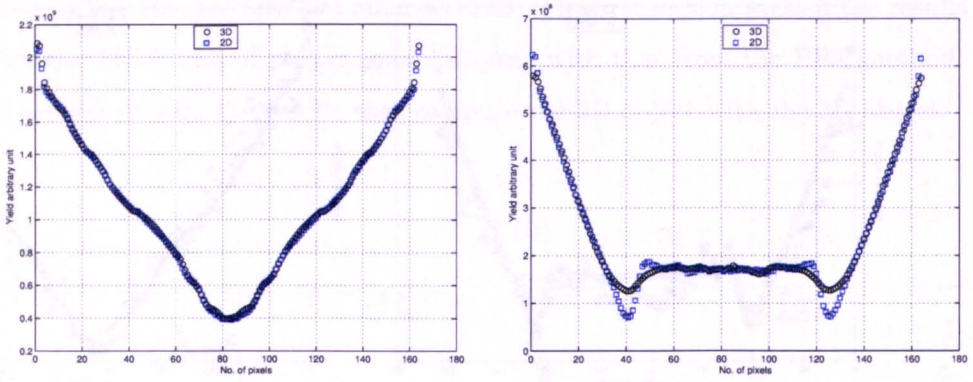

Figure 9.5: Exemplar vertical profiles through the decoded image of predicted 2D flat field distortion from the PRT method for a planar source compared with 3D source object after least squares fit to normalise the distribution: (a) planar square object of size 10×10 cm^2 compared with 3D object of 10×10×6 cm^3, (b) planar square object of size 5×5 cm^2 compared with 3D object of 5×5×6 cm^3.

(a) (b)

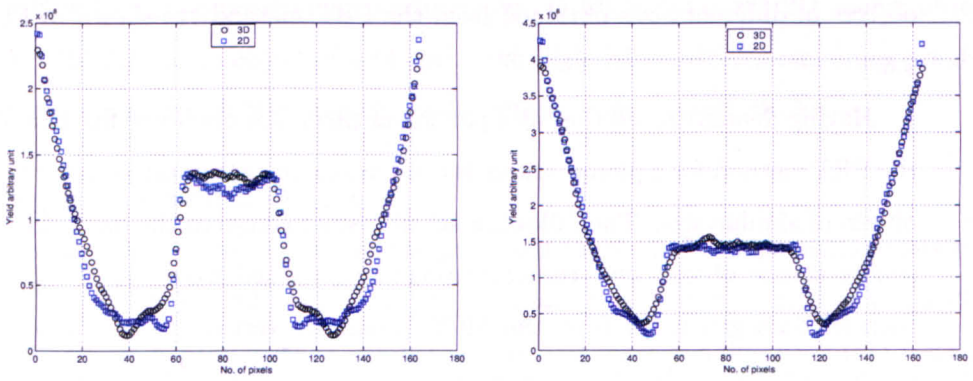

Figure 9.6: Exemplar vertical profiles through the decoded image of predicted 2D flat field distortion from the PRT method for a planar source compared with 3D source object after least squares fit to normalise the distribution: (a) planar square object of size 3×3 cm^2 compared with 3D object of 3×3×6 cm^3, (b) planar square object of size 4×4 cm^2 compared with 3D object of 4×4×6 cm^3.

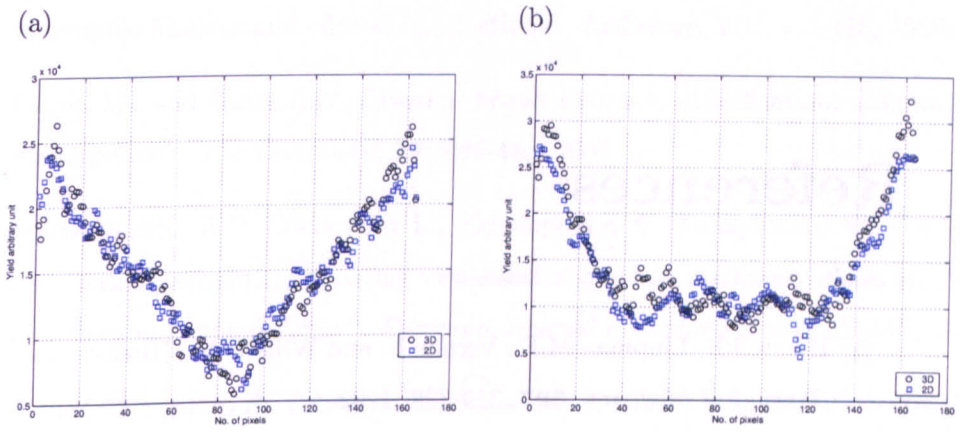

Figure 9.7: Exemplar vertical profiles through the decoded images of predicted 2D flat field distortion from the MCS method for a planar source compared with 3D source object after least squares fit to normalise the distribution: (a) planar square object of size 10×10 cm^2 compared with 3D object of 10×10×6 cm^3, (b) planar square object of size 5×5 cm^2 compared with 3D object of 5×5×6 cm^3.

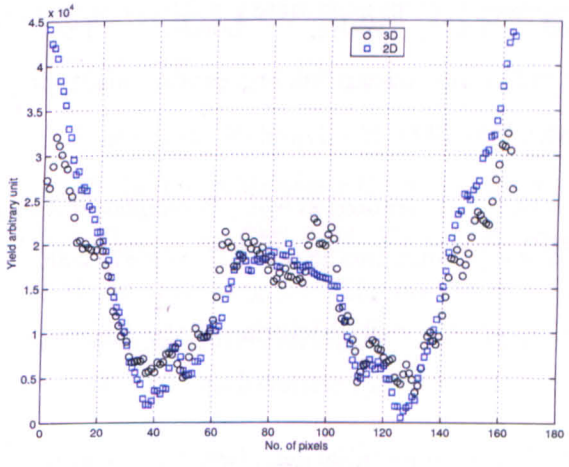

Figure 9.8: Exemplar vertical profiles through the decoded images of planar object compared with 3D source object. The planar square object of size 3×3 cm^2 compared with 3D object of 3×3×6 cm^3.

References

[1] Harris J.R, Lippman M.E., Verone U. and Willett W., "Breast cancer" *New England Journal of Medicine*, **327**, 319-328, 1992.

[2] The american cancer society, "Cancer facts and figures 2006", [http://www.cancer.org], retrieved on September. 2006.

[3] Cavalli F., Hansen H.H. and Kaye S.B., *Textbook of Medical Oncology*, Martin Dunits Ltd. ISBN: 1853172901, 1998.

[4] Kelsey J.L. and Gammon M.D., "The epidemiology of breast cancer", *Cancer*, **41**, 146-165, 1991.

[5] "Office for national statistics (2004) mortality statistics: Cause" England and Wales, London TSO, Cancer Research UK, [http://info.cancerresearchuk.org/cancerstats/types/breast/mortality/] retrieved on September, 2006.

[6] Tortora G.J. and Grabowski S.R., *Principles of Anatomy and Physiology*, New York, John Wiley & Sons, Inc. ISBN: 0471374687, 2000.

[7] The Cancer Council Victoria, [http://www.cancervic.org.au/cancer1/prevent/breasthealth/lcis.html], retrieved on Sept. 2006.

[8] Breast Cancer Organisation, [www.breastcancer.org/dcis_type_grade.html], retrieved on September, 2006.

[9] Sakorafas G.H., and Farley D.R., "Optimal management of ductal carcinoma in situ of the breast", *Surgical Oncology*, **12**, 4, 221-40, 2003.

[10] Dershaw D.D., Abramson A.F., and Kinne D.W., "Ductal carcinoma in situ: mammographic findings and clinical implications", *Radiology*, **170**, 411-415, 1989.

[11] Guray M., and Sahin A.A., "Benign breast diseases: classification, diagnosis, and management", *The Oncologist*, **11**, 435-449, 2006.

[12] Stefanoyiannis A.P, Costaridou L., Skiadopoulos S., Panayiotakis G., "A digital equalisation technique improving visualisation of dense mammary gland and breast periphery in mammography", *European Journal of Radiology*, **45**, 139-149, 2003.

[13] Pani R., Scopinaro F., Pellegrini R., Soluri A., Weinberg I.N., and Vincentis G. De, "The role of Compton background and breast compression on cancer detection in scintimammography", *Anticancer Research*, **17**, 3B, 1645-1649, 1997.

[14] Altman D.G., Bland J.M., "Diagnostic test 1: sensitivity and specificity", *British Medical Journal*, **308**, 1552, 1994.

[15] Altman D.G., Bland J.M., "Diagnostic test 2: predictive value", *British Medical Journal*, **309**, 102, 1994.

[16] Department of Health and Social Security, D. o. H. a. S., Ed., "Breast Cancer Screening: Report of a Working group chaired by Professor Sir Patrick Forrest", London, UK, H. M. S. O, 1986.

[17] Duffy S.W., Tabr L., Chen H.H., Holmqvist M., Yen M.F., Abdsalah S., Epstein B., Frodis E., Ljungberg E., Hedborg-Melander C., Sundbom A., Tholin M., Wiege M., kerlund A., Wu H.M., Tung T.S., Chiu Y.H., Chiu C.P., Huang C.C., Smith R.A., Rosn M., Stenbeck M., & Holmberg L., "The impact of organized mammography service screening on breast carcinoma mortality in seven Swedish counties". *Cancer*, **95**, 458-496, 2002.

[18] Kacl G.M., Liu P.F., Debatin J.F., Garzoli E., Caduff R.F., Krestin G.P., "Detection of breast cancer with conventional mammography and contrast-enhanced MR imaging", *European Radiology* , **8**, 2, 194-200, 1998.

[19] Kopans D.B., "The positive predictive value of mammography", *American Journal of Roentgen*, **158**, 521-526, 1992.

[20] Hendee W.R., "History and status of X-ray mammography." *Health Physics*, **69**, 5, 636-648, 1995.

[21] Sankararaman S., Karellas, Srinivasan Vedanthan, "Physical characteristics of a full-field digital mammography system" *Nuclear Instruments and Methods in Physics Research A*, **533**, 14, 560-570, 2004.

[22] James J.J., "The current status of digital mammography (Review)", *Clinical Radiology*, **59**, 1-10, 2004.

[23] Adler D.D., and Wahl R.L., "New methods for imaging the breast: techniques, findings, and potential", *American Journal of Roentgenology*, **164**, 19-30, 1995.

[24] Singletary S.E., Allred C., Ashley P., Bassett L.W., Berry D., Bland K.I., Borgen P.I., Clark G., Edge S.B., Hayes D.F., Hughes L.L., Hutter R.V.P, Morrow M., Page D.L., Recht A., Theriault R.L., Thor A., Weaver D.L., Wieand H.S., and Greene F.L., "Revision of the American joint Committee on cancer staging system for breast cancer", *journal of clinical oncology*, 20, 3628-3636, 2002.

[25] Strauss L.G., and Conti P.S., "The application of PET in clinical oncology", *Journal of Nuclear Medicine*, **32**, 4, 632-648, 1991.

[26] Stavrous A.T., Thickman D., Rapp C.L., Dennis M.A., Parker S.H., and Sisney G.A., "Solid breast nodule: use of sonography to distinguish between benign and malignant lesions", *Radiology*, **196**, 123-134, 1995.

[27] Weinreb J.C., and Newstead G., "MR Imaging of the Breast", *Radiology*, **196**, 593-610, 1995.

[28] Rankin S.C., "MRI of the breast", *British Journal of Radiology*, **73**, 872, 806-818, 2000.

[29] Sharp P.F., Gemmell H.G., and Smith F.W., *Practical nuclear medicine*, USA, Oxford University Press, ISBN: 0-19-26284-0, 1-12, 1998.

[30] Wahl R.L., "Current Status of PET in Breast Cancer Imaging, Staging, and Therapy", *Seminars in Roentgenology*, **36**, 3, 250-260, 2001.

[31] Adler L.P., Crowe J.P., Alkaisi N.K., and Sunshine J.L., "Evaluation of Breast Masses and Axillary Lymph Nodes with [F-18] 2-Deoxy-2-fluoro-D-glucose PET", *Radiology*, **187**, 3, 743-752, 1993.

[32] Strauss L.G., "PET in clinical oncology: current role for diagnosis and therapy monitoring in oncology", *The Oncologist*, **2**, 381-388, 1997.

[33] Price P., "Is there a future for PET in oncology?", *European Journal of Nuclear Medicine*, **24**, 6, 587-589, 1997.

[34] Bombardieri E., Aktolun C., Baum R.P., Bishof-Delaloye A., Buscombe J., Chatal J.F., Maffioli L. Moncayo R., Mortelmans L., and Reske S.N., "Breast scintigraphy: procedure guidelines for tumour imaging", *European Journal of Nuclear Medicine and Molecular Imaging*, **30**, 12, B107-B114, 2003.

[35] Maublant J., Zheng Z., Rapp M., Ollier M., Michelot J. and Veyre A. "In Vitro uptake of Technetium-99m-Teboroxime in carcinoma cells: comparison with Technetium-99m-Sestamibi and Thallium-201", *Journal of Nuclear Medicine*, **24**, 34, 1949-1952, 1993.

[36] Schillaci O., and Buscombe J.R., "Breast scintigraphy today: indications and limitations" *European Journal of Nuclear Medicine and Molecular Imaging*, **31**, S35-S45, 2004.

[37] Wiesenberger A.G., Barbosa F., Green T.D., Hoefer R., Keppel C., Kross B., Majewski S., Popor V., Wojcik R., and Wymer D.C., "A Combined Scintimammography/Stereotactic Core Biopsy X-ray", *Nuclear Science Symposium Conferece Record*, **3**, 2000

[38] Fondrinier E., Muratet J.P., Anglade E., Fauvet R., Breger V., Lorimier G., and Jallet P., "Clinical experience with ^{99m}Tc-MIBI scintimammography in patients with breast microcalcifications", *Breast*, **13**, 4, 316-320, 2004.

[39] Schillaci O., Scopinaro F., Spanu A., Donnetti M., Danieli R., Di Luzio E., Madeddu G., and David V., "Detection of axillary lymph node metastases in breast cancer with ^{99m}Tc tetrofosmin scintigraphy", *International Journal of Oncology*, **20**, 3, 483-487, 2002.

[40] Imbriaco M., Del Vecchio S., Riccardi A., Pace L., Di Salle F., Di Gennaro F., Salvatore M., Sodano A., "Scintimammography with ^{99m}Tc-MIBI versus dynamic MRI for non-invasive characterization of breast masses", *European Journal of Nuclear Medicine and Molecular Imaging*, **28**, 1, 2001.

[41] Buscome J.R., Cwikla J.B., Holloway B., Hilson A.J.W., "Prediction of the usefulness of combined mammography and scintimammography in suspected primary breast cancer using ROC curves", *Journal of Nuclear Medicine*, **42**, 3-8, 2001.

[42] Fahey F.H., Grow K.L., Webber R.L., Harkness B.A., Harkness B.A., Bayram E., and Hemler P.F., "Emission Tuned-Aperture Computed Tomography: A Novel Approach to Scintimammography." *Journal of Nuclear Medicine*, **42**, 7, 1121-1127, 2001.

[43] Scopinaro F., Ierardi M., Porfiri L.M., Tiberio N.S., De Vincentis G., Mezi S., Cannas P., Gigliotti T., Marzetti L., "^{99m}Tc-MIBI prone scintimammography in patients with high and intermediate risk mammography ", *Anticancer research*, **17**, 1635-1638, 1997.

[44] Gupta P., Waxman A., Nguyen K., Phillips E., Yadagar J., Silberman A., Memsic L., "Correlation of ^{99m}Tc-sestamibi uptake with histopathologic characteristics in patients with benign breast diseases", [Abstract], *Journal of Nuclear Medicine*, **37**, 5, 1122-1122, 1996.

[45] Coover L.R., Caravaglia G., Kunh P., "Scintimammography with dedicated breast camera detects and localizes occult carcinoma", *Journal of Nuclear Medicine*, **45**, 4, 553-558, 2004.

[46] Brem R.F., Schoonjans J.M., Kieper D.A., Majewski S., Goodman S., Civelek C., "High-resolution scintimammography: a pilot study", *Journal of Nuclear Medicine*, **43**, 909-915, 2002.

[47] Brem R.F., Kieper D.A., Rapelysea J.A., Majewski S., "Evaluation of a high-resolution, breast-specific, small-field-of-view gamma camera for the detection of breast cancer", *Nuclear Instruments and Methods in Physics Research Section A*, **497**, 1, 39-45, 2003.

[48] Rhodes D.J., O'Connor M.K., Phillips S.W., Smith R.L., Collins D.A., "Molecular breast imaging: a new technique using ^{99m}Tc- scintimammography to detect small tumours of the breast", *Mayo Clinic Proceedings*, **80**, 24-30, 2005.

[49] Brem R.F., Rapelyea J.A., Zisman G., Mohtashemi K., Raub J., Teal C.B., Majewski S., Welch B.L., "Occult breast cancer: scintimammography with high-resolution breast-specific gamma camera in women at high risk for breast cancer",*Radiology*, **237**, 1, 274-280, 2005.

[50] Scopinaro F., Pani R., De Vincentis G., Soluri A., Pellegrini R., Porfiri L.M., "High-resolution scintimammography improves the accuracy of technetium-99m methoxy-isobutylisonitrile scintimammography: use of a new dedicated gamma camera", *European Journal of Nuclear Medicine and Molecular Imaging*, **40**, 1279-1288, 1999.

[51] Taillefer R., "The Role of ^{99m}Tc-sestamibi and other conventional radiopharmaceuticals in breast cancer diagnosis", *Seminars in Nuclear Medicine*, **XXIX**, 1, 16-40, 1999.

[52] Hartsough N., Pi B., Gormley J., Conwell R., Ashburn W., "Performance characteristic of a compact, quantized gamma camera", [abstract], *Journal of Nuclear Medicine*, **40**, 227, 1999.

[53] Itti E., Patt B.E., Diggles L.E., MacDonald L., Iwanczyk J.S., Mishkin F.S. and Khalkhali I., "Improved scintimammography using a high-resolution camera mounted on an upright mammography gantry", *Nuclear Instruments and Methods in Physics Research*, **497**, 1, 1-8, 2003.

[54] Gamma Medica, LumaGEM, [http://www.gammamedica.com/products/luma.html], retrieved on July 2006.

[55] Gamma Medica, LumaGEM, [http://www.gammamedica.com/articles/ DiScan.pdf], retrieved on July 2006.

[56] Singh M., "An electronically collimated gamma camera for single photon emission computed tomography. Part I: Theoretical considerations and design criteria". *Medical Physics*, **10**, 4, 421-7, 1983.

[57] Singh M., Doria D., "An electronically collimated gamma camera for single photon emission computed tomography. Part II: Image reconstruction and preliminary experimental measurements", Medical Physics, **10**, 4, 428-35, 1983.

[58] Royle G.J., Speller R.D., "Design of a Compton camera for imaging 662 keV radionuclide distributions" *Nuclear Instruments and Methods in Physics Research A*, **1994**, 348, 623-626, 1994.

[59] Barrett H.H., "Fresnel Zone Plate Imaging in Nuclear Medicine", *Journal of Nuclear Medicine*, **4**, 6, 382-385, 1972.

[60] Cannon T.M., and Fenimore E.E., "Tomographic Imaging Using Uniformly Redundant Arrays", *Applied Optics* **18**, 7, 1052-1057, 1979.

[61] Palamer D., and Prince T.A., "A laboratory demonstration of high resolution hard X-ray and γ-ray imaging using a Fourier transform technique", *IEEE Transaction in Nuclear Science*, **32**, 17-21, 1987.

[62] Mertz L., and Young N.O., "Fresnel Transformation of Image", *Proceeding International Conference Optical Instrumentation*, Chapman & Hall, London, 305-312, 1961.

[63] Dicke R.H., "Scatter-hole Cameras for X-rays and gamma Ray", *Astro-physical Journal*, **153**, 2, L101-L106, 1968.

[64] Ables J.G, "Fourier transform photography: a new method for X-ray astronomy", *Proceeedings of the Astronomic Society of Australia*, **1**, 4, 172-173, 1968.

[65] Webb S., *The Physics of Medical Imaging*, Institute of Physics Publishing, Bristol and Philadelphia. ISBN: 0-85274-349-1, 1988.

[66] Barrett H.H. and Swindell W., *Radiological imaging: the theory of image formation, detection and Processing*, London, Academic Press, Inc, ISBN: 0-12-079601-5, 1981.

[67] Fenimore E.E., and Cannon T.M., "Uniformly redundant arrays", *Proceeding Digital Signal Processing Symposium*, **6**, 7, 479-493, 1977.

[68] Fenimore E.E., and Cannon T.M., "Coded aperture imaging with uniformly redundant array", *Applied Optics*, **17**, 3, 337-347, 1978.

[69] Gottesman, S.R., and Fenimore, E.E., "New family of binary arrays for coded aperture imaging", *Applied Optics*, **28**, 4344-4352, 1989.

[70] Fenimore E.E., and Cannon T.M., "Uniformly redundant arrays: digital reconstruction methods", *Applied Optics*, **20**, 10, 1858-1864, 1981.

[71] Fenimore, E.E., "Coded aperture imaging: predicted performance of uniformly redundant array", *Applied Optics* **17**, 22, 3562-3570, 1978.

[72] Meikle S.R., Fulton R.R., Eberl S., Dahlbom M., Wong K. and Fulham M.J., "An investigation of coded aperture imaging for small animal SPECT", *IEEE Transactions on nuclear science*, **NS-48**, 3, 816-821, 2001.

[73] Dunphy P., McConnell M., Owens A., Chupp E., Forrest D., and Googins J., "A balloon-borne coded aperture telescope for low-energy gamma-ray astronomy", *Nuclear Instruments and Methods in Physics Research Section A*, **274**, 362-379, 1989.

[74] Gemmill P.E., Chaney R.C., and Fenyves E.J., "Monte-Carlo simulation of a coded aperture SPECT apparatus using uniformly redundant arrays", *Imaging detectors in high energy and astroparticle physics*, Los Angeles, CA, Singapore, 81-115, 1995.

[75] Zhang L., Lanza R.C., Horn B.K.P., and Zimmerman R.E., "Three-dimensional coded aperture techniques in diagnostic nuclear medicine imaging". *SPIE Conference on Physics of Medical Imaging*, **3336**, 364-373, 1998.

[76] Vassilieva O.I. and R. C. Chaney, "Method for reducing background artifacts from images in single-photon emission computed tomography with a uniformly redundant array coded aperture" *Applied Optics*, **41**, 7, 1454-1461, 2002.

[77] Anger H.O., "Sintillation camera with multichannel collimators", *Journal of Nuclear Medicine*, **5**, 515-531, 1964.

[78] Anger H.O., "Survey of radioisotope cameras", *Instrument Society of America*, **5**, 311-344, 1966.

[79] Connolly P.L., Treves S.T., Davis R.T., and Zimmerman R., "Pediatric application of pinhole magnification imaging" *The Journal of Nuclear Medicine*, **40**, 11, 1896-1901, 1999.

[80] Amersham Health medencyclopaedia, "Encyclopaedia of Medical Imaging". [www.amershamhealth.com/medcyclopaedia/medical], retreived on March 2003.

[81] Sharp P.F., Dendy P.P., Keyes W.I., *Radionuclide Imaging Techniques*, London, UK, Academic Press, 1985.

[82] Ott R.J., Flower M.A.,Babich J.W. and Marsden P.K., "The Physics of Radioactive Imaging" in *The Physics of Medical Imaging* , Bristol, Adam Hilger, 142-157, 1988.

[83] Spanu A., Dettori G., Nuvoli S., Porcu A., Falchi A., Cottu P., Solinas M.E., Scanu A.M., Chessa F., Madeddu G., "^{99m}Tc-tetrofosmin SPET in the detection of both primary breast cancer and axillary lymph node metastasis", *European Journal of Nuclear Medicine*, **28**, 12, 1781-1794, 2001.

[84] Taillefer R., "Clinical application of ^{99m}Tc-sestamibi scintimammography", *Seminars in Nuclear Medicine*, **35**, 100-115, 2005.

[85] Khalkhali I., Mena I., and Jounne E. "Prone scintimammography in patients with suspicion of carcinoma of the breast", *Journal of American Colleage Surgery*, **178**, 491-497, 1994.

[86] Carvahlo P.A., Chiu M.L., kronaug J.F., "Subcellular distribution and analysis of ^{99m}Tc MIBI in isolated perfused rat heart", *Journal of Nuclear Medicine*, **33**, 1516-1521. 1992.

[87] Gopalan D., Bomanji J.B., Costa D.C., and Ell P.J., "Nuclear medicine in primary breast cancer imaging." *Clinical Radiology*, **57**, 7, 565-574, 2002.

[88] Mansi L., Rambaldi P.F., Procaccini E., Gregorio F.D., Laprovitera A., Picori B., and Vecchio W.D., "Scintimammography with ^{99m}Tc-tetrofosmin in the diagnosis of breast cancer and lymph node metastases", *European Journal of Nuclear Medicine*, **23**, 8, 932-939, 1996.

[89] Medical Advisory Secretariate, Ontario ministry of health and long-term care, "Scintimammography", Toronto: Ontario ministry of health and long-term care; 2003.

[90] Tolmos J., Cutrone J.A., Wang B., Vargas H.I., Stuntz M., Mishkin F.S., Diggles L.E., Venegas R.J., Klein S.R., Khalkhali I., "Scintimammographic analysis of

non-palpable breast lesions previously identified by conventional mammography", *Journal of the National Cancer Institute*, **90**, 11, 846-849, 1998.

[91] Derebek E., "Detection of bilateral multifocal breast cancer using ^{99m}Tc-sestamibi imaging: The role of delayed imaging", *Clinical Nuclear Medicine*, **24**, 8, 590-593, 1999.

[92] Itti E., Ahdoot H., Khalkhali I., "Scintimammography for the diagnosis of breast cancer", *Journal of Women's Imaging*, **4**, 2, 66-72, 2002.

[93] Bruening W., Launders J., Pinkney N., Kostinsky H., Schoelles K., Kurkelson C., "Effectiveness of non-invasive diagnostic tests for breast abnormalities: Comparative effectiveness review No.2" (Prepared by ECRI Evidence-Based Practice Center, Contract No. 290-02-0019), Rockville, MD: Agency for Healthcare Research and Quality. [www.effectivehealthcare.ahrq.gov/reports/final.cfm], retrieved on December 2006.

[94] Majewski S., Kieper D., Keppel C., "Optimization of dedicated scintimammography procedure using small detector prototypes and compressible breast phantoms", [abstract], *Presented at the IEEE Medical Imaging Conference*, Lyon, France, October, 2000.

[95] Brown C., "Multiplex imaging with multiple pinhole camera", *Journal of Applied Physics* **45**, 4, 1806-1810, 1974.

[96] Caroli E., Stephen J.B., Di Cocco G., Natalucci L., and Spizzichino A., "Coded aperture imaging in X- and γ-ray astronomy", *Space Science Reviews*, **45**, 349-403, 1987.

[97] Rogers W.L., Han K.S., Jones L.W., Beierwaltes W.H., "Application of a Fresnel zone plate to γ-ray imaging", *Journal of Nuclear Medicine*, **13**, 8, 612-615, 1972.

[98] Fenimore E.E., Cannon T.M., and Miller E.L., "comparison of Fresnel zone plates and uniformily redundent arrays", *SPIE*, **149**, 232-236, 1978.

[99] Busboom A., Elder-boll H., and Schotten H.D., "Uniformily redundant arrays", *Experimental Astronomy*, **8**, 97-123, 1998.

[100] Golay M.J.E., "Point arrays having compact, nonredundant autocorrelations", *Journal of the Optical Society of America*, **61**, 272, 1971.

[101] Gourlay A.R., and Stephen J.B., "Geometric coded apertures", *Applied Optics*, **22**, 24, 4042-4047, 1983.

[102] Gourlay A.R., and Young N.G., "Coded aperture imaging: a class of flexible mask designs", *Applied Optics*, **23**, 22, 4111-4117, 1984.

[103] Gourlay A.R., Stephen J.B., and Young N.G., "Geometrically designed coded aperture masks", *Nuclear Instruments and Methods in Physics Research A*, **221**, 54-55, 1984.

[104] Accorsi R.F., and Lanza R.C., "Near-field artifact reduction in coded aperture imaging", *Applied Opttics* **40**, 26, 4697-4705, 2001.

[105] Baumert L.D., *Lecture Notes in Mathematics No. 182: Cyclic Difference Sets*, (Berlin: Springer), 1971.

[106] MacWilliams F.J., and Sloane N.J.A., "Pseduo-Random Sequence and Arrays", *Proceeding of the IEEE* **64**, 1806, 1976.

[107] Calabro C., and Wolf J.K., "On the Synthesis of Two-Dimensional Arrays with Desirable Correlation Properties", *Information and Control*, **11**, 537-560, 1967.

[108] Jayanthi U.B., and Braga J., "Physical implementation of an antimask in URA based coded mask systems", *Nuclear Instruments and Methods in Physics Research*, **A310**, 685-689, 1991.

[109] Skinner G.K., "Imaging with Coded-Aperture Masks", *Nuclear Instruments and Methods in Physics Research A*, **221**, 33-40, 1984.

[110] Jiang S. Wu Z., Ma T., and Jin Y., "Design of Coded Aperture Collimator for High resolution & High sensitivity MicroSPECT", *Conference Record Nuclear Science Symposium and Medical Conference*, 2004.

[111] Briesmeister J.F., Ed., *MCNPC4B2 Monte Carlo N-Particle Transport Code System, Report CCC-660*, Los Alamos National Laborator, 1998.

[112] Ljungberg M., Strand S.E., King M.A., (Eds), *Monte Carlo Calculations in Nuclear Medicine: Applications in Diagnostic Imaging*, Institute of Physics Publishing, Bristol, 1998.

[113] Zaidi H., "Relevance of accurate Monte Carlo modeling in nuclear medical imaging", *Medical Physics*, **26**, 574-608, 1999.

[114] AssiK., Breton V., Buvat I., Comtat C, Jan S., Krieguer M., Lazaro D., Morel C., Rey M., Santin G., Simon L., Staelens S., Strul D., Vieira J., and Van de Walle R., "Monte Carlo simulation in PET and SPECT instrumentation using GATE", *Nuclear Instruments and Methods in Physics Research A*, **527**, 1-2 , 180-189, 2004.

[115] Carrier J.F., Archambault L., Beaulieu L., and Roy R., "Validation of GEANT4, an object-oriented Monte Carlo toolkit, for simulations in medical physics", *Medical Physics*, **31**, 3, 484-492, 2004.

[116] Briesmeister J.F., Ed., *MCNP-A General Monte Carlo N-Particle Transport Code, Version 4B*, LA-12625-M, 1997.

[117] Knoll G., *Radiation Detection and Measurement*,3rd ed., John Wiley and Sons Inc., New York, USA, 1999.

[118] Saripan M.I., Wells K., Petrou M., Alnafea M.A. and Guy M., "Design of a Multihole collimator gamma camera model for use in Monte Carlo simulation", *Proceeding of the Medical Image Understanding and Analysis*, **1**, 87-90, 2005.

[119] DeVries D.J., and Moore S.C.," Development and validation of a Monte Carlo simulation of photon transport in an Anger camera", *IEEE Transaction on Medical Imaging*, **9**, 430-438, 1990.

[120] Westmore M.A, "Study Into the Feasibility of Applying Symetrica Spectral Deconvolution Techniques to Gamma Camera Data", Masters thesis, Department of Physics, University of Surrey, September 2003.

[121] Beattie R.J.D., and Byrne. J., "A Monte Carlo program for evaluating the response of a scintillation counter to monoenergetic gamma rays" *Nuclear Instruments and Methods* **104**, 163168, 1972.

[122] DeVries D.J., and Moore S.C.,"Comparison of hexagonal hole and square hole collimator by Monte Carlo simulation", *IEEE Nuclear Science Symposium Conference*, **3**, 52-56, 2000.

[123] XCOM program, [http://physics.nist.gov/physrefData/xcom1.html], 2003.

[124] Alnafea M.A., Wells K., Spyrou N.M., and M. Guy, "A Near Field Correction for Coded Aperture Imaging in Scintimammography" *Conference Record on 2006 Nuclear Science Symposium and Medical Conference.*

[125] Gotoh H., and Yangi H., "Solid angle subtended by a rectangular slit", *Nuclear Instrument and Method in physics reasach* **221**, 56-59, 1971.

[126] Fenimore E.E., "Coded aperture Imaging: the modulation transfere function for uniformly redundant arrays", *Applied Optics*, **19**, 14, 2465-2471, 1980.

[127] Pani R., De Vincentis G., Scopinaro, F., "Dedicated gamma camera for single photon emission mammography (SPEM)", *IEEE Transaction in Nuclear Science*, **NS-45**, 3127-3133, 1998.

[128] ICRU, tissue substitutes in radiation dosimetry and measurement, Report 44 of the International Commission on Radiation Units and Measurements, 1989.

[129] Charalambous P.M., Dean A.J., Stephen J.B. and Young N.G.S., "Aberrations in Gamma-Ray imaging systems", *Nuclear instruments and Methods in physics reasach* **221**, 56-59, 1984.

[130] Mueller B., OConnor M.K., Blevis I., Rhodes D.J., Smith R., Collins D.A, and Phillips S.W., "Evaluation of a small cadmium zinc telluride detector for scintimammography" *Journal of Nuclear Medicine*, **44**, 602-606, 2003.

[131] Archer C.N., Tornai M. "Investigation of full-field CZT detector for emission Mammography", *Conference Record on 2004 Nuclear Science Symposium and Medical Conference*, 2667-2671, 2004.

[132] Rzeszotarski M.S., "The AAPM/RSNA physics tutorial for Residents", *Radiographics*, **19**, 765-782, 1999.

[133] Hammersley A., Ponman T., and Skinner G., "Reconstruction of images from a coded-aperture box camera", *Nuclear Instruments and Methods* **A 311**, 585-591, 1992.

[134] Hong B., Zhiping Mu and Liu Y., "A new approach of 3D SPECT reconstruction of near-field coded aperture imaging", *Proceedings of SPIE, Medical Imaging*, **6142**, 2006.

List of Publications:

The following publications have resulted from the work documented in this thesis.

1. M. I. Saripan, K. Wells, M. Petrou, **M. A. Alnafea** and M. Guy, "Design of a Multi-hole collimator gamma camera model for use in Monte Carlo simulation". *Proceeding of the Medical Image Understanding and Analysis.* 1:87-90, 2005.

2. K. Wells, **M. A. Alnafea**, A. Tumian, A. Zapros, M. I. Saripan,M. Guy and P. Hinton, "Optimal energy window selection for Emission Computed Tomography". *Conference Record on 2005 Nuclear Science Symposium and Medical Conference.* 4:2049-2053, 2005.

3. **M. A. Alnafea**, K. Wells, N. M. Spyrou, M. I. Saripan, M. Guy and and P. Hinton, "Preliminary results from a Monte Carlo study of breast tumour imaging with low energy high-resolution collimator and a modified uniformly-redundant array-coded aperture", *Nuclear Instrument and Method A* 563:146-149, 2006.

4. **M. A. Alnafea**, K. Wells, N. M. Spyrou, M. I. Saripan, M. Guy and and P. Hinton, "Optimisation of Coded Aperture Imaging with Gamma Camera System for Breast Tumour Imaging" [Abstract]. *Presented at the IWORID-7 Conference, Grenoble, France, 2005.*

5. **M. A. Alnafea**, K. Wells, N. M. Spyrou and M. Guy, "Preliminary Monte Carlo study of coded aperture imaging with a CZT gamma camera system for scintimammography", *Nuclear Instrument and Method A* 573:122-125, 2007.

6. **M. A. Alnafea**, K. Wells, N. M. Spyrou, and M. Guy, "A Near Field Correction for Coded Aperture Imaging in Scintimammography" *Conference Record on 2006 Nuclear Science Symposium and Medical Conference.*